

|   |                             |                                |  |  |  |  |
|---|-----------------------------|--------------------------------|--|--|--|--|
| <b>REPORT DOCUMENTATION PAGE</b>  |                             |                                |  |  | <i>Form Approved</i><br>OMB No. 0704-0188                            |  |
| The public reporting burden for this collection of information is estimated to average 1 hour per response, including the time for reviewing instructions, searching existing data sources, gathering and maintaining the data needed, and completing and reviewing the collection of information. Send comments regarding this burden estimate or any other aspect of this collection of information, including suggestions for reducing the burden, to Department of Defense, Washington Headquarters Services, Directorate for Information Operations and Reports (0704-0188), 1215 Jefferson Davis Highway, Suite 1204, Arlington, VA 22202-4302. Respondents should be aware that notwithstanding any other provision of law, no person shall be subject to any penalty for failing to comply with a collection of information if it does not display a currently valid OMB control number.<br><b>PLEASE DO NOT RETURN YOUR FORM TO THE ABOVE ADDRESS.</b> |                             |                                |  |  |  |  |
| <b>1. REPORT DATE (DD-MM-YYYY)</b><br>20-05-2015  |                             | <b>2. REPORT TYPE</b><br>Final |  |  | <b>3. DATES COVERED (From - To)</b><br>20120321 - 20150320           |  |
| <b>4. TITLE AND SUBTITLE</b><br><br>Topological insulators and superconductors for innovative devices   |                             |                                |  | <b>5a. CONTRACT NUMBER</b><br>FA2386-12-1-4038   |  |  |
|   |                             |                                |  | <b>5b. GRANT NUMBER</b><br>Grant 12RSZ078 124038 |  |  |
|   |                             |                                |  | <b>5c. PROGRAM ELEMENT NUMBER</b><br>61102F      |  |  |
| <b>6. AUTHOR(S)</b><br><br>Prof. Yoichi Ando  |                             |                                |  | <b>5d. PROJECT NUMBER</b>                        |  |  |
|   |                             |                                |  | <b>5e. TASK NUMBER</b>                           |  |  |
|   |                             |                                |  | <b>5f. WORK UNIT NUMBER</b>                      |  |  |
| <b>7. PERFORMING ORGANIZATION NAME(S) AND ADDRESS(ES)</b><br>Osaka University<br>8-1 Mohogaoka, Ibaraki<br>Osaka 567-0047<br>Japan  |                             |                                |  |  | <b>8. PERFORMING ORGANIZATION REPORT NUMBER</b><br><br>N/A           |  |
| <b>9. SPONSORING/MONITORING AGENCY NAME(S) AND ADDRESS(ES)</b><br><br>AOARD<br>UNIT 45002<br>APO AP 96338-5002  |                             |                                |  |  | <b>10. SPONSOR/MONITOR'S ACRONYM(S)</b><br><br>AFRL/AFOSR/IOA(AOARD) |  |
|   |                             |                                |  |  | <b>11. SPONSOR/MONITOR'S REPORT NUMBER(S)</b><br>AOARD-124038        |  |
| <b>12. DISTRIBUTION/AVAILABILITY STATEMENT</b><br><br>Distribution A: Approved for public release. Distribution is unlimited.   |                             |                                |  |  |  |  |
| <b>13. SUPPLEMENTARY NOTES</b>  |                             |                                |  |  |  |  |
| <b>14. ABSTRACT</b><br>Topological insulators are characterized by peculiar surface states hosting Dirac fermions with spinmomentum locking, which hold promise for various innovative devices. Similarly, topological superconductors are associated with exotic surface states, which often consist of Majorana fermions that may be a game changer for quantum computing.  |                             |                                |  |  |  |  |
| <b>15. SUBJECT TERMS</b><br><br>Electronic Materials, Superconducting Materials   |                             |                                |  |  |  |  |
| <b>16. SECURITY CLASSIFICATION OF:</b>  |                             |                                | <b>17. LIMITATION OF ABSTRACT</b><br><br>SAR | <b>18. NUMBER OF PAGES</b><br><br>82             | <b>19a. NAME OF RESPONSIBLE PERSON</b><br>Seng Hong, Ph.D.           |  |
| <b>a. REPORT</b><br><br>U   | <b>b. ABSTRACT</b><br><br>U | <b>c. THIS PAGE</b><br><br>U   |  |  | <b>19b. TELEPHONE NUMBER (Include area code)</b><br>+81-4-2511-2000  |  |

# **Final Report**

**Title:**

## **Topological Insulators and Superconductors for Innovative Devices**

**AFOSR/AOARD Reference Number:** AOARD-124038

**AFOSR/AOARD Program Manager:** Seng Hong, Ph.D.

**Period of Performance:** 21 March 2012 - 20 March 2015

**Submission Date:** 20 March 2015

**PI: Yoichi Ando**, Professor, Institute of Scientific and Industrial Research (ISIR), Osaka University

8-1 Mihogaoka, Ibaraki, Osaka 567-0047, Japan

Tel: +81-6-6879-8440 / Fax: +81-6-6879-8444

**Objectives:**

Topological insulators are characterized by peculiar surface states hosting Dirac fermions with spin-momentum locking, which hold promise for various innovative devices. Similarly, topological superconductors are associated with exotic surface states, which often consist of Majorana fermions that may be a game changer for quantum computing. This project builds on the past achievements of the PI to explore novel quantum phenomena in topological insulators and superconductors for their fundamental understanding and for conceiving devices with unprecedented functionalities. Specifically, the PI will seek to synthesize single crystals of topological insulators with low bulk carrier density; grow high-quality thin films of topological insulators and hybrid structures for device applications; build fundamental understanding of topological insulators; elucidate the novel topological superconducting state and the nature of helical Majorana fermions in superconductors derived from topological insulators; discover/synthesize new topological superconductors; and explore the ways to detect/manipulate Majorana fermions.

**Status of effort (200 words or less):**

The project went on very well and produced a number of important results. Most notably, we have achieved the experimental discovery of a new kind of topological material called "topological crystalline insulator", and the result was published in *Nature Physics*. In our investigations of novel physical properties of topological insulators, most notably we have demonstrated for the first time the "topological protection" of the surface transport in topological insulators (PRL) and we discovered a new phenomenon called "topological proximity effect" (*Nature Communications*). For spintronics, we have demonstrated the spin-electricity conversion induced by spin injection into the topological surface states (PRL); also, we have demonstrated the electrical detection of the spin polarization due to charge flow in the surface state (*Nano Lett.*). In the superconductivity research, we have identified two new promising candidates, In-doped SnTe (PRL) and  $\text{Cu}_x(\text{PbSe})_5(\text{Bi}_2\text{Se}_3)_6$  (PRB), for time-reversal-invariant topological superconductor to host helical Majorana fermions. In 2013, the PI has published an authoritative review article on topological insulator materials in *J. Phys. Soc. Jpn.* as an invited paper, which is highly regarded in the community and is already cited 121 times, establishing himself as a leading expert in this emerging field.

**Abstract of important results:**Experimental Discovery of "topological crystalline insulator"

[*Nature Physics* 8 (2012) 800-803]

In 2011, existence of a conceptually new class of topological materials called "topological crystalline insulator" has been theoretically proposed, and in 2012 its possible realization in the narrow-gap semiconductor SnTe was suggested based on first-principle calculations. We have experimentally discovered that SnTe is indeed such a new topological material hosting an *even number* of Dirac cones in the Brillouin zone (as opposed to an odd number of Dirac cones in topological insulators). One can consider topological crystalline insulators to be cousins of topological insulators; namely, the topological surface in the former is protected by a point-group symmetry of the crystal, while in the latter it is protected by the time-reversal symmetry. Our experimental discovery demonstrates that there can be many more kinds of topological materials other than the topological insulators, which greatly widens our scope of topological states of matter. Therefore, this result is of fundamental importance in condensed matter physics.

Because of the particular importance of this result to the physics community, our paper was highlighted in the News & Views section of *Nature Physics* as "The great topological expansion".

It should be mentioned that three preprints reporting the experimental discovery of a topological crystalline insulator were posted to the arXiv at nearly the same time in June 2012, and two of them, our paper and the other one from a Polish group, were published online on the same day (30 September 2012) in *Nature Physics* and in *Nature Materials*, respectively.

Discovery of a new candidate topological superconductor

[*Phys. Rev. Lett.* 109 (2012) 217004-(1-5)]

In 2011, we discovered that a superconducting doped topological insulator,  $\text{Cu}_x\text{Bi}_2\text{Se}_3$ , is possibly the first example of a time-reversal-invariant topological superconductor which hosts massless and helical Majorana

fermions on the surface. However, this material turned out to be intrinsically inhomogeneous, which hindered detailed studies of the possible topological superconductivity. In this work, we have discovered that a superconducting doped topological crystalline insulator,  $\text{Sn}_{1-x}\text{In}_x\text{Te}$ , presents a signature of surface Majorana fermions and, hence, this system is also a possible example of a time-reversal-invariant topological superconductor. Since this material is homogeneous and is 100% superconducting (as opposed to a limited superconducting volume fraction in  $\text{Cu}_x\text{Bi}_2\text{Se}_3$ ),  $\text{Sn}_{1-x}\text{In}_x\text{Te}$  offers a new and robust playground for studying the possible topological superconductivity. Furthermore, similarities between  $\text{Cu}_x\text{Bi}_2\text{Se}_3$  and  $\text{Sn}_{1-x}\text{In}_x\text{Te}$  point to a useful guiding principle for the search of topological superconductivity.

This paper was published in *Physical Review Letters*, but was also featured in the Editors' Choice section in *Science* as a highlight of the recent literature in Physics.

#### Achieving surface quantum oscillations in topological insulator thin films of $\text{Bi}_2\text{Se}_3$

[Adv. Mater. 24 (2012) 5581-5585]

We have developed a new protocol for the MBE-growth of the prototypical topological insulator  $\text{Bi}_2\text{Se}_3$  and succeeded in growing world-best thin films (in terms of the size of the atomically flat terraces and transport properties) of this material. Our films are of sufficiently high quality to consistently present Shubnikov-de Haas oscillations, which has so far been difficult to achieve in topological insulator thin films. This result was published in *Advanced Materials*, a prestigious journal in the materials science field (IF = 13.877).

#### Demonstration of the "topological protection" in transport properties of epitaxial $\text{Bi}_2\text{Se}_3$ thin films

[Phys. Rev. Lett. 109 (2012) 066803-(1-5)]

We have discovered in topological-insulator thin films that the metallic transport through the topological surface state is suddenly diminished when the film thickness becomes so thin that a 3D-to-2D crossover takes place. Such a dimensional crossover causes the 2D surface state to lose its topological protection, which in turn degrades the transport through the surface; in this sense, it is a striking manifestation of the topological protection. This result was published in *Physical Review Letters* and was selected for the Editors' Suggestion.

Furthermore, this paper was highlighted in the Synopsis section of *Physics*, which is an online journal of the American Physical Society to highlight a selection of papers from the *Physical Review* journals to publicize exceptional research.

#### Manipulation of the topological states and the bulk band gap using naturally-occurring heterostructures

[Phys. Rev. Lett. 109 (2012) 236804-(1-5)]

We have synthesized bulk single crystals of a homologous series  $(\text{PbSe})_5(\text{Bi}_2\text{Se}_3)_{3m}$ , which form naturally-occurring heterostructures of a topological insulator,  $\text{Bi}_2\text{Se}_3$ , and an ordinary insulator, PbSe. In these compounds, we discovered that the topological surface state is encapsulated in each  $\text{Bi}_2\text{Se}_3$  block. This means that the "bulk" transport in this material is essentially a sum of 2D transport channels through all the  $\text{Bi}_2\text{Se}_3$  blocks, indicating that one can utilize the topological transport properties as "bulk" properties in this class of bulk single crystals. Furthermore, we found that the quantum confinement effect causes the bulk band gap to be enhanced, pointing to a way to make topological insulators useful at room temperature.

This work pioneers a conceptually new strategy, utilization of the naturally-occurring heterostructures in bulk crystals, for materials developments of topological insulators.

#### Anomalous Dressing of Dirac Fermions in the Topological Surface States

[Phys. Rev. Lett. 110 (2013) 217601 (Editors' Suggestion)]

By using ultra-high resolution angle-resolved photoemission spectroscopy (ARPES) developed at ISSP, University of Tokyo, we have succeeded in observing the hitherto-undetected strong coupling between Dirac fermions and low-energy phonons on the surface of topological insulators. This coupling shows up as a new mode and is likely to be indicative of the novel collective mode called Spin-Plasmon which is peculiar to the topological surface state where the spin and the momentum are locked to each other.

#### Elucidation of the topological surface states in the candidate topological superconductor $\text{Sn}_{1-x}\text{In}_x\text{Te}$

[Phys. Rev. Lett. 110 (2013) 206804]



In 2012, we discovered that SnTe is a new type of topological material called topological crystalline insulator. We also found in the same year that the superconductor  $\text{Sn}_{1-x}\text{In}_x\text{Te}$ , which derived from SnTe, presents signatures of surface Andreev bound states that are indicative of a topological nature of its superconducting state. In this PRL paper, we have determined the Fermi surface of  $\text{Sn}_{1-x}\text{In}_x\text{Te}$  and demonstrated that its normal state above  $T_c$  preserves the topological surface state.

Robust protection from backscattering in the topological insulator  $\text{Bi}_{1.5}\text{Sb}_{0.5}\text{Te}_{1.7}\text{Se}_{1.3}$   
[Phys. Rev. Lett. 112 (2014) 136802-(1-5)]

In this paper, we studied the momentum dependence of the electron scattering in the topological surface state to evaluate the robustness of the topological protection. The technique employed was the so-called quasiparticle interference, which uses STM to detect the standing waves of electrons that emerge as a result of impurity scattering. It was found that not only the  $180^\circ$  backscattering but also a wide range of backscattering angles of  $100^\circ$ -- $180^\circ$  is effectively prohibited in the topological surface state. The unexpectedly robust protection from backscattering is a good news for applications.

Demonstration of topological surface transport in topological crystalline insulator SnTe thin films  
[Phys. Rev. B 89 (2014) 121302(R)]

Although SnTe was found to be a topological crystalline insulator (TCI) in 2012, its surface transport properties has not been observed due to the difficulty in preparing suitable samples. We have succeeded in growing high-quality thin films of SnTe with the MBE technique by using a novel buffer layer,  $\text{Bi}_2\text{Te}_3$ . Thanks to the high mobility of the topological surface state of SnTe, this heterostructure allowed us to detect the Shubnikov-de Haas oscillations coming from the topological surface state of SnTe. It was confirmed that two different types of Dirac cones, which are peculiar to TCIs, indeed exist on the surface. This is the first work to detect the characteristic Dirac fermions on the topological surface state of a TCI with transport measurements.

Spin-electricity conversion induced by spin injection into the topological surface states  
[Phys. Rev. Lett. 113 (2014) 196601-(1-5)]

By employing the spin pumping technique to utilize the ferromagnetic resonance, we have succeeded in observing the spin-electricity conversion on the surface of bulk-insulating topological insulators. In this experiment, we pumped spins into the surface states and observed the electromotive force to show up as a result of the spin-momentum locking.

This is one of the first reports to experimentally demonstrate the potential of topological insulators for spintronics applications.

Electrical detection of the spin polarization due to charge flow in the topological surface state  
[Nano Lett. 14 (2014) 6226-6230]

By injecting current from a nano-fabricated ferromagnetic contact into a bulk-insulating topological insulator, we found that the interface resistance depends on the direction of the spin polarization.

This is the first successful transport experiment of the spin injection into the topological surface state.

Development of efficient top gates on topological insulator thin films  
[Appl. Phys. Lett. 104 (2014) 161614-(1-5)]

The tunability of the chemical potential for a wide range encompassing the Dirac point is important for many future devices based on topological insulators. We have developed a protocol to fabricate highly efficient top gates without degrading the film quality on bulk-insulating  $(\text{Bi}_{1-x}\text{Sb}_x)_2\text{Te}_3$  thin films epitaxially grown on sapphire substrates. Important ingredients of the protocol are the in-situ deposited  $\text{Al}_2\text{O}_3$  capping layer and a low-temperature deposition of  $\text{SiN}_x$  dielectric layer using hot-wire CVD. Using the fabricated top gate, we have succeeded in ambipolar gating of the surface states, which means that we can control the Fermi level through the Dirac point to both electron- and hole-doped sides.

Discovery of a new superconductor derived from topological insulator heterostructure  
[Phys. Rev. B 90 (2014) 220504(R)-(1-5)]

We have discovered a new superconductor derived from a topological insulator. Importantly, the specific-heat behavior of this new superconductor gives evidence for unconventional superconductivity. This is the first "superconducting topological insulator" material to present bulk signatures of unconventional (and hence topological) superconductivity.

Discovery of Topological proximity effect in a topological insulator hybrid

[Nature Communications 6 (2015) 6547-(1-6)]

We discovered a novel phenomenon termed "topological proximity effect", which occurs between a metallic ultrathin film and a three-dimensional topological insulator. Specifically, we grew one bilayer of bismuth metal on top of the three-dimensional topological insulator TlBiSe<sub>2</sub>, and by using spin- and angle-resolved photoemission spectroscopy, we found evidence that the topological Dirac-cone state migrates from the surface of TlBiSe<sub>2</sub> to the attached one-bilayer Bi.

This discovery points to a new route to manipulating the topological properties of materials.

**Topics:**

- 1) The PI has been included in the **Thomson Reuters List of Highly Cited Researchers 2014** in the field of Physics (there are 144 physicists worldwide selected as Highly Cited Researchers 2014).
- 2) The PI has received the 2014 **Inoue Prize for Science** for his pioneering research on topological insulators and superconductors. This prize is awarded each year to five outstanding Japanese researchers under 50 years of age selected from all fields of natural science. The prize consists of 2 million JPY and a gold medal.
- 3) The PI has received the 2014 **Osaka Science Prize** for his pioneering research on topological insulators and superconductors. This prize is awarded each year to two scientists aged 50 or under for their outstanding contributions to science accomplished in the Greater Osaka Area. The prize money is 1.5 million JPY.
- 4) The PI has received the **Osaka University Presidential Award** for Achievement in Research in 2012 and 2014.
- 5) The PI has wrote a **textbook of topological insulators** in Japanese for graduate students ["Introduction to Topological Insulators" by Yoichi Ando (single author), 251 pages, published by Kodansha, Tokyo, on July 10, 2014]. This book is highly reputed and sells well.

**Personnel Supported:**

Fan Yang, Postdoctoral Researcher  
Mario Novak, Postdoctoral Researcher  
Subhamoy Ghatak, Postdoctoral Researcher  
Zhiwei Wang, Postdoctoral Researcher

**List of publications is prepared in a separate sheet.**

**Invited Talks:**

1. Yoichi Ando, "Topological Superconductivity Based on Topological Insulators", International Conference on Topological Quantum Phenomena (TQP2014), Kyoto University, December 18, 2014.
2. Yoichi Ando, "Topological Insulators and Superconductors", Workshop on Novel Quantum States in Condensed Matter (NQS2014), Yukawa Institute for Theoretical Physics, Kyoto University, November 13, 2014.

3. Yoichi Ando, "Progress toward Topological Insulator Devices", 32nd International Conference on the Physics of Semiconductors (ICPS 2014), Austin, Texas, August 10-15, 2014.
4. Yoichi Ando, "Topological Insulators and Superconductors", New Trends in Topological Insulators 2 (NTTI2), Berlin, July 7-10, 2014.
5. Yoichi Ando, "Topological Insulators and Superconductors", OIST International Workshop on Novel Quantum Materials and Phases (NQMP2014), Okinawa Institute of Science and Technology (OIST), Okinawa, May 14, 2014.
6. Yoichi Ando, "Superconducting Topological Insulators", Theo Murphy International Scientific Meeting *Emergence of New Exotic States at Interfaces with Superconductors*, The Royal Society at Chicheley Hall, UK, March 28, 2014.
7. Yoichi Ando, "New Topological Materials: Topological Crystalline Insulators and Topological Superconductors", 18th International Winterschool on New Developments in Solid State Physics, Mauterndorf, Austria, February 27, 2014.
8. Yoichi Ando, "Topological Insulators and Superconductors: Materials Frontier", Quantum Matter and Materials **Colloquium**, University of Cologne, Germany, February 12, 2014.
9. Yoichi Ando, "Materials Efforts for Topological Insulators and Superconductors", FIRST International Symposium on Topological Quantum Technology, University of Tokyo, Hongo, January 30, 2014.
10. Yoichi Ando, "Transport Studies of Topological Insulators" (**Keynote Talk**), Trends in NanoTechnology (TNT Japan 2014), Tokyo Big Sight, Tokyo, January 29, 2014.
11. Yoichi Ando, "Spin Pumping into the Surface State of Topological Insulators", Workshop on {\it Topological matter, Superconductivity and Majorana}, Institute for Advanced Study, Hong Kong University of Science and Technology (HKUST), Hong Kong, January 14, 2014.
12. Yoichi Ando, "Topological Insulators and Superconductors: Materials Frontier", **Colloquium**, Department of Physics, University of California Santa Barbara, CA, December 3, 2013.
13. Yoichi Ando, "Transport Studies of Topological Insulators", International Symposium on Nanoscale Transport and Technology (ISNTT2013), NTT Atsugi R&D Center, Kanagawa, November 27, 2013.
14. Yoichi Ando, "Experimental Studies of Topological Insulators and Superconductors", FIRST-QS<sup>2</sup>C Workshop on *Emergent Phenomena of Correlated Materials*, Shinagawa Intercity Hall, Tokyo, November 16, 2013.
15. Yoichi Ando, "Topological Insulators and Superconductors: Materials Frontier", **Colloquium**, Max-Planck Institute for Solid State Research, October 29, 2013.
16. Yoichi Ando, "Topological Insulators and Superconductors", CIFAR Quantum Materials Program Meeting, Vancouver, October 19, 2013.
17. Yoichi Ando, "Topological Insulators and Superconductors: Materials Frontier", Symposium *Frontiers of Solid State Physics*, Institute of Science and Technology Austria, Vienna, October 11, 2013.
18. Yoichi Ando, "Summary and Outlook of New Materials Discoveries of Topological Insulators and Superconductors", Symposium on Topological Insulators and Superconductors, 2013 Fall Meeting of the Physical Society of Japan, Tokushima University, September 27, 2013.

19. Yoichi Ando, "Experimental Studies of Topological Insulators and Superconductors", International Workshop on *Superconductivity Research Advanced by New Materials and Spectroscopies*, Institute for Materials Research, Tohoku University, Sendai, July 23-25, 2013.
20. Yoichi Ando, "Possible Bulk Topological Superconductors with Time-Reversal Invariance", Conference on *Majorana Physics in Condensed Matter*, Ettore Majorana Foundation and Center for Scientific Culture, Erice, Italy, July 13, 2013.
21. Yoichi Ando, "Experimental Studies of Topological Insulators and Superconductors", 2013 Swiss Workshop on Materials with Novel Electronic Properties, Les Diablerets, Switzerland, June 28, 2013.
22. Yoichi Ando, "Possible Topological Superconductivity in Doped Topological Insulators", International Workshop on *Majoranas in Solid State*, Peking University, Beijing, June 7, 2013.
23. Yoichi Ando, "Searching for Possible Topological Superconductors with Time-Reversal Invariance", Gordon Research Conference on Superconductivity, Les Diablerets, Switzerland, May 15, 2013.
24. Yoichi Ando, "Exploring Topological Insulator and Superconductor Materials", QS<sup>2</sup>C Theory Forum: International Symposium on Strongly Correlated Quantum Science, University of Tokyo, January 27, 2013.
25. Yoichi Ando, "Exploring Topological Insulator and Superconductor Materials", International Symposium Nanoscience and Quantum Physics (nanoPHYS'12), International House of Japan, Roppongi, Tokyo, December 18, 2012.
26. Yoichi Ando, "Topological Insulators and Superconductors: Materials Frontier", **Colloquium**, Department of Physics, Harvard University, November 9, 2012.
27. Yoichi Ando, "Topological Insulators and Topological Superconductors", Seminar, Department of Physics, Okayama University, October 25, 2012.
28. Yoichi Ando, "Topological Insulators and Topological Superconductors", **Colloquium**, Department of Physics, University of Tokyo, October 19, 2012.
29. Yoichi Ando, "Topological Insulators and Topological Superconductors", Seminar, Department of Physics, Nagoya University, October 11, 2012.
30. Yoichi Ando, "Present Status and Future Prospect of the Experimental Research of Topological Insulators and Superconductors", Symposium on Topological Insulators and Superconductors, 2012 Fall Meeting of the Physical Society of Japan, Yokohama National University, September 18, 2012.
31. Yoichi Ando, "Topological Insulators and Superconductors: Materials Frontier", GLAM Special Seminar, Geball Laboratory for Advanced Materials, Stanford University, September 13, 2012.
32. Yoichi Ando, "Topological Insulators and Superconductors: Materials Frontier", Special Seminar, Department of Electrical Engineering, UCLA, September 10, 2012.
33. Yoichi Ando, "Probing the Exotic Surface States in Topological Insulators and Superconductors", CECAM Workshop on Topological Materials, Bremen, Germany, August 13, 2012.
34. Yoichi Ando, "Topological Insulators: A New Materials Frontier", Super-PIRE 2nd Workshop, Hyatt Regency Bethesda, Maryland, August 3, 2012.
35. Yoichi Ando, "Experiments Toward Identifying a Topological Superconductor", **Keynote Talk**, International Conference on Materials & Mechanisms of Superconductivity (M2S 2012), Washington DC, August 1, 2012.
36. Yoichi Ando, "Probing the Exotic Surface States in Topological Insulators and Superconductors", Japanese-German Symposium 2012, Shuzenji, Japan, July 14-17, 2012.

37. Yoichi Ando, "Probing the Exotic Surface States in Topological Insulators and Superconductors", The 19th International Conference on Magnetism (ICM 2012), Busan, Korea, July 12, 2012.
38. Yoichi Ando, "Probing the Exotic Surface States in Topological Insulators and Superconductors", Advanced Research Workshop on Non-equilibrium and Coherent Phenomena at Nanoscale (Meso-2012), Landau Institute, Chernogolovka, Russia, June 17, 2012.
39. Yoichi Ando, "Topological Insulators and Superconductors: Materials Frontier", Seminar, Air Force Research Laboratory, Dayton, OH, June 1, 2012.
40. Yoichi Ando, "Progress in Topological Insulator Materials for 2D Devices", NSF/AFOSR Workshop on 2D Materials and Devices Beyond Graphene, Arlington, VA, May 31, 2012.
41. Yoichi Ando, "Transport Studies of the Exotic Surface States in Topological Insulators and Superconductors", International Workshop on Strongly Correlated Electron Systems in High Magnetic Fields (SCEF), Les Houches, France, May 24, 2012.
42. Yoichi Ando, "Topological Insulators and Superconductors: Materials Frontier", **Colloquium**, Physics Section, EPFL, Lausanne, May 21, 2012.

#### **Inventions:**

- (a) Discoveries, inventions, or patent disclosures: None.
- (b) DD Form 882, "Report of Inventions and Subcontractors": Negative report

#### **Honors/Awards:**

- 1) Osaka Science Prize (Osaka City & Osaka Prefecture)  
for Pioneering Research of Topological Insulators and Superconductors  
(October 29, 2014)
- 2) Osaka University Presidential Award for Achievement in Research (Osaka University)  
(July 8, 2014)
- 3) Thomson-Reuters Highly Cited Researcher 2014 in Physics  
(June 19, 2014)
- 4) The 30th Inoue Prize for Science (Inoue Foundation for Science)  
for *Pioneering Research of Topological Insulators and Superconductors*  
(February 4, 2014)
- 5) The 17th Superconductivity Science and Technology Award (The Society of Non-Traditional Technology)  
for *Theory and Demonstration of Topological Superconductors*  
(April 16, 2013)
- 6) Osaka University Presidential Award for Achievement in Research  
(August 1, 2012)

**Software and/or Hardware (if they are specified in the contract as part of final deliverables):** None.

**1. Publications Produced under AFOSR/AOARD Grant No. 124038  
(3/21/2012 - 03/20/2015)**

- [1] T. Shoman, A. Takayama, T. Sato, S. Souma, T. Takahashi, T. Oguchi, Kouji Segawa, and Yoichi Ando,  
Topological proximity effect in a topological insulator hybrid,  
**Nature Commun.** **6** (2015) 6547-(1-6) (published on March 12, 2015).
- [2] Yoshito Onishi, Zhi Ren, Kouji Segawa, Wawrzyniec Kaszub, Maciej Lorenc, Yoichi Ando, and Koichiro Tanaka,  
Ultrafast carrier relaxation through Auger recombination in the topological insulator  $\text{Bi}_{1.5}\text{Sb}_{0.5}\text{Te}_{1.7}\text{Se}_{1.3}$ ,  
**Phys. Rev. B** **91** (2015) 085306-(1-12) (**Editors' Suggestion**, published on February 17, 2015).
- [3] Mario Novak, Satoshi Sasaki, Kouji Segawa, and Yoichi Ando,  
Large linear magnetoresistance in the Dirac semimetal TlBiSSe,  
**Phys. Rev. B** **91** (2015) 041203(R)-(1-4) (published on January 20, 2015).
- [4] Shunsuke Yoshizawa, Fumitaka Nakamura, Alexey A. Taskin, Takushi Iimori, Kan Nakatsuji, Iwao Matsuda, Yoichi Ando, and Fumio Komori,  
Scanning tunneling spectroscopy study of quasiparticle interference on the dual topological insulator  $\text{Bi}_{1-x}\text{Sb}_x$ ,  
**Phys. Rev. B** **91** (2015) 045423-(1-6) (published on January 20, 2015).
- [5] Satoshi Sasaki, Kouji Segawa, and Yoichi Ando,  
Superconductor derived from a topological insulator heterostructure,  
**Phys. Rev. B** **90** (2014) 220504(R)-(1-5) (published on December 1, 2014).
- [6] Y. Shiomi, K. Nomura, Y. Kajiwara, K. Eto, M. Novak, Kouji Segawa, Yoichi Ando, and E. Saitoh,  
Spin-Electricity Conversion Induced by Spin Injection into Topological Insulators,  
**Phys. Rev. Lett.** **113** (2014) 196601-(1-5) (published on November 3, 2014).
- [7] Yuichiro Ando, Takahiro Hamasaki, Takayuki Kurokawa, Kouki Ichiba, Fan Yang, Mario Novak, Satoshi Sasaki, Kouji Segawa, Yoichi Ando, and Masashi Shiraishi,  
Electrical Detection of the Spin Polarization Due to Charge Flow in the Surface State of the Topological Insulator  $\text{Bi}_{1.5}\text{Sb}_{0.5}\text{Te}_{1.7}\text{Se}_{1.3}$ ,  
**Nano Lett.** **14** (2014) 6226-6230 (published on October 20, 2014).
- [8] Kouji Segawa, A. A. Taskin, and Yoichi Ando,  
 $\text{Pb}_5\text{Bi}_{24}\text{Se}_{41}$ : A New Member of the Homologous Series Forming Topological Insulator Heterostructures,  
**J. Solid State Chem.** **221** (2015) 196-201 (published on October 13, 2014).
- [9] Luke J. Sandilands, Anjan A. Reijnders, Markus Kriener, Kouji Segawa, Satoshi Sasaki, Yoichi Ando, and Kenneth S. Burch,  
Doping-dependent charge dynamics in  $\text{Cu}_x\text{Bi}_2\text{Se}_3$ ,  
**Phys. Rev. B** **90** (2014) 094503-(1-6) (published on September 10, 2014).
- [10] Fan Yang, A. A. Taskin, Satoshi Sasaki, Kouji Segawa, Yasuhide Ohno, Kazuhiko Matsumoto, and Yoichi Ando,  
Top gating of epitaxial  $(\text{Bi}_{1-x}\text{Sb}_x)_2\text{Te}_3$  topological insulator thin films,  
**Appl. Phys. Lett.** **104** (2014) 161614-(1-5) (published on April 25, 2014).
- [11] Sunghun Kim, Shunsuke Yoshizawa, Yukiaki Ishida, Kazuma Eto, Kouji Segawa, Yoichi Ando, Shik Shin, and Fumio Komori,  
Robust protection from backscattering in the topological insulator  $\text{Bi}_{1.5}\text{Sb}_{0.5}\text{Te}_{1.7}\text{Se}_{1.3}$ ,  
**Phys. Rev. Lett.** **112** (2014) 136802-(1-5) (published on April 1, 2014).
- [12] A. A. Taskin, Fan Yang, Satoshi Sasaki, Kouji Segawa, and Yoichi Ando,  
Topological surface transport in epitaxial SnTe thin films grown on  $\text{Bi}_2\text{Te}_3$ ,  
**Phys. Rev. B** **89** (2014) 121302(R)-(1-5) (Rapid Communications) (published on March 17, 2014).

- [13] M. Nomura, S. Souma, A. Takayama, T. Sato, T. Takahashi, K. Eto, Kouji Segawa, and Yoichi Ando,  
Relationship between Fermi surface warping and out-of-plane spin polarization in topological insulators: A view from spin- and angle-resolved photoemission,  
**Phys. Rev. B** **89** (2014) 045134-(1-6). (published on January 27, 2014).
- [14] Y. Tanaka, T. Shoman, K. Nakayama, S. Souma, T. Sato, T. Takahashi, M. Novak, Kouji Segawa, and Yoichi Ando,  
Two types of Dirac-cone surface states on the (111) surface of the topological crystalline insulator SnTe,  
**Phys. Rev. B** **88** (2013) 235126 -(1-5) (**Editors' Suggestion**) (published on December 26, 2013).
- [15] Mario Novak, Satoshi Sasaki, Markus Kriener, Kouji Segawa, and Yoichi Ando,  
Unusual nature of fully gapped superconductivity in In-doped SnTe,  
**Phys. Rev. B** **88** (2013) 140502(R)-(1-5) (Rapid Communications; published on October 7, 2013).
- [16] Yoichi Ando,  
Topological Insulator Materials,  
**J. Phys. Soc. Jpn.** **82** (2013) 102001-(1-32) (**Invited review paper**) (published on September 3, 2013).
- [17] Yoichi Ando, Kouji Segawa, Satoshi Sasaki, and M. Kriener,  
Experimental studies of the topological superconductor  $\text{Cu}_x\text{Bi}_2\text{Se}_3$ ,  
**J. Phys.: Conf. Ser.** **449** (2011) 012033-(1-5). [Proceedings of the 10th International Conference on Materials and Mechanisms of Superconductivity (M2S-X), Washington DC, July 29 – August 3, 2012] (published on July 17, 2013).
- [18] Takeshi Kondo, Y. Nakashima, Y. Ota, Y. Ishida, W. Malaeb, K. Okazaki, S. Shin, M. Kriener, Satoshi Sasaki, Kouji Segawa, and Yoichi Ando,  
Anomalous Dressing of Dirac Fermions in the Topological Surface State of  $\text{Bi}_2\text{Se}_3$ ,  $\text{Bi}_2\text{Te}_3$ , and Cu-Doped  $\text{Bi}_2\text{Se}_3$ ,  
**Phys. Rev. Lett.** **110** (2013) 217601-(1-5) (**Editors' Suggestion**) (published on May 23, 2013).
- [19] T. Sato, Y. Tanaka, K. Nakayama, S. Souma, T. Takahashi, S. Sasaki, Z. Ren, A. A. Taskin, Kouji Segawa, and Yoichi Ando,  
Fermiology of the Strongly Spin-Orbit Coupled Superconductor  $\text{Sn}_{1-x}\text{In}_x\text{Te}$ : Implications for Topological Superconductivity,  
**Phys. Rev. Lett.** **110** (2013) 206804-(1-5) (published on May 17, 2013).
- [20] Y. Tanaka, T. Sato, K. Nakayama, S. Souma, T. Takahashi, Zhi Ren, M. Novak, Kouji Segawa, and Yoichi Ando,  
Tunability of the  $k$ -space location of the Dirac cones in the topological crystalline insulator  $\text{Pb}_{1-x}\text{Sn}_x\text{Te}$ ,  
**Phys. Rev. B** **87** (2013) 155105-(1-5) (published on April 2, 2013).
- [21] Zhi Ren, M. Kriener, A. A. Taskin, Satoshi Sasaki, Kouji Segawa, and Yoichi Ando,  
Anomalous metallic state above the upper critical field of the conventional three-dimensional superconductor  $\text{AgSnSe}_2$  with strong intrinsic disorder,  
**Phys. Rev. B** **87** (2013) 064512-(1-6) (published on Feb. 28, 2013).
- [22] D. K. Pratt, S. Chang, W. Tian, A. A. Taskin, Yoichi Ando, J. L. Zarestky, A. Kreyssig, A. I. Goldman, and R. J. McQueeney,  
Checkerboard to stripe charge ordering transition in  $\text{TbBaFe}_2\text{O}_5$ ,  
**Phys. Rev. B** **87** (2013) 045127-(1-5) (published on Feb. 6, 2013).
- [23] K. Nakayama, K. Eto, Y. Tanaka, T. Sato, S. Souma, T. Takahashi, Kouji Segawa, and Yoichi Ando,  
Manipulation of Topological States and the Bulk Band Gap Using Natural Heterostructures of a Topological Insulator,  
**Phys. Rev. Lett.** **109** (2012) 236804-(1-5) (published on Dec. 4, 2012).

- [24] Satoshi Sasaki, Zhi Ren, A. A. Taskin, Kouji Segawa, Liang Fu, and Yoichi Ando,  
Odd-Parity Pairing and Topological Superconductivity in a Strongly Spin-Orbit Coupled  
Semiconductor,  
**Phys. Rev. Lett.** **109** (2012) 217004-(1-5) (published on Nov. 21, 2012).
- [25] M. Kriener, Kouji Segawa, Satoshi Sasaki, and Yoichi Ando,  
Anomalous suppression of the superfluid density in the  $\text{Cu}_x\text{Bi}_2\text{Se}_3$  superconductor upon  
progressive Cu intercalation,  
**Phys. Rev. B** **86** (2012) 180505(R)-(1-5) (**Editors' Suggestion**, published on Nov. 19, 2012)).
- [26] S. Souma, M. Komatsu, M. Nomura, T. Sato, A. Takayama, T. Takahashi, K. Eto, Kouji Segawa,  
and Yoichi Ando,  
Spin Polarization of Gapped Dirac Surface States Near the Topological Phase Transition in  
 $\text{TlBi}(\text{S}_{1-x}\text{Se}_x)_2$ ,  
**Phys. Rev. Lett.** **109** (2012) 186804-(1-5) (published on Nov. 2, 2012).
- [27] Y. Tanaka, Zhi Ren, T. Sato, K. Nakayama, S. Souma, T. Takahashi, Kouji Segawa, and  
Yoichi Ando,  
Experimental realization of a topological crystalline insulator in  $\text{SnTe}$ ,  
**Nature Physics** **8** (2012) 800-803 (published on Sep. 30, 2012).
- [28] A. A. Taskin, Satoshi Sasaki, Kouji Segawa, and Yoichi Ando,  
Achieving Surface Quantum Oscillations in Topological Insulator Thin Films of  $\text{Bi}_2\text{Se}_3$ ,  
**Adv. Mater.** **24** (2012) 5581-5585 (published on Aug. 21, 2012).
- [29] Kouji Segawa, Zhi Ren, Satoshi Sasaki, Tetsuya Tsuda, Susumu Kuwabata, and Yoichi Ando,  
Ambipolar transport in bulk crystals of a topological insulator by gating with ionic liquid,  
**Phys. Rev. B** **86** (2012) 075306-(1-7) (published on Aug. 14, 2012).
- [30] A. A. Taskin, Satoshi Sasaki, Kouji Segawa, and Yoichi Ando,  
Manifestation of Topological Protection in Transport Properties of Epitaxial  $\text{Bi}_2\text{Se}_3$  Thin Films,  
**Phys. Rev. Lett.** **109** (2012) 066803-(1-5) (**Editors' Suggestion**, featured in *Physics* Synopsis,  
published on Aug. 9, 2012)).
- [31] A. A. Schafgans, K. W. Post, A. A. Taskin, Yoichi Ando, Xiao-Liang Qi, B. C. Chapler, and D. N.  
Basov,  
Landau level spectroscopy of surface states in the topological insulator  $\text{Bi}_{0.91}\text{Sb}_{0.09}$  via  
magneto-optics,  
**Phys. Rev. B** **85** (2012) 195440-(1-6) (**Editors' Suggestion**, published on May 17, 2012)).
- [32] Zhi Ren, A. A. Taskin, Satoshi Sasaki, Kouji Segawa, and Yoichi Ando,  
Fermi level tuning and a large activation gap achieved in the topological insulator  $\text{Bi}_2\text{Te}_2\text{Se}$  by Sn  
doping,  
**Phys. Rev. B** **85** (2012) 155301-(1-6) (**Editors' Suggestion**, published on April 3, 2012)).



# Experimental realization of a topological crystalline insulator in SnTe

Y. Tanaka<sup>1</sup>, Zhi Ren<sup>2</sup>, T. Sato<sup>1\*</sup>, K. Nakayama<sup>1</sup>, S. Souma<sup>3</sup>, T. Takahashi<sup>1,3</sup>, Kouji Segawa<sup>2</sup> and Yoichi Ando<sup>2\*</sup>

**A topological insulator is an unusual quantum state of matter, characterized by the appearance, at its edges or on its surface, of a gapless metallic state that is protected by time-reversal symmetry<sup>1,2</sup>. The discovery of topological insulators has stimulated the search for other topological states protected by other symmetries<sup>3–7</sup>, such as the recently predicted<sup>8</sup> topological crystalline insulator (TCI) in which the metallic surface states are protected by the mirror symmetry of the crystal. Here we present experimental evidence for the TCI phase in tin telluride (SnTe), which has been predicted to be a TCI (ref. 9). Our angle-resolved photoemission spectra show the signature of a metallic Dirac-cone surface band, with its Dirac point slightly away from the edge of the surface Brillouin zone in SnTe. Such a gapless surface state is absent in a cousin material, lead telluride, in line with the theoretical prediction.**

The surface state of three-dimensional (3D) topological insulators is characterized by a spin non-degenerate Dirac-cone energy dispersion protected by time-reversal symmetry. In topological insulators, the time-reversal symmetry plays a key role in characterizing the topological properties such as the quantum spin Hall effect, the dissipation-less spin current and the magnetoelectric effect<sup>10–13</sup>. In contrast, in TCIs, the metallic surface states are protected by the mirror symmetry (reflection symmetry) of the crystal<sup>8</sup>. The TCIs are characterized by a new topological invariant called the mirror Chern number, instead of the  $Z_2$  invariant in topological insulators. Intuitively, the existence of mirror symmetry allows one to divide the Hilbert space into left and right, and considering only one of them can single out a non-trivial topology that is otherwise cancelled and undetected. Therefore, even when an insulator is trivial in the topological insulator sense, it can still be non-trivial in the TCI sense when it possesses a mirror symmetry and its mirror Chern number is non-zero<sup>8,9</sup>. Indeed, it was recently shown<sup>9</sup> that such a situation is realized in an insulating crystal having the rock-salt structure (in which the {001}, {110} and {111} surfaces have mirror symmetry with respect to the (110) mirror plane, see Fig. 1a) when a band inversion occurs at the high-symmetry L points of the bulk Brillouin zone; intriguingly, it was further predicted<sup>9</sup>, on the basis of tight-binding calculations, that a narrow-gap IV–VI semiconductor SnTe is such a TCI, whereas the isostructural PbTe is not. It is thus of particular importance to experimentally examine the possibility of the TCI phase in these semiconductors, to establish the concept of this new topological state of matter and possibly to find topological phenomena beyond the framework of known topological materials.

In our angle-resolved photoemission spectroscopy (ARPES) experiment, we paid particular attention to the momentum space around the  $\bar{X}$  point of the surface Brillouin zone corresponding to a projection of the L point of the bulk Brillouin zone where a direct bulk bandgap resides<sup>14–16</sup> and the appearance of topological surface states is predicted<sup>9</sup>; note that the (110) mirror plane is projected to the  $\bar{\Gamma}\bar{X}$  high-symmetry line in the surface Brillouin zone (Fig. 1a). Our extensive ARPES measurements of the occupied states suggest that the bulk-band maximum is indeed located around the  $\bar{X}$  point (see Supplementary Fig. S1). As shown in Fig. 1b, the ARPES intensity at the Fermi level ( $E_F$ ) measured with the photon energy  $h\nu = 21.2$  eV on the (001) surface exhibits a bright intensity pattern centred around the  $\bar{X}$  point and is elongated along the  $\bar{\Gamma}\bar{X}$  direction. The band dispersion along two selected cuts (red arrows in Fig. 1b) exhibits a linearly dispersive feature crossing  $E_F$ , as shown in Fig. 1c,d. The top of this Dirac-like band is located not at the  $\bar{X}$  point but at a point slightly away from it (called here the  $\bar{\Lambda}$  point), as one can infer from the band dispersion along the  $\bar{\Gamma}\bar{X}$  cut (Fig. 1e,f) showing the band maxima on both sides of the  $\bar{X}$  point ( $\bar{\Lambda}_1$  and  $\bar{\Lambda}_2$  for the first and second surface Brillouin zones, respectively). Such a characteristic M-shaped dispersion is not expected from the bulk-band calculations at any  $k_z$  (wave vector perpendicular to the surface) values<sup>14–16</sup>, but is predicted for the surface band<sup>9</sup> (Supplementary Information), suggesting that the observed Dirac-like band originates from the surface states.

To further examine whether the Dirac-like band is of surface or bulk origin, we have carried out an ARPES measurement along the cut crossing the  $\bar{\Lambda}$  point for various photon energies. As one immediately recognizes in Fig. 1g–j, the energy position of the band is stationary with respect to the  $h\nu$  variation. In fact, when we plot the extracted dispersions for different photon energies in the same panel, they overlap each other within the experimental uncertainties of  $\sim 0.05$  eV (near  $E_F$ ) to  $\sim 0.1$  eV (at higher binding energy,  $E_B$ ), demonstrating the surface origin of the Dirac-like band. Note that the broadening of the spectra on the right-hand side of the branch at higher  $E_B$  evident in Fig. 1h–j is probably due to a mixture of the bulk state whose energy position changes with  $h\nu$ , although the bulk state is obviously very broad and we could not clearly resolve its dispersion.

We note that, because as-grown crystals of SnTe tend to show a heavily hole-doped nature<sup>16–18</sup>, a key to the present observation of the Dirac-like band was to reduce hole carriers in the crystal by minimizing Sn vacancies during the growth procedure. In fact, the Dirac-like surface state was not resolved in the previous ARPES study<sup>16</sup>, mainly owing to the heavily hole-doped nature

<sup>1</sup>Department of Physics, Tohoku University, Sendai 980-8578, Japan, <sup>2</sup>Institute of Scientific and Industrial Research, Osaka University, Ibaraki, Osaka 567-0047, Japan, <sup>3</sup>WPI Research Center, Advanced Institute for Materials Research, Tohoku University, Sendai 980-8577, Japan.

\*e-mail: t-sato@arpes.phys.tohoku.ac.jp; y\_ando@sanken.osaka-u.ac.jp.

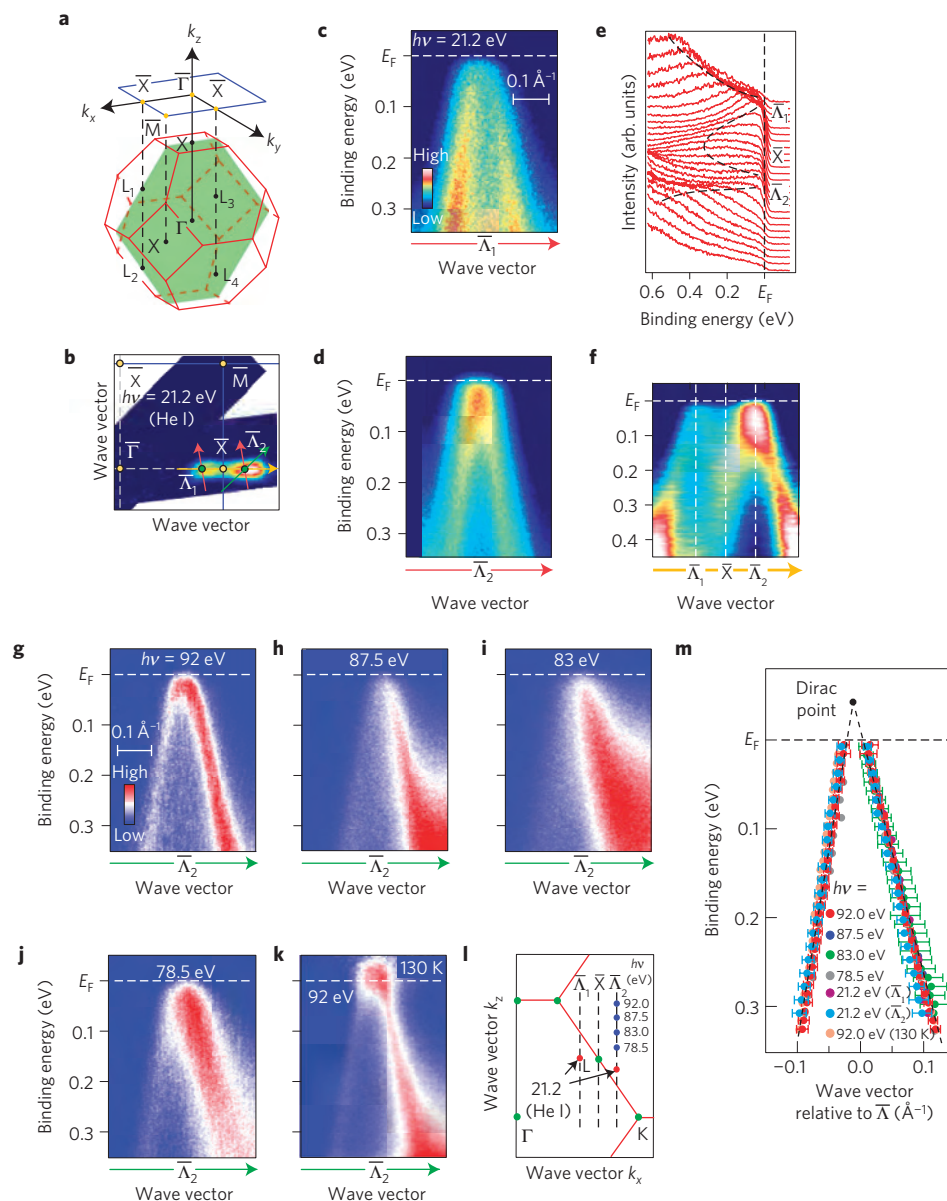


**Figure 1 | Dirac-like band dispersion in SnTe.** **a**, The bulk Brillouin zone (red lines) and the corresponding (001) surface Brillouin zone (blue lines). The (110) mirror plane is indicated by the green shaded area. **b**, ARPES intensity mapping at  $E_F$  for  $T = 30$  K for SnTe plotted as a function of the 2D wave vector measured with the He I line ( $h\nu = 21.2$  eV); this intensity is obtained by integrating the spectra within  $\pm 10$  meV of  $E_F$ . **c,d**, Near- $E_F$  ARPES intensity measured at  $h\nu = 21.2$  eV as a function of the wave vector and  $E_B$  along the cut crossing the  $\bar{\Lambda}_1$  and  $\bar{\Lambda}_2$  point (red arrows in **b**), respectively. **e,f**, Energy distribution curves (**e**) along the  $\bar{\Gamma}\bar{X}$  cut (yellow arrow in **b**) measured at  $h\nu = 21.2$  eV, and the corresponding intensity plot (**f**). The dashed lines in **e** are a guide to the eyes to trace the band dispersion. **g-j**, ARPES intensity measured at  $T = 30$  K with various photon energies across the cut crossing the  $\bar{\Lambda}_2$  point (green arrow in **b**). **k**, The same as in **g** but measured at  $T = 130$  K. The ARPES intensity is divided by the Fermi-Dirac distribution function convoluted with the instrumental resolution. **l**, A slice of the bulk Brillouin zone in the (110) plane, together with the momentum points in which the ARPES data for **c,d** and **g-k** were obtained;  $k_z$  values were estimated by using the inner-potential value of 8.5 eV as determined by the normal-emission ARPES measurement. **m**, Comparison of the band dispersion for various photon energies extracted by tracking the peak position of momentum distribution curves obtained along the green arrow in **b**; error bars are shown for the data at  $h\nu = 92$ , 83, and 21.2 eV, and they reflect the uncertainties originating from the momentum resolution and the standard deviation in the peak positions of momentum distribution curves. The  $h\nu = 83$  eV data are particularly broad at high  $E_B$ , which is partly due to a mixing of the bulk band.

of the sample (chemical potential was located  $\sim 0.5$  eV lower when compared with our data). Furthermore, a downward band bending, possibly due to a loss of Te atoms on cleaving, was obviously taking place near the surface (Supplementary Information), which further worked in our favour.

As shown in Fig. 1k, the ARPES data at  $T = 130$  K divided by the Fermi-Dirac distribution function indicate that the left- and right-hand side dispersion branches actually merge into a

single peak above  $E_F$ . The Dirac-point energy is estimated to be 0.05 eV above  $E_F$  from a linear extrapolation of the two dispersion branches (Fig. 1m) that were determined from the peak positions in the momentum distribution curves; furthermore, the Dirac band velocities extracted from the dispersions are 4.5 and 3.0 eV  $\text{\AA}$ , for the left- and right-hand side branches, respectively. One can see in Fig. 1m that the band dispersion exhibits no discernible change with temperature (compare the 30 K and 130 K data for  $h\nu = 92$  eV).

Distribution A: Approved for public release. Distribution is unlimited.

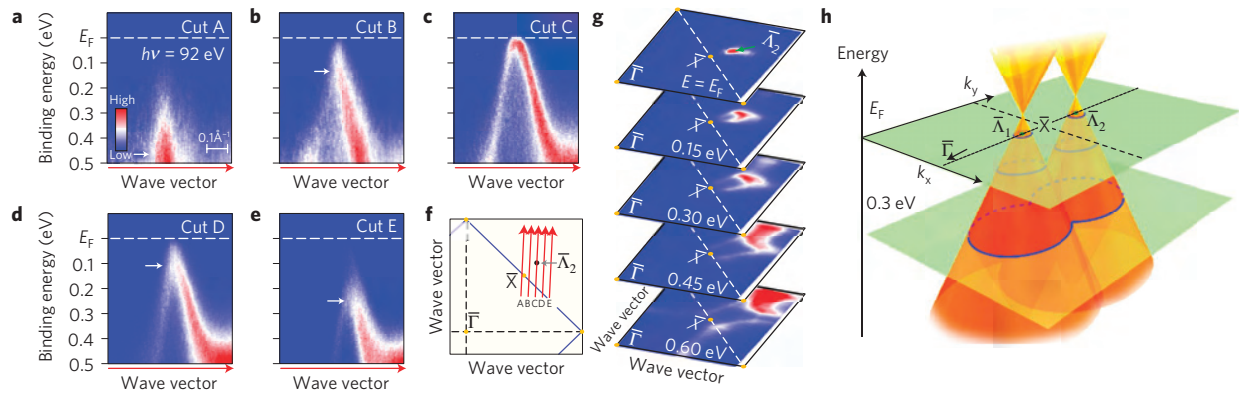


**Figure 2 | Two-dimensional band dispersion of SnTe.** **a–e**, Near- $E_F$  ARPES intensity for SnTe as a function of the wave vector and  $E_B$  measured at  $h\nu = 92$  eV along the cuts (A–E) around the  $\bar{\Lambda}_2$  point shown by the red arrows in the surface Brillouin zone in **f**. The white arrow marks the top of the dispersion. **f**, Surface Brillouin zone and the momentum cuts of the measurement (red arrows). **g**, ARPES intensity mappings for SnTe in a 2D wave-vector plane at various  $E_B$  values. Note that the intensity distribution for  $E_B \geq 0.45$  eV is strongly affected by the bulk-band contributions. **h**, Schematic 2D band dispersions near  $E_F$  depicting the evolution of the surface Dirac cones. The blue circles show energy contours for representative  $E_B$  slices, highlighting the Lifshitz transition<sup>9</sup> (see Supplementary Information for details).

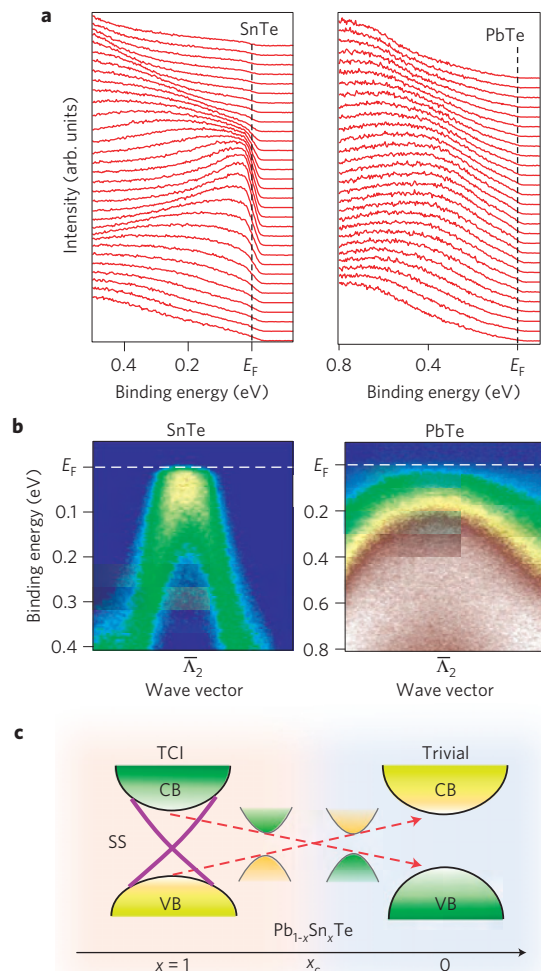


**Figure 3 | Comparison of the band structure between SnTe and PbTe.**

**a**, Near- $E_F$  energy distribution curves around the  $\bar{\Lambda}$  point for SnTe and PbTe measured with  $h\nu = 21.2$  eV; note that the energy axes are different for SnTe and PbTe. **b**, Corresponding ARPES-intensity plots. **c**, Schematic illustration of the evolution of the band dispersion in  $\text{Pb}_{1-x}\text{Sn}_x\text{Te}$  expected from the present ARPES experiment. SS, CB, and VB denote the surface state, the bulk conduction band and the bulk valence band, respectively.

One may argue that in SnTe the well-known rhombohedral distortion<sup>19</sup> would break the mirror symmetry with respect to the (110) plane and destroy the signature of the Dirac-cone surface states. However, one can safely exclude this possibility in the present experiment, because the rhombohedral phase transition temperature is known to be strongly dependent on the carrier density<sup>19</sup> and in our samples the transition occurs well below 30 K (the temperature of our ARPES measurements), which is corroborated by the absence of a kink in the temperature dependence of the resistivity (see Supplementary Fig. S6). In addition, the (001) surface of the cubic structure has two mirror planes, and the rhombohedral distortion breaks the mirror symmetry of only one of those two mirror planes. This means that two of the original four Dirac cones remain gapless in the rhombohedral phase; furthermore, as the rhombohedral distortion in SnTe is weak (it induces only 1.6% displacement of the atomic positions<sup>19</sup>), the expected result is an opening of a small gap at the Dirac point in the other two Dirac cones. Therefore, the small rhombohedral distortion, even when it happens, will not significantly change the surface state spectrum.

To further elucidate the topology of the Dirac cone in detail, we have determined the whole band dispersion in the 2D momentum space. By selecting a specific photon energy ( $h\nu = 92$  eV), owing to the matrix-element effects, we found it possible to pick up the dispersion of a single Dirac cone centred at the  $\bar{\Lambda}_2$  point ( $\bar{\Lambda}_2$  Dirac cone) while suppressing the intensity of the  $\bar{\Lambda}_1$  Dirac cone. Figure 2a–e shows the near- $E_F$  ARPES intensity measured along several cuts (A–E) around the  $\bar{\Lambda}_2$  point. Along cut A (Fig. 2a), the surface band has its top at an  $E_B$  of 0.45 eV. On moving from cut A to E, the band maximum (white arrow) approaches  $E_F$  (cuts A–B), passes  $E_F$  (cut C), and then disperses back again towards higher  $E_B$  (cuts D–E). This result establishes the cone-shaped dispersion of the Dirac-like band in the 2D momentum space as in three-dimensional topological insulators<sup>1,2</sup> and graphene<sup>20</sup>. In passing, we have surveyed electronic states throughout the Brillouin zone and found no evidence for other metallic surface states (Supplementary Fig. S1) and thus conclude that the surface electronic states consist of four Dirac cones in the first surface Brillouin zone. This indicates that this material is not a topological insulator but is a TCI owing to an even number of band-inversion points<sup>9</sup> that is reflected in the number of Dirac cones.

As shown in the ARPES-intensity contour plots in Fig. 2g for several  $E_B$  slices, the Dirac cone in SnTe is anisotropic and slightly elongated along the  $\bar{\Gamma}\bar{X}$  direction, and its topology shows a Lifshitz



transition as a function of band filling: namely, at  $E_B = 0.15$  eV the cross-section is closed and is elongated towards  $\bar{X}$ , but it becomes open at  $E_B = 0.30$  eV, suggesting that it is reconnected with the Dirac cone on the other side of  $\bar{X}$  (see Supplementary Fig. S5); at  $E_B \geq 0.45$  eV, the bulk band creates strong intensities and partly smears the surface state. This Lifshitz transition is interesting, because it would accompany a marked change in the Dirac-carrier properties and provide another ingredient in the physics of topological insulators. The observed evolution in the 2D band dispersion presenting a double Dirac-cone structure is schematically depicted in Fig. 2h. Although SnTe samples are always p-type, one can access the upper part of this double cone by using scanning tunnelling microscopy or field-effect-transistor devices.

To see how unique SnTe is among isostructural IV–VI semiconductors, we have performed an ARPES measurement of PbTe and directly compared the near- $E_F$  electronic states around the  $\bar{\Lambda}$  point, as shown in Fig. 3a,b. The PbTe single crystals used here were specially tuned to be only weakly electron doped and were of very high quality, with an electron mobility of  $60,000 \text{ cm}^2 \text{ V}^{-1} \text{ s}^{-1}$  (Supplementary Information). Intriguingly, the spectral feature of PbTe shows no evidence for the metallic Dirac-like band, and exhibits only a broad feature originated from the top of the bulk valence band<sup>21</sup>, suggesting that this material is an ordinary (trivial) insulator. Note that this broad feature is intrinsic and is not due to a bad crystallinity, because deeper bands show clear dispersions (Supplementary Information). This naturally suggests that a topological phase transition takes place in a solid-solution system  $\text{Pb}_{1-x}\text{Sn}_x\text{Te}$  (Fig. 3c). This conclusion agrees with the tight-binding calculation<sup>9</sup> that predicted that the valence bands at four L points in SnTe are inverted relative to PbTe, resulting in different mirror Chern numbers (2 versus 0). One can thus infer that the bulk bandgap closes at a critical  $x$  value,  $x_c$ , accompanied by a parity change of the valence-band wavefunction and an emergence/disappearance of the Dirac-cone surface state. Therefore, the present results have established the TCI phase in SnTe, which is in contrast to the trivial nature of isostructural PbTe. Our results unambiguously demonstrate the validity of the concept of TCIs and suggests the existence of many more kinds of topological material.

## Methods

High-quality single crystals of SnTe and PbTe were grown by a modified Bridgman method in sealed evacuated quartz-glass tubes from high-purity elements (Sn (99.99%), Pb (99.998%), Te (99.999%)). To obtain SnTe crystals with minimal Sn vacancy, a starting ratio of Sn/Te = 51:49 was chosen and, after melting the elements at high temperature, the tube was slowly cooled to 770 °C (which is only 20 °C below the melting point) and quenched into cold water; the carrier density estimated from the Hall coefficient was  $2 \times 10^{20} \text{ cm}^{-3}$ , which is lower than usual<sup>17,18</sup>. PbTe crystals were grown with a starting composition of Pb/Te = 1.005:1 by slowly cooling the melt from 980 °C to 700 °C at  $2^\circ \text{C h}^{-1}$  and holding at 700 °C for 12 h; the carrier density in the resulting crystals was very low at  $1.7 \times 10^{17} \text{ cm}^{-3}$ . Both SnTe and PbTe single crystals are single domain and show good crystallinity in X-ray Laue analysis, and their detailed transport properties are described in the Supplementary Information. ARPES measurements were performed with the MBS-A1 and VG-Scienta SES2002 electron analysers with a high-intensity helium discharge lamp at Tohoku University and also with tunable synchrotron lights at the beamline BL28A at the Photon Factory (KEK). To excite photoelectrons, we used the He I $\alpha$  resonance line ( $h\nu = 21.218$  eV) and the circularly polarized lights of 50–100 eV at Tohoku University and the Photon Factory, respectively. The energy and angular resolutions were set at 10–30 meV and  $0.2^\circ$ , respectively. Samples were cleaved *in situ* along the (001) crystal plane in an ultrahigh vacuum of  $1 \times 10^{-10}$  torr at room temperature. A shiny mirror-like surface was obtained after cleaving the samples, confirming their high quality. The Fermi level of the samples was referenced to that of a gold film evaporated onto the sample holder.

Received 23 June 2012; accepted 7 September 2012;  
published online 30 September 2012

## References

- Hasan, M. Z. & Kane, C. L. Colloquium: Topological insulators. *Rev. Mod. Phys.* **82**, 3045–3067 (2010).
- Qi, X.-L. & Zhang, S.-C. Topological insulators and superconductors. *Rev. Mod. Phys.* **83**, 1057–1110 (2011).
- Schnyder, A. P., Ryu, S., Furusaki, A. & Ludwig, A. W. W. Classification of topological insulators in three spatial dimensions. *Phys. Rev. B* **78**, 195125 (2008).
- Kitaev, A. Periodic table for topological insulators and superconductors. Preprint at <http://arxiv.org/abs/0901.2686v2> (2009).
- Ran, Y. Weak indices and dislocations in general topological band structures. Preprint at <http://arxiv.org/abs/1006.5454v2> (2010).
- Mong, R. S. K., Essin, A. M. & Moore, J. E. Antiferromagnetic topological insulators. *Phys. Rev. B* **81**, 245209 (2010).
- Li, R., Wang, J., Qi, X.-L. & Zhang, S.-C. Dynamical axion field in topological magnetic insulators. *Nature Phys.* **6**, 284–288 (2010).
- Fu, L. Topological crystalline insulators. *Phys. Rev. Lett.* **106**, 106802 (2011).
- Hsieh, T. H. *et al.* Topological crystalline insulators in the SnTe material class. *Nature Commun.* **3**, 982 (2012).
- Kane, C. L. & Mele, E. J.  $Z_2$  topological order and the quantum spin Hall effect. *Phys. Rev. Lett.* **95**, 146802 (2005).
- Bernevig, B. A., Hughes, T. L. & Zhang, S.-C. Quantum spin Hall effect and topological phase transition in HgTe quantum wells. *Science* **314**, 1757–1761 (2006).
- Xu, C. & Moore, J. E. Stability of the quantum spin Hall effect: Effects of interactions, disorder, and  $Z_2$  topology. *Phys. Rev. B* **73**, 045322 (2006).
- Qi, X.-L., Hughes, T. L. & Zhang, S.-C. Topological field theory of time-reversal invariant insulators. *Phys. Rev. B* **78**, 195424 (2008).
- Tung, Y. W. & Cohen, M. L. Relativistic band structure and electronic properties of SnTe, GeTe, and PbTe. *Phys. Rev.* **180**, 823–826 (1969).
- Melvin, J. S. & Hendry, D. C. Self-consistent relativistic energy bands for tin telluride. *J. Phys. C* **12**, 3003–3012 (1979).
- Littlewood, P. B. *et al.* Band structure of SnTe studied by photoemission spectroscopy. *Phys. Rev. Lett.* **105**, 086404 (2010).
- Richard Burke, J. Jr, Allgaier, R. S., Houston, B. B., Babiskin, J. & Siebenmann, P. G. Shubnikov-de Haas effect in SnTe. *Phys. Rev. Lett.* **14**, 360–361 (1965).
- Allgaier, R. S. & Houston, B. Weak-field magnetoresistance and the valence-band structure of SnTe. *Phys. Rev. B* **5**, 2186–2197 (1972).
- Iizumi, M., Hamaguchi, Y., Komatsubara, K. F. & Kato, Y. Phase transition in SnTe with low carrier concentration. *J. Phys. Soc. Jpn* **38**, 443–449 (1975).
- Bostwick, A., Ohta, T., Seyller, T., Horn, K. & Rotenberg, E. Quasiparticle dynamics in graphene. *Nature Phys.* **3**, 36–40 (2007).
- Nakayama, K., Sato, T., Takahashi, T. & Murakami, H. Doping induced evolution of Fermi surface in low carrier superconductor TI-doped PbTe. *Phys. Rev. Lett.* **100**, 227004 (2008).

## Acknowledgements

We thank L. Fu for stimulating discussions. We also thank M. Komatsu, M. Nomura, E. Ieki, T. Takahashi, N. Inami, H. Kumigashira and K. Ono for their assistance in ARPES measurements, and T. Ueyama and K. Eto for their assistance in crystal growth. This work was supported by JSPS (NEXT Program and KAKENHI 23224010), JST-CREST, MEXT of Japan (Innovative Area Topological Quantum Phenomena), AFOSR (AOARD 124038) and KEK-PF (proposal number: 2012S2-001).

## Author contributions

Y.T., T.S., K.N., S.S. and T.T. performed ARPES measurements. Z.R., K.S. and Y.A. carried out the growth of the single crystals and their characterizations. Y.T., T.S. and Y.A. conceived the experiments and wrote the manuscript.

## Additional information

Supplementary information is available in the online version of the paper. Reprints and permissions information is available online at [www.nature.com/reprints](http://www.nature.com/reprints). Correspondence and requests for materials should be addressed to T.S. or Y.A.

## Competing financial interests

The authors declare no competing financial interests.

# Odd-Parity Pairing and Topological Superconductivity in a Strongly Spin-Orbit Coupled Semiconductor

Satoshi Sasaki,<sup>1</sup> Zhi Ren,<sup>1</sup> A. A. Taskin,<sup>1</sup> Kouji Segawa,<sup>1</sup> Liang Fu,<sup>2,\*</sup> and Yoichi Ando<sup>1,†</sup>

<sup>1</sup>*Institute of Scientific and Industrial Research, Osaka University, Ibaraki, Osaka 567-0047, Japan*

<sup>2</sup>*Department of Physics, Massachusetts Institute of Technology, Cambridge, Massachusetts 02139, USA*

(Received 23 July 2012; published 21 November 2012)

The existence of topological superconductors preserving time-reversal symmetry was recently predicted, and they are expected to provide a solid-state realization of itinerant massless Majorana fermions and a route to topological quantum computation. Their first likely example,  $\text{Cu}_x\text{Bi}_2\text{Se}_3$ , was discovered last year, but the search for new materials has so far been hindered by the lack of a guiding principle. Here, we report point-contact spectroscopy experiments suggesting that the low-carrier-density superconductor  $\text{Sn}_{1-x}\text{In}_x\text{Te}$  is accompanied by surface Andreev bound states which, with the help of theoretical analysis, would give evidence for odd-parity pairing and topological superconductivity. The present and previous finding of possible topological superconductivity in  $\text{Sn}_{1-x}\text{In}_x\text{Te}$  and  $\text{Cu}_x\text{Bi}_2\text{Se}_3$  suggests that odd-parity pairing favored by strong spin-orbit coupling is likely to be a common underlying mechanism for materializing topological superconductivity.

DOI: 10.1103/PhysRevLett.109.217004

PACS numbers: 74.45.+c, 03.65.Vf, 73.20.At, 74.20.Rp

Topological superconductors (TSCs) have become a research frontier in the study of topologically ordered electronic states of matter [1–4]. As a superconducting (SC) cousin of topological insulators [5,6], a TSC supports gapless surface quasiparticle states consisting of massless Majorana fermions as its distinctive characteristic. Majorana fermions are peculiar in that particles are their own antiparticles [7], and they are currently attracting significant interest because of their potential for fault-tolerant topological quantum computing [8]. The  $p$ -wave superconductor  $\text{Sr}_2\text{RuO}_4$  has been widely discussed [9] to be an example of a chiral TSC associated with spontaneous time-reversal symmetry breaking [10]. More recently, time-reversal-invariant TSCs were theorized and attracted much attention [6]. Lately, the  $\text{Cu}_x\text{Bi}_2\text{Se}_3$  superconductor [11] has been theoretically proposed [4] and experimentally identified [12] as the first likely example of such a TSC. However,  $\text{Cu}_x\text{Bi}_2\text{Se}_3$  crystals are intrinsically inhomogeneous [13] and it has been difficult to elucidate the nature of the surface Majorana fermions. Naturally, discoveries of new TSC materials are strongly called for. In this context,  $\text{Cu}_x\text{Bi}_2\text{Se}_3$  is peculiar in that it is a superconductor obtained by doping a topological insulator, and such materials are few and far between; consequently, the prospect of finding new TSC materials in doped topological insulators is not very bright.

Nevertheless, the discovery of possible topological superconductivity in  $\text{Cu}_x\text{Bi}_2\text{Se}_3$  suggested that other TSCs might also be found in low-carrier-density semiconductors whose Fermi surface is centered around time-reversal-invariant momenta [14–16]. This motivated us to look for signatures of topological superconductivity in In-doped SnTe (denoted  $\text{Sn}_{1-x}\text{In}_x\text{Te}$ ) [17,18] whose Fermi surface depicted in Fig. 1(a) satisfies the above criteria.

In this Letter, by performing point-contact spectroscopy on  $\text{Sn}_{1-x}\text{In}_x\text{Te}$  single crystals, we found evidence for the existence of a surface Andreev bound state (ABS), which is a hallmark of an unconventional superconductivity [19]. Knowing that the symmetry and low-energy physics of this material [20] allows only three types of superconducting gap functions and that all possible unconventional states are topological, it is possible to conclude that  $\text{Sn}_{1-x}\text{In}_x\text{Te}$  is likely to be a TSC. This discovery not only enriches the family of possible TSC materials for their detailed investigations, but also points to a common mechanism for topological superconductivity, providing a guiding principle for the search of TSCs.

It is known that In in  $\text{Sn}_{1-x}\text{In}_x\text{Te}$  acts as an acceptor and suppresses the ferroelectric structural phase transition (SPT) in SnTe. Above  $x \simeq 0.04$  the SPT is completely suppressed and the system becomes a robust superconductor whose  $T_c$  gradually increases with  $x$  up to  $\sim 2$  K at  $x \simeq 0.10$  [18]. Specific-heat measurements have confirmed bulk superconductivity with possibly a strong pairing interaction for  $x = 0.044$  (where  $T_c = 1.0$  K) [18], but no experiment to detect the surface ABS has been carried out so far. In this Letter, we focus on samples with  $x = 0.045$  to avoid complications associated with the SPT.

SnTe crystallizes in the rocksalt structure (space group  $Fm\bar{3}m$ ) and hence possesses the  $O_h$  point-group symmetry. Our In-doped single crystals were grown by a vapor transport method. High-purity elements of Sn (99.99%), Te (99.999%), and In (99.99%) were used as starting materials. The In concentration was measured with inductively coupled plasma atomic emission spectroscopy and was confirmed to be consistent with the observed  $T_c$  [18]. The crystallographic orientation of the surface plane was confirmed by the x-ray Laue analysis to be (001).

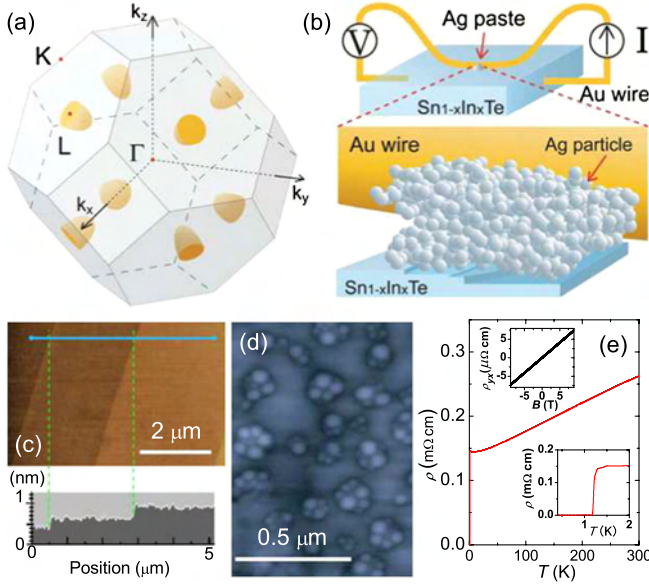


FIG. 1 (color online). SnTe and the soft point-contact spectroscopy. (a) The Fermi surfaces of  $p$ -type SnTe are centered around the four equivalent  $L$  points, which belong to the time-reversal-invariant momenta, in the bulk Brillouin zone of the cubic NaCl structure with fcc Bravais lattice. (b) Schematic picture of the soft point-contact spectroscopy experiment. (c) Atomic force microscope picture of an as-grown faceted surface of  $\text{Sn}_{1-x}\text{In}_x\text{Te}$  single crystal and its height profile. (d) Atomic force microscope picture of the Ag particles on the measured surface after the gold wire is removed. (e) Temperature dependence of the resistivity of the measured sample ( $x = 0.045$ ), showing no sign of structural phase transition. Lower inset shows a magnified view near the SC transition at 1.2 K. Upper inset shows the magnetic-field dependence of the Hall resistivity  $\rho_{yx}$  showing completely  $B$ -linear behavior, which indicates that the second valence band maxima, even if slightly populated, plays little role in our sample; the slope gives the carrier density of  $8 \times 10^{20} \text{ cm}^{-3}$ .

The resistivity and the Hall resistivity were measured in the Hall-bar geometry with a six-probe method on the same crystal [Fig. 1(e)]. The Quantum Design Physical Properties Measurement System was used as a platform to cool the samples down to 0.37 K and apply magnetic fields up to 9 T. The upper critical field  $H_{c2}$  defined by a sharp resistivity onset was 0.3 T at 0.37 K [Fig. 2(e)].

We performed conductance spectroscopy on the faceted (001) as-grown surface [Fig. 1(c)] of  $\text{Sn}_{1-x}\text{In}_x\text{Te}$  single crystals with  $x = 0.045$  [ $T_c = 1.2$  K, see Fig. 1(e)] using a soft point-contact technique [21] [Fig. 1(b)] which was successfully applied to  $\text{Cu}_x\text{Bi}_2\text{Se}_3$  [12] to reveal its possible TSC nature. The soft point contacts were prepared by putting a tiny drop of silver paste below a 30- $\mu\text{m}$ -diameter gold wire [Fig. 1(b)]; an atomic force microscope image of the silver nanoparticles on a measured surface is shown in Fig. 1(d). The  $dI/dV$  spectra were measured with a lock-in technique by sweeping a dc current that is superimposed with a small amplitude [1.8  $\mu\text{A}$  (rms), corresponding to

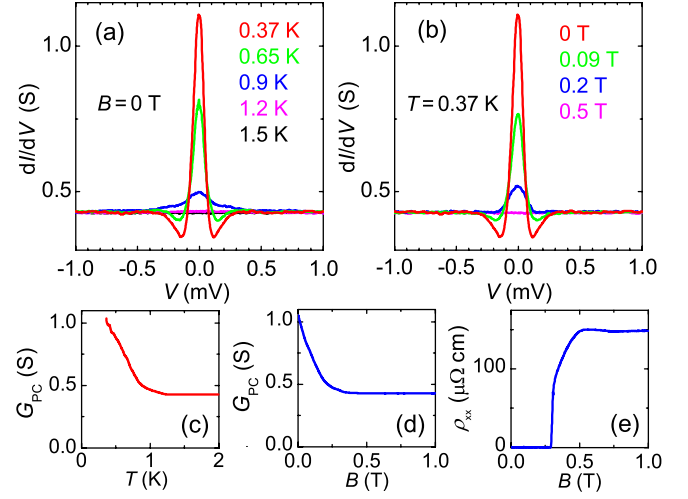


FIG. 2 (color online). Conductance spectra of  $\text{Sn}_{1-x}\text{In}_x\text{Te}$ . (a) Bias-voltage ( $V$ ) dependence of the differential conductance,  $[dI/dV](V)$ , at various temperatures in 0 T. (b)  $[dI/dV](V)$  in various magnetic fields at 0.37 K. (c) Temperature dependence of the zero-bias conductance in 0 T, showing its enhancement of more than a factor of 2 in the SC state at low temperature. (d) Magnetic-field ( $B$ ) dependence of the zero-bias conductance at 0.37 K. (e)  $B$  dependence of the resistivity  $\rho_{xx}$  at 0.37 K showing that 0.5 T is enough to completely suppress superconductivity.

0.7 A/cm<sup>2</sup>] ac current, and a quasi-four-probe configuration was employed to read the voltage between a normal metal (silver paste) and the sample (see Ref. [12] for details). We show in the Supplemental Material [22] that this technique yields ordinary Andreev reflection spectra [23] when applied to the conventional  $s$ -wave superconductor Sn.

When applied to  $\text{Sn}_{1-x}\text{In}_x\text{Te}$ , this technique allowed us to observe an intriguing signature of ABS [24] [Figs. 2(a) and 2(b)] rather than the ordinary Andreev reflection; namely, the bias-voltage dependence of the differential conductance  $dI/dV$  presents a pronounced peak at zero voltage (i.e., Fermi level) accompanied by dips on its sides at the energy scale of the SC gap ( $\pm 0.1$  meV). In the case of the ordinary Andreev reflection [23], as one can see in Fig. S1 of the Supplemental Material [22], two peaks, rather than dips, should be observed at the SC gap energy at low enough temperatures. Moreover, in our data for  $\text{Sn}_{1-x}\text{In}_x\text{Te}$ , the point-contact conductance at zero energy,  $G_{PC}$ , in the SC state becomes more than twice the normal-state value [Figs. 2(c) and 2(d)], which is impossible for Andreev reflections [23] and points to the existence of ABS on the surface [19,24].

The large magnitude of the observed zero-bias conductance peak (ZBCP) is already a strong indication that it is due to an ABS, but it is prudent to examine the possible relevance of other origins of the ZBCP, such as heating effect [25], reflectionless tunneling [26], and magnetic Kondo scattering [27]. In this respect, the magnetic-field dependence of the spectra [Fig. 2(b)] gives evidence



against those other possibilities (see the Supplemental Material [22] for details) and one can conclude with reasonable confidence that the observed ZBCP is caused by an inherent surface ABS. This conclusion points to an unconventional SC state in  $\text{Sn}_{1-x}\text{In}_x\text{Te}$ .

To identify the nature of the SC state in  $\text{Sn}_{1-x}\text{In}_x\text{Te}$ , we first note that the Fermi surface in the normal state consists of four ellipsoids centered at four  $L$  points of the fcc Brillouin zone. The conduction and valence bands in the vicinity of each  $L$  point are described by the  $k \cdot p$  Hamiltonian [20]:

$$H(\mathbf{k}) = m\sigma_z + v\sigma_x(k_1s_2 - k_2s_1) + v_3k_3\sigma_y. \quad (1)$$

Here  $k_3$  is the momentum along the threefold axis  $\Gamma L$ ;  $k_2$  is along the twofold axis  $LK$ .  $s_i$  and  $\sigma_i$  are Pauli matrices associated with spin and orbital degrees of freedom, respectively. Specifically, the two orbitals labeled by  $\sigma_z = \pm 1$  are mainly derived from the  $p$  orbitals of Sn and Te atoms, respectively. We emphasize that at  $L$  points these two types of  $p$  orbitals have opposite parity and do not mix. The four-band Hamiltonian (1) of  $\text{Sn}_{1-x}\text{In}_x\text{Te}$  at the  $L$  points of the fcc lattice is essentially equivalent to that of  $\text{Cu}_x\text{Bi}_2\text{Se}_3$  at the  $\Gamma$  point of the rhombohedral lattice [14], both of which are dictated by the underlying  $D_{3d}$  point group symmetry.

We now discuss the possible pairing symmetries. Since the four  $L$  points are invariant under the inversion of crystal momentum  $\mathbf{k} \rightarrow -\mathbf{k}$ , superconducting order parameters with zero total momentum correspond to pairing *within* each Fermi pocket, and therefore consist of four components on the four Fermi pockets:  $\vec{\Delta} = (\Delta_1, \Delta_2, \Delta_3, \Delta_4)$ . Each  $\Delta_j$  can be classified by the representations of  $D_{3d}$ , a subgroup of the  $O_h$  point group for In-doped SnTe that leaves  $L_j$  invariant. For the Hamiltonian (1) at a given  $L_j$ , there are four types of momentum-independent gap functions  $\Delta_j$  with different internal spin and orbital structures, corresponding to the  $A_{1g}$ ,  $A_{1u}$ ,  $A_{2u}$ , and  $E_u$  representations of  $D_{3d}$  [4]. Furthermore, depending on the relative phases between  $\Delta_1, \dots, \Delta_4$ ,  $\vec{\Delta}$  belong to different representations of the  $O_h$  point group. It is beyond the scope of this Letter to exhaust all possibilities. Instead, we consider those superconducting states that do not spontaneously break any lattice symmetry, in accordance with all experimental facts known so far. There are three such states corresponding to the following one-dimensional representations of  $O_h$  point group:  $A_{1g}$ ,  $A_{1u}$ , and  $A_{2u}$ . [The  $E_u$  state breaks the threefold rotation symmetry around (111) axis.]

Among these three states,  $A_{1g}$  is even parity and fully gapped, which corresponds to an  $s$ -wave superconductor and does not have a surface ABS. Both  $A_{1u}$  and  $A_{2u}$  states are unconventional superconductors with odd-parity pairing. The  $A_{1u}$  state is fully gapped and realizes an odd-parity TSC. The topological invariant is given by  $N = \sum_j N_j$ , where  $|N_j| = 1$  is the invariant associated with each Fermi surface and its sign is given by  $\text{sgn}(\Delta_j)$  [15]. Importantly, the four

components  $\Delta_1, \dots, \Delta_4$  are related by rotation symmetry and have the same sign in the  $A_{1u}$  state. As a result, the  $A_{1u}$  state of In-doped SnTe is a TSC with  $|N| = 4$ , which supports topologically protected surface ABS.

The odd-parity  $A_{2u}$  state has point nodes at the intersection of each Fermi pocket with the  $\Gamma L$  line. These nodes are protected by the mirror symmetry of the fcc crystal structure. While it is impossible to define a 3D topological invariant for a gapless phase, one can still define “weak” topological invariants associated with 2D time-reversal-invariant planes in the Brillouin zone [28,29] that are fully gapped. For the  $A_{2u}$  state in In-doped SnTe, any plane that passes a *single*  $L$  point and avoids the nodes satisfies the criterion for 2D odd-parity TSC [4,30] and has a nonzero weak topological invariant. As a result, the  $A_{2u}$  state has topologically protected ABS, similar to those in the  $A_{2u}$  state of  $\text{Cu}_x\text{Bi}_2\text{Se}_3$  theoretically demonstrated earlier [12].

From the above analysis, we conclude that the two odd-parity states  $A_{1u}$  and  $A_{2u}$  are topologically nontrivial and support ABS that can naturally give rise to the observed ZBCP. We further propose an electron-phonon mechanism for odd-parity pairing in  $\text{Sn}_{1-x}\text{In}_x\text{Te}$ . First, we note that SnTe has a soft TO phonon at  $\mathbf{q} = \mathbf{0}$ , which couples strongly to *interband* electronic excitations [31]. This phonon mode corresponds to the displacement of Sn and Te sublattices relative to each other. It becomes unstable and leads to the SPT at low temperature. The SPT temperature is suppressed by In doping [18]. As one can see in Fig. 1(e), the temperature dependence of the resistivity shows no kink down to  $T_c$ , which indicates that the SPT is completely suppressed in our sample; according to the phase diagram [18], this is reasonable for  $x = 0.045$ . This suggests that the TO phonon remains stable. Moreover, proximity to the SPT suggests that the tendency toward ferroelectricity is strong, which naturally points to an attractive interaction between Sn and Te  $p$  orbitals.

Assuming that such an *interorbital* attraction from electron-phonon coupling is the origin for superconductivity, we can now theoretically deduce the pairing symmetry of  $\text{Sn}_{1-x}\text{In}_x\text{Te}$  by following a similar analysis as was done for  $\text{Cu}_x\text{Bi}_2\text{Se}_3$  [4]. Essentially, the spin-orbit coupled band structure (1) cooperates with the above attractive interaction to favor the pairing between Sn and Te orbitals. Because the two orbitals have opposite parity, as mentioned earlier, one may conclude that the pairing symmetry in  $\text{Sn}_{1-x}\text{In}_x\text{Te}$  is most likely odd parity. A detailed theory of the pairing mechanism and a full determination of the type of odd-parity pairing is beyond the scope of this Letter and will be presented elsewhere [32]. In any case, since the even-parity state does not produce a surface ABS but both odd-parity states in  $\text{Sn}_{1-x}\text{In}_x\text{Te}$  do, our experimental observation strongly suggests that the odd-parity pairing is realized in this material, which agrees with the above theoretical consideration for the pairing mechanism. Given that the two possible odd-parity states are both topological

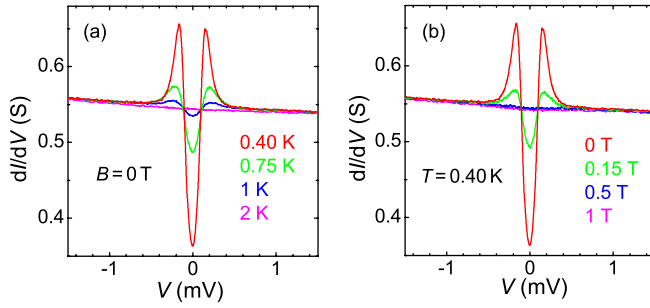


FIG. 3 (color online). Conductance spectra of  $\text{Pb}_{1-x}\text{Tl}_x\text{Te}$ . (a) Bias-voltage ( $V$ ) dependence of the differential conductance,  $[dI/dV](V)$ , at various temperatures in 0 T. (b)  $[dI/dV](V)$  in various magnetic fields at 0.40 K. The sample ( $x = 0.013$ ) measured here had zero-resistivity  $T_c$  of 1.35 K and carrier density of  $1.3 \times 10^{20} \text{ cm}^{-3}$ .

as already discussed, the present observation leads to the conclusion that  $\text{Sn}_{1-x}\text{In}_x\text{Te}$  is likely to be a TSC. Note that the similarities in both band structure and pairing symmetry between  $\text{Cu}_x\text{Bi}_2\text{Se}_3$  and  $\text{Sn}_{1-x}\text{In}_x\text{Te}$  naturally suggest that the calculations of the surface ABS performed for  $\text{Cu}_x\text{Bi}_2\text{Se}_3$  [12,14,33,34] should also hold qualitatively for  $\text{Sn}_{1-x}\text{In}_x\text{Te}$ . This means that the observed ZBCP is exactly what is theoretically expected for this type of TSC. In passing, it is useful to note that, in the conductance spectra of previously known candidate TSCs ( $\text{Sr}_2\text{RuO}_4$  [35] and  $\text{Cu}_x\text{Bi}_2\text{Se}_3$  [12]), the unusual dip at the SC gap energy scale has been consistently observed, bearing strong similarity to the present spectra.

Finally, we have also studied a similar superconducting material  $\text{Pb}_{1-x}\text{Tl}_x\text{Te}$  with the same point-contact technique [36]. Both  $\text{Sn}_{1-x}\text{In}_x\text{Te}$  and  $\text{Pb}_{1-x}\text{Tl}_x\text{Te}$  superconduct at 1–2 K [37], crystallize in rocksalt structure, and have similar band structures. Nevertheless, we found no evidence for a TSC state in  $\text{Pb}_{1-x}\text{Tl}_x\text{Te}$  (Fig. 3); the observed data are consistent with the Andreev reflection spectra of conventional SC state with a low contact transparency (close to the tunneling limit). The occurrence of the conventional SC state here is probably because the pairing interaction in  $\text{Pb}_{1-x}\text{Tl}_x\text{Te}$  is dominated by the charge Kondo mechanism [37] which leads to ordinary  $s$ -wave pairing. This comparison seems to indicate the importance of the TO phonon for TSC in this class of materials.

The discovery of possible topological superconductivity in  $\text{Sn}_{1-x}\text{In}_x\text{Te}$  reported here is instructive for further explorations of new TSCs: It gives us a guiding principle to look for semiconductors with strong spin-orbit coupling and having Fermi surfaces surrounding time-reversal-invariant momenta, because the likely occurrence of TSC in both  $\text{Cu}_x\text{Bi}_2\text{Se}_3$  and  $\text{Sn}_{1-x}\text{In}_x\text{Te}$  strongly suggests a common mechanism. In addition, this discovery has practical importance: While the previously discovered candidate material  $\text{Cu}_x\text{Bi}_2\text{Se}_3$  suffers a problem of intrinsic inhomogeneity [13] which hindered detailed studies, high-quality single crystals of  $\text{Sn}_{1-x}\text{In}_x\text{Te}$  with 100% SC volume fraction

are readily available. Hence,  $\text{Sn}_{1-x}\text{In}_x\text{Te}$  would make it possible to explore the new topological state of matter, the time-reversal-invariant TSC, on a robust platform for the first time.

We thank T. Ueyama and R. Yoshida for technical assistance. This work was supported by JSPS (NEXT Program and KAKENHI 24740237), MEXT (Innovative Area “Topological Quantum Phenomena” KAKENHI), and AFOSR (AOARD 124038).

\*liangfu@mit.edu

†y\_ando@sanken.osaka-u.ac.jp

- [1] A. P. Schnyder, S. Ryu, A. Furusaki, and A. W. W. Ludwig, *Phys. Rev. B* **78**, 195125 (2008).
- [2] M. M. Salomaa and G. E. Volovik, *Phys. Rev. B* **37**, 9298 (1988).
- [3] X.-L. Qi, T. L. Hughes, S. Raghu, and S.-C. Zhang, *Phys. Rev. Lett.* **102**, 187001 (2009).
- [4] L. Fu and E. Berg, *Phys. Rev. Lett.* **105**, 097001 (2010).
- [5] M. Z. Hasan and C. L. Kane, *Rev. Mod. Phys.* **82**, 3045 (2010).
- [6] X.-L. Qi and S.-C. Zhang, *Rev. Mod. Phys.* **83**, 1057 (2011).
- [7] F. Wilczek, *Nat. Phys.* **5**, 614 (2009).
- [8] J. Alicea, *Rep. Prog. Phys.* **75**, 076501 (2012); C. W. J. Beenakker, *arXiv:1112.1950*.
- [9] Y. Maeno, S. Kittaka, T. Nomura, S. Yonezawa, and K. Ishida, *J. Phys. Soc. Jpn.* **81**, 011009 (2012).
- [10] N. Read and D. Green, *Phys. Rev. B* **61**, 10267 (2000).
- [11] Y. S. Hor, A. J. Williams, J. G. Checkelsky, P. Roushan, J. Seo, Q. Xu, H. W. Zandbergen, A. Yazdani, N. P. Ong, and R. J. Cava, *Phys. Rev. Lett.* **104**, 057001 (2010).
- [12] S. Sasaki, M. Kriener, K. Segawa, K. Yada, Y. Tanaka, M. Sato, and Y. Ando, *Phys. Rev. Lett.* **107**, 217001 (2011).
- [13] M. Kriener, K. Segawa, Z. Ren, S. Sasaki, S. Wada, S. Kuwabata, and Y. Ando, *Phys. Rev. B* **84**, 054513 (2011).
- [14] T. H. Hsieh and L. Fu, *Phys. Rev. Lett.* **108**, 107005 (2012).
- [15] Y. Qi and L. Fu, APS March Meeting, <http://meetings.aps.org/Meeting/MAR12/Event/168229>.
- [16] K. Michaeli and L. Fu, *Phys. Rev. Lett.* **109**, 187003 (2012).
- [17] G. S. Bushmarina, I. A. Drabkin, V. V. Kompaniets, R. V. Parfen'ev, D. V. Shamshur, and M. A. Shakhov, *Sov. Phys. Solid State* **28**, 612 (1986).
- [18] A. S. Erickson, J.-H. Chu, M. F. Toney, T. H. Geballe, and I. R. Fisher, *Phys. Rev. B* **79**, 024520 (2009).
- [19] S. Kashiwaya and Y. Tanaka, *Rep. Prog. Phys.* **63**, 1641 (2000).
- [20] T. H. Hsieh, H. Lin, J. Liu, W. Duan, A. Bansil, and L. Fu, *Nat. Commun.* **3**, 982 (2012).
- [21] D. Daghero and R. S. Gonnelli, *Supercond. Sci. Technol.* **23**, 043001 (2010).
- [22] Supplemental Material at <http://link.aps.org/supplemental/10.1103/PhysRevLett.109.217004> for supplemental data and discussions.
- [23] G. E. Blonder, M. Tinkham, and T. M. Klapwijk, *Phys. Rev. B* **25**, 4515 (1982).



- [24] Y. Tanaka and S. Kashiwaya, *Phys. Rev. Lett.* **74**, 3451 (1995).
- [25] G. Sheet, S. Mukhopadhyay, and P. Raychaudhuri, *Phys. Rev. B* **69**, 134507 (2004).
- [26] C. W. J. Beenakker, *Phys. Rev. B* **46**, 12841(R) (1992).
- [27] L. Y. L. Shen and J. M. Rowell, *Phys. Rev.* **165**, 566 (1968).
- [28] J. E. Moore and L. Balents, *Phys. Rev. B* **75**, 121306 (2007).
- [29] L. Fu, C. L. Kane, and E. J. Mele, *Phys. Rev. Lett.* **98**, 106803 (2007).
- [30] M. Sato, *Phys. Rev. B* **81**, 220504(R) (2010).
- [31] S. Sugai, K. Murase, S. Katayama, S. Takaoka, S. Nishi, and H. Kawamura, *Solid State Commun.* **24**, 407 (1977).
- [32] L. Fu *et al.* (to be published).
- [33] A. Yamakage, K. Yada, M. Sato, and Y. Tanaka, *Phys. Rev. B* **85**, 180509(R) (2012).
- [34] L. Hao and T. K. Lee, *Phys. Rev. B* **83**, 134516 (2011).
- [35] S. Kashiwaya, H. Kashiwaya, H. Kambara, T. Furuta, H. Yaguchi, Y. Tanaka, and Y. Maeno, *Phys. Rev. Lett.* **107**, 077003 (2011).
- [36]  $\text{Pb}_{1-x}\text{Tl}_x\text{Te}$  single crystals were grown by a vapor transport method using high-purity elements of Pb (99.998%), Te (99.999%), and Tl (99.999%). The Tl concentration was measured with inductively coupled plasma atomic emission spectroscopy and was consistent with the  $T_c$  value [37]. For the point-contact experiments,  $\text{Pb}_{1-x}\text{Tl}_x\text{Te}$  crystals were cleaved at room temperature in air to obtain a good (001) surface.
- [37] Y. Matsushita, H. Bluhm, T. H. Geballe, and I. R. Fisher, *Phys. Rev. Lett.* **94**, 157002 (2005).

# Achieving Surface Quantum Oscillations in Topological Insulator Thin Films of $\text{Bi}_2\text{Se}_3$

A. A. Taskin, Satoshi Sasaki, Kouji Segawa, and Yoichi Ando\*

The three-dimensional (3D) topological insulators (TIs) realize a new quantum state of matter where insulating bulk states coexist with metallic surface states<sup>[1]</sup> due to a nontrivial topology of the Hilbert space spanned by the valence band wavefunctions. The surface states of TIs are peculiar in that they are comprised of spin-filtered, massless Dirac fermions that hold promise for novel spintronics and topological quantum computations.<sup>[2–4]</sup> However, the progress in real applications of TIs depends crucially on the quality of the materials used. The charge transport in most TI materials available today is dominated by the residual bulk conduction<sup>[5]</sup> caused by defects,<sup>[6]</sup> and the surface conductance has been successfully measured only in limited cases.<sup>[7–16]</sup> In this respect, the molecular beam epitaxy (MBE) is potentially a very promising technique for the synthesis of TIs because of the relatively low deposition temperature at which defect concentrations can be reduced in comparison with those in bulk crystals grown in thermal equilibrium. Moreover, thin films of TIs provide a suitable platform for realizing various artificial TI structures and devices, such as quantum wells, heterojunctions, and hybrid systems with other materials like ferromagnets. However, most of the MBE films of TIs grown so far<sup>[17–22]</sup> have a surface carrier mobility that is too low for reliable detection of surface conductance, even though in thin films the surface-to-bulk ratio is significantly increased in comparison with bulk single crystals.

Here, we demonstrate that one can greatly improve the quality of  $\text{Bi}_2\text{Se}_3$  epitaxial films grown on insulating sapphire substrates by increasing the substrate temperature during growth. As revealed by atomic force microscopy (AFM), a higher growth temperature leads to a larger size of grown terraces, which is correlated with improved transport parameters such as the phase coherence length governing the weak antilocalization (WAL) behavior. Although  $\text{Bi}_2\text{Se}_3$  does not grow on a sapphire substrate when its temperature is higher than  $\approx 270^\circ\text{C}$  due to a weak interaction of Bi and Se adatoms with the substrate, this obstacle can be overcome by employing a two-step deposition method, which has been applied to various materials in the past and was recently reported to be effective for  $\text{Bi}_2\text{Se}_3$ .<sup>[18,22]</sup> We show that thin films grown by this method with the temperature of the second step raised to  $300\text{--}320^\circ\text{C}$  have

high enough surface mobility to exhibit pronounced Subnikov-de Haas (SdH) oscillations, which provide a powerful tool for probing surface Dirac fermions.

The building block of the layered  $\text{Bi}_2\text{Se}_3$  is a quintuple layer (QL) as shown in **Figure 1a**. The surface is terminated by Se atoms without dangling bonds, resulting in only weak van der Waals forces. Due to a weak interaction of Bi and Se with a substrate, an epitaxial growth with very much relaxed lattice matching conditions, known as van der Waals epitaxy,<sup>[23]</sup> is possible at the very beginning as schematically shown in **Figure 1b**. A key parameter of the MBE growth is the temperature of deposition that determines the rate of adsorption/desorption of Bi and Se atoms as well as their surface diffusion. The AFM topographic images of our  $\text{Bi}_2\text{Se}_3$  films grown at various second-step temperatures clearly show that increasing the substrate temperature greatly improves the size of the terraces, as can be clearly seen in **Figure 1c–f**. Note that, in the two-step deposition procedure employed for those films, the initial 1–2 QLs of  $\text{Bi}_2\text{Se}_3$  were deposited at a low temperature of  $110\text{--}130^\circ\text{C}$ , at which sticking of adatoms to the substrate is very good, but their diffusion is very slow; naturally, the quality of the films in this initial state is poor, as indicated by blurred streaks in the reflection high-energy electron diffraction (RHEED) pattern (**Figure 2a**). After finishing this first deposition, the temperature of the substrate was slowly raised to  $300\text{--}320^\circ\text{C}$  and the rest of the film was deposited (at an even higher temperature, the initial ultrathin film will evaporate and no growth will proceed). We observed that, thanks to the surface diffusion of Bi and Se, the quality of the initial ultrathin film grown in the first step improves considerably during the heating up of the substrate before starting the successive deposition, as can be judged from the sharpening of streaks in the RHEED pattern (**Figure 2b**). Hence, the growth in the second step actually proceeds on a film of sufficiently high crystallinity, and any number of QLs can be deposited with high crystalline quality (as exemplified in **Figure 2c**) at  $300\text{--}320^\circ\text{C}$ . The best quality films have been obtained at temperatures around  $300^\circ\text{C}$  (**Figure 1f**).

Due to the van der Waals nature of the epitaxy, the growth of unstrained thin films is expected from the first QL. Indeed, as follows from the comparison of the distance between streaks shown in **Figure 2a–c**, the  $\text{Bi}_2\text{Se}_3$  film starts to grow practically immediately on the sapphire with its own lattice constant without any noticeable sign of relaxation. The high quality of our films grown at high temperatures, including ultrathin ones, is evident from the X-ray diffraction patterns shown in **Figure 2d**; here, in addition to the diffraction peaks of  $\text{Bi}_2\text{Se}_3$ , the Kiessig oscillations, which are an indication of smooth interfaces and high homogeneity (uniform structure),<sup>[24]</sup> are clearly seen in all the films. For the low-angle Kiessig fringes shown in **Figure 2e**,

Prof. A. A. Taskin, Prof. S. Sasaki, Prof. K. Segawa,  
Prof. Y. Ando  
Institute of Scientific and Industrial Research  
Osaka University  
8-1 Mihogaoka, Ibaraki, Osaka 567-0047, Japan  
E-mail: y\_ando@sanken.osaka-u.ac.jp



DOI: 10.1002/adma.201201827

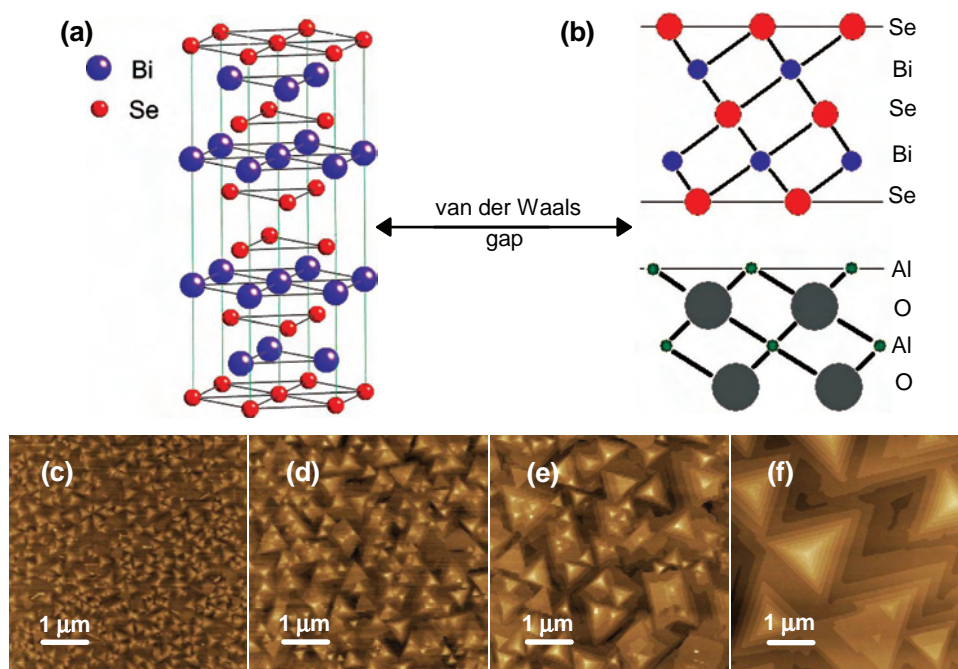


**Figure 1.** MBE growth of  $\text{Bi}_2\text{Se}_3$  thin films on sapphire. (a) Schematic picture of the  $\text{Bi}_2\text{Se}_3$  crystal structure (two quintuple layers are shown). (b) Schematic picture of the van der Waals epitaxy of  $\text{Bi}_2\text{Se}_3$  on sapphire (0001). (c–f) AFM topographic images of  $\text{Bi}_2\text{Se}_3$  thin films with the thickness of  $\approx 40$  QLs grown at different second-step temperatures: (c) 220 °C; (d) 260 °C; (e) 280 °C; (f) 320 °C.

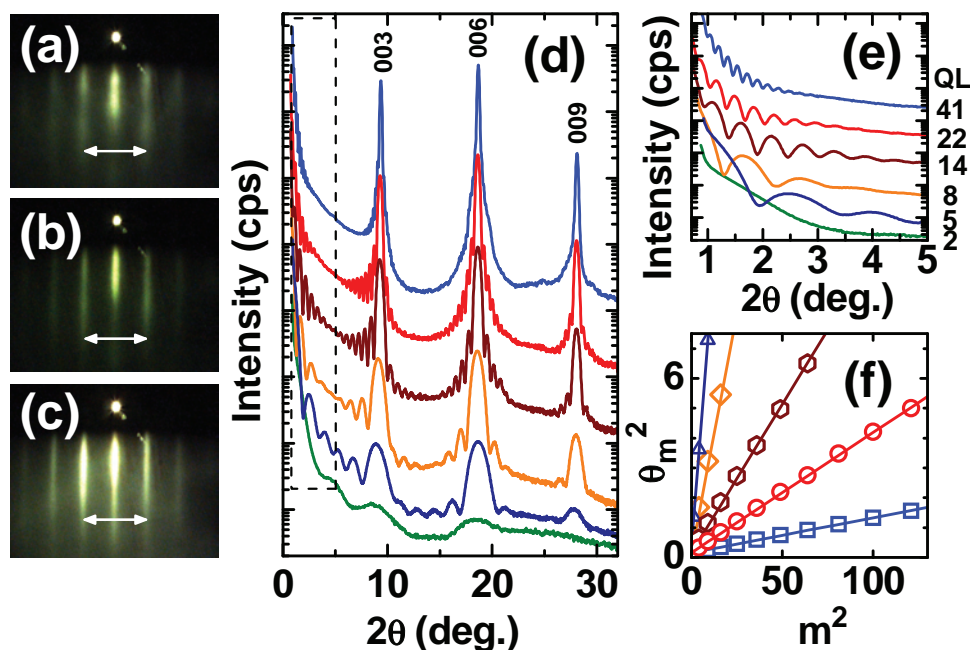


**Figure 2.** Structural characterization of  $\text{Bi}_2\text{Se}_3$  thin films. (a–c) RHEED pattern measured along the  $(11\bar{2}0)$  direction after (a) deposition of 2 QLs of  $\text{Bi}_2\text{Se}_3$  at 130 °C, (b) raising the temperature to 300 °C (without deposition), and (c) the additional deposition of 20 QLs of  $\text{Bi}_2\text{Se}_3$  at 300 °C. The distance between streaks, which corresponds to the lateral unit cell parameters, does not change during the deposition. (d,e) X-ray diffraction patterns for films with different thicknesses, showing clear Kiessig oscillations; the low-angle portion of the data enclosed by a dashed square in (d) is enlarged in (e). (f) The angular position,  $\theta_m$ , of the intensity maxima seen in (e) are plotted against the Kiessig fringe order,  $m$ . The slope of the linear fit to the data gives the film thickness.

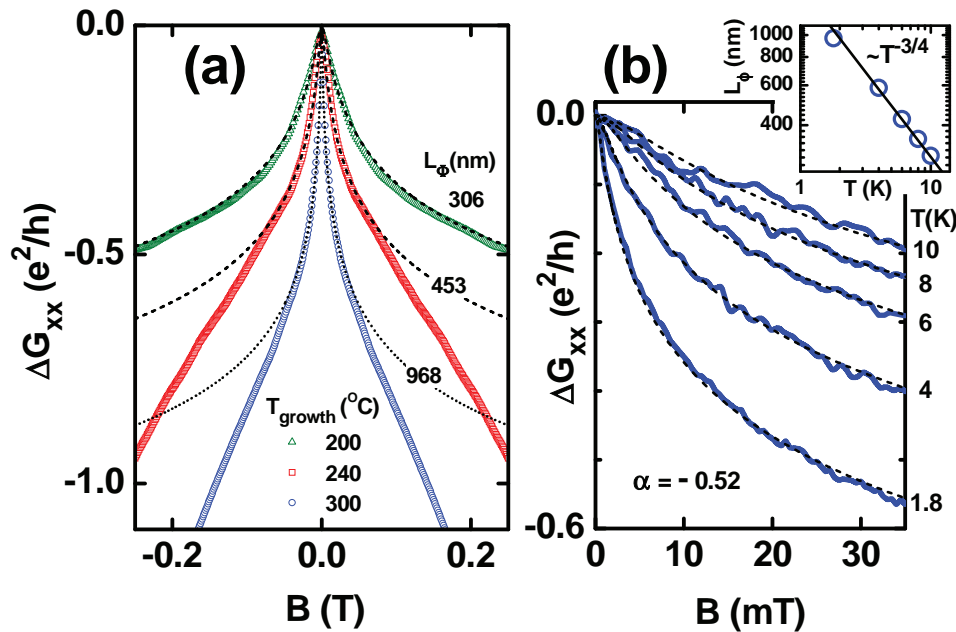


**Figure 3.** WAL behavior in  $\text{Bi}_2\text{Se}_3$  thin films. (a) Magnetic field dependence of  $G_{xx}$  measured at 1.8 K in  $\approx 40$  QL-thick films grown at different second-step temperatures. Dashed lines are the fits of the HLN formula (see text) to the low-field portion of the data. (b) WAL behavior measured at different temperatures in the film grown at 300 °C. Inset shows the temperature dependence of the phase coherence length obtained from the fittings shown in the main panel by dashed lines.

the angular position,  $\theta_m$ , of the intensity maxima depends on the Kiessig fringe order,  $m$ , as<sup>[24]</sup>

$$\theta_m^2 = \alpha_c^2 + m^2 (\lambda/2t)^2 \quad (1)$$

where  $\alpha_c$  is the critical angle of the total external reflection of the  $\text{Bi}_2\text{Se}_3$  layer,  $\lambda$  is the X-ray wavelength, and  $t$  is the film thickness. Figure 2f shows the plot of  $\theta_m^2$  vs.  $m^2$  for several films. The fitting of Equation 1 to the data gives an estimate of the film thickness, which agrees very well with those obtained by AFM measurements.

The improvement in the quality of the grown films has a profound effect on the transport properties of charge carriers. A dramatic manifestation of such an improvement can be found in the WAL behavior, which reflects both the Dirac nature of the surface states and the strong spin-orbit interaction in the bulk of TIs.<sup>[25,26]</sup> Since the destructive quantum interference between time-reversed paths responsible for the WAL is quickly suppressed in a perpendicular magnetic field, a signature of the WAL behavior is a cusp in the magnetoconductance  $\Delta G_{xx}(B)$ ;<sup>[25,26]</sup> the sharpness of the cusp essentially depends on the phase coherence length,  $L_\phi$ , which is the characteristic scale for quantum interference effects. This length determines the phase-coherent transport that can be destroyed by inelastic scattering and, thus,  $L_\phi$  can be a measure of the quality of the films. The exact behavior of  $\Delta G_{xx}(B)$  is described by the Hikami-Larkin-Nagaoka (HLN) formula:<sup>[27]</sup>

$$\Delta G_{xx}(B) = \alpha (e^2/\pi h) [\Psi(\hbar/4e L_\phi B + 1/2) - \ln(\hbar/4e L_\phi B)] \quad (2)$$

where  $\Psi$  is the digamma function and the prefactor  $\alpha$  should be  $-1/2$  if there is only one channel responsible for the WAL

behavior. **Figure 3** shows the magnetoconductance of several films with thicknesses of  $\approx 40$  QLs grown at different substrate temperatures. The dashed lines are the fits with Equation 2. The obtained  $\alpha$  is close to  $-1/2$  for all films (implying that the top and bottom surfaces are coupled through the bulk<sup>[25,26]</sup> to form a single effective channel for the phase-coherent transport), and  $L_\phi$  depends strongly on the growth conditions (Figure 3a); namely, the higher the temperature of the substrate at the second step, the longer the phase coherence length, which reaches almost 1  $\mu\text{m}$  in the best films. It is worth noting that the bulk carrier density in those films is about  $1 \times 10^{19} \text{ cm}^{-3}$  and is essentially independent of the growth temperature, while the bulk mobility increases steadily with increasing substrate temperature (from  $390 \text{ cm}^2 \text{ V}^{-1} \text{ s}^{-1}$  in the film grown at 200 °C to  $880 \text{ cm}^2 \text{ V}^{-1} \text{ s}^{-1}$  in the film grown at 300 °C). Figure 3b shows how the WAL behavior measured in the film grown at 300 °C changes with temperature. All the data from 1.8 to 10 K fit well using the HLN formula (Equation 2). The obtained  $L_\phi$  changes as  $\approx T^{-3/4}$  (shown in the inset of Figure 3b), which is a characteristic power law for the 3D electron-electron interaction dephasing mechanism<sup>[28]</sup> and points to the dominance of the scattering in the bulk channel.

The most direct indication of the high quality of epitaxial TI thin films is the high mobility of their surface charge carriers. Our films grown at the optimized conditions consistently show high enough mobility to produce pronounced quantum oscillations. **Figure 4** presents an example of the SdH oscillations observed in a 120-QL-thick film. A 2D character of oscillations is clearly seen from the angular dependence of  $dR_{xx}/dB$  measured in tilted magnetic fields: when the oscillation data for various magnetic field angles are plotted as a function of



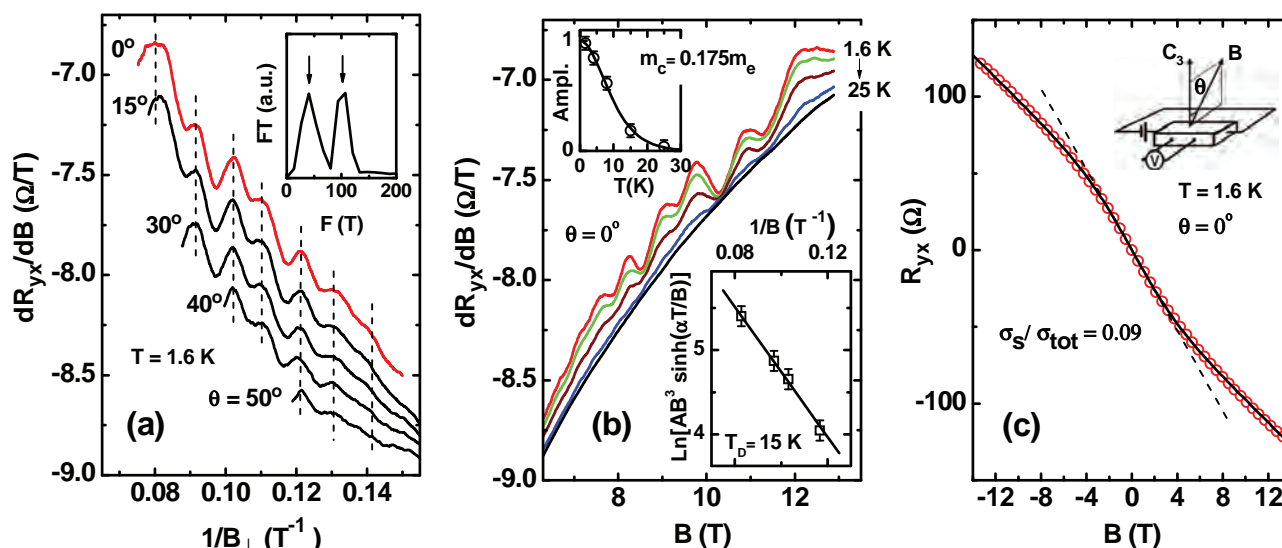


**Figure 4.** Surface SdH oscillations in the 120-QL-thick film. (a)  $dR_{yx}/dB$  measured in tilted magnetic fields and plotted as a function of  $1/B_{\perp}$  ( $= 1/B\cos\theta$ ); curves are shifted vertically for clarity. Dashed lines mark the positions of maxima, which depend only on  $B_{\perp}$ . Inset shows the Fourier transform of  $dR_{yx}/dB$  measured at  $\theta = 0^\circ$ , which reveals two frequencies coming from two surfaces. (b)  $dR_{yx}/dB$  measured at  $\theta = 0^\circ$  at different temperatures. Upper inset shows the temperature dependence of the oscillation amplitude, yielding the cyclotron mass of  $0.175m_e$ . Lower inset shows the Dingle plot of  $dR_{yx}/dB$  oscillations at 1.6 K (in the axis label,  $A$  is the amplitude of  $dR_{yx}/dB$ ); the slope gives the Dingle temperature of 15 K. (c) Fitting of the three-band model to the  $R_{yx}(B)$  data at 1.6 K, in which the surface carrier concentrations are fixed by the SdH frequencies. The fitting yields a bulk carrier density of  $6.2 \times 10^{18} \text{ cm}^{-3}$ , a bulk carrier mobility of  $730 \text{ cm}^2 \text{ V}^{-1} \text{ s}^{-1}$ , and a surface carrier mobility of  $1800 \text{ cm}^2 \text{ V}^{-1} \text{ s}^{-1}$ . Inset shows the geometry of transport experiments.

$1/B\cos\theta$ , one can see that maxima (and minima) of  $dR_{yx}/dB$  depend solely on the perpendicular component of the magnetic field,  $B_{\perp}$  ( $= B\cos\theta$ ), as shown in Figure 4a by vertical dashed lines. Hence, the oscillations are obviously coming from the surface, since the bulk states are still in the 3D regime at this thickness. The inset shows the Fourier transform of the oscillations at  $\theta = 0^\circ$ , revealing two frequencies,  $F_1 = 40 \text{ T}$  and  $F_2 = 102 \text{ T}$ , presumably coming from two surfaces (top and bottom) of the film. These frequencies directly give the size of the Fermi surfaces of 2D charge carriers,  $k_{F1} = 3.5 \times 10^6 \text{ cm}^{-1}$  and  $k_{F2} = 5.5 \times 10^6 \text{ cm}^{-1}$ , which correspond to spin-filtered concentrations of surface electrons,  $n_{s1} = 9.7 \times 10^{11} \text{ cm}^{-2}$  and  $n_{s2} = 2.4 \times 10^{12} \text{ cm}^{-2}$ , respectively, if we assume their Dirac nature. It is worth noting that if the SdH oscillations were due to a trivial 2D electron gas (2DEG) which may form due to possible band bending near the surface, the obtained  $k_F$  would be too small to consistently account for the Hall data (Figure 4c), because it imposes an unrealistic constraint on the concentration of bulk carriers.<sup>[29]</sup> From the temperature dependence of the SdH oscillations shown in Figure 4b, the cyclotron mass,  $m_c = 0.175m_e$  ( $m_e$  is the free electron mass), is obtained by fitting the standard Lifshitz-Kosevich theory<sup>[30]</sup> to the temperature dependence of the oscillation amplitude (upper inset of Figure 4b). The Fermi velocity,  $v_F \approx 3 \times 10^7 \text{ cm/s}$ , estimated from  $m_c$ , is consistent with the value expected for Dirac fermions in  $\text{Bi}_2\text{Se}_3$ .<sup>[31]</sup> The Dingle plot shown in the lower inset of Figure 4b gives the Dingle temperature of 15 K, which corresponds to the quantum scattering time of  $8 \times 10^{-14} \text{ s}$ , giving the lower bound<sup>[8]</sup> of  $800 \text{ cm}^2 \text{ V}^{-1} \text{ s}^{-1}$  for the surface mobility. A more accurate value can be obtained from the Hall measurements (Figure 4c), in

which  $R_{yx}(B)$  shows different slopes at low (dashed line in Figure 4c) and high fields due to the contributions of multiple (two 2D and one 3D) transport channels. By fixing the concentrations of surface electrons based on the SdH frequencies, a fitting of the three-band model<sup>[8,10]</sup> to the  $R_{yx}(B)$  data reliably separates the surface and the bulk contributions to the transport, revealing that about 9% of the total conductance of this 120-QL-thick film is due to the surface and that the mobility of surface electrons is as high as  $1800 \text{ cm}^2 \text{ V}^{-1} \text{ s}^{-1}$ , which correspond to a mean free path of  $\approx 50 \text{ nm}$ .

In summary, we demonstrate that high quality  $\text{Bi}_2\text{Se}_3$  epitaxial films can be grown on insulating sapphire substrates by increasing the substrate temperature during deposition to  $300\text{--}320^\circ\text{C}$ . Since the first epilayer of  $\text{Bi}_2\text{Se}_3$  does not form on sapphire at such high temperatures, it is necessary to employ a two-step deposition method, in which the initial deposition is performed at  $110\text{--}130^\circ\text{C}$ . The films grown by this method acquire superb transport properties such as a long phase coherence length (approaching  $1 \mu\text{m}$ ) important for studying quantum interference effects and a high surface mobility ( $\approx 1800 \text{ cm}^2 \text{ V}^{-1} \text{ s}^{-1}$ ) indispensable for probing and manipulating surface Dirac fermions. This achievement is an important step toward establishing a suitable MBE growth technique for TI materials.

## Experimental Section

$\text{Bi}_2\text{Se}_3$  films were grown by MBE on sapphire (0001) under Se-rich conditions. We employed a two-step deposition procedure described in

the main text. Bi (99.9999%) and Se (99.999%) were both evaporated from standard Knudsen cells. The  $\text{Se}_2(\text{Se}_4)/\text{Bi}$  flux ratio was kept between 15 and 20. The growth rate, which is determined by the Bi flux, was kept at 0.2–0.3 QL/min. The thickness was measured with AFM after the growth by scanning a scratch made on the film.

The resistivity was measured by a standard four-probe method on a rectangular sample deposited on a substrate with the size of approximately  $15 \text{ mm} \times 4 \text{ mm}$ . Six ohmic contacts were made with silver paste and cured at room temperature. For all measurements except for the angular dependence of the Shubnikov-de Haas oscillations, the magnetic field was applied perpendicular to the plane of the film. The  $R_{xx}(B)$  and  $R_{yx}(B)$  were measured simultaneously by sweeping the magnetic field between  $\pm 14 \text{ T}$  at fixed temperatures.

## Acknowledgements

We thank V.G. Mansurov for helpful suggestions about MBE growth. This work was supported by the Japan Society for the Promotion of Science (NEXT Program), MEXT of Japan (Innovative Area “Topological Quantum Phenomena” KAKENHI 22103004), and AFOSR (AOARD 104103 and 124038) research grants.

Received: May 6, 2012

Revised: July 27, 2012

Published online: August 21, 2012

- [1] M. Z. Hasan, C. L. Kane, *Rev. Mod. Phys.* **2010**, *82*, 3045.
- [2] J. E. Moore, *Nature* **2010**, *464*, 194.
- [3] X. L. Qi, S.-C. Zhang, *Rev. Mod. Phys.* **2011**, *83*, 1057.
- [4] L. Fu, C. L. Kane, *Phys. Rev. Lett.* **2008**, *100*, 096407.
- [5] H. Cao, J. Tian, I. Miotkowski, T. Shen, J. Hu, S. Qiao, Y. P. Chen, *Phys. Rev. Lett.* **2012**, *108*, 215803.
- [6] D. O. Scanlon, P. D. C. King, R. P. Singh, A. de la Torre, S. McKeown Walker, G. Balakrishnan, F. Baumberger, C. R. A. Catlow, *Adv. Mater.* **2012**, *24*, 2154.
- [7] D. X. Qu, Y. S. Hor, J. Xiong, R. J. Cava, N. P. Ong, *Science* **2010**, *329*, 821.
- [8] Z. Ren, A. A. Taskin, S. Sasaki, K. Segawa, Y. Ando, *Phys. Rev. B* **2010**, *82*, 241306.
- [9] J. G. Analytis, R. D. McDonald, S. C. Riggs, J.-H. Chu, G. S. Boebinger, I. R. Fisher, *Nat. Phys.* **2010**, *10*, 960.
- [10] A. A. Taskin, Z. Ren, S. Sasaki, K. Segawa, Y. Ando, *Phys. Rev. Lett.* **2011**, *107*, 016801.
- [11] B. Sacépé, J. B. Oostinga, J. Li, A. Ubalini, N. J. G. Couto, E. Giannini, A. F. Morpurgo, *Nat. Commun.* **2011**, *2*, 575.
- [12] Z. Ren, A. A. Taskin, S. Sasaki, K. Segawa, Y. Ando, *Phys. Rev. B* **2011**, *84*, 075316.
- [13] S. S. Hong, J. J. Cha, D. Kong, Y. Cui, *Nat. Commun.* **2012**, *3*, 757.
- [14] Z. Ren, A. A. Taskin, S. Sasaki, K. Segawa, Y. Ando, *Phys. Rev. B* **2012**, *85*, 155301.
- [15] M. Lang, L. He, F. Xiu, X. Yu, J. Tang, Y. Wang, X. Kou, W. Jiang, A. V. Fedorov, K. L. Wang, *ACS Nano* **2012**, *6*, 295.
- [16] L. He, F. Xiu, X. Yu, M. Teague, W. Jiang, Y. Fan, X. Kou, M. Lang, Y. Wang, G. Huang, N.-C. Yeh, K. L. Wang, *Nano Lett.* **2012**, *12*, 1486.
- [17] G. Zhang, H. Qin, J. Teng, J. Guo, Q. Guo, X. Dai, Z. Fang, K. Wua, *Appl. Phys. Lett.* **2009**, *95*, 053114.
- [18] H. D. Li, Z. Y. Wang, X. Kan, X. Guo, H. T. He, Z. Wang, J. N. Wang, T. L. Wong, N. Wang, M. H. Xie, *New J. Phys.* **2010**, *12*, 103038.
- [19] Y.-Y. Li, G. Wang, X.-G. Zhu, M.-H. Liu, C. Ye, X. Chen, Y.-Y. Wang, K. He, L.-L. Wang, X.-C. Ma, H.-J. Zhang, X. Dai, Z. Fang, X.-C. Xie, Y. Liu, X.-L. Qi, J.-F. Jia, S.-C. Zhang, Q.-K. Xue, *Adv. Mater.* **2010**, *22*, 4002.
- [20] A. Richardella, D. M. Zhang, J. S. Lee, A. Koser, D. W. Rench, A. L. Yeats, B. B. Buckley, D. D. Awschalom, N. Samarth, *Appl. Phys. Lett.* **2010**, *97*, 262104.
- [21] X. Chen, X.-C. Ma, K. He, J.-F. Jia, Q.-K. Xue, *Adv. Mater.* **2011**, *23*, 1162.
- [22] N. Bansal, Y. S. Kim, E. Edrey, M. Brahlek, Y. Horibe, K. Iida, M. Tanimura, G.-H. Li, T. Feng, H.-D. Lee, T. Gustafsson, E. Andrei, S. Oh, *Thin Solid Films* **2011**, *520*, 224.
- [23] A. Koma, *J. Cryst. Growth* **1999**, *201/202*, 236.
- [24] U. Pietsch, V. Holý, T. Baumbach, *High-resolution X-ray Scattering. From Thin Films to Lateral Nanostructures*, Springer, New York **2004**.
- [25] J. Chen, X. Y. He, K. H. Wu, Z. Q. Ji, L. Lu, J. R. Shi, J. H. Smet, Y. Q. Li, *Phys. Rev. B* **2011**, *83*, 241304(R).
- [26] H. Steinberg, J. B. Laloë, V. Fatemi, J. S. Moodera, P. Jarillo-Herrero, *Phys. Rev. B* **2011**, *84*, 233101.
- [27] S. Hikami, A. I. Larkin, Y. Nagaoka, *Prog. Theor. Phys.* **1980**, *63*, 707.
- [28] B. Altshuler, A. Aronov, in *Electron-electron Interaction in Disordered Conductors* (Eds: A. L. Efros, M. Pollak), Elsevier, Amsterdam **1985**.
- [29] The obtained  $k_F = 3.5 \times 10^6 \text{ cm}^{-1}$  implies that the Fermi energy,  $E_F$ , of the putative 2DEG would be 31 meV, and hence the bulk  $E_F$  in the conduction band must be smaller than 31 meV, since the conduction band must be bent downward near the surface for a 2DEG to form. This implies that the maximum possible bulk carrier density is  $1.1 \times 10^{18} \text{ cm}^{-3}$ ; however, this is incompatible with the  $R_{yx}(B)$  data which points to the existence of  $\approx 6 \times 10^{18} \text{ cm}^{-3}$  of electrons.
- [30] D. Shoenberg, *Magnetic Oscillations in Metals*, Cambridge University Press, Cambridge **1984**.
- [31] Y. Xia, D. Qian, D. Hsieh, L. Wray, A. Pal, H. Lin, A. Bansil, D. Grauer, Y. S. Hor, R. J. Cava, M. Z. Hasan, *Nat. Phys.* **2009**, *5*, 398.



# Manifestation of Topological Protection in Transport Properties of Epitaxial $\text{Bi}_2\text{Se}_3$ Thin Films

A. A. Taskin, Satoshi Sasaki, Kouji Segawa, and Yoichi Ando\*

*Institute of Scientific and Industrial Research, Osaka University, Ibaraki, Osaka 567-0047, Japan*

(Received 9 April 2012; published 9 August 2012)

The massless Dirac fermions residing on the surface of three-dimensional topological insulators are protected from backscattering and cannot be localized by disorder, but such protection can be lifted in ultrathin films when the three-dimensionality is lost. By measuring the Shubnikov–de Haas oscillations in a series of high-quality  $\text{Bi}_2\text{Se}_3$  thin films, we revealed a systematic evolution of the surface conductance as a function of thickness and found a striking manifestation of the topological protection: The metallic surface transport abruptly diminishes below the critical thickness of  $\sim 6$  nm, at which an energy gap opens in the surface state and the Dirac fermions become massive. At the same time, the weak antilocalization behavior is found to weaken in the gapped phase due to the loss of  $\pi$  Berry phase.

DOI: [10.1103/PhysRevLett.109.066803](https://doi.org/10.1103/PhysRevLett.109.066803)

PACS numbers: 73.25.+i, 71.18.+y, 72.20.My, 73.20.At

In topological insulators (TIs) the energy states are fundamentally modified from ordinary insulators by strong spin-orbit interactions, giving rise to a topologically distinct state of matter with a gapped insulating bulk and a gapless metallic surface [1]. Various interesting phenomena, including surface transport of spin-filtered Dirac fermions that are immune to localization, have been predicted and raised expectations for novel applications [2–4]. However, the progress in real applications of TIs crucially relies on the ability to manipulate the surface current in transport experiments. At present, such basic characterization as the surface conductance measurement has been possible only in a few cases in single crystals [5–12] because of the dominance of bulk transport caused by unintentional doping due to defects. Molecular beam epitaxy (MBE) is a promising technique for the synthesis of TIs [13–18] owing, in part, to the relatively low deposition temperature at which defect concentrations can be reduced from those in bulk crystals grown in thermal equilibrium. So far, using MBE-grown films, angle-resolved photoemission spectroscopy (ARPES) [19] and scanning tunneling spectroscopy (STS) [20] have provided useful information about the topological surface state (SS), and in transport experiments, such phenomena as weak antilocalization (WAL) and gate-controlled ambipolar transport have been reported [21,22]. Also, since the MBE technique gives a precise control over film thickness, transport measurements for widely varying surface-to-bulk conductivity ratio have been performed [23–25], although a reliable separation of surface Dirac electrons from bulk carriers has been hindered by a relatively low mobility of carriers in available thin films. Recently, we have succeeded in growing high-quality epitaxial films of  $\text{Bi}_2\text{Se}_3$  that have a sufficiently high surface electron mobility to present pronounced Shubnikov–de Haas (SdH) oscillations. This made it possible to directly probe the surface conductance and the topological protection of the SS.

The immunity of the surface Dirac fermions to localization has a twofold origin [1–3]. One is the  $\pi$  Berry phase associated with massless Dirac fermions [26], which protects them from weak localization through destructive interference of time-reversed paths. The other is the peculiar spin-momentum locking which nulls the backscattering probability [1–3]. Those mechanisms are collectively called topological protection. Recently, it was found [19,27–31] that when TIs are thinned to the extent that the top and bottom surface states feel each other, their hybridization leads to an opening of the gap at the Dirac point and results in a degenerate, massive Dirac dispersion. This gapped state obviously violates the topological protection, but its consequence in the surface transport properties has not been duly addressed. In fact, this question is important because recently a lot of attention has been paid to the way to open a gap at the Dirac point [32] to realize topological magnetoelectric effects [33]. One may expect that unless the chemical potential is located exactly within the gap, the metallic surface transport is largely unaffected by the gap opening because states are kept being available for transport at the Fermi level. However, in the present work it turned out that the change in the Dirac spectrum deep in the occupied state has a profound effect on the physics at the Fermi level.

The growth of  $\text{Bi}_2\text{Se}_3$  films occurs in a layer-by-layer manner, in which the 0.95-nm thick Se-Bi-Se-Bi-Se quintuple layer (QL) constitutes the basic unit [19]. Our systematic magnetotransport measurements for varying thickness reveal a sudden diminishment of the surface transport below the critical thickness of  $\sim 6$  QL, below which the energy gap opens in the Dirac spectrum [19]. We also observed that the weak antilocalization behavior [21,22] quickly weakens below the critical thickness. We discuss that those striking effects are due to acquired degeneracy of the surface states [29] and loss of their  $\pi$  Berry phase [34,35] in the gapped phase.

Our MBE films were grown under Se-rich conditions on insulating sapphire (0001) substrates whose size was approximately  $15 \times 4 \text{ mm}^2$ . To obtain films of high enough quality to present SdH oscillations, we employed a two-step deposition procedure [36,37]. Both Bi (99.9999%) and Se (99.999%) were evaporated from standard Knudsen cells. The  $\text{Se}_2(\text{Se}_4)/\text{Bi}$  flux ratio was kept between 15–20. The growth rate, which is determined by the Bi flux, was kept at 0.2–0.3 QL/min. The resistance  $R_{xx}$  and the Hall resistance  $R_{yx}$  were measured in the Hall bar geometry by a standard six-probe method on rectangular samples on which the contacts were made with silver paste at the perimeter and cured at room temperature under pressure of  $\sim 1 \text{ Pa}$ . The magnetic field was swept between  $\pm 14 \text{ T}$  at fixed temperatures and was always applied perpendicular to the films, except for the angular-dependence measurements of the Shubnikov–de Haas oscillations.

An atomic force microscopy (AFM) image of our relatively thick (50 QL) film is shown in Fig. 1(a), where a large, atomically flat area of  $\sim 1 \mu\text{m}^2$  and several sharp terraces with the height of exactly 1 QL can be clearly seen. The reflection high-energy electron diffraction (RHEED) pattern with sharp  $1 \times 1$  streaks [Fig. 1(a) inset] and sharp x-ray diffraction peaks [Fig. 1(b)] are also indications of the high crystal quality of our films.

Temperature dependencies of the sheet resistance,  $R_s(T)$ , measured in films with systematically changed thickness  $t$  down to 2 QL are shown in Fig. 1(c). The  $R_s(T)$  behavior is metallic in thick films, but below  $t = 5 \text{ QL}$ , it starts to show an upturn at low temperatures. In particular, the sharp divergence in  $R_s$  for  $T \rightarrow 0$  in the 2-QL film is indicative of strong Anderson localization and an insulating ground state (see Supplemental Material [37]).

The breakthrough in the present work is that our films exhibit pronounced two-dimensional (2D) SdH oscillations

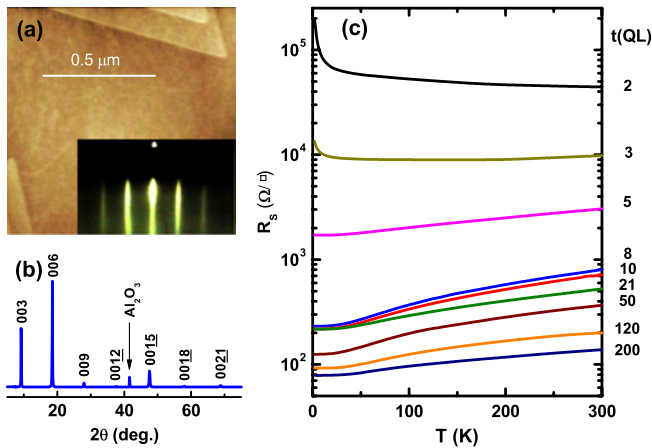


FIG. 1 (color online). (a) AFM image of a 50-nm thick  $\text{Bi}_2\text{Se}_3$  film showing atomically flat terraces with 1-QL steps. Inset: typical RHEED pattern. (b) X-ray diffraction pattern of a 200-QL film. (c) Temperature dependences of  $R_s$  for different thickness.

to provide a direct way to probe the surface charge transport. As an example, the analysis of the SdH oscillations in the 10-QL film is shown in Fig. 2. The 2D character of the oscillations is evident in Fig. 2(a), where the positions of the maxima and minima depend only on the perpendicular component of the magnetic field,  $B_\perp$ . The oscillation frequency  $F = 106.8 \text{ T}$  is obtained from the Fourier transform [lower inset of Fig. 2(c)], and this is a direct measure of the Fermi wave number  $k_F = 5.7 \times 10^6 \text{ cm}^{-1}$ . As we discuss in detail in the Supplemental Material [37], if the SdH oscillations are due to the trivial 2D electron gas which may form due to a band bending near the surface [38], this  $k_F$  is so small that it imposes too strong a constraint on the possible bulk Fermi level, which makes it impossible to consistently explain the transport data. Hence, we identify the oscillations to be due to surface Dirac fermions, and the obtained  $k_F$  gives their density  $n_s = 2.6 \times 10^{12} \text{ cm}^{-2}$ .

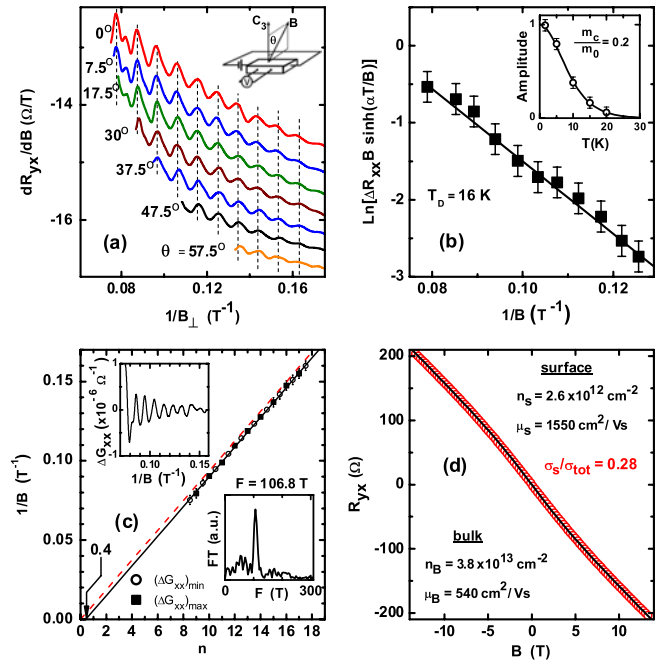


FIG. 2 (color online). Surface SdH oscillations in the 10-QL film. (a)  $dR_{yx}/dB$  in tilted magnetic fields, plotted as a function of  $1/B_\perp$  ( $= 1/B \cos\theta$ ); curves are shifted vertically for clarity. Dashed lines mark the positions of maxima. Inset shows the geometry of the experiment. (b) Dingle plot of the oscillations in  $\Delta R_{xx}$  at 1.6 K, obtained after subtracting a smooth background from  $R_{xx}(B)$ , giving the Dingle temperature of 16 K. Inset:  $T$ -dependence of the SdH amplitude for  $\theta = 0^\circ$ . (c) Landau-level fan diagram for oscillations in  $G_{xx}$  measured at  $T = 1.6 \text{ K}$  and  $\theta = 0^\circ$ ; following Ref. [43], integers  $n$  (half-integers  $n + \frac{1}{2}$ ) are assigned to the minima (maxima) in  $\Delta G_{xx}$ . The solid line is a linear fitting to the data with the slope fixed at  $F = 106.8 \text{ T}$ ; the dashed line has the same slope and extrapolates to zero. Upper inset shows  $\Delta G_{xx}$  vs  $1/B$  after subtracting a smooth background; lower inset shows its Fourier transform giving  $F = 106.8 \text{ T}$ . (d) Fitting of the two-band model to the  $R_{yx}(B)$  data at 1.6 K.



In this 10-QL film, we observed only a single frequency, but we usually see two frequencies in other films (see Fig. S3 of the Supplemental Material [37]), suggesting that the top and bottom surfaces have somewhat different  $n_s$ . The temperature dependence of the oscillation amplitude [Fig. 2(b) inset] gives the cyclotron mass  $m_c = 0.2m_0$  ( $m_0$  is the free electron mass) [39] which in turn gives the Fermi velocity  $v_F = 3.3 \times 10^7 \text{ cm s}^{-1}$ . This  $v_F$  is consistent with the ARPES data [40] as well as the STS data [20,41] for the Dirac cone. The obtained  $k_F$  value corresponds to the Fermi level of  $\sim 0.16 \text{ eV}$  above the Dirac point for the topological surface state, which points to a slight upward band bending [42]. The Dingle analysis [Fig. 2(b); see the Supplemental Material [37] for details] yields the mobility  $\mu_s = 1330 \text{ cm}^2 \text{ V}^{-1} \text{ s}^{-1}$ . Finally, Fig. 2(c) shows the Landau-level fan diagram for the oscillations in conductance  $G_{xx}$ , where the positions of the minima in  $\Delta G_{xx}$  (shown in the upper inset) are plotted as a function of  $n$  [43]. Here, to minimize the error occurring from extrapolation [12], we fix the slope of the linear fitting by using  $F = 106.8 \text{ T}$  obtained from the Fourier analysis and determine the intercept  $n = 0.40 \pm 0.04$  (solid line); this is very close to the ideal value of 0.5 for Dirac electrons bearing the  $\pi$  Berry phase [44], giving further confidence in the origin of the SdH oscillations. For comparison, a straight line with the same slope to give zero Berry phase is shown in Fig. 2(c) with a dashed line, which is obviously inconsistent with the experimental data.

To estimate the contribution of the SS in the overall transport in this 10-QL film, we use the magnetic-field dependence of the Hall resistivity,  $R_{yx}(B)$  [Fig. 2(d)], which is not linear in  $B$  and thus signifies the presence of at least two types of carriers. The fitting of a standard two-band model [6,8,45] to the data, in which  $n_s$  is fixed by the SdH frequency, gives the surface contribution to the total conductance,  $G_s/G_{\text{tot}}$ , of 28%. The  $\mu_s$  value obtained from this fitting is close to the SdH result, assuring the consistency of our analysis.

The same analysis can be applied to all measured films with  $t \geq 8 \text{ QL}$ , in which we consistently observed SdH oscillations [37]. Evolutions of the transport parameters with changing  $t$  are summarized in Figs. 3(a)–3(c). We note that by tracing the evolution of the SdH oscillations starting from thick films, we can distinguish the topological SS from the 2D quantum-well state of the bulk origin [37] as the source of the SdH oscillations.

Our main finding is that the surface transport abruptly diminishes below a critical thickness  $t_c$  which is located between 5 and 8 QL. This change is most convincingly manifested in the behavior of  $R_{yx}(B)$ , which suddenly becomes  $B$ -linear in films with  $t \leq 5 \text{ QL}$  [Fig. 3(d)]; this indicates that the transport becomes suddenly dominated by only one type of carriers. Correspondingly, the SdH oscillations disappear for  $t < t_c$ . More quantitatively, assuming that  $n_s$  is essentially unchanged through  $t_c$  [dashed

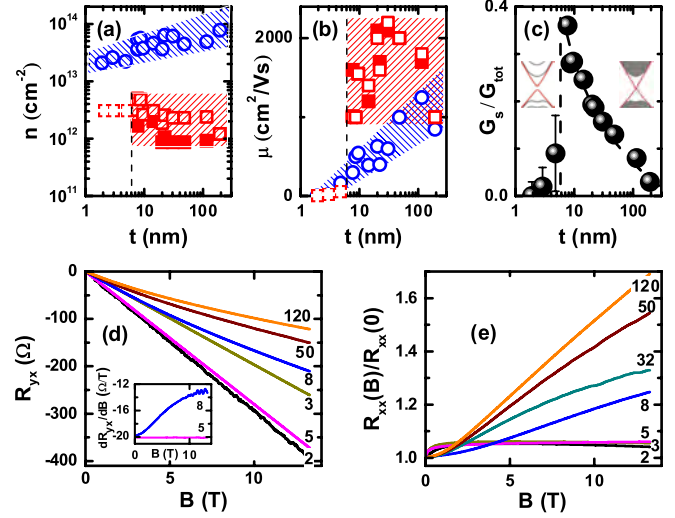


FIG. 3 (color online). (a) Squares are the  $n_s$  obtained from SdH oscillations (open and filled squares represent two different surfaces of the same film) and the dashed squares are an extrapolation of the trend above  $t_c$ ; circles are the sheet density of bulk carriers obtained from two-band analyses. (b) Mobilities of surface (squares) and bulk (circles) carriers obtained from two-band analyses. (c)  $G_s/G_{\text{tot}}$  obtained from the data in (a) and (b). Insets are schematic pictures of the energy bands for the two regimes. (d)  $R_{yx}(B)$  at 1.6 K for various thickness shown in QL unit; inset shows the derivative  $dR_{yx}/dB$  for the 5 and 8 QL films (5-QL data are shifted for clarity). (e)  $R_{yx}(B)/R_{yx}(0)$  of the same films.

squares in Fig. 3(a)], one can estimate that  $\mu_s$  must be suddenly degraded by more than an order of magnitude in samples with  $t < t_c$  [dashed squares in Fig. 3(b)] for  $R_{yx}(B)$  to become linear and be governed by bulk carriers [37]. The magnetoresistance behavior shown in Fig. 3(e) also presents a qualitative change below  $t_c$ , showing a negative slope at high fields. This evolution is best represented in the  $t$  dependence of  $G_s/G_{\text{tot}}$  [Fig. 3(c)], which shows a steady increase with decreasing  $t$  to reflect the change in the surface-to-bulk ratio, but it drops sharply below  $t_c$  to signify that the surface transport is abruptly diminished.

This observation naturally calls for the question whether the observed diminishment of the surface transport in ultrathin films might be related to a lowering of the quality in thinner films. In this respect, our ultrathin films remain essentially flat and smooth across  $t_c$ , with the surface bumpiness of only  $\sim 1 \text{ QL}$  (see Fig. S10 in the Supplemental Material [37]). This observation, combined with the fact that  $G_s/G_{\text{tot}}$  increases steadily with decreasing  $t$  until it reaches  $t_c$ , testifies against the above concern.

In addition to the above results, we found a striking change in the WAL behavior [21,22] below  $t = 5 \text{ QL}$ . Figure 4(a) shows the magnetoconductance of our films measured in perpendicular magnetic fields at 1.6 K. Dashed lines are the fitting with the Hikami-Larkin-Nagaoka formula [46],

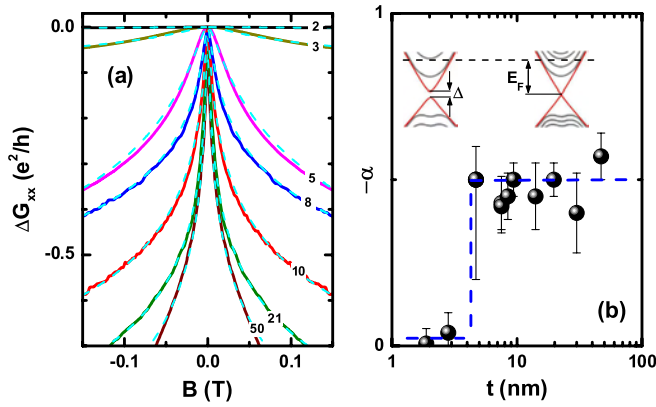


FIG. 4 (color online). (a) WAL behavior in sheet conductance at 1.6 K for various thicknesses shown in QL units; dashed lines are the fittings using Eq. (1). (b) Thickness dependence of  $\alpha$ . Inset shows schematic energy bands above and below the critical thickness.

$$\Delta G_{xx}(B) = \alpha \frac{e^2}{\pi h} \left[ \Psi\left(\frac{\hbar}{4eL_\phi^2 B} + \frac{1}{2}\right) - \ln\left(\frac{\hbar}{4eL_\phi^2 B}\right) \right], \quad (1)$$

where  $\Psi$  is the digamma function and  $L_\phi$  is the phase coherence length. The prefactor  $\alpha$  should be  $-\frac{1}{2}$  for each transport channel that either carries a  $\pi$  Berry phase [26] or bears a strong spin-orbit interaction [46]. In our analysis,  $\alpha$  and  $L_\phi$  are the only fitting parameters and Fig. 4(b) shows the  $t$  dependence of obtained  $\alpha$  (see the Supplemental Material [37] for details). For  $t \geq 5$  QL, we observed  $\alpha \approx -\frac{1}{2}$  similar to that reported for metallic  $\text{Bi}_2\text{Se}_3$  thin films, where top and bottom surfaces are connected through bulk electrons [21,22]. The change to  $\alpha \approx 0$  observed for  $t \leq 3$  QL is in accord with the diminishment of the surface transport channel and the eventual localization of the bulk state. A similar tendency was also observed in previous studies [23–25], although the decrease in  $\alpha$  was less pronounced, probably due to a larger metallicity of the measured samples.

Now we discuss the origin of our observations. As was already found in  $\text{Bi}_2\text{Se}_3$  ultrathin films by ARPES [19], an energy gap in the SS opens at the Dirac point below  $t_c \approx 6$  QL. Obviously, our transport measurements reflect this change in the Dirac dispersion. The gap is due to hybridization between top and bottom surfaces [schematically shown in the Fig. 4(b) inset], and such a hybridization gap  $\Delta$  changes the massless Dirac dispersion  $E = \pm \hbar v_F k$  into a massive one  $E = \pm \sqrt{(\hbar v_F k)^2 + (\Delta/2)^2}$  [29,34]. For  $\text{Bi}_2\text{Se}_3$ ,  $\Delta$  is about 0.25 eV at  $t = 2$  QL [19]. In our films, the Fermi level is estimated to be  $\sim 0.16$  eV above the Dirac point, so even in our thinnest film the Fermi level is not in the gap but crosses the SS as schematically shown in the inset of Fig. 4(b). Hence, the observed drastic suppression of the surface transport is *not* due to the disappearance of surface carriers but is likely due to an enhanced scattering of the carriers [47].

The gap opening also has a profound effect on the Berry phase  $\phi_B$  of the surface band  $\psi_k(r)$ . In the simplest case,  $\phi_B$  is given by [34]

$$\phi_B = -i \int_0^{2\pi} d\varphi \left\langle \psi_k(r) \left| \frac{\partial \psi_k(r)}{\partial \varphi} \right. \right\rangle = \pi \left( 1 - \frac{\Delta}{E_F} \right), \quad (2)$$

and hence the Berry phase is reduced from  $\pi$  when a gap opens. This lifts the immunity of the SS from weak localization. Also, this change in  $\phi_B$  weakens the WAL in the SS [35]. It is useful to note that in Fig. 4(a) the WAL was still observed for  $t = 5$  QL which is below  $t_c$ , but this is natural because the small  $\Delta$  at this  $t$  [19] makes the deviation of  $\phi_B$  from  $\pi$  to be small.

More importantly, in the gapped phase, the SS becomes degenerate [29], which means that now for each momentum both up and down spin states are available. This opens the backscattering channel and significantly reduces the surface mobility. Actually, the hybridization of top and bottom surfaces means that the system is no longer truly three-dimensional (3D), so it is natural that the topological properties of 3D TIs are lost in the gapped phase, in full agreement with recent *ab initio* density functional studies of TI thin films [30,31]. In this respect, the present observation is a spectacular manifestation of the topological protection of the SS in 3D TIs.

We thank V. G. Mansurov for helpful suggestions about MBE growth. We also thank S. Oh, M. Sato, and Y. Tanaka for useful discussions. This work was supported by JSPS (NEXT Program), MEXT (Innovative Area “Topological Quantum Phenomena” KAKENHI), and AFOSR (AOARD 104103 and 124038).

\*y\_ando@sanken.osaka-u.ac.jp

- [1] M. Z. Hasan and C. L. Kane, *Rev. Mod. Phys.* **82**, 3045 (2010).
- [2] J. E. Moore, *Nature (London)* **464**, 194 (2010).
- [3] X.-L. Qi and S.-C. Zhang, *Rev. Mod. Phys.* **83**, 1057 (2011).
- [4] L. Fu and C. L. Kane, *Phys. Rev. Lett.* **100**, 096407 (2008).
- [5] D. X. Qu, Y. S. Hor, J. Xiong, R. J. Cava, and N. P. Ong, *Science* **329**, 821 (2010).
- [6] Z. Ren, A. A. Taskin, S. Sasaki, K. Segawa, and Y. Ando, *Phys. Rev. B* **82**, 241306(R) (2010).
- [7] J. G. Analytis, R. D. McDonald, S. C. Riggs, J.-H. Chu, G. S. Boebinger, and I. R. Fisher, *Nature Phys.* **6**, 960 (2010).
- [8] A. A. Taskin, Z. Ren, S. Sasaki, K. Segawa, and Y. Ando, *Phys. Rev. Lett.* **107**, 016801 (2011).
- [9] B. Sacépé, J. B. Oostinga, J. Li, A. Ubalini, N. J. G. Couto, E. Giannini, and A. F. Morpurgo, *Nature Commun.* **2**, 575 (2011).
- [10] Z. Ren, A. A. Taskin, S. Sasaki, K. Segawa, and Y. Ando, *Phys. Rev. B* **84**, 075316 (2011).
- [11] S. S. Hong, J. J. Cha, D. Kong, and Y. Cui, *Nature Commun.* **3**, 757 (2012).

- [12] Z. Ren, A. A. Taskin, S. Sasaki, K. Segawa, and Y. Ando, *Phys. Rev. B* **85**, 155301 (2012).
- [13] X. Chen, X.-C. Ma, K. He, J.-F. Jia, and Q.-K. Xue, *Adv. Mater.* **23**, 1162 (2011).
- [14] G. Zhang, H. Qin, J. Teng, J. Guo, Q. Guo, X. Dai, Z. Fang, and K. Wu, *Appl. Phys. Lett.* **95**, 053114 (2009).
- [15] A. Richardella, D. M. Zhang, J. S. Lee, A. Koser, D. W. Rench, A. L. Yeats, B. B. Buckley, D. D. Awschalom, and N. Samarth, *Appl. Phys. Lett.* **97**, 262104 (2010).
- [16] H. D. Li, Z. Y. Wang, X. Kan, X. Guo, H. T. He, Z. Wang, J. N. Wang, T. L. Wong, N. Wang, and M. H. Xie, *New J. Phys.* **12**, 103038 (2010).
- [17] N. Bansal *et al.*, *Thin Solid Films* **520**, 224 (2011).
- [18] M. Lang, L. He, F. Xiu, X. Yu, J. Tang, Y. Wang, X. Kou, W. Jiang, A. V. Fedorov, and K. L. Wang, *ACS Nano* **6**, 295 (2012).
- [19] Y. Zhang *et al.*, *Nature Phys.* **6**, 584 (2010).
- [20] P. Cheng *et al.*, *Phys. Rev. Lett.* **105**, 076801 (2010).
- [21] J. Chen, X. Y. He, K. H. Wu, Z. Q. Ji, L. Lu, J. R. Shi, J. H. Smet, and Y. Q. Li, *Phys. Rev. B* **83**, 241304(R) (2011).
- [22] H. Steinberg, J. B. Lal  e, V. Fatemi, J. S. Moodera, and P. Jarillo-Herrero, *Phys. Rev. B* **84**, 233101 (2011).
- [23] Y. S. Kim, M. Brahlek, N. Bansal, E. Edrey, G. A. Kapilevich, K. Iida, M. Tanimura, Y. Horibe, S.-W. Cheong, and S. Oh, *Phys. Rev. B* **84**, 073109 (2011).
- [24] M. Liu *et al.*, *Phys. Rev. B* **83**, 165440 (2011).
- [25] N. Bansal, Y. S. Kim, M. Brahlek, E. Edrey, and S. Oh, [arXiv:1104.5709](https://arxiv.org/abs/1104.5709).
- [26] T. Ando, T. Nakanishi, and R. Saito, *J. Phys. Soc. Jpn.* **67**, 2857 (1998).
- [27] J. Linder, T. Yokoyama, and A. Sudbo, *Phys. Rev. B* **80**, 205401 (2009).
- [28] C.-X. Liu, H. J. Zhang, B. Yan, X.-L. Qi, T. Frauenheim, X. Dai, Z. Fang, and S.-C. Zhang, *Phys. Rev. B* **81**, 041307(R) (2010).
- [29] H.-Z. Lu, W.-Y. Shan, W. Yao, Q. Niu, and S.-Q. Shen, *Phys. Rev. B* **81**, 115407 (2010).
- [30] K. Park, J. J. Heremans, V. W. Scarola, and D. Minic, *Phys. Rev. Lett.* **105**, 186801 (2010).
- [31] J. Chang, L. F. Register, S. K. Banerjee, and B. Sahu, *Phys. Rev. B* **83**, 235108 (2011).
- [32] T. Sato, K. Segawa, K. Kosaka, S. Souma, K. Nakayama, K. Eto, T. Minami, Y. Ando, and T. Takahashi, *Nature Phys.* **7**, 840 (2011).
- [33] X.-L. Qi, T. L. Hughes, and S.-C. Zhang, *Phys. Rev. B* **78**, 195424 (2008).
- [34] H.-Z. Lu, J. Shi, and S.-Q. Shen, *Phys. Rev. Lett.* **107**, 076801 (2011).
- [35] H.-Z. Lu and S.-Q. Shen, *Phys. Rev. B* **84**, 125138 (2011).
- [36] Two-step deposition growth has been applied to various systems in the past. For  $\text{Bi}_2\text{Se}_3$ , it has been recently reported in Refs. [16,17].
- [37] See Supplemental Material at <http://link.aps.org/supplemental/10.1103/PhysRevLett.109.066803> for supplemental data and discussions.
- [38] M. Bianchi, D. Guan, S. Bao, J. Mi, B. B. Iversen, P. D. C. King, and P. Hofmann, *Nature Commun.* **1**, 128 (2010).
- [39] D. Shoenberg, *Magnetic Oscillations in Metals* (Cambridge University Press, Cambridge, England, 1984).
- [40] Y. Xia *et al.*, *Nature Phys.* **5**, 398 (2009).
- [41] T. Hanaguri, K. Igarashi, M. Kawamura, H. Takagi, and T. Sasagawa, *Phys. Rev. B* **82**, 081305(R) (2010).
- [42] Similar upward band bending has been observed in pure  $\text{Bi}_2\text{Se}_3$  crystals [J. G. Analytis, J.-H. Chu, Y. Chen, F. Corredor, R. D. McDonald, Z. X. Shen, and I. R. Fisher, *Phys. Rev. B* **81**, 205407 (2010)], in Sb-doped  $\text{Bi}_2\text{Se}_3$  crystals [7], and in  $\text{Bi}_{1.5}\text{Sb}_{0.5}\text{Te}_{1.7}\text{Se}_{1.3}$  crystals [8], so it is not unusual.
- [43] J. Xiong, Y. Luo, Y.-H. Khoo, S. Jia, R. J. Cava, and N. P. Ong, [arXiv:1111.6031](https://arxiv.org/abs/1111.6031).
- [44] A. A. Taskin and Y. Ando, *Phys. Rev. B* **84**, 035301 (2011).
- [45] N. W. Ashcroft and D. N. Mermin, *Solid State Physics* (Holt-Saunders, Tokyo, 1976).
- [46] S. Hikami, A. I. Larkin, and Y. Nagaoka, *Prog. Theor. Phys.* **63**, 707 (1980).
- [47] In a very recent paper reporting SdH oscillations in a 6-QL film [L. He *et al.*, *Nano Lett.* **12**, 1486 (2012)], the Fermi level was pinned in the gap and hence the detected physics was different. Similarly, an insulating behavior has been observed in an exfoliated 3.5-nm-thick crystal, but it was realized by tuning the Fermi level into the gap by gating [S. Cho, N. P. Butch, J. Paglione, and M. S. Fuhrer, *Nano Lett.* **11**, 1925 (2011)].

# Manipulation of Topological States and the Bulk Band Gap Using Natural Heterostructures of a Topological Insulator

K. Nakayama,<sup>1,\*</sup> K. Eto,<sup>2</sup> Y. Tanaka,<sup>1</sup> T. Sato,<sup>1,†</sup> S. Souma,<sup>3</sup> T. Takahashi,<sup>1,3</sup> Kouji Segawa,<sup>2</sup> and Yoichi Ando<sup>2,‡</sup>

<sup>1</sup>*Department of Physics, Tohoku University, Sendai 980-8578, Japan*

<sup>2</sup>*Institute of Scientific and Industrial Research, Osaka University, Ibaraki, Osaka 567-0047, Japan*

<sup>3</sup>*WPI Research Center, Advanced Institute for Materials Research, Tohoku University, Sendai 980-8577, Japan*

(Received 29 June 2012; published 4 December 2012)

We have performed angle-resolved photoemission spectroscopy on  $(\text{PbSe})_5(\text{Bi}_2\text{Se}_3)_{3m}$ , which forms a natural multilayer heterostructure consisting of a topological insulator and an ordinary insulator. For  $m = 2$ , we observed a gapped Dirac-cone state within the bulk band gap, suggesting that the topological interface states are effectively encapsulated by block layers; furthermore, it was found that the quantum confinement effect of the band dispersions of  $\text{Bi}_2\text{Se}_3$  layers enhances the effective bulk band gap to 0.5 eV, the largest ever observed in topological insulators. For  $m = 1$ , the Dirac-like state is completely gone, suggesting the disappearance of the band inversion in the  $\text{Bi}_2\text{Se}_3$  unit. These results demonstrate that utilization of naturally occurring heterostructures is a new promising strategy for manipulating the topological states and realizing exotic quantum phenomena.

DOI: [10.1103/PhysRevLett.109.236804](https://doi.org/10.1103/PhysRevLett.109.236804)

PACS numbers: 73.20.-r, 71.20.-b, 75.70.Tj, 79.60.-i

Three-dimensional (3D) topological insulators (TIs) realize a topological quantum state associated with unusual metallic surface states which appear within the bulk band gap [1,2]. The topological surface states are characterized by a Dirac-cone energy dispersion with a helical spin texture. Owing to the peculiar spin texture, the Dirac fermions in the TIs are immune to backward scattering by nonmagnetic impurities or disorder [3,4] and carry dissipationless spin current [5], holding promise for exploring fundamental physics, spintronics, and quantum computing [1,2]. However, there are a number of challenges that need to be overcome before TIs meet those promises. For example, while experimental realizations of novel topological phenomena depend crucially on the inherent robustness of the topological surface states against perturbations, it turned out to be difficult to maintain stable surface properties under ambient atmosphere [6,7]. Also, potential applications of TIs for a wide range of devices working at room temperature require a large bulk band gap, but the gap value reported to date is  $\sim 0.35$  eV at most [1,8]. Such a situation has been a hindrance for realizing novel topological phenomena and device applications of TIs, calling for a conceptually new approach to the manipulation of material properties of TIs.

A commonly used strategy for such a manipulation is the chemical substitution of constituent elements, as has been widely tried in systems based on  $\text{Bi}_2\text{Se}_3$  and  $\text{Bi}_2\text{Te}_3$  [6,9–14]. Another, potentially more effective approach is the heterostructure engineering where one can alter the stacking sequence of layers or insert different building blocks into the crystal, which may trigger gigantic quantum effects and/or new physical phenomena. However, this route has not been seriously explored in 3D TIs owing to a limited number of TI materials discovered to date.

In this Letter, we demonstrate that utilization of naturally occurring heterostructures in bulk crystals containing TI units is a promising pathway to overcome the aforementioned problems. Specifically, we show high-resolution angle-resolved photoemission spectroscopy (ARPES) data for lead-based (Pb-based) homologous series,  $(\text{PbSe})_5(\text{Bi}_2\text{Se}_3)_{3m}$ , which forms a natural multilayer heterostructure consisting of a TI and an ordinary insulator. Our results suggest that quantum confinement effects due to the characteristic layer stacking of this homologous series result in the “capping” of the topological states and the largest bulk band gap among known TIs. In addition, the states near the Fermi energy were found to present a drastic change between  $m = 1$  and 2, probably reflecting a band inversion in the  $\text{Bi}_2\text{Se}_3$  unit.

In tetradymite  $\text{Bi}_2\text{Se}_3$ , the ordered Se-Bi-Se-Bi-Se quintuple layer (QL) forms the basic unit, which is stacked along the (111) direction. In the case of our Pb-based compound whose chemical composition can be expressed as  $[(\text{PbSe})_5]_n[(\text{Bi}_2\text{Se}_3)_3]_m$ , the crystal consists of  $m$  QLs of  $\text{Bi}_2\text{Se}_3$  sandwiched by adjacent  $n$  bilayers of  $\text{PbSe}$  [15,16] [Fig. 1(a)], thus offering an excellent example to systematically alter the building blocks of the crystal, and is suitable for investigating new functional properties of TIs. We performed ARPES measurements for a fixed  $n$  value ( $n = 1$ ) with  $m = 1$  ( $\text{Pb}_5\text{Bi}_6\text{Se}_{14}$ ) and  $m = 2$  ( $\text{Pb}_5\text{Bi}_{12}\text{Se}_{23}$ ). The data are compared with those for  $\text{Bi}_2\text{Se}_3$ , which can be viewed as a member of this homologous series with  $(n, m) = (1, \infty)$ .

High-quality single crystals of  $(\text{PbSe})_5[(\text{Bi}_2\text{Se}_3)_3]_m$  were grown by a modified Bridgman method using high purity elements (Pb 99.998%, Bi and Se 99.9999%) in a sealed evacuated quartz tube. The phase diagram of the Pb-Bi-Se ternary system is very complicated [17], which



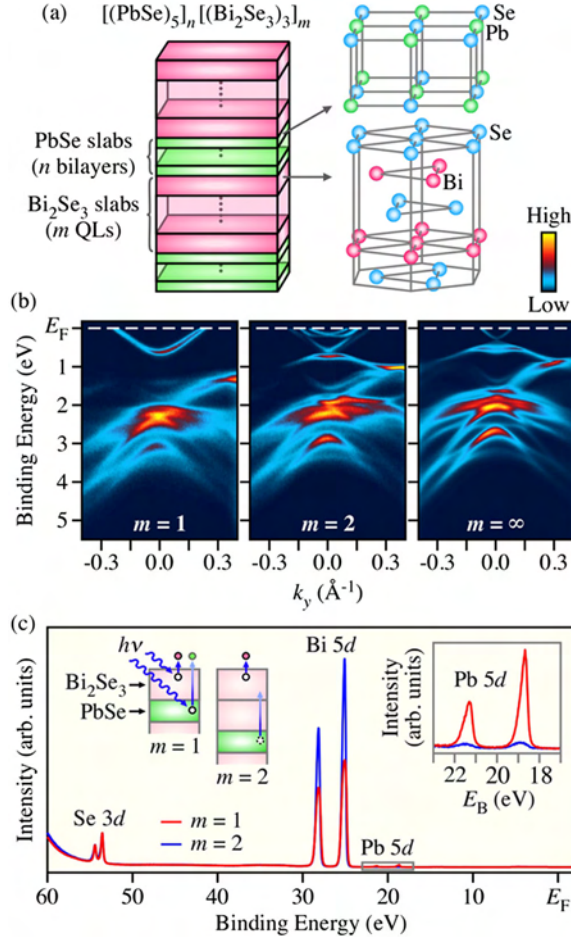


FIG. 1 (color online). (a) Schematic illustration of the building blocks of  $[(\text{PbSe})_5]_n[(\text{Bi}_2\text{Se}_3)_3]_m$  homologous series. (b) Comparison of the valence-band ARPES intensities of  $(\text{PbSe})_5(\text{Bi}_2\text{Se}_3)_3$  for  $m = 1, 2$ , and  $\infty$ , plotted as a function of  $E_B$  and wave vector measured along the  $\bar{\Gamma}\bar{K}$  cut of the Brillouin zone at  $T = 30$  K with  $h\nu = 60$  eV. (c) Normal-emission photoemission spectra in a wide energy region for  $m = 1$  and  $2$  measured with  $h\nu = 80$  eV at  $T = 30$  K. The right-hand inset shows a magnified view around the Pb-5d core levels. Schematic illustration of the cleaved surface and the photoemission process for  $m = 1$  and  $2$  is also displayed in the left-hand inset.

causes various crystal phases to compete during the crystal growth and one typically finds multiple phases in a boule grown by the Bridgman method. For this experiment, the starting composition was chosen to be  $\text{Pb}:\text{Bi}:\text{Se} = 2:2:5$ , and after the growth, the dominant phase in the boule was found to be different for the top and bottom parts of the boule. We chose the targeted phase (i.e.,  $m = 1$  or  $2$ ) based on the x-ray diffraction analysis of the crystals cut out from the boule. Nevertheless, it turned out from the ARPES measurements that a finite amount of mixtures of different phases in the bulk crystal are unavoidable (e.g., a few percent of  $m = 2$  domains are mixed in the  $m = 1$  sample as confirmed by the x-ray diffraction measurement). Hence, we focused the light beam to a small spot

( $\sim 0.1$  mm) and scanned the beam-spot position on the cleaved surface to make sure that the ARPES data are taken on a single domain of the desired phase. We confirmed that the ARPES data from the same domain give essentially the same result even when the nominal composition of bulk crystal is different. ARPES measurements were performed with a VG-Scienta SES2002 electron analyzer with a tunable synchrotron light at the beam line BL28A at Photon Factory (KEK). We used circularly polarized lights of 36–60 eV. The energy and angular resolutions were set at 15–30 meV and  $0.2^\circ$ , respectively. Samples were cleaved *in situ* along the (111) crystal plane in an ultrahigh vacuum of  $1 \times 10^{-10}$  Torr. A shiny mirror-like surface was obtained after cleaving the samples, confirming its high quality. The Fermi level ( $E_F$ ) of the samples was referenced to that of a gold film evaporated onto the sample holder.

We first show in Fig. 1(b) the valence-band ARPES intensity maps in the binding energy ( $E_B$ ) versus momentum ( $\mathbf{k}$ ) plane measured along the  $\bar{\Gamma}\bar{K}$  cut of the Brillouin zone, compared for  $m = 1, 2$ , and  $\infty$ . They exhibit common characteristics below  $E_B$  of  $\sim 1$  eV, suggesting that the spectral features for  $m = 1$  and  $2$  are essentially dominated by the contribution from the  $\text{Bi}_2\text{Se}_3$  layer. A closer look reveals that the overall band dispersions for  $m = 1$  and  $2$  are shifted downward with respect to that for  $m = \infty$ , likely due to an increase in Se vacancies caused by Pb substitution as also reported for other Pb-based TIs [18,19]. The dominant contribution from the  $\text{Bi}_2\text{Se}_3$  layer is also confirmed by the measurements of core levels. As shown in Fig. 1(c), the intensity of Pb-5d core levels is much weaker than that of Bi 5d in both  $m = 1$  and  $2$ , while their photoionization cross sections are similar [20]. This is likely to indicate that the topmost layer of the cleaved surface is the  $\text{Bi}_2\text{Se}_3$  QL in the present experimental condition. Moreover, the Pb-5d intensity observed for  $m = 2$  is much weaker than that for  $m = 1$  (right-hand inset), and this can be naturally understood if the top PbSe layer is located deeper beneath the surface in the  $m = 2$  case (see left-hand inset). In fact, a rough estimate that takes into account the finite photoelectron escape length (0.5 nm) and the depth of the topmost PbSe layer (1 and 2 nm for  $m = 1$  and  $2$ , respectively) suggests an order of magnitude weaker Pb-5d intensity for  $m = 2$ , which is in line with the present experimental result. The downside of this situation is that we are unable to measure the confinement effect in the PbSe unit and its resultant band gap, which is 0.27 eV in bulk PbSe.

A side-by-side comparison of the band dispersions near  $E_F$  in Figs. 2(a) and 2(b) clearly shows a marked difference in  $m = 1, 2$ , and  $\infty$ . Specifically, the band structure for  $m = 1$  contains a single, parabolic electronlike band, while that for  $m = 2$  is composed of multiple bands. The band structure at  $m = 2$  is also distinct from that at  $m = \infty$ , where a simple X-shaped Dirac-cone surface state shows up.

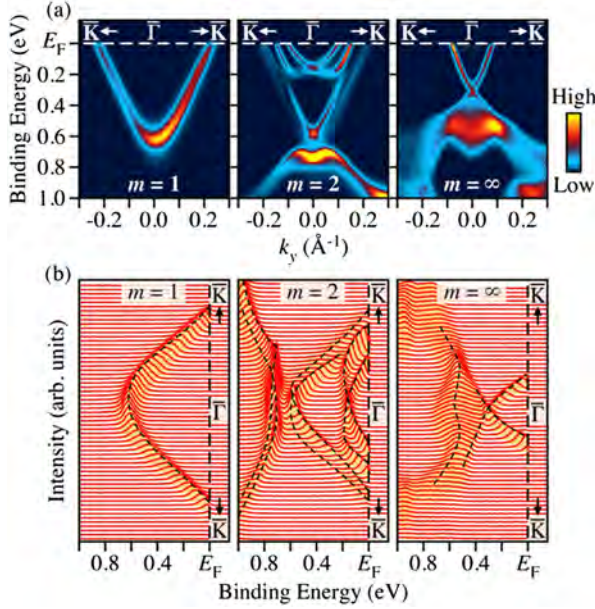


FIG. 2 (color online). (a),(b) Comparison of near- $E_F$  ARPES intensity (a) and corresponding energy dispersion curves (b). Dashed curves in (b) are a guide to the eyes.

We argue that such a striking difference in the near- $E_F$  electronic states originates from the difference in the number of  $\text{Bi}_2\text{Se}_3$  QLs in a unit cell, which is inferred from the fact that the ARPES data for  $m=1$  and 2 bear spectral signatures resembling those of  $\text{Bi}_2\text{Se}_3$  ultrathin films [21]; namely, the  $m=1$  data show only the upper parabola, as was the case for 1-QL film, and the  $m=2$  data present a gap with the lower band having a shallow dip at the top, similarly to the case for 2-QL film. This strongly suggests that the electronic states for  $m=1$  and 2 are quantized due to electron confinement within the  $\text{Bi}_2\text{Se}_3$  layer, which would be expected in view of the insulating nature of the PbSe block layer indicated by the absence of any additional  $E_F$  crossing bands [22].

To gain further insights into the origin of the difference between  $m=1$  and 2, it is useful to examine the  $m=2$  data in detail. As shown in Figs. 3(a) and 3(b), the near- $E_F$  dispersions for  $m=2$  are composed of six dispersive features labeled A–F, all of which show no photon-energy dependence signifying negligible dispersion along the momentum perpendicular to the surface ( $k_z$ ) and hence their 2D nature. The electronlike bands A and B cross at the  $\bar{\Gamma}$  point at  $E_B = 0.16$  eV and form two concentric Fermi surfaces [A and B in Fig. 3(c)], which indicates that their origin is the quantized bulk conduction bands with Rashba splitting [23,24]. The bands C and D in Fig. 3(a) are more dispersive than the bands A and B and cross  $E_F$  outside the bands A and B. They should essentially originate from the topological Dirac-cone states because (i) their overall dispersions overlap with the Dirac-cone surface states for  $m=\infty$  [see Fig. 3(b)] and (ii) the corresponding Fermi surfaces [C and D in Fig. 3(c)] exhibit a hexagonal

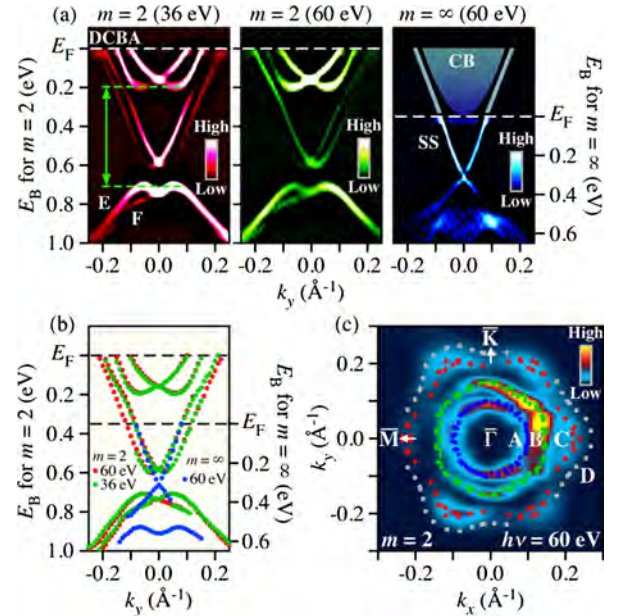


FIG. 3 (color online). (a) Second-derivative ARPES intensities near the  $\bar{\Gamma}$  point for  $m=2$  plotted as a function of  $k_y$  and  $E_B$  measured at  $\hbar\nu=36$  (left) and 60 eV (center), compared to that for  $m=\infty$  (right, measured with  $\hbar\nu=60$  eV) which is shifted downward by 0.35 eV to take into account the doping difference. Gray (green) arrows and dashed lines depict a conservative estimate of the bulk band gap of 0.5 eV, judged from the energy difference between the edges of the bands B and E. Notice that band E is likely of the surface origin and, hence, the true bulk band gap may well be larger than 0.5 eV. The band dispersions expected for  $m=\infty$  above  $E_F$  are also illustrated. (b) Direct comparison of the band dispersions obtained from the peak positions in the energy distribution curves for  $m=2$  and  $\infty$ ; the dispersions for  $m=\infty$  are shifted downward to account for the doping difference. (c) ARPES intensity mapping at  $E_F$  for  $m=2$  plotted as a function of 2D wave vector. The intensity is obtained by integrating the spectral intensity within  $\pm 10$  meV of  $E_F$ . The Fermi vector of each pocket is plotted by dots.

deformation similar to the case of  $m=\infty$  [9,25]. It is therefore most natural to interpret that the bands C, D, E, and F originally arise as two topological interface states of the 2-QL  $\text{Bi}_2\text{Se}_3$  unit at its top and bottom, but the proximity of the top and bottom interfaces causes the two topological states to hybridize and open a gap [21,26,27]; furthermore, those hybridized states are Rashba split due to the inversion-symmetry breaking at the surface. In fact, the bands C and D seem to smoothly connect to bands E and F, respectively, at the higher  $E_B$  side (see the schematic in Fig. 5). Note that the Rashba splitting in the upper branch of the hybridized topological states has already been reported in ultrathin films [21]. The present result is probably the first observation of the existence of topological states at the heterostructure *interface* of a bulk crystal. It should be noted that while bands C–F for  $m=2$  essentially originate from the topological states, the  $m=2$  system is not strictly topological because of the presence



of a gap in the topological states and the even number of  $E_F$  crossings of the bands between two time-reversal-invariant momenta (i.e., the  $\bar{\Gamma}$  and  $\bar{M}$  points). In this context, the  $m = 2$  phase is similar to a typical Rashba system.

The next important issue is the origin of the marked difference between  $m = 1$  and 2. As discussed above, the 2D states C, D, E, and F observed for  $m = 2$  are most likely of topological origin. In contrast, the parabola observed near  $E_F$  for  $m = 1$  does not have a corresponding lower branch, which can also be seen in the isoenergy cuts of the spectra shown in Fig. 4, suggesting that its origin is distinct from a gapped Dirac cone. In Ref. [21], the absence of the lower branch in the 1-QL film was proposed to be due to bonding with the substrate; similarly, we speculate that the standard model Hamiltonian [28] is not applicable to 1 QL of  $\text{Bi}_2\text{Se}_3$  sandwiched by PbSe layers and the band inversion is not taking place at the  $\Gamma$  point (a similar conclusion was also proposed in Ref. [29]). In this case, the observed parabola for  $m = 1$  is simply the degenerate lowest subband of the quantum confined conduction band.

Figure 5 summarizes the evolution of the near- $E_F$  electronic structure upon varying  $m$ , highlighting the topological or nontopological nature of the phases. The hybridization gap in the Dirac-cone interface states observed for  $m = 2$  is gradually reduced with increasing  $m$ , and it disappears at a characteristic  $m$  value,  $m_c$ , above which the coherent coupling between two adjacent interface states

becomes negligibly weak. This change across  $m_c$  can be considered to be a nontopological to topological crossover. In contrast to the regular topological phase transition that accompanies a band inversion, this crossover is triggered by the 3D to 2D crossover of the system and the resultant loss of the characteristics of 3D topological insulators. It is also inferred that a band inversion takes place between  $m = 1$  and 2, and this change is responsible for the observed marked difference of the band structure between the two. One can view such an evolution of electronic states as a consequence of the finite size effect in TI slabs embedded in naturally occurring heterostructures. Note that the critical thickness  $m_c$  is expected to be 6 QLs from the previous systematic ARPES and transport studies of  $\text{Bi}_2\text{Se}_3$  ultrathin films [21,30]. Therefore, the fabrication of a system with  $m \geq 6$  would be useful for realizing novel topological phenomena and TI-based applications which utilize the topologically protected interface states.

Perhaps more importantly, our results bear important implications on the band-gap engineering of TIs. Namely, as shown in Fig. 3, the magnitude of the bulk band gap for  $m = 2$  is at least 0.5 eV, which is much larger than that for  $m = \infty$  ( $\sim 0.3$  eV) [31] and is the largest ever observed in TIs. (Note that we are measuring the “bulk” band gap in the outermost  $\text{Bi}_2\text{Se}_3$  unit; measurements of the inner  $\text{Bi}_2\text{Se}_3$  units would require a bulk-sensitive experiment with hard x ray or low-energy photons.) This demonstrates that the bulk band gap can be enhanced by taking advantage of the quantization of the bulk bands in heterostructures.

It is useful to note that the existence of topological 2D states at the interfaces contained in naturally occurring heterostructures has a practical importance. It is well

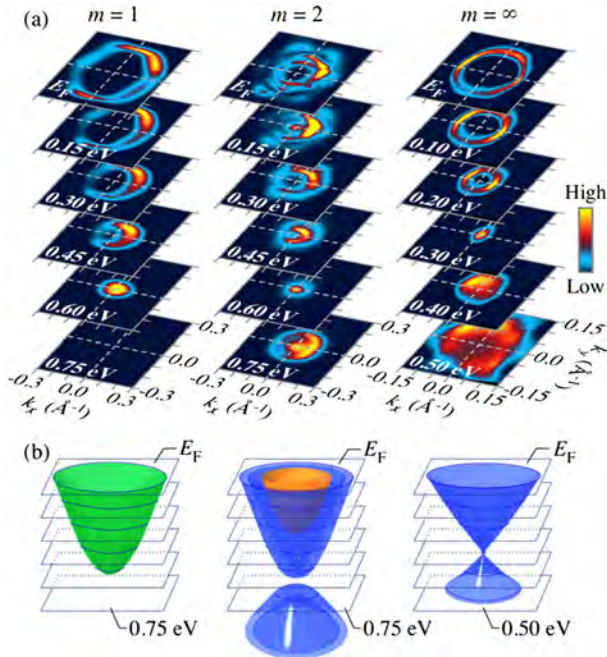


FIG. 4 (color online). (a) ARPES intensity mappings for  $m = 1$ , 2, and  $\infty$  as a function of 2D wave vector at various  $E_B$ 's. (b) Schematic 3D plots of the near- $E_F$  band dispersions showing the energy positions at which the 2D intensity mappings in (a) are displayed.

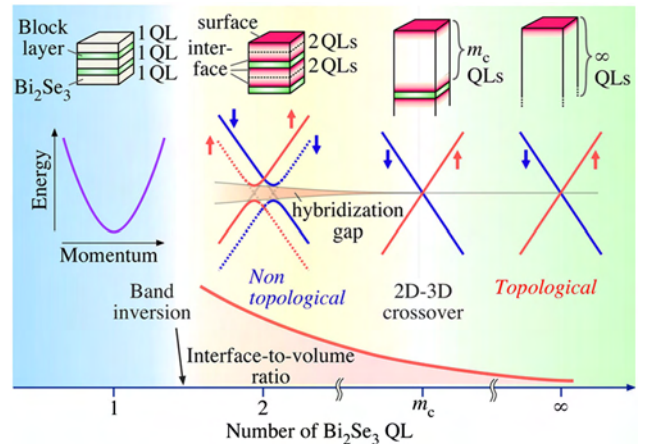


FIG. 5 (color online). Schematic band diagrams and illustrations of the heterostructures for various  $m$ . Dark (red) area in heterostructures depicts the topological interface (surface) states.  $m_c$  is the characteristic thickness where the hybridization gap between two topological interface states starts to open. The interface-to-volume ratio is also shown schematically at the bottom.

known that the surface of 3D TIs is prone to chemical reactions in ambient atmosphere [6,7,24], which has hampered transport studies of topological surface states that are prerequisite to device applications, calling for an efficient means to avoid surface degradation. Obviously, the topological interfaces found here reside in bulk crystals and hence are efficiently encapsulated from ambient atmosphere. Moreover, those interface states naturally lead to sizable interface-to-volume ratio (see Fig. 5), which would enhance their usabilities.

In conclusion, our ARPES measurements of  $(\text{PbSe})_5 \times (\text{Bi}_2\text{Se}_3)_{3m}$  revealed a Rashba splitting of topological 2D states for  $m = 2$ , providing the first experimental evidence for the existence of topological states at the heterostructure interface in the bulk. The natural multilayer structure leads to the capping of topological interface states and sizable interface-to-volume ratio. We also found that the band dispersions of  $\text{Bi}_2\text{Se}_3$  layers are quantized due to confinement effects and exhibit a drastic change upon varying  $m$ . In particular, the largest bulk band gap ever observed in a TI is achieved at  $m = 2$ . Those results demonstrate that naturally occurring heterostructures are a promising playground for realizing novel topological phenomena and device applications of TIs.

We thank T. Arakane, M. Komatsu, K. Yoshimatsu, H. Kumigashira, and K. Ono for their assistance in ARPES measurements. This work was supported by JSPS (NEXT Program, KAKENHI 23224010, and Grant-in-Aid for JSPS Fellows 23.4376), JST-CREST, MEXT of Japan (Innovative Area “Topological Quantum Phenomena”), AFOSR (AOARD 124038), and KEK-PF (Proposal No. 2012S2-001).

---

\*k.nakayama@arpes.phys.tohoku.ac.jp

†t-sato@arpes.phys.tohoku.ac.jp

‡y\_ando@sanken.osaka-u.ac.jp

- [1] M.Z. Hasan and C.L. Kane, *Rev. Mod. Phys.* **82**, 3045 (2010).
- [2] X.-L. Qi and S.-C. Zhang, *Rev. Mod. Phys.* **83**, 1057 (2011).
- [3] P. Roushan, J. Seo, C. V. Parker, Y. S. Hor, D. Hsieh, D. Qian, A. Richardella, M. Z. Hasan, R. J. Cava, and A. Yazdani, *Nature (London)* **460**, 1106 (2009).
- [4] J. Seo, P. Roushan, H. Beidenkopf, Y. S. Hor, R. J. Cava, and A. Yazdani, *Nature (London)* **466**, 343 (2010).
- [5] C.L. Kane and E. J. Mele, *Science* **314**, 1692 (2006).
- [6] A. A. Taskin, Z. Ren, S. Sasaki, K. Segawa, and Y. Ando, *Phys. Rev. Lett.* **107**, 016801 (2011).
- [7] D. Kong and Y. Cui, *Nat. Chem.* **3**, 845 (2011).
- [8] T. Sato, K. Segawa, H. Guo, K. Sugawara, S. Souma, T. Takahashi, and Y. Ando, *Phys. Rev. Lett.* **105**, 136802 (2010).
- [9] Y. L. Chen *et al.*, *Science* **325**, 178 (2009).
- [10] D. Hsieh *et al.*, *Nature (London)* **460**, 1101 (2009).
- [11] J. G. Checkelsky, Y. Hor, M.-H. Liu, D.-X. Qu, R. Cava, and N. P. Ong, *Phys. Rev. Lett.* **103**, 246601 (2009).
- [12] J. G. Analytis, R. D. McDonald, S. C. Riggs, J.-H. Chu, G. S. Boebinger, and I. R. Fisher, *Nat. Phys.* **6**, 960 (2010).
- [13] N. P. Butch, K. Kirshenbaum, P. Syers, A. B. Sushkov, G. S. Jenkins, H. D. Drew, and J. Paglione, *Phys. Rev. B* **81**, 241301(R) (2010).
- [14] Z. Ren, A. A. Taskin, S. Sasaki, K. Segawa, and Y. Ando, *Phys. Rev. B* **84**, 075316 (2011).
- [15] M. G. Kanatzidis, *Acc. Chem. Res.* **38**, 359 (2005).
- [16] Y. Zhang, A. P. Wilkinson, P. L. Lee, S. D. Shastri, D. Shu, D.-Y. Chung, and M. G. Kanatzidis, *J. Appl. Crystallogr.* **38**, 433 (2005).
- [17] L. E. Shelimova, O. G. Karpinskii, and V. S. Zemsikov, *Inorg. Mater. (USSR)* **44**, 927 (2008).
- [18] S. Souma, K. Eto, M. Nomura, K. Nakayama, T. Sato, T. Takahashi, K. Segawa, and Y. Ando, *Phys. Rev. Lett.* **108**, 116801 (2012).
- [19] S. V. Eremeev *et al.*, *Nat. Commun.* **3**, 635 (2012).
- [20] J. J. Yeh and I. Lindau, *At. Data Nucl. Data Tables* **32**, 1 (1985).
- [21] Y. Zhang *et al.*, *Nat. Phys.* **6**, 584 (2010).
- [22] We did not clearly observe the quantization of valence bands below  $E_B \sim 1$  eV, which might be due to the shorter photohole lifetime (larger linewidth broadening) for deeper-lying valence-band states and/or the band hybridization between the  $\text{Bi}_2\text{Se}_3$  and  $\text{PbSe}$  units below  $E_B \sim 1$  eV.
- [23] P. D. C. King *et al.*, *Phys. Rev. Lett.* **107**, 096802 (2011).
- [24] H. M. Benia, C. Lin, K. Kern, and C. R. Ast, *Phys. Rev. Lett.* **107**, 177602 (2011).
- [25] K. Kuroda *et al.*, *Phys. Rev. Lett.* **105**, 076802 (2010).
- [26] C.-X. Liu, H. J. Zhang, B. Yan, X.-L. Qi, T. Frauenheim, X. Dai, Z. Fang, and S.-C. Zhang, *Phys. Rev. B* **81**, 041307 (R) (2010).
- [27] H.-Z. Lu, W. Y. Shan, W. Yao, Q. Niu, and S. Q. Shen, *Phys. Rev. B* **81**, 115407 (2010).
- [28] H. J. Zhang, C.-X. Liu, X.-L. Qi, X. Dai, Z. Fang, and S.-C. Zhang, *Nat. Phys.* **5**, 438 (2009).
- [29] Y. Sakamoto, T. Hirahara, H. Miyazaki, S. I. Kimura, and S. Hasegawa, *Phys. Rev. B* **81**, 165432 (2010).
- [30] A. A. Taskin, S. Sasaki, K. Segawa, and Y. Ando, *Phys. Rev. Lett.* **109**, 066803 (2012).
- [31] Y. Xia *et al.*, *Nat. Phys.* **5**, 398 (2009).





# Anomalous Dressing of Dirac Fermions in the Topological Surface State of $\text{Bi}_2\text{Se}_3$ , $\text{Bi}_2\text{Te}_3$ , and Cu-Doped $\text{Bi}_2\text{Se}_3$

Takeshi Kondo,<sup>\*</sup> Y. Nakashima, Y. Ota, Y. Ishida, W. Malaeb, K. Okazaki, and S. Shin<sup>†</sup>  
*ISSP, University of Tokyo, Kashiwa, Chiba 277-8581, Japan*

M. Kriener, Satoshi Sasaki, Kouji Segawa, and Yoichi Ando<sup>‡</sup>  
*Institute of Scientific and Industrial Research, Osaka University, Osaka 567-0047, Japan*  
(Received 29 December 2012; published 23 May 2013)

Quasiparticle dynamics on the topological surface state of  $\text{Bi}_2\text{Se}_3$ ,  $\text{Bi}_2\text{Te}_3$ , and superconducting  $\text{Cu}_x\text{Bi}_2\text{Se}_3$  are studied by 7 eV laser-based angle resolved photoemission spectroscopy. We find strong mode couplings in the Dirac-cone surface states at energies of  $\sim 3$  and  $\sim 15$ – $20$  meV associated with an exceptionally large coupling constant  $\lambda$  of  $\sim 3$ , which is one of the strongest ever reported for any material. This result is compatible with the recent observation of a strong Kohn anomaly in the surface phonon dispersion of  $\text{Bi}_2\text{Se}_3$ , but it appears that the theoretically proposed “spin-plasmon” excitations realized in helical metals are also playing an important role. Intriguingly, the  $\sim 3$  meV mode coupling is found to be enhanced in the superconducting state of  $\text{Cu}_x\text{Bi}_2\text{Se}_3$ .

DOI: [10.1103/PhysRevLett.110.217601](https://doi.org/10.1103/PhysRevLett.110.217601)

PACS numbers: 79.60.-i, 71.38.Cn, 72.15.Nj, 73.20.-r

Topological insulators (TIs) are a new class of materials with Dirac fermions appearing on the surface [1]. The nature of Dirac fermions has already been actively studied in the graphitic materials [2], and it has been elucidated that the Dirac band dispersion is anomalously renormalized by such effects as electron-phonon interaction, electron-hole pair generation, and electron-plasmon coupling, leading to various intriguing properties [3–5]. While topological insulators are essentially understood within the noninteracting topological theory [6–8], the Dirac fermions realized in actual materials would be affected by non-trivial many body interactions, and hence the investigation of the quasiparticle dynamics is important for extending our understanding beyond the noninteracting regime. Since the Dirac fermions in TIs are distinct from those in graphitic materials in terms of their helical spin texture as well as possible interactions with a separate bulk electronic state, the low-energy excitations in the topological surface state are of particular interest. Indeed, such excitations are important not only for understanding many body interactions in the topological surface state, but also for assessing the stability of putative Majorana fermions that are expected to emerge on the surface of superconducting TIs [9,10].

In this context, there are already indications of the significance of many body interactions in the topological surface state. For example, a pronounced Kohn anomaly to indicate a strong electron-phonon coupling was recently observed in the surface phonon branch of  $\text{Bi}_2\text{Se}_3$  [11]; scanning tunneling spectroscopy (STS) uncovered an intriguing feature with finely resolved sharp peaks at low energies ( $< 20$  meV) in the Landau-level spectra [12], pointing to an anomalous increase in the quasiparticle lifetime near the Fermi energy ( $E_F$ ). Theoretically, it has

been proposed that a novel low-energy collective mode called “spin plasmon” emerges as a consequence of the spin-momentum locking in the topological surface state [13]. Therefore, it is important to elucidate how the Dirac dispersion is renormalized close to  $E_F$ . However, so far the angle-resolved photoemission spectroscopy (ARPES) has not been able to detect any significant renormalization in the Dirac dispersions in TIs [14], possibly because of the lack of sufficient energy resolutions.

In this Letter, we demonstrate that the Dirac dispersion of the topological surface state is indeed anomalously renormalized, by using state-of-the-art ARPES with a 7-eV laser photon source. The availability of ultrahigh energy resolution ( $\sim 1$  meV) and extremely low temperature ( $\sim 1$  K) [15] enabled us to detect low-energy kinks in the dispersion at  $\sim 3$  and  $\sim 15$ – $20$  meV, giving evidence for hitherto-undetected mode couplings. The analysis of the kinks leads to the estimate of the coupling constant  $\lambda$  of as large as  $\sim 3$ , which is one of the largest reported for any material [16,17]. Nevertheless, we observed no overall band reconstruction down to the lowest temperature, indicating that the topological surface state are protected from density-wave formations, which is usually expected to occur with such an extremely strong coupling with bosons [18–22].

Single crystals of  $\text{Bi}_2\text{Se}_3$  and  $\text{Bi}_2\text{Te}_3$  were grown by melting stoichiometric amounts of elemental shots in sealed evacuated quartz glass tubes. Superconducting samples of  $\text{Cu}_{0.24}\text{Bi}_2\text{Se}_3$  with  $T_c$  of 3.5 K and a shielding fraction of  $\sim 30\%$  [see Fig. 3(a)] were prepared by electrochemically intercalating Cu into the pristine  $\text{Bi}_2\text{Se}_3$  [23–26]. ARPES measurements were performed using a Scienta R4000 hemispherical analyzer with an ultraviolet laser ( $h\nu = 6.994$  eV) at the Institute for Solid State Physics (ISSP), University of Tokyo [27,28].

Figures 1(a1)–(a5) and (b1)–(b5) show the ARPES data of  $\text{Bi}_2\text{Se}_3$  and  $\text{Bi}_2\text{Te}_3$ , respectively. The Dirac cones are clearly seen in the dispersion maps [see Figs. 1(a2) and (b2)], and the Fermi surface (FS) shapes are very different between the two compounds [see Figs. 1(a3) and (b3)]. In this experiment, we did not observe any quantum-well states which emerge when adsorption of residual gases on the surface causes charge doping [29–34]. Also, our data are free from spectral intensity from the bulk conduction band, as can be clearly seen in Figs. 1(a1) and (b1) where the momentum distribution curves (MDCs) at  $E_F$  show only two sharp peaks from the surface state. This situation prevents complex scattering channels that could affect the spectral line shape and complicates the interpretation of renormalization effects [35,36].

The novel feature in our data is that the MDC-derived band dispersions [see Figs. 1(a4) and (b4)] obviously

deviate from straight lines, pointing to a large mass enhancement; the renormalized slope of the dispersion close to  $E_F$  is shown by dashed lines. As shown in the upper insets of Figs. 1(a4) and (b4), we calculate the energy difference between the putative linear dispersion and the measured one to estimate the strength of the coupling as a function of energy. We found anomalies at two energies,  $\sim -15$  and  $\sim -3$  meV, indicative of electron couplings with two different kinds of collective modes.

The effects of the couplings should also be observed in the energy dependence of the MDC peak width ( $\Delta k$ ). In Figs. 1(a5) and (b5), we plot the obtained spectrum of  $\Delta k$  for  $\text{Bi}_2\text{Se}_3$  and  $\text{Bi}_2\text{Te}_3$ , respectively; as expected,  $\Delta k(E)$  presents kinks at the two energy scales,  $\sim -(15\text{--}20)$  and  $\sim -3$  meV, which are better seen in the insets. The  $\sim -3$  meV kink marks the onset of an anomalous increase in the magnitude of  $\Delta k(E)$  toward  $E_F$ , which is unusual; we have confirmed the reproducibility of this low-energy feature in many samples and concluded that it is an intrinsic property of the topological surface state.

To understand the complex behavior of the band dispersions revealed at low energy, we examine the shapes of the energy distribution curves (EDCs) around  $k_F$  shown in Fig. 2(c). In Fig. 2(d), those original EDCs are divided by the Fermi function at the measured temperature of 7 K convoluted with the experimental energy resolution to remove the effect of the Fermi cutoff. In the resulting curves, one can identify up to three shoulderlike features [an example for  $k_x - k_F^{\text{EDC}} = 0.018 \text{ \AA}^{-1}$  is shown in Fig. 2(b)], and the energy positions of those features are plotted on the ARPES image shown in Fig. 2(a). One can see in Fig. 2(d) that one of the shoulderlike features on the curves actually corresponds to the maximum; the dispersion of this maximum close to  $k_F$  is also plotted in Fig. 2(a) with thick filled symbols, and this dispersion is fitted with a parabolic dashed line in Fig. 2(a), giving a significantly enhanced effective mass of  $0.83m_e$  ( $m_e$  is the free-electron mass). For comparison, we also plot a putative band dispersion with a mass of  $0.14m_e$ , which was estimated for the bulk band from quantum oscillations [37]. The mass enhancement realized in the topological state is remarkable. Even more surprisingly, the estimated value of  $\lambda = v_0/v_F - 1$  ( $v_0$  and  $v_F$  are the bare-electron velocity [38] and the renormalized Fermi velocity, respectively) is as large as  $\sim 3$  as demonstrated in Fig. 2(a), which is one of the strongest couplings ever reported in any material [16,17]. This value is also much larger than that previously reported ( $\lambda < 0.3$ ) for  $\text{Bi}_2\text{Se}_3$  based on less straightforward estimates [14,39].

Perhaps the most direct way to demonstrate the strong mode coupling is to present the peak-dip-hump structure in the EDCs. In Fig. 2(e), we show EDCs at  $k_F$  and beyond, where the peak-dip-hump shape is usually emphasized, and indeed, a clear dip can be seen at  $\sim -16$  meV

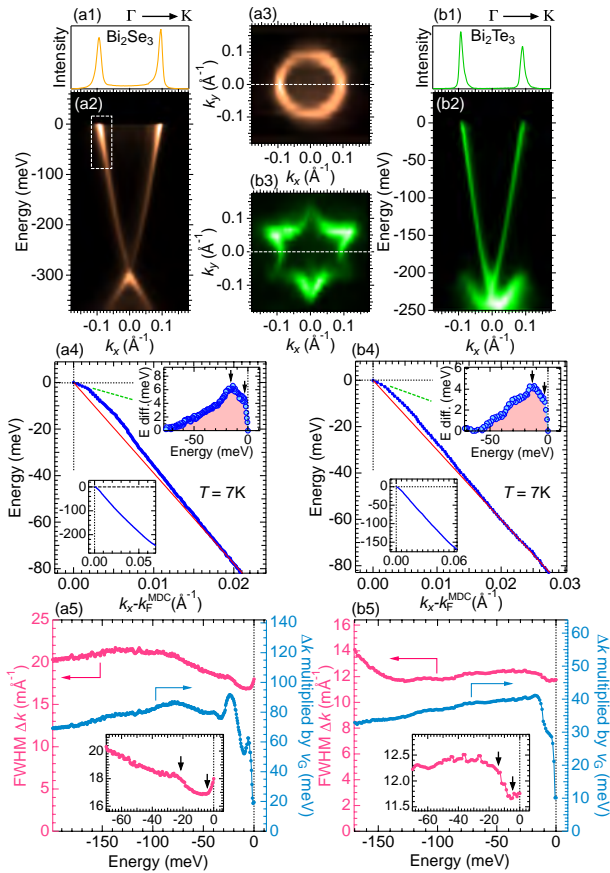


FIG. 1 (color online). Data for (a1)–(a5)  $\text{Bi}_2\text{Se}_3$  and (b1)–(b5)  $\text{Bi}_2\text{Te}_3$ . (a1),(b1) MDC at  $E_F$ . (a2),(b2) Band dispersion map along  $\Gamma$ –K [dashed lines in (a3) and (b3)]. (a3),(b3) Fermi surface map. (a4),(b4) MDC-derived band dispersions near  $E_F$  obtained from the data shown in panels (a2) and (b2). The same dispersion over a wide energy range is shown in the lower-left inset. The upper-right inset plots the energy difference from the linear dispersion. (a5),(b5) MDC peak width  $\Delta k$  [full width at half maximum (FWHM)], and the  $\Delta k(E)$  multiplied by the group velocity  $v_G(E)$ . The inset shows the  $\Delta k(E)$  close to  $E_F$ .

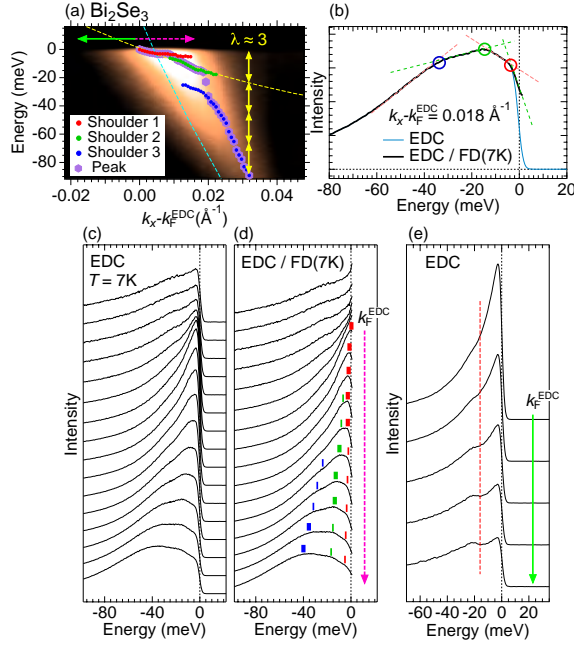


FIG. 2 (color online). Data for  $\text{Bi}_2\text{Se}_3$  within a narrow range near  $E_F$  marked in Fig. 1(a2). (a) ARPES image; parabolic bands (dashed lines) with a mass of  $0.83m_e$  and  $0.14m_e$  [37] are superimposed. (b) Typical EDC with three features. (c) EDCs near  $k_F$  on the occupied-state side, and (d) those divided by the Fermi function at  $T = 7$  K. Energies of shoulderlike structures [circles in (b) and bars in (d)] are plotted on (a). The energy eigenvalue for each  $k$ ,  $\varepsilon(k)$ , which is determined by the energy positions at which the spectral intensity becomes maximum, are indicated in (d) with bold bars, and plotted in (a) with thick filled hexagons. (e) EDCs beyond  $k_F$  (unoccupied-state side). The dashed line indicates the energy of the spectral dip.

(dashed line). On the other hand, the  $\sim 3$  meV mode does not give rise to such a peak-dip-hump feature in  $\text{Bi}_2\text{Se}_3$ , manifesting itself only as a weak kink in EDCs.

Intriguingly, we found that a peak-dip-hump structure becomes visible at  $\sim 3$  meV in superconducting samples of Cu-doped  $\text{Bi}_2\text{Se}_3$ . Figures 3(b2) and (b3) show the EDCs of  $\text{Cu}_{0.24}\text{Bi}_2\text{Se}_3$  with  $T_c = 3.5$  K measured above and below  $T_c$ , respectively. The peak-dip-hump structure is seen at  $\sim 3$  meV below  $T_c$  but it is gone above  $T_c$ . We also measured the pristine  $\text{Bi}_2\text{Se}_3$  at the same condition ( $T = 1.5$  K), but did not observe the peak-dip-hump [see Fig. 3(d2)]. Furthermore, we doped the surface of the pristine sample up to a doping level similar to that of  $\text{Cu}_{0.24}\text{Bi}_2\text{Se}_3$  by exposing it to residual gases [compare Figs. 3(c1) and (d1)], but again, the peak-dip-hump structure is not observed [see Fig. 3(c2)]. Obviously, the enhancement of the  $\sim 3$  meV mode coupling has something to do with the superconductivity, and the origin of this enhancement needs to be scrutinized in future studies. In passing, we note that we did not detect any signature of the superconducting energy gap in the present experiment, probably because the superconductivity is inhomogeneous

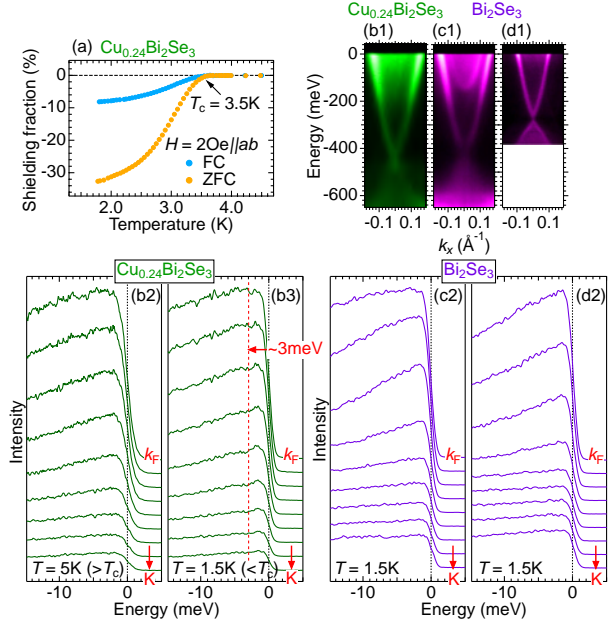


FIG. 3 (color online). Data for  $\text{Cu}_{0.24}\text{Bi}_2\text{Se}_3$  superconductor with  $T_c = 3.5$  K and the pristine  $\text{Bi}_2\text{Se}_3$ . (a) Field-cooled (FC) and zero-field-cooled (ZFC) data of the superconducting shielding fraction of the sample used for ARPES experiments. Band dispersion map along  $\Gamma$ -K for (b1)  $\text{Cu}_{0.24}\text{Bi}_2\text{Se}_3$ , (c1) aged, and (d1) fresh surfaces of  $\text{Bi}_2\text{Se}_3$ . EDCs of  $\text{Cu}_{0.24}\text{Bi}_2\text{Se}_3$  close to  $k_F$  measured (b2) above  $T_c$  and (b3) below  $T_c$ . The dashed line in (b3) indicates the spectral dip. EDCs of the pristine  $\text{Bi}_2\text{Se}_3$  close to  $k_F$  for (c2) aged and (d2) fresh surfaces.

in this material [26]. More elaborate studies would be required to nail down the topological superconductivity in  $\text{Cu}_x\text{Bi}_2\text{Se}_3$  [25] by ARPES experiments.

Now we show the relevance of the mode couplings to the scattering rate ( $1/\tau$ ), which we try to extract from our data in two ways: one simply uses the peak width of the EDCs ( $\Delta\varepsilon = 1/\tau$ ), the raw data of which are shown in Figs. 4(b) and 4(c); the other calculates the product of the MDC width and the renormalized group velocity  $v_G(E)$  ( $\Delta k v_G \approx 1/\tau$ ), where  $v_G(E)$  is obtained by differentiating the  $\varepsilon(k)$  data shown in Figs. 1(a4) and (b4). The  $1/\tau$  scattering rate is not exactly the same as the imaginary part of the self-energy, because it now includes the effect of the real part. However, multiplying  $\Delta k$  by  $v_G$  would cancel the effect of the spectral-weight shift due to mode couplings, which can cause the unusual upturn of  $\Delta k$  toward  $E_F$  seen in Figs. 1(a5) and (b5), and it makes the proper energy dependence of the scattering rate become visible. Indeed, the  $E$  dependence of  $\Delta k v_G$  is consistent with that of  $\Delta\varepsilon$  (which is a straightforward measure of the scattering rate of quasiparticles), as shown in Fig. 4(a) for  $\text{Bi}_2\text{Te}_3$ . Reassuringly, the behavior of  $\Delta k v_G$  in both  $\text{Bi}_2\text{Se}_3$  and  $\text{Bi}_2\text{Te}_3$  clearly reflects the mode couplings at  $\sim 20$  and  $\sim 3$  meV [see Figs. 1(a5) and (b5)], corroborating the existence of two modes.



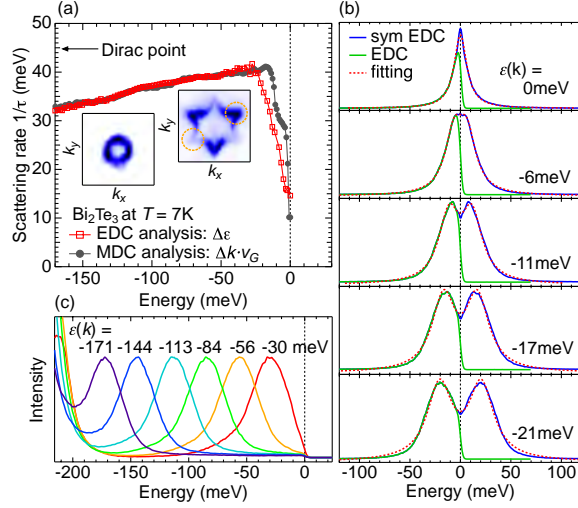


FIG. 4 (color online). Results for  $\text{Bi}_2\text{Te}_3$ . (a) Scattering rate ( $1/\tau$ ) estimated from EDC peak width  $\Delta\epsilon$  (FWHM) as well as from the MDC peak width multiplied by the group velocity  $\Delta k v_G$ . Insets show the ARPES map at  $-150$  meV (left) and  $E_F$  (right). (b) Estimation of  $\Delta\epsilon$  by fitting double Lorentzians to the symmetrized EDCs. (c) EDCs far from  $k_F$ ; the energy eigenvalue for each  $k$ ,  $\epsilon(k)$ , corresponds to the peak position in each EDC.

One may notice in Fig. 4(a) that both  $\Delta\epsilon$  and  $\Delta k v_G$  reduce sharply toward  $E_F$ . This behavior appears to be consistent with the STS result showing a sharpening of Landau-level peaks at low energies ( $< 20$  meV) [12]. Another notable feature in  $1/\tau$  is that it gradually decreases toward the Dirac point. This is unusual, because a monotonic increase in the electron-electron interaction with increasing binding energy is usually expected in conventional metals [40]. We speculate that this unusual behavior is a consequence of the fact that the penetration depth of the surface state increases as the momentum moves away from the Dirac point [41], which makes the surface state gradually gain some bulk character. In fact, a feature to suggest such a variation is seen in the energy-contour maps plotted in the inset of Fig. 4(a): the contour near the Dirac point (left image) is almost circular, but close to  $E_F$  (right image), it exhibits a  $C_3$  modulation reflecting the symmetry of the bulk.

Now we discuss the most crucial question, namely, the origin of the bosons causing the anomalies at  $\sim -(15-20)$  and  $\sim -3$  meV in the ARPES spectra. A plausible candidate for the higher binding-energy one is the out-of-plane optical phonon mode  $A_{1g}^2$  with  $\omega = 21$  and  $16$  meV for  $\text{Bi}_2\text{Se}_3$  and  $\text{Bi}_2\text{Te}_3$ , respectively [42,43]. It seems that  $\Delta k$  begins to decrease toward  $E_F$  [see Figs. 1(a5) and (b5)] at almost the same energy as that of the  $A_{1g}^2$  mode. Also, the relevance of the phonon coupling is supported by the fact that the mode energy observed in  $\text{Bi}_2\text{Se}_3$  ( $\sim 20$  meV) is higher than that in  $\text{Bi}_2\text{Te}_3$  ( $\sim 15$  meV), which is consistent with the mass difference between Se and Te ( $\sqrt{m_{\text{Te}}/m_{\text{Se}}} = 1.27$ ).

As for the  $\sim 3$  meV mode, there are two possible origins. One is the optical mode of surface phonons. Recently, a strong Kohn anomaly was detected by a helium atom surface scattering (HASS) experiment in a phonon branch of  $\text{Bi}_2\text{Se}_3$  [11] at approximately  $2k_F^{\text{Dirac}}$  ( $k_F^{\text{Dirac}}$  is the Fermi momentum on the Dirac cone) with the characteristic energy of  $\sim 3$  meV, and this Kohn anomaly was attributed to the surface optical phonon mode [11]. While this Kohn anomaly [44] may actually play some role in the strong renormalization observed in our ARPES data, the  $\lambda$  value obtained in the HASS experiment for the relevant phonons was only  $0.43$  [47], which is too small to account for the very strong coupling observed here for the  $\sim 3$  meV mode. Therefore, the surface optical phonons alone are obviously not sufficient for understanding the lower energy mode, and we need to seek additional ingredients.

In this respect, another, more promising, origin of the  $\sim 3$  meV mode is the theoretically proposed spin plasmon, which is suggested to have a maximum energy of  $\sim 2.2$  meV [13]. This mode consists of coupled plasmons and spin waves, and unlike the Kohn anomaly [21], it is expected for the round FS as in  $\text{Bi}_2\text{Se}_3$  [13]. Indeed, in our ARPES data the  $\sim 3$  meV mode coupling is obviously stronger in  $\text{Bi}_2\text{Se}_3$  than in  $\text{Bi}_2\text{Te}_3$  where the FS is warped. The unusual upturn observed in the MDC width toward  $E_F$  [see the insets of Figs. 1(a5) and (b5)] could be interpreted to signify increasingly stronger interactions of the Dirac fermions with spin plasmons near  $E_F$ . Note that such strong interactions between the two are expected only when the plasmon spectrum does not overlap with the continuum of electron-hole excitations [3,48], and hence the plasmon coupling should dominate the scatterings with  $q \sim 0$ . Therefore, it is natural that the quasiparticle scattering is enhanced toward  $E_F$  in this spin-plasmon scenario. All told, it is most likely that the large-angle scattering ( $q \sim 2k_F$ ) by the surface optical phonons and the small-angle scattering ( $q \ll 2k_F$ ) by the spin plasmons are both playing roles in the enormously strong mass enhancement observed near  $E_F$  on the topological surface state.

In conclusion, we have investigated the quasiparticle dynamics in the topological surface state of  $\text{Bi}_2\text{Se}_3$ ,  $\text{Bi}_2\text{Te}_3$ , and  $\text{Cu}_x\text{Bi}_2\text{Se}_3$ . We found strong mode couplings at binding energies of  $\sim 15-20$  and  $\sim 3$  meV. The coupling to the  $A_{1g}^2$  phonons is proposed as the candidate for the former mode. As for the  $\sim 3$  meV mode, there are two possible origins. One is the optical mode of surface phonons. The other is the spin plasmons, which are theoretically proposed as low-energy excitations of the helically spin-polarized Dirac fermions. Intriguingly, despite the extremely large mass enhancement factor  $\lambda$  of  $\sim 3$ , the topological surface state remains free from any band reconstruction down to the lowest temperature, indicating that the helical Dirac cone is protected from density-wave formations which are naturally expected for a system with extremely strong couplings to bosons.

This work is supported by JSPS (FIRST Program, NEXT Program, KAKENHI 23740256 and KAKENHI 24740218), MEXT (Innovative Area “Topological Quantum Phenomena” KAKENHI 22103004), and AFOSR (AOARD 124038).

\*kondo1215@issp.u-tokyo.ac.jp

†shin@issp.u-tokyo.ac.jp

‡y\_ando@sanken.osaka-u.ac.jp

- [1] M. Z. Hasan and C. L. Kane, *Rev. Mod. Phys.* **82**, 3045 (2010).
- [2] A. H. Castro Neto, N. M. R. Peres, K. S. Novoselov, and A. K. Geim, *Rev. Mod. Phys.* **81**, 109 (2009).
- [3] A. Bostwick, T. Ohta, T. Seyller, K. Horn, and E. Rotenberg, *Nat. Phys.* **3**, 36 (2007).
- [4] Y. Zhang, V. W. Brar, F. Wang, C. Girit, Y. Yayon, M. Panlasigui, A. Zettl, and M. F. Crommie, *Nat. Phys.* **4**, 627 (2008).
- [5] Y. Liu, L. Zhang, M. K. Brinkley, G. Bian, T. Miller, and T.-C. Chiang, *Phys. Rev. Lett.* **105**, 136804 (2010).
- [6] L. Fu, C. L. Kane, and E. J. Mele, *Phys. Rev. Lett.* **98**, 106803 (2007).
- [7] J. E. Moore and L. Balents, *Phys. Rev. B* **75**, 121306(R) (2007).
- [8] X.-L. Qi, T. L. Hughes, and S.-C. Zhang, *Phys. Rev. B* **78**, 195424 (2008).
- [9] L. Fu and C. L. Kane, *Phys. Rev. Lett.* **100**, 096407 (2008).
- [10] P. Hosur, P. Ghaemi, R. S. K. Mong, and A. Vishwanath, *Phys. Rev. Lett.* **107**, 097001 (2011).
- [11] X. Zhu, L. Santos, R. Sankar, S. Chikara, C. Howard, F. C. Chou, C. Chamon, and M. El-Batanouny, *Phys. Rev. Lett.* **107**, 186102 (2011).
- [12] T. Hanaguri, K. Igarashi, M. Kawamura, H. Takagi, and T. Sasagawa, *Phys. Rev. B* **82**, 081305(R) (2010).
- [13] S. Raghu, S. B. Chung, X.-L. Qi, and S.-C. Zhang, *Phys. Rev. Lett.* **104**, 116401 (2010).
- [14] Z.-H. Pan, A. V. Fedorov, D. Gardner, Y. S. Lee, S. Chu, and T. Valla, *Phys. Rev. Lett.* **108**, 187001 (2012).
- [15] K. Okazaki *et al.*, *Science* **337**, 1314 (2012).
- [16] W. L. McMillan, *Phys. Rev.* **167**, 331 (1968).
- [17] P. Hofmann, I. Y. Sklyadneva, E. D. L. Rienks, and E. V. Chulkov, *New J. Phys.* **11**, 125005 (2009).
- [18] K. Nasu, *Phys. Rev. B* **44**, 7625 (1991).
- [19] C. R. Ast and H. Höchst, *Phys. Rev. Lett.* **90**, 016403 (2003).
- [20] Y. M. Koroteev, G. Bihlmayer, J. Gayone, E. Chulkov, S. Blügel, P. Echenique, and Ph. Hofmann, *Phys. Rev. Lett.* **93**, 046403 (2004).
- [21] E. W. Plummer, J. Shi, S.-J. Tang, E. Rotenberg, and S. D. Kevan, *Prog. Surf. Sci.* **74**, 251 (2003).
- [22] L. Fu, *Phys. Rev. Lett.* **103**, 266801 (2009).
- [23] M. Kriener, K. Segawa, Z. Ren, S. Sasaki, S. Wada, S. Kuwabata, and Y. Ando, *Phys. Rev. B* **84**, 054513 (2011).
- [24] M. Kriener, K. Segawa, Z. Ren, S. Sasaki, and Y. Ando, *Phys. Rev. Lett.* **106**, 127004 (2011).
- [25] S. Sasaki, M. Kriener, K. Segawa, K. Yada, Y. Tanaka, M. Sato, and Y. Ando, *Phys. Rev. Lett.* **107**, 217001 (2011).
- [26] M. Kriener, K. Segawa, S. Sasaki, and Y. Ando, *Phys. Rev. B* **86**, 180505(R) (2012).
- [27] T. Kiss *et al.*, *Phys. Rev. Lett.* **94**, 057001 (2005).
- [28] T. Kiss, T. Shimojima, K. Ishizaka, A. Chainani, T. Togashi, T. Kanai, X.-Y. Wang, C.-T. Chen, S. Watanabe, and S. Shin, *Rev. Sci. Instrum.* **79**, 023106 (2008).
- [29] P. D. C. King *et al.*, *Phys. Rev. Lett.* **107**, 096802 (2011).
- [30] M. Bianchi, R. C. Hatch, J. Mi, B. B. Iversen, and P. Hofmann, *Phys. Rev. Lett.* **107**, 086802 (2011).
- [31] Z.-H. Zhu *et al.*, *Phys. Rev. Lett.* **107**, 186405 (2011).
- [32] H. M. Benia, C. Lin, K. Kern, and C. R. Ast, *Phys. Rev. Lett.* **107**, 177602 (2011).
- [33] L. A. Wray, S.-Y. Xu, Y. Xia, D. Hsieh, A. V. Fedorov, Y. S. Hor, R. J. Cava, A. Bansil, H. Lin, and M. Z. Hasan, *Nat. Phys.* **7**, 32 (2011).
- [34] M. Bianchi, D. Guan, S. Bao, J. Mi, B. B. Iversen, P. D. C. King, and P. Hofmann, *Nat. Commun.* **1**, 128 (2010).
- [35] S. R. Park, W. S. Jung, C. Kim, D. J. Song, C. Kim, S. Kimura, K. D. Lee, and N. Hur, *Phys. Rev. B* **81**, 041405(R) (2010).
- [36] S. R. Park *et al.*, *New J. Phys.* **13**, 013008 (2011).
- [37] K. Eto, Z. Ren, A. A. Taskin, K. Segawa, and Y. Ando, *Phys. Rev. B* **81**, 195309 (2010).
- [38]  $v_0$  was estimated from the slope of the putative linear dispersion in the absence of mode couplings, shown as solid straight lines in Figs. 1(a4) and (b4).
- [39] R. C. Hatch, M. Bianchi, D. Guan, S. Bao, J. Mi, B. B. Iversen, L. Nilsson, L. Hornekær, and P. Hofmann, *Phys. Rev. B* **83**, 241303(R) (2011).
- [40] T. Valla, A. V. Fedorov, P. D. Johnson, and S. L. Hulbert, *Phys. Rev. Lett.* **83**, 2085 (1999).
- [41] W. Zhang, R. Yu, H.-J. Zhang, X. Dai, and Z. Fang, *New J. Phys.* **12**, 065013 (2010).
- [42] W. Richter, H. Kohler, and C. R. Becker, *Phys. Status Solidi B* **84**, 619 (1977).
- [43] K. M. F. Shahil, M. Z. Hossain, D. Teweldebrhan, and A. A. Balandin, *Appl. Phys. Lett.* **96**, 153103 (2010).
- [44] It is useful to note that the Kohn anomaly is typically accompanied by an extensive FS nesting and is very anisotropic [21,45,46]; however, in Bi<sub>2</sub>Se<sub>3</sub> no nesting is present [see Fig. 1(a3)] and the HASS experiment found the anomaly to be isotropic [11]. Hence, the Kohn anomaly in Bi<sub>2</sub>Se<sub>3</sub> is obviously unusual.
- [45] E. Hulpke and J. Lüdecke, *Phys. Rev. Lett.* **68**, 2846 (1992).
- [46] E. Rotenberg, J. Schaefer, and S. D. Kevan, *Phys. Rev. Lett.* **84**, 2925 (2000).
- [47] X. Zhu, L. Santos, C. Howard, R. Sankar, F. C. Chou, C. Chamon, and M. El-Batanouny, *Phys. Rev. Lett.* **108**, 185501 (2012).
- [48] P. Hawrylak, *Phys. Rev. Lett.* **59**, 485 (1987).

# Fermiology of the Strongly Spin-Orbit Coupled Superconductor $\text{Sn}_{1-x}\text{In}_x\text{Te}$ : Implications for Topological Superconductivity

T. Sato,<sup>1</sup> Y. Tanaka,<sup>1</sup> K. Nakayama,<sup>1</sup> S. Souma,<sup>2</sup> T. Takahashi,<sup>1,2</sup> S. Sasaki,<sup>3</sup> Z. Ren,<sup>3</sup> A. A. Taskin,<sup>3</sup>  
Kouji Segawa,<sup>3</sup> and Yoichi Ando<sup>3</sup>

<sup>1</sup>*Department of Physics, Tohoku University, Sendai 980-8578, Japan*

<sup>2</sup>*WPI Research Center, Advanced Institute for Materials Research, Tohoku University, Sendai 980-8577, Japan*

<sup>3</sup>*Institute of Scientific and Industrial Research, Osaka University, Ibaraki, Osaka 567-0047, Japan*

(Received 24 December 2012; published 17 May 2013)

We have performed angle-resolved photoemission spectroscopy on the strongly spin-orbit coupled low-carrier density superconductor  $\text{Sn}_{1-x}\text{In}_x\text{Te}$  ( $x = 0.045$ ) to elucidate the electronic states relevant to the possible occurrence of topological superconductivity, as recently reported for this compound based on point-contact spectroscopy. The obtained energy-band structure reveals a small holelike Fermi surface centered at the  $L$  point of the bulk Brillouin zone, together with a signature of a topological surface state, indicating that this material is a doped topological crystalline insulator characterized by band inversion and mirror symmetry. A comparison of the electronic states with a band-noninverted superconductor possessing a similar Fermi surface structure,  $\text{Pb}_{1-x}\text{Ti}_x\text{Te}$ , suggests that the anomalous behavior in the superconducting state of  $\text{Sn}_{1-x}\text{In}_x\text{Te}$  is related to the peculiar orbital characteristics of the bulk valence band and/or the presence of a topological surface state.

DOI: [10.1103/PhysRevLett.110.206804](https://doi.org/10.1103/PhysRevLett.110.206804)

PACS numbers: 73.20.-r, 71.20.-b, 75.70.Tj, 79.60.-i

Topological insulators are a novel quantum state of matter in which the bulk is an insulator with an “inverted” energy gap induced by a strong spin-orbit coupling, which leads to the emergence of unusual gapless edge or surface states protected by time-reversal symmetry [1,2]. The discovery of topological insulators triggered the search for their superconducting (SC) analogues, topological superconductors (TSCs) [2]. TSCs are accompanied by gapless Andreev bound states at the edge or surface [3–7], which characterize the nontrivial topology of the bulk state and are often composed of Majorana fermions [8]. It has been suggested that Majorana fermions have potential application in fault-tolerant topological quantum computing [9,10] owing to the peculiar characteristic that particle is its own antiparticle [8]. The first plausible example of a TSC preserving time-reversal symmetry was copper-doped bismuth selenide ( $\text{Cu}_x\text{Bi}_2\text{Se}_3$ ) [11–14], in which helical Majorana fermions are predicted to emerge [13]. The electronic properties of  $\text{Cu}_x\text{Bi}_2\text{Se}_3$  have been intensively investigated by transport and spectroscopic studies including angle-resolved photoemission spectroscopy (ARPES) [15–19], but it has been difficult to elucidate the nature of its superconducting state, partly because of the intrinsic inhomogeneity of this system [20].

Very recently, it was postulated that indium-doped tin telluride ( $\text{Sn}_{1-x}\text{In}_x\text{Te}$ , called In-SnTe here), a low-carrier density superconductor based on a narrow-gap IV-VI semiconductor, represents a new type of TSC, based on the observation of a pronounced zero-bias conductance peak in point-contact spectra below the SC transition temperature ( $T_c$ ) indicative of an unconventional surface Andreev bound states [21]. In contrast, a similar low-carrier density superconductor, thallium-doped lead telluride ( $\text{Pb}_{1-x}\text{Ti}_x\text{Te}$ , called

Tl-PbTe here), appears to have no surface Andreev bound state and is likely to be nontopological [21]. These results are particularly intriguing in view of the fact that SnTe was recently shown to represent a new type of topological state called topological crystalline insulator (TCI) [22] associated with topologically protected surface states that emerge due to a combination of band inversion and mirror symmetry [23,24]. In contrast, PbTe is not a TCI [23]. Thus, it is of great importance to experimentally establish the nature of the Fermi surface (FS) and the band dispersions of In-SnTe and Tl-PbTe for both the bulk and the surface to clarify the electronic states relevant to the possible occurrence of topological superconductivity.

In this Letter, we report high-resolution ARPES studies of In-SnTe and Tl-PbTe. Our most important result is that the topological surface state exists in In-SnTe, although it is significantly broadened compared to pristine SnTe due to strong quasiparticle scattering caused by In doping. On the other hand, no surface state was found in Tl-PbTe, which strongly suggests that the valence band of In-SnTe is inverted relative to Tl-PbTe, as is the case with their parent compounds. In addition, we were able to elucidate the bulk FS topology of In-SnTe for two different cleavage planes (111) and (001), which gives conclusive evidence that the bulk FS is located at  $L$  points of the bulk Brillouin zone (BZ).

High-quality single crystals of In-SnTe and pristine SnTe were grown by the vapor transport and the modified Bridgman methods, respectively. Details of the sample preparations were described elsewhere [21,23]. The indium concentration was determined to be  $x = 0.045$  with inductively coupled plasma atomic emission spectroscopy. This is consistent with the observed  $T_c$  value of 1.2 K



[25]. ARPES measurements were performed with the MBS-A1 and VG-Scienta SES2002 electron analyzers with a high-intensity helium discharge lamp at Tohoku University and also with tunable synchrotron lights at the beam line BL-7U at UVSOR as well as at the beam line BL28A at Photon Factory. To excite photoelectrons, we used the He I $\alpha$  resonance line ( $h\nu = 21.218$  eV), linearly polarized 12–40 eV light, and circularly polarized 50–100 eV light, at Tohoku University, UVSOR, and Photon Factory, respectively. The energy and angular resolutions were set at 10–30 meV and  $0.2^\circ$ , respectively. Samples were cleaved *in situ* along the (001) or (111) crystal plane in an ultrahigh vacuum of  $1 \times 10^{-10}$  Torr. A shiny mirror-like surface was obtained after cleaving the samples, confirming its high quality. The Fermi level ( $E_F$ ) of the samples was referenced to that of a gold film evaporated onto the sample holder.

Figure 1 displays the FS and band dispersions of the (001)-cleaved surface measured at  $T = 30$  K with various  $h\nu$  for In-SnTe. In this sample orientation, the surface BZ projected onto the (001) plane is tetragonal, and the surface  $\bar{X}$  point corresponds to the projection of the  $L$  point in the bulk BZ [Fig. 1(a)]; note that we define in-plane reciprocal lattice vectors  $k_x$  and  $k_y$  rotated by  $45^\circ$  with respect to those of the standard fcc lattice for convenience of the data presentation. As shown in Fig. 1(b), we clearly observe multiple dispersive bands in the valence-band region derived from Te  $5p$  orbitals [26], and the features are consistent with the previous ARPES data of pristine SnTe [23]. We also find a relatively weak dispersive feature approaching  $E_F$  near the  $\bar{X}$  point, which is attributed to the top of the valence band. To elucidate the FS topology in the three-dimensional (3D)  $\mathbf{k}$  (wave vector) space, we have mapped out the intensity at  $E_F$  as a function of the in-plane wave vector ( $k_x$  and  $k_y$ ) for various photon energies, and the result is shown in Fig. 1(c). One can see in the plot for  $h\nu = 92$  eV

that there is a single intensity spot centered at a point slightly away from  $\bar{X}$  in the second BZ (right-hand side), which originates from the holelike dispersion as seen in the near- $E_F$  band dispersion along the  $\bar{\Gamma}\bar{X}$  cut [Fig. 1(d)].

Upon varying the photon energy, the bright intensity center in the FS mapping systematically changes its  $\mathbf{k}$  location in the BZ. For instance, the intensity is peaked exactly at the  $\bar{X}$  point for  $h\nu = 21$  eV, whereas the peak for  $h\nu = 18$  eV is located a little closer to the  $\bar{\Gamma}$  point in the first BZ (left-hand side). Such a variation in the intensity profile is also reflected in the band dispersion along the  $\bar{\Gamma}\bar{X}$  cut shown in Fig. 1(d) in which the  $\mathbf{k}$  position of the band top changes upon  $h\nu$  variation, as is traced by arrows. This demonstrates a considerable  $k_z$  (wave vector perpendicular to the surface) dispersion of the band, suggesting that the observed spectral feature is dominated by the bulk contribution. To elucidate the 3D FS topology in more detail, we have mapped in Fig. 1(e) the ARPES intensity at  $E_F$  in the  $k_x$ - $k_z$  plane, which clarifies that the FS is centered at the  $L$  point of the bulk BZ and has an ellipsoidal shape elongated along the  $\bar{\Gamma}L$  direction (note that the longer axis of the ellipsoid appears to be slightly tilted with respect to the  $\bar{\Gamma}L$  direction, but this is probably an artifact resulting from a finite  $k_z$  broadening). Such an elongated shape of the bulk FS well explains the observed change in the in-plane FS mapping and the band dispersion in Figs. 1(c) and 1(d). We thus conclude that the bulk FS of In-SnTe is composed of a hole pocket at the  $L$  point. This is consistent with the band calculation [26] and the hole-doping nature of In substitution for Sn [25].

To further elucidate the bulk FS topology of In-SnTe, we have also investigated the electronic states for the (111)-cleaved surface. The (111)-oriented samples for the ARPES measurements were selected by carefully picking up those pieces that present sixfold-symmetric x-ray Laue diffraction spots, while (001)-oriented samples can be

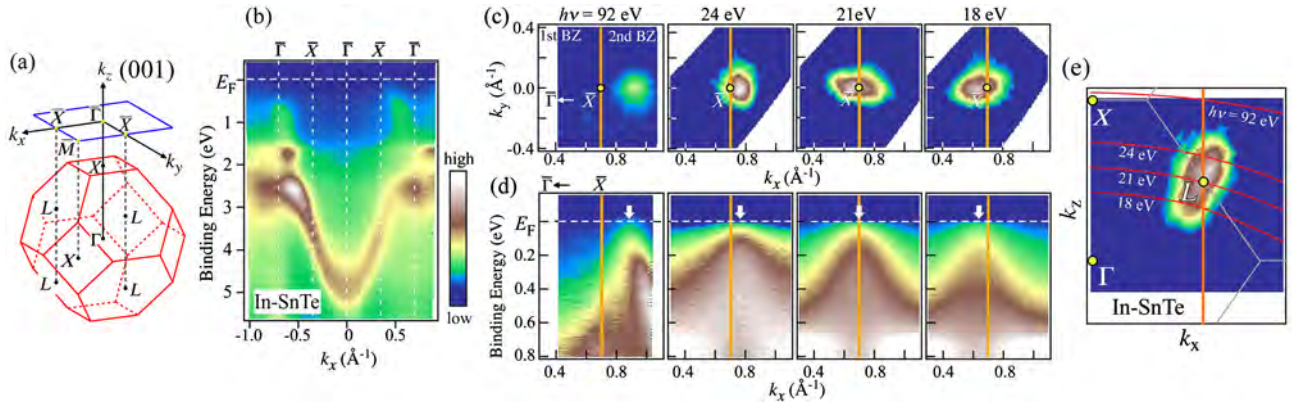


FIG. 1 (color online). (a) Bulk fcc BZ and corresponding tetragonal (001) surface BZ. (b) Valence-band ARPES intensity as a function of  $k_x$  and binding energy ( $E_B$ ) for In-SnTe ( $x = 0.045$ ) on the (001)-cleaved surface measured with  $h\nu = 92$  eV at  $T = 30$  K. (c) ARPES intensity mapping at  $E_F$  plotted as a function of in-plane wave vector ( $k_x$  and  $k_y$ ) measured with various photon energies; this intensity is obtained by integrating the spectra within  $\pm 10$  meV of  $E_F$ . (d) Corresponding near- $E_F$  band dispersion along the  $\bar{\Gamma}\bar{X}$  cut.  $\mathbf{k}$  location of the local maxima of the valence band is indicated by a white arrow in (d). (e) ARPES intensity mapping at  $E_F$  plotted as a function of  $k_x$  and  $k_z$  obtained from the measurement by sweeping the photon energy. Measured  $\mathbf{k}$  cuts in the  $k_x$ - $k_z$  plane for different photon energies are also indicated by solid red curves. Inner-potential value  $V_0$  is 8.5 eV, which is the same as pristine SnTe [23].

easily distinguished with their fourfold-symmetric Laue spots. In the (111) geometry, the surface BZ is hexagonal, and the  $\bar{\Gamma}$  ( $\bar{M}$ ) point corresponds to the projection of the  $L$  and  $\Gamma$  ( $X$  and  $L$ ) points of the bulk BZ [Fig. 2(a)]. We have performed ARPES measurements at  $h\nu = 92$  eV and covered a wide  $\mathbf{k}$  region extending to the second  $\bar{M}$  point of the surface BZ. As illustrated in Fig. 2(b), the measured cut (solid blue curve) is apart from the bulk  $L$  point at the  $\bar{M}$  point in the negative  $k_x$  region ( $\bar{M}_{-1}$ ), whereas in the positive  $k_x$  region, the cut nearly crosses the  $L$  point in both the first and second BZ boundaries (indicated by  $\bar{M}_{+1}$  and  $\bar{M}_{+2}$ , respectively). Reflecting such a difference in the  $k_z$  location, the intensity at  $E_F$  [Fig. 2(c)] around the  $\bar{M}_{-1}$  point in the FS mapping is very weak [see also the band dispersion in Fig. 2(d)] while the intensity around the  $\bar{M}_{+1}$

and  $\bar{M}_{+2}$  points is prominent. This gives conclusive evidence for the presence of a small bulk FS at the  $L$  point. Note that the band dispersion along the direction parallel to the BZ boundary [cuts A–C shown in Fig. 2(c)] also supports this conclusion, because the band approaches or touches  $E_F$  only around the  $\bar{M}$  point [Fig. 2(e)].

The next issue to be clarified is the effect of indium substitution on the electronic states of SnTe. As already mentioned, pristine SnTe was recently identified as a TCI [22–24,27,28], in which a topologically nontrivial Dirac-cone surface state appears; importantly, the  $\mathbf{k}$  location of the Dirac point, defined  $\bar{\Lambda}$  point, is slightly away from the time-reversal-invariant  $\bar{X}$  point, leading to a pair of Dirac cones to appear near  $\bar{X}$  [23]. Figures 3(a) and 3(b) show a direct comparison of near- $E_F$  ARPES intensity between pristine and In-doped SnTe measured along a  $\mathbf{k}$  cut crossing the  $\bar{\Lambda}$  point. A highly dispersive holelike band is clearly visible in pristine SnTe. This band is attributed to an admixture of the bulk and surface bands with dominant contribution from the surface state near  $E_F$ , as confirmed by the  $h\nu$  independence of the band dispersion for  $|E_B| < 0.2$  eV [23]. On the other hand, the overall dispersive feature is significantly broader in In-SnTe. In fact, a direct comparison of selected momentum distribution curves (MDCs) at  $E_B = 0.1, 0.3$ , and  $0.5$  eV in Fig. 3(d) and their numerical fittings suggests that the MDC width for In-SnTe, which reflects the inverse lifetime of quasiparticles (i.e., their scattering rate), is about 3 times larger than that for SnTe, in line with the transport results [21,23] showing  $\sim 5$  times shorter lifetime in In-SnTe.

Nevertheless, it is still possible to extract the intrinsic band dispersion for In-SnTe despite the broad spectral feature, by taking second derivatives of the MDCs as displayed in Fig. 3(c). The result of such an analysis clearly shows a linearly dispersive holelike band approaching  $E_F$ , which is similar to what is found in pristine SnTe; indeed, the extracted band dispersions for SnTe and In-SnTe shown in Fig. 3(e) overlap with each other for both  $h\nu = 21$  and  $92$  eV within the experimental uncertainty (note that the chemical-potential difference between the two compounds is estimated to be less than 10 meV from the Sn  $4d$  core-level measurements, well within the uncertainty of the extracted band dispersion of  $\pm 20$  meV). This result demonstrates that the surface state is likely to be present in the vicinity of  $E_F$  in In-SnTe, even though it is significantly broadened and thus is less visible due to the enhanced quasiparticle scattering rate caused by the Coulomb potential originating from the charged impurity ( $\text{In}^{3+}$ ) which substitutes  $\text{Sn}^{2+}$  [25]. This conclusion is further supported by our observation of the “ $M$ ”-shaped band dispersion along the  $\bar{\Gamma}\bar{X}$  cut [Fig. 3(f)], which can be regarded as a fingerprint of the Dirac-cone surface state of a TCI such as SnTe [23] and  $\text{Pb}_{0.6}\text{Sn}_{0.4}\text{Te}$  [27] in which the calculated bulk-band structure never shows any  $M$ -shaped dispersion near  $E_F$  [26,27]. It is remarkable that the surface state remains robust despite the significant increase in the

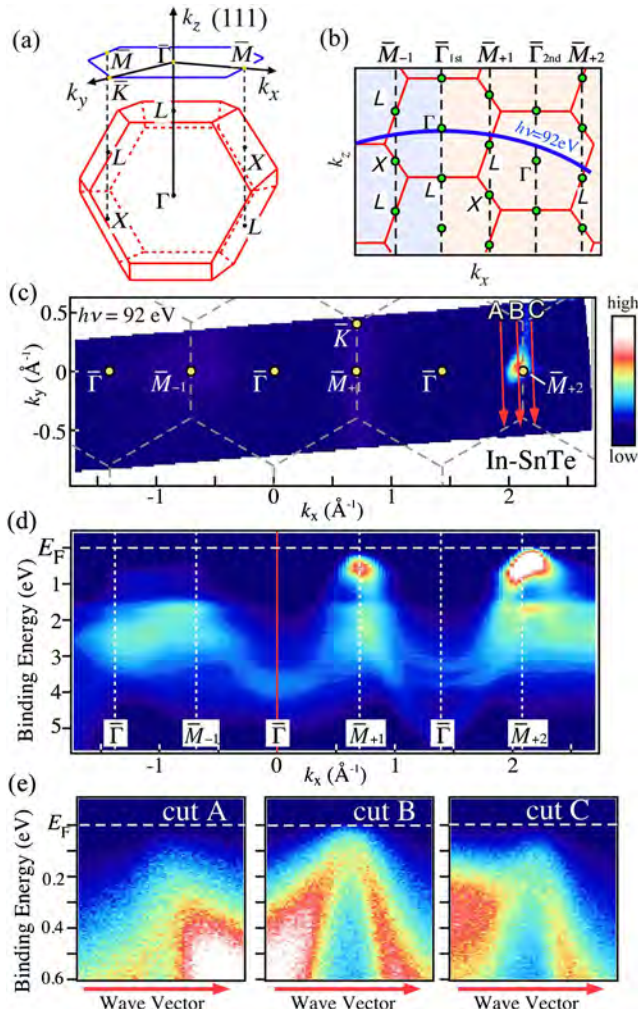


FIG. 2 (color online). (a) Bulk fcc BZ and corresponding hexagonal (111) surface BZ. (b) Bulk BZ in the  $k_x$ - $k_z$  plane together with a measured cut for  $h\nu = 92$  eV (solid blue curve). (c) ARPES intensity mapping at  $E_F$  covering a wide  $\mathbf{k}$  region for In-SnTe plotted as a function of in-plane wave vector measured at  $h\nu = 92$  eV on the (111)-cleaved surface. (d) Valence-band ARPES intensity as a function of  $k_x$  and  $E_B$ . (e) Near- $E_F$  ARPES intensity as a function of wave vector and  $E_B$  along representative  $\mathbf{k}$  cuts (A–C) in the surface BZ shown by red arrows in (c).



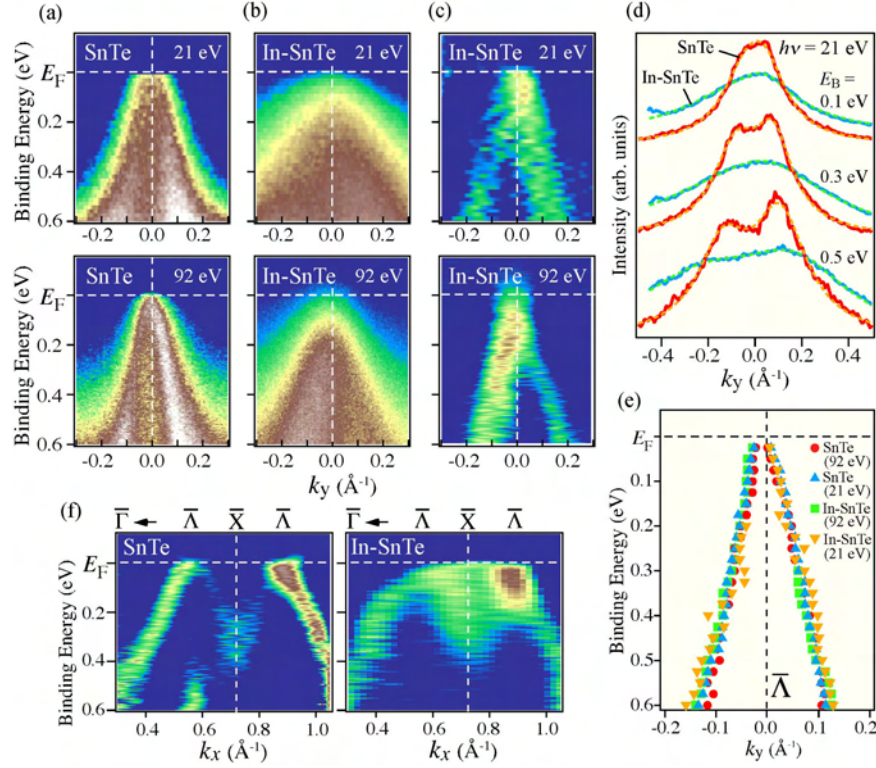


FIG. 3 (color online). (a), (b) Comparison of near- $E_F$  intensity as a function of  $k_y$  and  $E_B$  across the  $\bar{\Lambda}$  point between (a) pristine SnTe and (b) In-SnTe measured with  $h\nu = 21$  eV (top) and 92 eV (bottom) for the (001)-cleaved surface. (c) Second derivative of the data in (b), which was taken along the  $k_y$  direction. (d) Comparison of the MDCs at  $E_B = 0.1, 0.3$ , and  $0.5$  eV between pristine SnTe and In-SnTe for  $h\nu = 21$  eV (red and light blue curves) together with the result of numerical fittings (orange and green dashed curves) to each MDC by assuming two Lorentzians. (e) Band dispersions for  $h\nu = 21$  and 92 eV extracted by tracing the peak position of the second derivatives of the MDCs for SnTe and In-SnTe. (f) Comparison of the band dispersion for  $h\nu = 21$  eV derived from the second derivatives of the MDCs along the  $\bar{\Gamma}\bar{X}$  cut between pristine SnTe (left) and In-SnTe (right).

scattering rate due to the charged-impurity scattering, which is understandable in view of the topological protection against localization guaranteed by mirror symmetry.

Now we turn our attention to the electronic states of TI-PbTe which is regarded as a non-TSC counterpart of In-SnTe [21]. As shown in the FS mapping at  $E_F$  for the (001)-cleaved surface, there is a bright intensity spot around the  $\bar{X}$  point for  $h\nu = 21$  eV [Fig. 4(a)] whose intensity center moves away from the  $\bar{X}$  point at  $h\nu = 92$  eV [Fig. 4(b)]. This spot originates from a highly dispersive holelike band with a finite  $k_z$  dispersion, as demonstrated in Figs. 4(c) and 4(d) for  $h\nu = 92$  and 87.5 eV. These observations are essentially similar to those in In-SnTe (see Fig. 1), indicating that there is a small hole pocket centered at the  $L$  point also in TI-PbTe [29]. Despite this commonality in the bulk FS topology between In-SnTe and TI-PbTe, we found that the surface state is absent in TI-PbTe, unlike In-SnTe. As demonstrated in Fig. 4(e), there is no signature of the  $M$ -shaped band in TI-PbTe along the  $\bar{\Gamma}\bar{X}$  cut. Therefore, it is most likely that the band inversion is absent in TI-PbTe as is the case with the parent compound PbTe [23], which means that the valence band parity is opposite between the two superconductors, In-SnTe and TI-PbTe.

Now we briefly discuss the implications of our results for the possible occurrence of topological superconductivity in

In-SnTe but not in TI-PbTe. First, the present experiments elucidate that the bulk band inversion, which makes SnTe a TCI, is kept unchanged in In-SnTe. This gives solid footing to the argument [21] that the pairing between Sn and Te  $p$  orbitals possessing opposite parity would lead to an odd-parity SC state that can be shown to be topological. Thus, if the odd-parity pairing is indeed realized, In-SnTe is a 3D TSC. On the other hand, the absence of band inversion in TI-PbTe suggests that Pb and Te  $p$  orbitals relevant at the Fermi level have the same parity, which precludes the above mechanism for odd-parity pairing. Second, the existence of the topological surface state at  $E_F$  can be responsible for unusual SC properties in In-SnTe, because the opening of the bulk SC gap may lead to an opening of a separate, proximity-induced SC gap in the topological surface state [1,2,18]; in this case, even if the bulk SC is a conventional BCS type, the surface may host a 2D TSC. In this regard, it would be important to perform bulk-sensitive measurements to separate the effects from unconventional pairing symmetry and  $s$ -wave superconductivity of the surface states. Proximity-induced superconductivity in the topological surface state of a TCI has not yet been addressed theoretically. Thus, the consequences of such behavior, including the existence of Majorana fermions, is an interesting topic for future work. Our observation of the

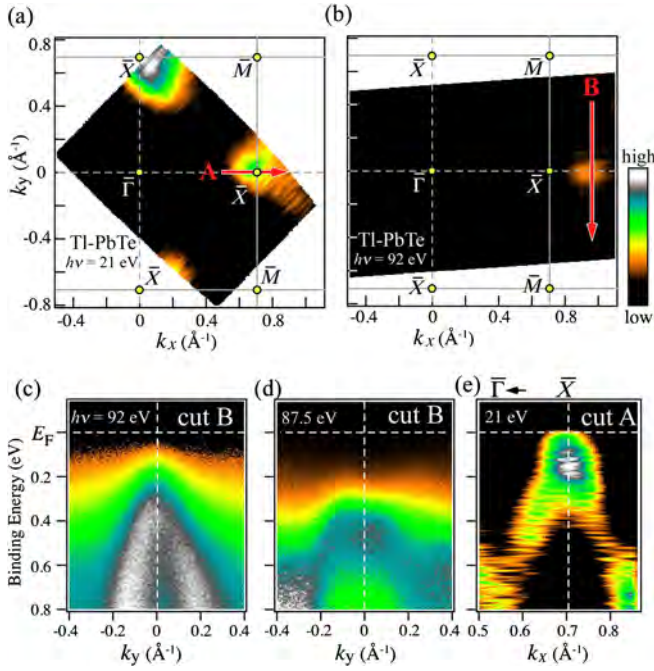


FIG. 4 (color online). (a), (b) ARPES intensity mapping for TI-PbTe ( $x = 0.013$ ) at  $E_F$  measured on the (001)-cleaved surface at  $T = 30$  K with  $h\nu = 21$  and  $92$  eV, respectively, plotted as a function of in-plane wave vector. (c), (d) Near- $E_F$  ARPES intensity as a function of  $k_y$  and  $E_B$  along a  $\mathbf{k}$  cut across the  $\bar{\Gamma}$  point [red arrow in (b)] for  $h\nu = 92$  and  $87.5$  eV, respectively. (e) Band dispersion derived from the second derivatives of the MDCs along the  $\bar{\Gamma}\bar{X}$  cut for TI-PbTe.

topological surface state in In-SnTe in the normal state assures that this material provides a fertile ground for the study of TSC irrespective of whether the putative odd-parity pairing is realized in the bulk.

In summary, we have performed ARPES experiments on In-SnTe and TI-PbTe to elucidate the energy-band structures underlying their SC states. We could barely resolve the topological surface state characteristic of a TCI in In-SnTe despite the significant broadening of the spectra due to enhanced quasiparticle scatterings caused by In doping. This gives evidence for an inverted band structure as in pristine SnTe and points to interesting physics associated with either the odd-parity pairing in the bulk or the proximity-induced superconductivity in the surface state of a doped TCI below  $T_c$ , a situation which has not been addressed theoretically to date. In contrast, in TI-PbTe we found no surface state, probably due to the absence of band inversion in this compound. These results are in good correspondence with the recent point-contact spectroscopy experiment [21] which found a pronounced zero-bias conductance peak in In-SnTe but only conventional Andreev reflection in TI-PbTe.

We thank Liang Fu for stimulating discussions. We also thank M. Nomura, T. Shoman, K. Honma, H. Kumigashira, K. Ono, M. Matsunami, and S. Kimura for their assistance in ARPES measurements and T. Ueyama and K. Eto for

their assistance in crystal growth. This work was supported by JSPS (NEXT Program and KAKENHI 23224010), JST-CREST, MEXT of Japan (Innovative Area “Topological Quantum Phenomena”), AFOSR (AOARD 124038), the Mitsubishi Foundation, KEK-PF (Proposal No. 2012S2-001), and UVSOR (Proposal No. 24-536).

- [1] M. Z. Hasan and C. L. Kane, *Rev. Mod. Phys.* **82**, 3045 (2010).
- [2] X.-L. Qi and S.-C. Zhang, *Rev. Mod. Phys.* **83**, 1057 (2011).
- [3] A. P. Schnyder, S. Ryu, A. Furusaki, and A. W. W. Ludwig, *Phys. Rev. B* **78**, 195125 (2008).
- [4] M. M. Salomaa and G. E. Volovik, *Phys. Rev. B* **37**, 9298 (1988).
- [5] N. Read and D. Green, *Phys. Rev. B* **61**, 10 267 (2000).
- [6] X.-L. Qi, T. L. Hughes, S. Raghu, and S.-C. Zhang, *Phys. Rev. Lett.* **102**, 187001 (2009).
- [7] M. Sato, *Phys. Rev. B* **81**, 220504(R) (2010).
- [8] F. Wilczek, *Nat. Phys.* **5**, 614 (2009).
- [9] J. Alicea, *Rep. Prog. Phys.* **75**, 076501 (2012).
- [10] C. W. J. Beenakker, *Annu. Rev. Condens. Matter Phys.* **4**, 113 (2013).
- [11] Y. S. Hor, A. J. Williams, J. G. Checkelsky, P. Roushan, J. Seo, Q. Xu, H. W. Zandbergen, A. Yazdani, N. P. Ong, and R. J. Cava, *Phys. Rev. Lett.* **104**, 057001 (2010).
- [12] M. Kriener, K. Segawa, Z. Ren, S. Sasaki, and Y. Ando, *Phys. Rev. Lett.* **106**, 127004 (2011).
- [13] L. Fu and E. Berg, *Phys. Rev. Lett.* **105**, 097001 (2010).
- [14] S. Sasaki, M. Kriener, K. Segawa, K. Yada, Y. Tanaka, M. Sato, and Y. Ando, *Phys. Rev. Lett.* **107**, 217001 (2011).
- [15] T. Kirzhner, E. Lahoud, K. B. Chaska, Z. Salman, and A. Kanigel, *Phys. Rev. B* **86**, 064517 (2012).
- [16] T. V. Bay, T. Naka, Y. K. Huang, H. Luigjes, M. S. Golden, and A. de Visser, *Phys. Rev. Lett.* **108**, 057001 (2012).
- [17] M. Kriener, K. Segawa, S. Sasaki, and Y. Ando, *Phys. Rev. B* **86**, 180505(R) (2012).
- [18] L. A. Wray, S.-Y. Xu, Y. Xia, Y. S. Hor, D. Qian, A. V. Fedorov, H. Lin, A. Bansil, R. J. Cava, and M. Z. Hasan, *Nat. Phys.* **6**, 855 (2010).
- [19] Y. Tanaka *et al.*, *Phys. Rev. B* **85**, 125111 (2012).
- [20] M. Kriener, K. Segawa, Z. Ren, S. Sasaki, S. Wada, S. Kuwabata, and Y. Ando, *Phys. Rev. B* **84**, 054513 (2011).
- [21] S. Sasaki, Z. Ren, A. A. Taskin, K. Segawa, L. Fu, and Y. Ando, *Phys. Rev. Lett.* **109**, 217004 (2012).
- [22] L. Fu, *Phys. Rev. Lett.* **106**, 106802 (2011).
- [23] Y. Tanaka, Z. Ren, T. Sato, K. Nakayama, S. Souma, T. Takahashi, K. Segawa, and Y. Ando, *Nat. Phys.* **8**, 800 (2012).
- [24] T. H. Hsieh, H. Lin, J. Liu, W. Duan, A. Bansil, and L. Fu, *Nat. Commun.* **3**, 982 (2012).
- [25] A. S. Erickson, J. H. Chu, M. F. Toney, T. H. Geballe, and I. R. Fisher, *Phys. Rev. B* **79**, 024520 (2009).
- [26] P. B. Littlewood *et al.*, *Phys. Rev. Lett.* **105**, 086404 (2010).
- [27] S. Y. Xu *et al.*, *Nat. Commun.* **3**, 1192 (2012).
- [28] P. Dziawa *et al.*, *Nat. Mater.* **11**, 1023 (2012).
- [29] K. Nakayama, T. Sato, T. Takahashi, and H. Murakami, *Phys. Rev. Lett.* **100**, 227004 (2008).

# Robust Protection from Backscattering in the Topological Insulator $\text{Bi}_{1.5}\text{Sb}_{0.5}\text{Te}_{1.7}\text{Se}_{1.3}$

Sunghun Kim,<sup>1,\*</sup> Shunsuke Yoshizawa,<sup>1</sup> Yukiaki Ishida,<sup>1</sup> Kazuma Eto,<sup>2</sup> Kouji Segawa,<sup>2</sup>  
Yoichi Ando,<sup>2,†</sup> Shik Shin,<sup>1</sup> and Fumio Komori<sup>1,‡</sup>

<sup>1</sup>*Institute for Solid State Physics, The University of Tokyo, Kashiwa, Chiba 277-8581, Japan*

<sup>2</sup>*Institute of Scientific and Industrial Research, Osaka University, Ibaraki, Osaka 567-0047, Japan*

(Received 11 October 2013; published 1 April 2014)

Electron scattering in the topological surface state (TSS) of the topological insulator  $\text{Bi}_{1.5}\text{Sb}_{0.5}\text{Te}_{1.7}\text{Se}_{1.3}$  was studied using quasiparticle interference observed by scanning tunneling microscopy. It was found that not only the  $180^\circ$  backscattering but also a wide range of backscattering angles of  $100^\circ$ – $180^\circ$  are effectively prohibited in the TSS. This conclusion was obtained by comparing the observed scattering vectors with the diameters of the constant-energy contours of the TSS, which were measured for both occupied and unoccupied states using time- and angle-resolved photoemission spectroscopy. The robust protection from backscattering in the TSS is good news for applications, but it poses a challenge to the theoretical understanding of the transport in the TSS.

DOI: 10.1103/PhysRevLett.112.136802

PACS numbers: 73.20.-r, 68.37.Ef, 78.47.da, 79.60.-i

Three-dimensional topological insulators (TIs) are accompanied by gapless surface states due to a nontrivial  $Z_2$  topology of the bulk wave functions [1–3]. Such a topological surface state (TSS) of a 3D TI is peculiar in that it is helically spin polarized, which leads to a suppression of electron scatterings due to spin mismatch between the eigenstates before and after the scattering [1,3]; in particular,  $180^\circ$  backscattering is expected to be absent, because  $+\mathbf{k}$  and  $-\mathbf{k}$  states have completely opposite spins. Such a protection of the TSS from backscattering has been elucidated to play a key role in maintaining a high mobility of the carriers in the TSS [4], and this characteristic is one of the reasons why TIs are an appealing platform for various device applications [5].

In STM experiments, the suppression of backscattering in TIs has been inferred from the measurements of quasiparticle interference (QPI) in  $\text{Bi}_{1-x}\text{Sb}_x$  [6],  $\text{Bi}_2\text{Te}_3$  [7,8], and  $\text{Bi}_2\text{Se}_3$  [9], as well as in Ca- and Mn-doped  $\text{Bi}_2\text{Te}_3$  and  $\text{Bi}_2\text{Se}_3$  [10]. In  $\text{Bi}_{1-x}\text{Sb}_x$ , which has multiple surface bands, strong interference was observed only between those surface bands that have the same spin orientation. On the other hand, in  $\text{Bi}_2\text{Te}_3$  and  $\text{Bi}_2\text{Se}_3$ , where the TSS consists of a single Dirac cone, no interference has been detected unless the Dirac cone becomes significantly warped at energies away from the Dirac point [7–11]; remember, in those materials a term proportional to  $k^3\sigma_z$  describing the cubic spin-orbit coupling shows up in the effective Hamiltonian [12], which results in hexagonal warping of the Dirac cone that has been experimentally observed by angle-resolved photoemission spectroscopy (ARPES) [13,14].

In those previous experiments, the suppression of backscattering due to the helical spin polarization of the TSS was only qualitatively elucidated, because no QPI was observed for intraband scatterings in  $\text{Bi}_{1-x}\text{Sb}_x$  nor for circular constant-energy contours of the TSS in  $\text{Bi}_2\text{Te}_3$  and

$\text{Bi}_2\text{Se}_3$ . In other words, it has not been clear to what extent the backscattering is suppressed as a function of scattering angle when the scattering takes place within the same surface band whose constant-energy contour is not warped. Even though such information is crucial for establishing concrete understanding of the transport in the TSS, until recently no TI material has allowed us to observe QPI in an unwarped Dirac cone.

This situation has changed with the recent discovery of the TI material  $\text{Bi}_{2-x}\text{Sb}_x\text{Te}_{3-y}\text{Se}_y$  [15,16]. This is the first TI material in which the surface-dominated transport was achieved in bulk single crystals [16], and the Fermi energy  $E_F$  can be tuned in the bulk band gap by changing the composition along particular combinations of  $(x, y)$  to realize the maximally charge-compensated state [15,17]. The alloyed nature of this material is expected to cause long-range potential fluctuations [6], which would lead to relatively strong scattering of long-wavelength electrons (i.e., Bloch electrons with small  $k$ ), even though the surface carrier mobility is high enough to present clear Shubnikov–de Haas oscillations [16]. Indeed, a recent STM study of  $\text{Bi}_{1.5}\text{Sb}_{0.5}\text{Te}_{1.7}\text{Se}_{1.3}$  found QPI to be observable [18] despite the weak warping of the Dirac cone. Therefore,  $\text{Bi}_{2-x}\text{Sb}_x\text{Te}_{3-y}\text{Se}_y$  offers a promising platform for quantitatively understanding one of the most important characteristics of TIs, the suppression of backscattering, in a nearly ideal Dirac cone.

In this Letter, we elucidate how the elastic scattering among the helically spin-polarized surface electrons of  $\text{Bi}_{1.5}\text{Sb}_{0.5}\text{Te}_{1.7}\text{Se}_{1.3}$  is suppressed as a function of the scattering angle and electron energy in the unwarped portion of the Dirac cone. Such information became available because elastic scattering of electrons manifests itself in the QPI down to energies close to the Dirac-point energy  $E_D$ , thanks to the long-range potential fluctuations



in this material. We found that there is a sharp threshold for the length of the scattering vector, above which the QPI intensity is abruptly diminished. Such a threshold points to the existence of a well-defined critical scattering angle beyond which elastic scattering is suddenly suppressed. By comparing the length of the critical scattering vector in the QPI with the diameters of the constant-energy contours of the TSS, we found that the maximum scattering angle is  $\sim 100^\circ$  and is independent of the energy location, as long as the bulk scattering channel does not intervene. For this comparison, we measured the dispersions of the unoccupied states by using time-resolved ARPES (TrARPES) implementing a pump-probe method, because in this material  $E_F$  is located very close to  $E_D$  and a major part of the upper Dirac cone is unmeasurable with usual ARPES.

The single crystals of  $\text{Bi}_{1.5}\text{Sb}_{0.5}\text{Te}_{1.7}\text{Se}_{1.3}$  were grown by melting stoichiometric mixtures of high-purity elements in sealed quartz tubes as described in Ref. [15]. The crystal structure was confirmed by x-ray diffraction. Experiments using STM and TrARPES were performed in two separated UHV systems. After a clean surface was prepared by cleaving the crystal in UHV of better than  $2 \times 10^{-8}$  Pa at room temperature, the sample was transferred *in situ* in UHV either to the cooled stage in the STM chamber or to the TrARPES chamber.

The STM images and tunneling spectra were taken at 5 K using a cryogenic STM with an electrochemically etched W tip. The tip apex and its metallic density of states were checked by scanning a clean Pt(111) surface. Topographic images were obtained using a constant-current mode. For the study of QPI, differential-conductance ( $dI/dV$ ) spectroscopy was performed using a standard lock-in technique with a bias-voltage modulation of 5 – 10 mV<sub>rms</sub> at 496 Hz. The  $dI/dV$  curve was measured at every point of a  $256 \times 256$  grid on the surface. The obtained data were plotted as a function of position to make a  $dI/dV$  map. The constant-energy  $dI/dV$  maps were Fourier transformed (FT), and the peaks due to the surface lattice were used for the calibration of the wave-vector space. The FT patterns were symmetrized with respect to the sixfold symmetry, on the basis of the  $C_{3v}$  symmetry of the cleaved surface.

In the TrARPES experiments, we used 1.5 eV (pump) and 5.9 eV (probe) pulsed photons from an amplified Ti: sapphire laser system with repetition rate of 250 kHz [19]. The pulse widths were 170 and 250 fs and the spot diameters were  $\sim 0.4$  and  $\sim 0.2$  mm for the 1.5 and 5.9 eV photons, respectively. The time delay between the pump and the probe pulses was optimized to clarify the unoccupied TSS band in the bulk band gap [20]. Photoelectrons from the cleaved surface cooled to 5 K were detected by a hemispherical analyzer. The energy resolution of the photoelectrons was 15 meV.

Typical STM images of the cleaved surface at 5 K are shown in Figs. 1(a) and 1(b). In the magnified image, surface atoms are recognized with a distribution of the

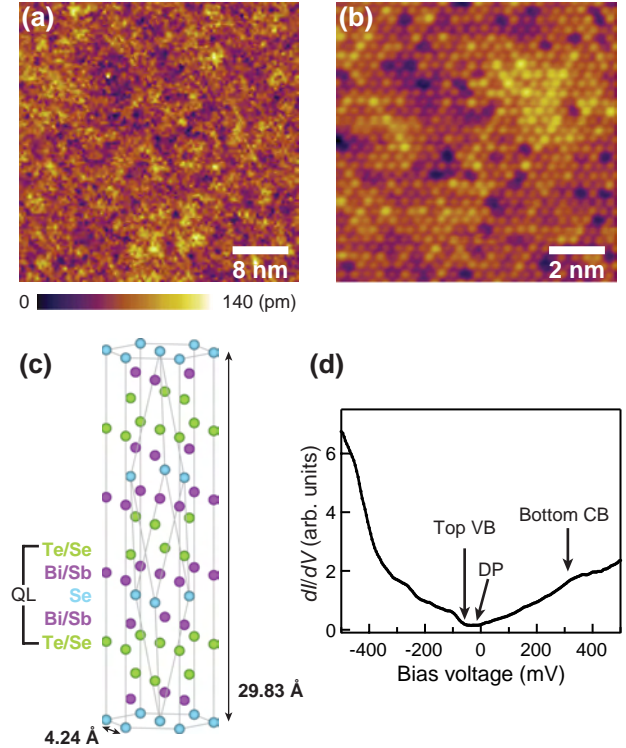


FIG. 1 (color online). (a),(b) STM images of a cleaved surface of  $\text{Bi}_{1.5}\text{Sb}_{0.5}\text{Te}_{1.7}\text{Se}_{1.3}$ . Protrusions are Te or Se atoms at the surface. The density of surface point defects is less than 3%. The sample bias voltage and tunneling current were  $-0.4$  V and 20 pA in (a) and  $-0.6$  V and 100 pA in (b). (c) Crystal structure of  $\text{Bi}_{1.5}\text{Sb}_{0.5}\text{Te}_{1.7}\text{Se}_{1.3}$ . (d) Typical differential-conductance curve measured on a cleaved surface at 5 K. The positions of the top of the bulk valence band, the Dirac point, and the bottom of the bulk conduction band are marked by arrows. The latter is known from the result of TrARPES.

apparent height. The  $\text{Bi}_{1.5}\text{Sb}_{0.5}\text{Te}_{1.7}\text{Se}_{1.3}$  crystal consists of quintuple-layer units of (Te/Se)-(Bi/Sb)-Se-(Bi/Sb)-(Te/Se) that are stacked and weakly bonded by the van der Waals force, as schematically shown in Fig. 1(c). The cleavage occurs along the van der Waals gap, and the flat cleaved surface is always the Te/Se layer. The local density of states fluctuates because of the inhomogeneous distributions of Te and Se, as well as those of Bi and Sb, in the crystal. Thus, the observed distribution of the apparent height of the surface atoms is attributed to the electronic effect due to the alloying in the Bi/Sb and Te/Se layers.

An example of the point tunneling spectrum is shown in Fig. 1(d). The Dirac-point energy  $E_D$  can be defined as the minimum in  $dI/dV$  and varies over the surface (the variation of the point spectra and the distribution of  $E_D$  are shown in Ref. [21]). The average location of  $E_D$  is  $10 \pm 15$  meV below  $E_F$ . In the point tunneling spectra [Fig. 1(d) and Ref. [21]], the differential conductance rapidly increases below  $E_D$  compared to that above  $E_D$ . This is because the top of the bulk valence band, which can

be recognized as a clear shoulder in the  $dI/dV$  curve in Fig. 1(d), is located just below  $E_D$ . The bottom of the bulk conduction band is, however, not very clear in the tunneling spectrum.

Figures 2(a) and 2(b) show  $dI/dV$  maps of the cleaved surface for two selected sample bias voltages  $V_B$  in the bulk band gap, and the corresponding FT images are shown in Figs. 2(c) and 2(d) [21]. The cross sections of the FT images at the two  $V_B$  values are shown in Figs. 2(e) and 2(f) for the two high-symmetry directions,  $\bar{\Gamma}$ - $\bar{K}$  and  $\bar{\Gamma}$ - $\bar{M}$ . In each cross section, one notices a steep decrease of the scattering amplitude with increasing scattering-vector length  $q$ . Such a steep decrease in the scattering amplitude

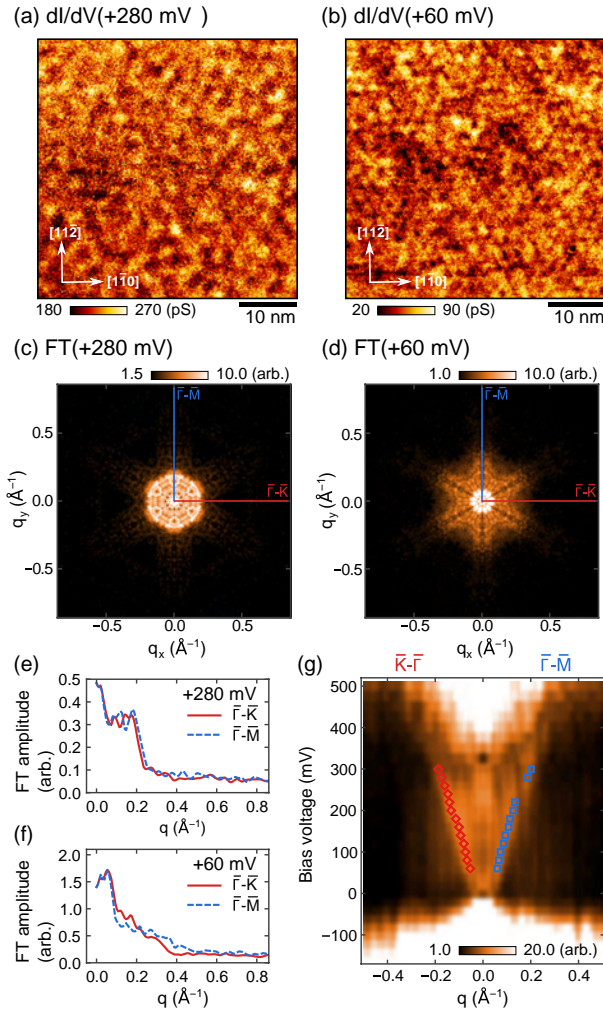


FIG. 2 (color online). (a),(b) Differential-conductance images of the cleaved surface for  $V_B$  of (a) 280 mV and (b) 60 mV in the bulk band gap. (c),(d) Corresponding FT amplitude images. (e), (f) Cross sections of the FT amplitude for the images (c) and (d), respectively. The results in the  $\bar{\Gamma}$ - $\bar{K}$  (solid red line) and  $\bar{\Gamma}$ - $\bar{M}$  (dotted blue line) directions are shown. (g) FT amplitude images as functions of  $V_B$  and the scattering-vector length  $q$  in the  $\bar{\Gamma}$ - $\bar{K}$  (left) and  $\bar{\Gamma}$ - $\bar{M}$  (right) directions. Diamond (red) and square (blue) symbols indicate the critical scattering-vector lengths in the two directions.

was observed in the  $V_B$  range of 60–300 mV. This range corresponds to the energy window where the TSS is located in the bulk band gap. Our data indicate that the electron scattering within the TSS is rapidly diminished when the scattering-vector length exceeds a certain critical value. Hence, we call it critical scattering-vector length and denote it  $q_{cx}$  and  $q_{cy}$  for  $\bar{\Gamma}$ - $\bar{K}$  and  $\bar{\Gamma}$ - $\bar{M}$  directions, respectively. Obviously, they both increase with increasing  $V_B$ ; to substantiate this trend, the FT amplitudes in the  $\bar{\Gamma}$ - $\bar{K}$  and  $\bar{\Gamma}$ - $\bar{M}$  directions are shown in Fig. 2(g) as an image on the scattering-vector length  $q$  versus  $V_B$  plane, and the critical scattering-vector lengths are marked by red and blue symbols on the image. The critical lengths increase with increasing energy, and the slope is reproducible in other regions of the surface [21].

To quantitatively understand the implications of the observed critical scattering-vector lengths, information regarding the TSS dispersion above  $E_F$  is important. Such information is unavailable with the ordinary ARPES, but the TrARPES makes it possible to measure it with a high resolution. To demonstrate the power of TrARPES, Figs. 3(a) and 3(b) compare the results of TrARPES at 5 K before and after filling the unoccupied side by the pump-induced electrons. The cut is along the  $\bar{\Gamma}$ - $\bar{K}$  direction. The band dispersion of the TSS was observed up to 0.25 eV above  $E_F$ , as shown in Fig. 3(b); the unoccupied states at

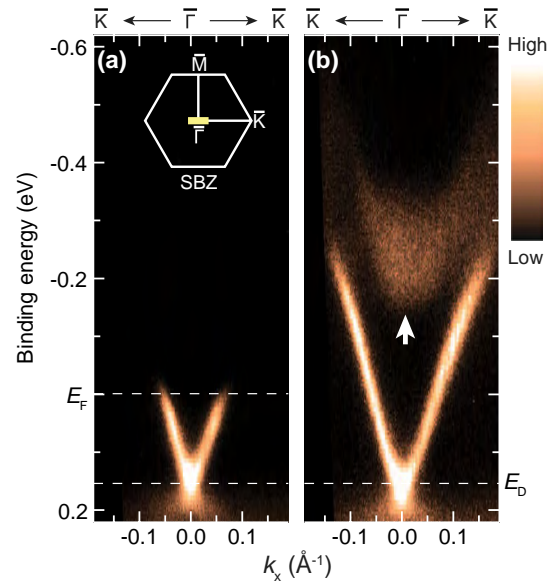


FIG. 3 (color online). (a),(b) Photoemission intensity images of the cleaved surface of  $\text{Bi}_{1.5}\text{Sb}_{0.5}\text{Te}_{1.7}\text{Se}_{1.3}$  plotted along the  $\bar{\Gamma}$ - $\bar{K}$  direction; images (a) and (b) were obtained before ( $-0.8$  ps) and after ( $+1.1$  ps) filling the unoccupied states with the 1.5 eV pump photons, respectively. Dispersions above the Fermi level became visible by pumping electrons into the unoccupied side. The bottom of the unoccupied bulk conduction band is indicated by an arrow. The inset of (a) shows the surface Brillouin zone, together with the range covered by the TrARPES measurements shown as a short thick line.



the center of the surface Brillouin zone in this figure are naturally assigned to the bulk states, on the basis of the electronic states of  $\text{Bi}_2\text{Te}_3$  and  $\text{Bi}_2\text{Se}_3$  [13,14]. The band shape [21] of the TSS shown in Fig. 3(a) is consistent with the previous result [17]. Judging from the spectrum width, the distribution of  $E_D$  over the measured region is as narrow as that estimated by the  $dI/dV$  maps [21]. We note that  $E_D$  in those ARPES data is located at 0.15 eV below  $E_F$ , which is lower than that observed in the tunneling spectrum shown in Fig. 1(d). This difference can be explained by the electron doping from adsorbates such as hydrogen that often occurs during ARPES measurements at low temperature [22]. In spite of the shift of  $E_D$ , the band velocity of TSS remains the same, so that it does not affect the discussions hereafter [21].

The velocity of the surface band was obtained by analyzing the momentum distribution curves [21], and is  $4.9 \times 10^5$  m/s for  $E - E_D > 80$  meV. Below that energy, it decreases as in the previous reports [3,23,24] on  $\text{Bi}_2\text{Se}_3$ . No significant difference in the band dispersion was observed between the  $\bar{\Gamma}-\bar{M}$  and  $\bar{\Gamma}-\bar{K}$  directions by TrARPES for energies up to 100 meV above  $E_F$  within our experimental accuracy. This means that the cross section of the TSS is close to circular in this energy range, and warping would become noticeable only at higher energies.

Knowing the TSS dispersion above  $E_F$  for  $\text{Bi}_{1.5}\text{Sb}_{0.5}\text{Te}_{1.7}\text{Se}_{1.3}$ , we are now in the position to make quantitative analysis of the critical scattering-vector lengths found in the QPI data. In Fig. 4(a),  $q_{\text{cx}}$  and  $q_{\text{cy}}$  are compared with the diameter of the cross section of the Dirac cone TSS observed by TrARPES. Here, the origin of the energy is commonly set to be  $E_D$ . The critical scattering-vector lengths is about 75% of the corresponding diameter of the TSS at any energy between 90 and 310 meV above  $E_D$ . Note that if scattering is allowed for the scattering angle  $\theta$ , of up to  $180^\circ$  (i.e., no restriction for backscattering),  $q_c$  should be equal to the diameter of the TSS. Hence, the fact that  $q_c$  is limited to 75% of the diameter of the TSS means that the allowed scattering angle has a maximum, which can be easily calculated to be  $100^\circ$ . This situation is schematically depicted in Figs. 4(c) and 4(d) for circular and warped cross sections of the TSS. Figure 4(b) graphically shows that this maximum scattering angle does not change with energy. This result indicates that not only the  $180^\circ$  backscattering but also a rather wide range of backscattering angle of  $100^\circ$ – $180^\circ$  are effectively prohibited due to the spin mismatch between the initial and final states in the TSS. This is good news for applications to utilize the protection of the TSS from backscattering.

The spin-mismatch mechanism for the present helical-spin system introduces an angle-dependent factor to the scattering probability. This factor is given [25] as  $1 + \cos\theta$ . The probability decreases rapidly with increasing  $\theta$  for  $\theta \gtrsim 90^\circ$ , and completely vanishes at  $\theta = 180^\circ$ ; this explains the strong suppression of scatterings for a relatively wide range of the scattering angle, at least qualitatively.

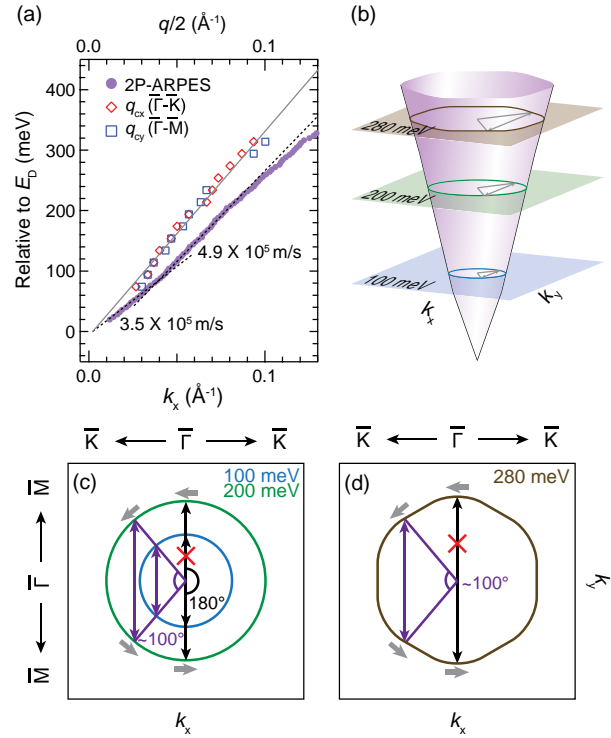


FIG. 4 (color online). (a) The critical scattering-vector lengths  $q_{\text{cx}}$  and  $q_{\text{cy}}$  and the diameter of constant-energy contour of the TSS are plotted for various energies from  $E_D$  to  $E_D + 310$  meV;  $q_{\text{cx}}$  and  $q_{\text{cy}}$  were obtained from Fig. 2(g), and the diameter of the TSS in the  $\bar{\Gamma}-\bar{K}$  direction was calculated from Fig. 3(b). (b) Schematic picture of the energy-dependent shape of the upper Dirac cone together with the available scattering vectors at representative energies. (c),(d) Schematic pictures for circular and warped TSS, respectively, to indicate that the critical scattering-vector lengths being 75% of the diameter of TSS corresponds to the maximum scattering angle of  $100^\circ$ ; any scattering with a larger angle requires longer scattering vectors and hence is prohibited.

Naturally, further theoretical study including the realistic scattering potential in the present TSS is strongly called for to account for this robust protection from backscattering.

In summary, we found critical scattering-vector lengths in the QPI, beyond which elastic scattering of electrons in the TSS is significantly suppressed. The comparison with the TSS dispersions for the unoccupied states obtained from TrARPES allowed us to conclude that the protection from backscattering in the TSS occurs not only for  $180^\circ$  but also for a rather wide range of angles of  $100^\circ$ – $180^\circ$ . Also, such a wide angle range for the protection from backscattering is found to be essentially independent of the energy until the Dirac cone becomes warped and/or the bulk scattering events intervene. At energies higher than 300 meV, we found hexagonal patterns in the FT-QPI images that come from warping of the Dirac cone, and in this energy range the critical scattering vector was not clearly observed, indicating a different mechanism of the protection from backscattering in the warped Dirac cone.

The authors thank Y. Ozawa and T. Otsu for their improvement in the TrARPES measurements. This work was partly supported by JSPS (KAKENHI No. 21244048 and No. 25220708, and FIRST program), MEXT (Innovative Area “Topological Quantum Phenomena” KAKENHI), and AFOSR (AOARD 124038).

\*kimsh@issp.u-tokyo.ac.jp

†y\_ando@sanken.osaka-u.ac.jp

‡komori@issp.u-tokyo.ac.jp

- [1] M. Z. Hasan and C. L. Kane, *Rev. Mod. Phys.* **82**, 3045 (2010).
- [2] X.-L. Qi and S.-C. Zhang, *Rev. Mod. Phys.* **83**, 1057 (2011).
- [3] Y. Ando, *J. Phys. Soc. Jpn.* **82**, 102001 (2013).
- [4] A. A. Taskin, S. Sasaki, K. Segawa, and Y. Ando, *Phys. Rev. Lett.* **109**, 066803 (2012).
- [5] J. E. Moore, *Nature (London)* **464**, 194 (2010).
- [6] P. Roushan, J. Seo, C. V. Parker, Y. S. Hor, D. Hsieh, D. Qian, A. Richardella, M. Z. Hasan, R. J. Cava, and A. Yazdani, *Nature (London)* **460**, 1106 (2009).
- [7] T. Zhang, P. Cheng, X. Chen, J.-F. Jia, X. Ma, K. He, L. Wang, H. Zhang, X. Dai, Z. Fang, X. Xie, and Q.-K. Xue, *Phys. Rev. Lett.* **103**, 266803 (2009).
- [8] Z. Alpichshev, J. G. Analytis, J.-H. Chu, I. R. Fisher, Y. L. Chen, Z. X. Shen, A. Fang, and A. Kapitulnik, *Phys. Rev. Lett.* **104**, 016401 (2010).
- [9] T. Hanaguri, K. Igarashi, M. Kawamura, H. Takagi, and T. Sasagawa, *Phys. Rev. B* **82**, 081305 (2010).
- [10] H. Beidenkopf, P. Roushan, J. Seo, L. Gorman, I. Drozdov, Y. S. Hor, R. J. Cava, and A. Yazdani, *Nat. Phys.* **7**, 939 (2011).
- [11] X. Zhou, C. Fang, W.-F. Tsai, and J. P. Hu, *Phys. Rev. B* **80**, 245317 (2009).
- [12] L. Fu, *Phys. Rev. Lett.* **103**, 266801 (2009).
- [13] Y. L. Chen, J. G. Analytis, J.-H. Chu, Z. K. Liu, S.-K. Mo, X. L. Qi, H. J. Zhang, D. H. Lu, X. Dai, Z. Fang, S. C. Zhang, I. R. Fisher, Z. Hussain, and Z.-X. Shen, *Science* **325**, 178 (2009).
- [14] K. Kuroda, M. Arita, K. Miyamoto, M. Ye, J. Jiang, A. Kimura, E. E. Krasovskii, E. V. Chulkov, H. Iwasawa, T. Okuda, K. Shimada, Y. Ueda, H. Namatame, and M. Taniguchi, *Phys. Rev. Lett.* **105**, 076802 (2010).
- [15] Z. Ren, A. A. Taskin, S. Sasaki, K. Segawa, and Y. Ando, *Phys. Rev. B* **84**, 165311 (2011).
- [16] A. A. Taskin, Z. Ren, S. Sasaki, K. Segawa, and Y. Ando, *Phys. Rev. Lett.* **107**, 016801 (2011).
- [17] T. Arakane, T. Sato, S. Souma, K. Kosaka, K. Nakayama, M. Komatsu, T. Takahashi, Z. Ren, K. Segawa, and Y. Ando, *Nat. Commun.* **3**, 636 (2012).
- [18] W. Ko, I. Jeon, H. W. Kim, H. Kwon, S.-J. Kahng, J. Park, J. S. Kim, S. W. Hwang, and H. Suh, *Sci. Rep.* **3**, 2656 (2013).
- [19] Y. Ishida, T. Togashi, K. Yamamoto, M. Tanaka, T. Taniuchi, T. Kiss, M. Nakajima, T. Suemoto, and S. Shin, *Sci. Rep.* **1**, 64 (2011).
- [20] J. A. Sobota, S. Yang, J. G. Analytis, Y. L. Chen, I. R. Fisher, P. S. Kirchmann, and Z.-X. Shen, *Phys. Rev. Lett.* **108**, 117403 (2012). Electrons are first excited by the pump pulse to the empty bands with the energy higher than that of the TSS band, and after the interband scattering, the TSS band is highly occupied with a certain delay time.
- [21] See Supplemental Material at <http://link.aps.org/supplemental/10.1103/PhysRevLett.112.136802> for additional STM images, spectra, and discussion on the artifacts in the FT images and on the TrARPES analyses.
- [22] R. Jiang, L.-L. Wang, M. Huang, R. S. Dhaka, D. D. Johnson, T. A. Lograsso, and A. Kaminski, *Phys. Rev. B* **86**, 085112 (2012).
- [23] Y. L. Chen, J.-H. Chu, J. G. Analytis, Z. K. Liu, K. Igarashi, H.-H. Kuo, X. L. Qi, S. K. Mo, R. G. Moore, D. H. Lu, M. Hashimoto, T. Sasagawa, S. C. Zhang, I. R. Fisher, Z. Hussain, and Z. X. Shen, *Science* **329**, 659 (2010).
- [24] K. Kuroda, M. Ye, A. Kimura, S. V. Eremin, E. E. Krasovskii, E. V. Chulkov, Y. Ueda, K. Miyamoto, T. Okuda, K. Shimada, H. Namatame, and M. Taniguchi, *Phys. Rev. Lett.* **105**, 146801 (2010).
- [25] I. A. Nechaev, M. F. Jensen, E. D. L. Rienks, V. M. Silkin, P. M. Echenique, E. V. Chulkov, and P. Hofmann, *Phys. Rev. B* **80**, 113402 (2009).

# Topological surface transport in epitaxial SnTe thin films grown on Bi<sub>2</sub>Te<sub>3</sub>

A. A. Taskin,<sup>\*</sup> Fan Yang, Satoshi Sasaki, Kouji Segawa, and Yoichi Ando<sup>†</sup>

*Institute of Scientific and Industrial Research, Osaka University, Ibaraki, Osaka 567-0047, Japan*

(Received 5 May 2013; published 17 March 2014)

The topological crystalline insulator SnTe has been grown epitaxially on a Bi<sub>2</sub>Te<sub>3</sub> buffer layer by molecular beam epitaxy. In a 30-nm-thick SnTe film, *p*- and *n*-type carriers are found to coexist, and Shubnikov–de Haas oscillation data suggest that the *n*-type carriers are Dirac fermions residing on the SnTe (111) surface. This transport observation of the topological surface state in a *p*-type topological crystalline insulator became possible due to a downward band bending on the free SnTe surface, which appears to be of intrinsic origin.

DOI: [10.1103/PhysRevB.89.121302](https://doi.org/10.1103/PhysRevB.89.121302)

PACS number(s): 73.25.+i, 71.18.+y, 72.20.My, 73.20.At

The energy band inversion and time-reversal symmetry (TRS) are the main ingredients for realizing a nontrivial topology in  $Z_2$  topological insulators (TIs) [1–4]. Recently, the family of TIs has been extended by the introduction of topological crystalline insulators [5,6] where the topology is protected by a point-group symmetry of the crystal lattice rather than by TRS. The first material predicted to be a TCI was SnTe [6], in which the band inversion at an even number of time-reversal-invariant momenta (TRIMs) leads to a trivial  $Z_2$  topological invariant, but its mirror symmetry gives rise to a nontrivial mirror Chern number  $n_M = -2$  to guarantee the existence of topologically protected gapless surface states (SSs) on any surface containing a mirror plane. Angle-resolved photoemission spectroscopy (ARPES) experiments have confirmed the existence of Dirac-like SSs on the (001) surface of SnTe [7] and related compounds [8,9], generating a lot of interest in TCIs [10,11]. Naturally, an important next step is to elucidate the topological SSs with transport experiments, as was done for  $Z_2$  TIs [12–21].

However, probing the SSs in SnTe by transport experiments is a challenge, because of a high concentration of bulk holes ( $10^{20}$  to  $10^{21}$  cm<sup>-3</sup>) [22]. Nevertheless, in thin films, an enhanced surface-to-bulk ratio and a high surface mobility expected for topologically-protected SSs [23,24] might make it possible to probe them in quantum oscillations. To obtain high-quality thin films by molecular beam epitaxy (MBE) [25–32], lattice matching of the substrate is crucial. In this regard, while BaF<sub>2</sub> is the usual choice of substrate for SnTe [33] with its  $\sim 1.6\%$  lattice matching, we noticed that rhombohedral Bi<sub>2</sub>Te<sub>3</sub> may be a better choice, at least for the (111) growth direction, with the lattice matching of  $\sim 1.5\%$ . Furthermore, the building block of Bi<sub>2</sub>Te<sub>3</sub> is a Te-Bi-Te-Bi-Te quintuple layer (QL) terminated with a hexagonal Te plane, which naturally accommodates the Sn layer of the SnTe in the (111) plane [see Fig. 1(d)].

Here, we show that high-quality SnTe thin films can indeed be grown by MBE on Bi<sub>2</sub>Te<sub>3</sub> and that they are actually suitable for probing the topological SSs in transport experiments. Those films present Shubnikov–de Haas (SdH) oscillations composed of two close frequencies, whose dependence on the magnetic-field direction signifies that the observed oscillations stem from two-dimensional (2D) Fermi

surfaces (FSs). Furthermore, the phase of the oscillations indicates that the 2D carriers are Dirac electrons bearing the Berry phase of  $\pi$ . Measurements of the *I*-*V* characteristics across the SnTe/Bi<sub>2</sub>Te<sub>3</sub> interface and careful considerations of the energy-band diagram in this heterostructure lead us to conclude that the Dirac electrons reside on the top surface of SnTe.

The MBE growth was performed in an ultrahigh vacuum chamber with the base pressure better than  $5 \times 10^{-8}$  Pa. Before deposition of SnTe, a thin layer of high-quality Bi<sub>2</sub>Te<sub>3</sub> was grown under Te-rich conditions on sapphire substrates [34] with a two-step deposition procedure similar to that used for Bi<sub>2</sub>Se<sub>3</sub> films [27,29,35]. Both Bi (99.9999%) and Te (99.9999%) were evaporated from standard Knudsen cells. The Te<sub>2</sub>(Te<sub>4</sub>)/Bi flux ratio was kept at  $\sim 20$ . The growth rate, which is determined by the Bi flux, was kept at 0.3 nm/min. After growing  $\sim 30$  nm of the Bi<sub>2</sub>Te<sub>3</sub> layer, Sn (99.999%) and Te were co-evaporated, keeping the Te<sub>2</sub>(Te<sub>4</sub>)/Sn flux ratio at  $\sim 40$ , substrate temperature at 300 °C, and the growth rate at 0.4 nm/min. The resistivity  $\rho_{xx}$  and the Hall resistivity  $\rho_{yx}$  of the films were measured in a Hall-bar geometry by a standard six-probe method on rectangular samples on which the contacts were made with silver paste or indium near the perimeter. The magnetic field was swept between  $\pm 14$  T at fixed temperatures.

A critical ingredient for the epitaxial SnTe growth in the present experiment is the high quality of the Bi<sub>2</sub>Te<sub>3</sub> buffer layer. Figure 1(a) shows an atomic force microscopy (AFM) image of a 40-nm-thick Bi<sub>2</sub>Te<sub>3</sub> thin film grown on sapphire substrate. Large equilateral triangles with atomically flat terraces, which have a height of exactly 1 QL, can be easily recognized. An AFM image of a 30-nm-thick SnTe film grown on top of such Bi<sub>2</sub>Te<sub>3</sub> buffer layer is shown in Fig. 1(b). Triangles are still clearly seen on the surface, giving evidence for an epitaxial growth. The height of the terraces is  $\sim 0.4$  nm, which agrees with the periodicity of the rocksalt lattice along the (111) direction [Fig. 1(d)]. [An image for a larger area with clear triangular morphology is shown in the Supplemental Material (SM) [36].]

The high structural quality of both Bi<sub>2</sub>Te<sub>3</sub> and SnTe films as well as the very smooth nature of the interface between them can be judged from the Kiessig fringes [36,37] in the x-ray diffraction (XRD) measurements [Fig. 1(c); see also SM for more details]. The inset of Fig. 1(c) shows the XRD pattern for a wider angle range, in which SnTe only yields ( $2n, 2n, 2n$ ) Bragg peaks to confirm the (111) growth direction.

<sup>\*</sup>taskin@sanken.osaka-u.ac.jp

<sup>†</sup>y\_ando@sanken.osaka-u.ac.jp



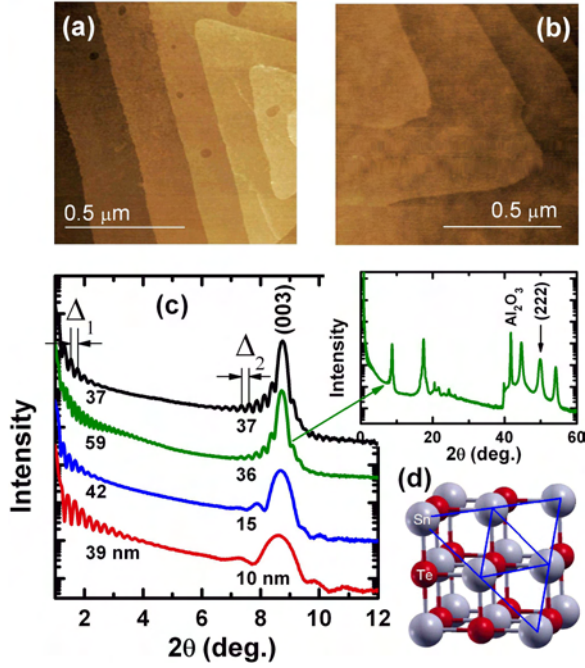


FIG. 1. (Color online) SnTe/Bi<sub>2</sub>Te<sub>3</sub> heterostructure. (a) AFM image of the Bi<sub>2</sub>Te<sub>3</sub> layer showing atomically flat terraces with 1-QL steps. (b) AFM image of the SnTe film grown on Bi<sub>2</sub>Te<sub>3</sub> buffer layer. The step height of the terraces is  $\sim 0.4$  nm. (c) Low-angle XRD patterns of a series of SnTe films grown on Bi<sub>2</sub>Te<sub>3</sub> of different thickness. The total film thickness  $d_t$  given by the distance  $\Delta_1$  of Kiessig fringes at grazing angles is shown to the left. The fringe distance  $\Delta_2$  near the (003) Bi<sub>2</sub>Te<sub>3</sub> Bragg peak gives the thickness of the Bi<sub>2</sub>Te<sub>3</sub> layer,  $d_b$ , which is shown near the peak. The SnTe layer thickness is given by  $d_t - d_b$ . Inset shows a wide-angle XRD pattern. (d) The rocksalt lattice of SnTe with its (111) plane marked by triangles.

Figure 2(a) shows the temperature dependence of the resistivity,  $\rho_{xx}(T)$ , in a 30-nm-thick SnTe film grown on 36-nm-thick Bi<sub>2</sub>Te<sub>3</sub>. There is no discernible kink in the data, suggesting that the structural phase transition observed in bulk SnTe [22,38,39] is absent in our thin films and that the mirror symmetry is kept intact down to low temperature [36]. In the magnetotransport properties, a downward cusp observed in  $\rho_{xx}(B)$  at very low fields [Fig. 2(b)] is a reflection of the weak antilocalization behavior which is expected for topological materials [40–42]. We also observe a coexistence of  $n$ - and  $p$ -type carriers in the sample which is evident from a sign change of the slope in  $\rho_{yx}(B)$  [Fig. 2(c)]. Importantly, we found that both  $\rho_{yx}(B)$  and  $\rho_{xx}(B)$  present SdH oscillations at high magnetic fields. To remove a large background and make the oscillations more visible, we employed second derivatives. Figure 2(d) shows  $d^2\rho_{yx}/dB^2$  measured in tilted magnetic fields at 1.5 K and plotted as a function of  $B \cos \theta$ , where  $\theta$  is the angle of the magnetic field from the surface normal. Since the maxima in the oscillations (marked by vertical dashed lines) appear at the same  $B \cos \theta$  upon changing  $\theta$ , the observed SdH oscillations clearly have a two-dimensional (2D) character. Note also that in our experiments, the SdH oscillations were not seen at tilting angles close to 90°, giving evidence against a three-dimensional (3D) FS as the origin of oscillations.

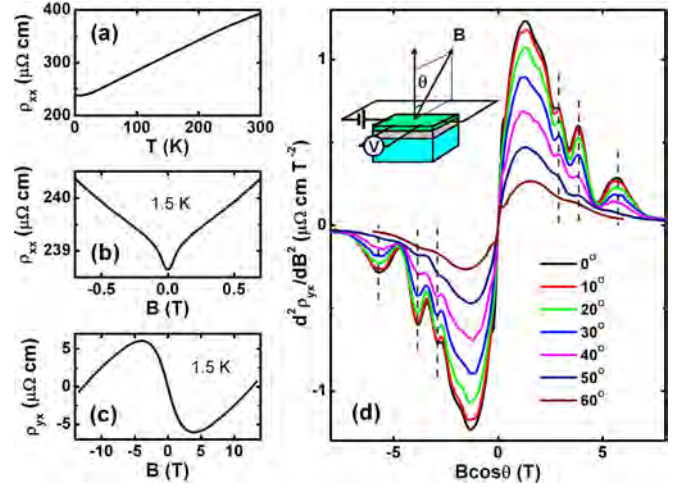


FIG. 2. (Color online) Transport properties of a 30-nm-thick SnTe film grown on a 36-nm Bi<sub>2</sub>Te<sub>3</sub> buffer layer. (a) Temperature dependence of  $\rho_{xx}$ . (b) Low-field  $\rho_{xx}(B)$  measured at 1.5 K. (c)  $\rho_{yx}(B)$  measured at 1.5 K. (d)  $d^2\rho_{yx}/dB^2$  at various angles are plotted vs  $B \cos \theta$ ; inset shows the measurement geometry. Dashed lines mark the maxima in the oscillations.

An important question is which of the  $n$ - or  $p$ -type carriers are responsible for the oscillations, and this can be answered in the following Landau-level (LL) index analysis. To properly construct the LL index plot, we use conductance  $G_{xx}$  and Hall conductance  $G_{xy}$  rather than  $\rho_{xx}$  and  $\rho_{yx}$  [4]. Figure 3(a) shows the plots of  $d^2G_{xx}/dB^2$  and  $d^2G_{xy}/dB^2$  vs  $1/B$ . The Fourier

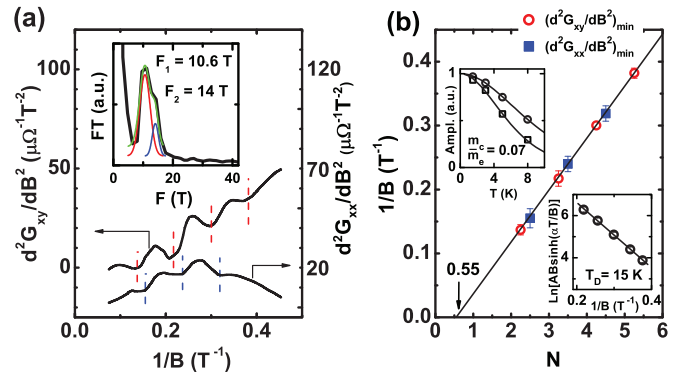


FIG. 3. (Color online) SdH oscillations. (a)  $d^2G_{xx}/dB^2$  and  $d^2G_{xy}/dB^2$  vs  $1/B$  measured at  $T = 1.5$  K and  $\theta = 0^\circ$ ; inset shows the Fourier transform of the  $d^2G_{xy}/dB^2$  oscillations revealing two close frequencies, 10.6 and 14 T (the upturn below  $\sim 5$  T is related to the background which slowly changes with  $B$ ). (b) LL index plot constructed from the minima in the oscillations of  $d^2G_{xx}/dB^2$  and  $d^2G_{xy}/dB^2$ . A half-integer index  $N + \frac{1}{2}$  is assigned to a minimum in  $d^2G_{xx}/dB^2$ . The index assignment for a minimum in  $d^2G_{xy}/dB^2$  depends on the sign of the carriers: The index  $N + \frac{1}{4}$  for electrons is consistent with the indices from  $G_{xx}$ , meaning that the SdH oscillations are produced by electrons. The solid line is a linear fitting to the data; its intercept of 0.55 on the  $N$ -index axis indicates the  $\pi$  Berry phase. Upper inset shows  $T$  dependencies of the SdH amplitudes measured at 2.67 T (squares) and 3.85 T (circles), both yielding  $m_c = 0.07m_0$ . Lower inset shows the Dingle plot for the data at 1.5 K, giving  $T_D = 15$  K.

transform of  $d^2G_{xy}/dB^2$  is shown in the inset of Fig. 3(a). Its main feature is a broadened peak with a shoulder, which can be well fitted with two Gaussians centered at frequencies of 10.6 and 14 T. The coexistence of two branches of oscillations is actually anticipated from weak beating patterns in the data. The two frequencies  $F_1 = 10.6$  T and  $F_2 = 14$  T correspond to orbits on the FSs with radii of  $k_F = 1.8 \times 10^6 \text{ cm}^{-1}$  and  $2.1 \times 10^6 \text{ cm}^{-1}$ , respectively. The corresponding 2D carrier densities  $n_s$  are  $2.6 \times 10^{11} \text{ cm}^{-2}$  and  $3.4 \times 10^{11} \text{ cm}^{-2}$  for each spin eigenvalue. Since the amplitude of the lower frequency oscillations is much larger than the amplitude of the higher frequency branch [see inset of Fig. 3(a)], the main contribution to the SdH oscillations is coming from the lower frequency branch; in such a case, the LL index plot constructed from weakly beating oscillations can still yield the correct phase factor for the lower frequency branch with reasonable accuracy (see SM for details). The constructed LL index plot [Fig. 3(b)] crosses the  $N$ -index axis at 0.55, which gives evidence for the Berry phase of  $\pi$  [43–45]. Also, the relative phase in the oscillations of  $d^2G_{xx}/dB^2$  and  $d^2G_{xy}/dB^2$  indicates that the carriers must be  $n$ -type (see SM for details). Therefore, the observed SdH oscillations can be concluded to be due to  $n$ -type 2D Dirac fermions bearing the  $\pi$  Berry phase. Note that even though the  $\text{Bi}_2\text{Te}_3$  layer contains a lot of  $n$ -type carriers (see SM), such carriers cannot be the source of the SdH oscillations, because the observed frequencies are an order of magnitude too low to represent the bulk FS of  $\text{Bi}_2\text{Te}_3$ .

The temperature dependence of the SdH amplitude [upper inset of Fig. 3(b)] gives the cyclotron mass  $m_c = 0.07m_0$  ( $m_0$  is the free electron mass) [46]. This value should mainly reflect the lower frequency branch of oscillations ( $F_1 = 10.6$  T) due to its dominance in the data, and we conclude that the upper limit of the Fermi velocity  $v_F (= \hbar k_F / m_c)$  of the dominant surface carriers is about  $3 \times 10^7 \text{ cm/s}$ . The Dingle analysis [lower inset of Fig. 3(b)] yields the Dingle temperature  $T_D$  of 15 K, from which the mean-free path of Dirac electrons  $l^{\text{SdH}} = 24 \text{ nm}$  and their mobility  $\mu_s^{\text{SdH}} = 2000 \text{ cm}^2/\text{Vs}$  are calculated [4]. Such a mobility is typical for best-quality SnTe films [33].

Now we discuss the origin of the observed  $n$ -type Dirac fermions. Both  $\text{Bi}_2\text{Te}_3$  and SnTe have topological surface states, and it is useful to consider the energy-band diagram of the heterojunction (shown in Fig. 4) formed by degenerate  $p^+$ -SnTe grown on the degenerate  $n^+$ - $\text{Bi}_2\text{Te}_3$ . The lineup of the conduction and valence bands at the interface of two semiconductors is of fundamental importance for understanding the properties of the heterojunction. Essentially, there are three possibilities: straddling, staggered, and broken-gap band lineups [47] (see SM for details). The vast majority of heterojunctions have a straddling lineup with conduction- and valence-band offsets of opposite sign; in this case, when the two sides are doped with opposite types of carriers, an insulating barrier layer will be formed at the interface of such a  $p$ - $n$  junction. The same holds true for the case of a staggered lineup, in which conduction- and valence-band offsets have the same sign with a finite overlap of the gaps. The situation is different for the most exotic broken-gap lineup, in which the bottom of the conduction band of one semiconductor goes below the top of the valence band of the other semiconductor as has been shown for InAs/GaSb heterostructures [48]. In this

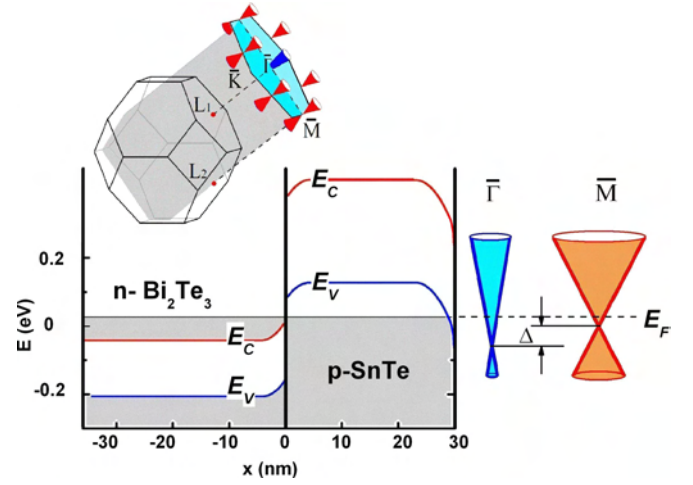


FIG. 4. (Color online) Energy-band diagram of  $n\text{-Bi}_2\text{Te}_3/p\text{-SnTe}$  heterojunction. The broken-gap band lineup is concluded from the  $I$ - $V$  characteristics of the heterojunction interface (see SM for details). Downward band bending on the free surface of SnTe gives rise to  $n$ -type doping of surface Dirac cones shown schematically on the right. The upper inset shows the bulk Brillouin zone of SnTe and its projection along the (111) direction to the surface Brillouin zone, which hosts two kinds of Dirac cones at  $\bar{\Gamma}$  and  $\bar{M}$ . The shaded plane is one of the three mirror planes  $\{110\}$ .

case, the system can behave as a semimetal without forming any barrier at the interface of a  $p$ - $n$  junction.

To determine which of the possible lineups is realized in our system, we measured  $I$ - $V$  curves across the interface in a sample where a part of the SnTe film has been etched away to make direct electrical contacts to both  $\text{Bi}_2\text{Te}_3$  and SnTe layers (see SM). We found the  $I$ - $V$  characteristics to show Ohmic behavior, which led us to conclude that the  $\text{SnTe}/\text{Bi}_2\text{Te}_3$  heterojunction most likely has the broken-gap lineup. In such a case, the Fermi level at the interface may lie above the bottom of the conduction band of  $\text{Bi}_2\text{Te}_3$  and below the top of the valence band of SnTe. Hence, while some exotic 2D state may be formed at the  $\text{Bi}_2\text{Te}_3/\text{SnTe}$  interface [49–51], such a state is not accessible due to the position of the Fermi level and it is unlikely that the 2D SdH oscillations come from this interface.

Another interface between  $\text{Bi}_2\text{Te}_3$  and sapphire is also an unlikely place for  $n$ -type Dirac fermions to reside on, because the Dirac point of the SS in  $\text{Bi}_2\text{Te}_3$  is situated below the top of its valence band [52]. This means that, in order for the SdH oscillations with frequencies of only 10–14 T to be observed, a very large upward band bending sufficient for creating an inversion layer would be required at the interface with sapphire. This is very unlikely and, in fact, we have never observed such low-frequency SdH oscillations in  $\text{Bi}_2\text{Te}_3$  films grown on sapphire.

Therefore, the only viable possibility is that the top SnTe surface has a sufficient downward band bending (Fig. 4) to host  $n$ -type Dirac fermions. Interestingly, such a band bending is naturally expected in materials with partially ionic bonding. For  $\text{Sn}^{2+}\text{Te}^{2-}$  films grown in the [111] direction, the stacking sequence of atomic planes is  $\text{Sn}^{2+}\text{-Te}^{2-}\dots$ , which brings about a dipole moment and leads to a diverging electrostatic energy (see SM). This situation is known as the



polar catastrophe [53] and cannot be realized in real materials; what actually happens is a partial charge compensation on the top and bottom surfaces to avoid the accumulation of electrostatic potential. In our system, the first atomic plane of the SnTe layer at the interface should be composed of  $\text{Sn}^{2+}$  and some of its positive charge is naturally compensated by  $n$ -type carriers of the  $\text{Bi}_2\text{Te}_3$  layer. On the free surface side, the termination is either with  $\text{Te}^{2-}$  or  $\text{Sn}^{2+}$  planes; since the SnTe layer begins with  $\text{Sn}^{2+}$ , the termination with  $\text{Te}^{2-}$  costs more electrostatic energy and  $\text{Sn}^{2+}$  termination is preferable (see SM). The resulting charge compensation leads to a downward band bending at the  $\text{Sn}^{2+}$ -terminated free surface as shown in Fig. 4. This offers a natural explanation of the observed  $n$ -type carriers at the free SnTe surface. Note that a strong downward band bending is also observed in ARPES experiments [54] when  $p$ -type SnTe single crystals are cleaved along the [111] direction in vacuum.

The above picture allows us to consistently understand the measured transport data. On the (111) plane of SnTe which is a TCI, there are four Dirac cones centered at four TRIMs in the surface Brillouin zone (BZ) [54,55]: one at  $\bar{\Gamma}$  and three at  $\bar{M}$  points which are projections of the four  $L$  points in the 3D BZ along the [111] direction as schematically shown in the inset of Fig. 4. The surface band calculations give different results for Te and Sn terminations [55,56]. For Te-terminated (111) surface, all Dirac points (DPs) touch the bottom of the conduction band, and it is impossible to realize  $n$ -type Dirac fermions irrespective of the position of the Fermi level. For the Sn-terminated (111) surface, on the other hand, the DPs are closer to the top of the valence band and Dirac electrons can be probed in transport experiments. Interestingly, epitaxially grown (111)-oriented films of a similar material,  $\text{Pb}_{1-x}\text{Sn}_x\text{Se}$ , were found to be preferentially terminated with Pb/Sn [57].

The observed two frequencies in the SdH oscillations are consistent with the existence of two types of Dirac cones on the free surface of SnTe reported in ARPES experiments [54]: the stronger, lower frequency branch is coming from electrons occupying the three Dirac cones at the  $\bar{M}$  points, while the weaker, higher frequency branch is coming from electrons

occupying the sole Dirac cone at the  $\bar{\Gamma}$  point. Importantly, the ARPES data show [54] that the Dirac point at  $\bar{\Gamma}$  is lower in energy than that at  $\bar{M}$ , resulting in a higher Fermi energy for the Dirac cone at  $\bar{\Gamma}$  (see Fig. 4) with a difference  $\Delta$  of  $\sim 170$  meV. It is worth noting that if oscillations were coming from the  $\text{Bi}_2\text{Te}_3$  surface, there would be only one frequency. The same is true for the SnTe/ $\text{Bi}_2\text{Te}_3$  interface, where the two Dirac cones at  $\bar{\Gamma}$  originating from SnTe and  $\text{Bi}_2\text{Te}_3$  should annihilate due to their opposite helicities [58]. The  $v_F$  of about  $3 \times 10^7$  cm/s obtained from our data may be attribute to the averaged  $v_F$  of highly anisotropic DPs at  $\bar{M}$  [56]. From  $F_1 = 10.6$  T ( $k_F = 1.8 \times 10^6$  cm $^{-1}$ ), the position of the Fermi level above the DPs at  $\bar{M}$  is estimated to be about 40 meV. For the DP at  $\bar{\Gamma}$ , according to the ARPES data [54], the Fermi velocity is much larger,  $v_F = 1.3 \times 10^7$  cm/s, and, for  $F_2 = 14$  T ( $k_F = 2.1 \times 10^6$  cm $^{-1}$ ), the position of the Fermi level would be about 180 meV above the DP. The energy difference of  $\sim 140$  meV between the two types of Dirac cones obtained in our transport experiments is close to the ARPES result of  $\Delta \sim 170$  meV, giving confidence that the observed 2D electrons indeed reside on the free surface of SnTe.

Finally, we mention that the observed SdH oscillations are prone to aging; namely, their amplitude was greatly reduced when we remeasured the sample after keeping it in nitrogen atmosphere for six months. This also supports the conclusion that the 2D oscillations are most likely coming from the free surface of SnTe. All in all, the present results demonstrate that the surface Dirac electrons residing on the (111) surface of SnTe can be accessed by transport measurements of high-quality films grown on a  $\text{Bi}_2\text{Te}_3$  buffer layer. These thin-film samples open new opportunities for experimentally exploring the physics of TCIs as well as for fabricating novel devices based on the unique nature of TCIs [59,60].

We thank J. Liu and L. Fu for helpful discussions, and M. Kishi for technical assistance with microfabrication of samples for  $I$ - $V$  measurements. This work was supported by JSPS (KAKENHI 24740237, 24540320, 25400328, and 25220708), MEXT (Innovative Area “Topological Quantum Phenomena” KAKENHI), and AFOSR (AOARD 124038).

- 
- [1] M. Z. Hasan and C. L. Kane, *Rev. Mod. Phys.* **82**, 3045 (2010).
  - [2] J. E. Moore, *Nature (London)* **464**, 194 (2010).
  - [3] X.-L. Qi and S.-C. Zhang, *Rev. Mod. Phys.* **83**, 1057 (2011).
  - [4] Y. Ando, *J. Phys. Soc. Jpn.* **82**, 102001 (2013).
  - [5] L. Fu, *Phys. Rev. Lett.* **106**, 106802 (2011).
  - [6] T. H. Hsieh, H. Lin, J. Liu, W. Duan, A. Bansil, and L. Fu, *Nat. Commun.* **3**, 982 (2012).
  - [7] Y. Tanaka, Z. Ren, T. Sato, K. Nakayama, S. Souma, T. Takahashi, K. Segawa, and Y. Ando, *Nat. Phys.* **8**, 800 (2012).
  - [8] P. Dziawa, B. J. Kowalski, K. Dybko, R. Buczko, A. Szczerbakow, M. Szot, E. Łusakowska, T. Balasubramanian, B. M. Wojek, M. H. Berntsen *et al.*, *Nat. Mater.* **11**, 1023 (2012).
  - [9] S.-Y. Xu, C. Liu, N. Alidoust, M. Neupane, D. Qian, I. Belopolski, J. D. Denlinger, Y. J. Wang, H. Lin *et al.*, *Nat. Commun.* **3**, 1192 (2012).
  - [10] A. Gyenis, I. K. Drozdov, S. Nadj-Perge, O. B. Jeong, J. Seo, I. Pletikosić, T. Valla, G. D. Gu, and A. Yazdani, *Phys. Rev. B* **88**, 125414 (2013).
  - [11] M. Safdar, Q. Wang, M. Mirza, Z. Wang, K. Xu, and J. He, *Nano Lett.* **13**, 5344 (2013).
  - [12] A. A. Taskin and Y. Ando, *Phys. Rev. B* **80**, 085303 (2009).
  - [13] A. A. Taskin, K. Segawa, and Y. Ando, *Phys. Rev. B* **82**, 121302(R) (2010).
  - [14] D.-X. Qu, Y. S. Hor, J. Xiong, R. J. Cava, and N. P. Ong, *Science* **329**, 821 (2010).
  - [15] J. G. Analytis, R. D. McDonald, S. C. Riggs, J.-H. Chu, G. S. Boebinger, and I. R. Fisher, *Nat. Phys.* **10**, 960 (2010).
  - [16] Z. Ren, A. A. Taskin, S. Sasaki, K. Segawa, and Y. Ando, *Phys. Rev. B* **82**, 241306(R) (2010).

- [17] A. A. Taskin, Z. Ren, S. Sasaki, K. Segawa, and Y. Ando, *Phys. Rev. Lett.* **107**, 016801 (2011).
- [18] B. Sacépé, J. B. Oostinga, J. Li, A. Ubalini, N. J. G. Couto, E. Giannini, and A. F. Morpurgo, *Nat. Commun.* **2**, 575 (2011).
- [19] S. S. Hong, J. J. Cha, D. Kong, and Y. Cui, *Nat. Commun.* **3**, 757 (2012).
- [20] L. He, F. Xiu, X. Yu, M. Teague, W. Jiang, Y. Fan, X. Kou, M. Lang, Y. Wang, G. Huang *et al.*, *Nano Lett.* **12**, 1486 (2012).
- [21] J. Xiong, Y. Luo, Y. H. Khoo, S. Jia, R. J. Cava, and N. P. Ong, *Phys. Rev. B* **86**, 045314 (2012).
- [22] R. Dornhaus, G. Nimtz, and B. Schlicht, *Narrow-Gap Semiconductors* (Springer-Verlag, New York, 1983).
- [23] D. Culcer, E. H. Hwang, T. D. Stanescu, and S. Das Sarma, *Phys. Rev. B* **82**, 155457 (2010).
- [24] A. A. Taskin, S. Sasaki, K. Segawa, and Y. Ando, *Phys. Rev. Lett.* **109**, 066803 (2012).
- [25] G. Zhang, H. Qin, J. Teng, J. Guo, Q. Guo, X. Dai, Z. Fang, and K. Wua, *Appl. Phys. Lett.* **95**, 053114 (2009).
- [26] A. Richardella, D. M. Zhang, J. S. Lee, A. Koser, D. W. Rench, A. L. Yeats, B. B. Buckley, D. D. Awschalom, and N. Samarth, *Appl. Phys. Lett.* **97**, 262104 (2010).
- [27] H. D. Li, Z. Y. Wang, X. Kan, X. Guo, H. T. He, Z. Wang, J. N. Wang, T. L. Wong, N. Wang, and M. H. Xie, *New J. Phys.* **12**, 103038 (2010).
- [28] X. Chen, X.-C. Ma, K. He, J.-F. Jia, and Q.-K. Xue, *Adv. Mater.* **23**, 1162 (2011).
- [29] N. Bansal, Y. S. Kim, E. Edrey, M. Brahlek, Y. Horibe, K. Iida, M. Tanimura, G.-H. Li, T. Feng, H.-D. Lee *et al.*, *Thin Solid Films* **520**, 224 (2011).
- [30] N. Bansal, Y. S. Kim, M. Brahlek, E. Edrey, and S. Oh, *Phys. Rev. Lett.* **109**, 116804 (2012).
- [31] M. Lang, L. He, F. Xiu, X. Yu, J. Tang, Y. Wang, X. Kou, W. Jiang, A. V. Fedorov, and K. L. Wang, *ACS Nano* **6**, 295 (2012).
- [32] X. Yu, L. He, M. Lang, W. Jiang, F. Xiu, Z. Liao, Y. Wang, X. Kou, P. Zhang, J. Tang *et al.*, *Nanotechnology* **24**, 015705 (2013).
- [33] A. Ishida, T. Tsuchiya, T. Yamada, D. Cao, S. Takaoka, M. Rahim, F. Felder, and H. Zogg, *J. Appl. Phys.* **107**, 123708 (2010).
- [34] J. J. Lee, F. T. Schmitt, R. G. Moore, I. M. Vishik, Y. Ma, and Z. X. Shen, *Appl. Phys. Lett.* **101**, 013118 (2012).
- [35] A. A. Taskin, S. Sasaki, K. Segawa, and Y. Ando, *Adv. Mater.* **24**, 5581 (2012).
- [36] See Supplemental Material at <http://link.aps.org/supplemental/10.1103/PhysRevB.89.121302> for supplemental data and discussion.
- [37] U. Pietsch, V. Holý, and T. Baumbach, *High-Resolution X-Ray Scattering: From Thin Films to Lateral Nanostructures* (Springer, New York, 2004).
- [38] K. L. I. Kobayashi, Y. Kato, Y. Katayama, and K. F. Komatsubara, *Phys. Rev. Lett.* **37**, 772 (1976).
- [39] S. Katayama and D. L. Mills, *Phys. Rev. B* **22**, 336 (1980).
- [40] J. Chen, H. J. Qin, F. Yang, J. Liu, T. Guan, F. M. Qu, G. H. Zhang, J. R. Shi, X. C. Xie, C. L. Yang *et al.*, *Phys. Rev. Lett.* **105**, 176602 (2010).
- [41] J. Chen, X. Y. He, K. H. Wu, Z. Q. Ji, L. Lu, J. R. Shi, J. H. Smet, and Y. Q. Li, *Phys. Rev. B* **83**, 241304(R) (2011).
- [42] H. Steinberg, J. B. Lalöe, V. Fatemi, J. S. Moodera, and P. Jarillo-Herrero, *Phys. Rev. B* **84**, 233101 (2011).
- [43] A. A. Taskin and Y. Ando, *Phys. Rev. B* **84**, 035301 (2011).
- [44] G. P. Mikitik and Y. V. Sharlai, *Phys. Rev. B* **85**, 033301 (2012).
- [45] A. R. Wright and R. H. McKenzie, *Phys. Rev. B* **87**, 085411 (2013).
- [46] D. Shoenberg, *Magnetic Oscillations in Metals* (Cambridge University Press, Cambridge, 1984).
- [47] H. Kroemer, *Rev. Mod. Phys.* **73**, 783 (2001).
- [48] H. Sakaki, L. L. Chang, R. Ludeke, Chin-An Chang, G. A. Sai-Halasz, and L. Esaki, *Appl. Phys. Lett.* **31**, 211 (1977).
- [49] D. Soriano, F. Ortmann, and S. Roche, *Phys. Rev. Lett.* **109**, 266805 (2012).
- [50] S. Eremeev, G. Landolt, T. V. Menshchikova, B. Slomski, Y. M. Koroteev, Z. S. Aliev, M. B. Babanly, J. Henk, A. Ernst, L. Patthey *et al.*, *Nat. Commun.* **3**, 365 (2012).
- [51] M. Koleini, T. Frauenheim, and B. Yan, *Phys. Rev. Lett.* **110**, 016403 (2013).
- [52] Y. L. Chen, J. G. Analytis, J.-H. Chu, Z. K. Liu, S.-K. Mo, X. L. Qi, H. J. Zhang, D. H. Lu, X. Dai, Z. Fang *et al.*, *Science* **325**, 178 (2009).
- [53] W. Weiss and W. Ranke, *Prog. Surf. Sci.* **70**, 1 (2002).
- [54] Y. Tanaka, T. Shoman, K. Nakayama, S. Souma, T. Sato, T. Takahashi, M. Novak, K. Segawa, and Y. Ando, *Phys. Rev. B* **88**, 235126 (2013).
- [55] J. Liu, W. Duan, and L. Fu, *Phys. Rev. B* **88**, 241303(R) (2013).
- [56] S. Safaei, P. Kacman, and R. Buczko, *Phys. Rev. B* **88**, 045305 (2013).
- [57] C. M. Polley, P. Dziawa, A. Reszka, A. Szczerbakow, R. Minikayev, J. Z. Domagala, S. Safaei, P. Kacman, R. Buczko, J. Adell *et al.*, *Phys. Rev. B* **89**, 075317 (2014).
- [58] T. Rauch, M. Flieger, J. Henk, and I. Mertig, *Phys. Rev. B* **88**, 245120 (2013).
- [59] J. Liu, T. H. Hsieh, P. Wei, W. Duan, J. Moodera, and L. Fu, *Nat. Mater.* **13**, 178 (2014).
- [60] C. Fang, M. J. Gilbert, and B. A. Bernevig, *Phys. Rev. Lett.* **112**, 046801 (2014).

# Spin-Electricity Conversion Induced by Spin Injection into Topological Insulators

Y. Shiomi,<sup>1</sup> K. Nomura,<sup>1</sup> Y. Kajiwara,<sup>1</sup> K. Eto,<sup>2</sup> M. Novak,<sup>2</sup> Kouji Segawa,<sup>2</sup> Yoichi Ando,<sup>2</sup> and E. Saitoh<sup>1,3,4,5</sup>

<sup>1</sup>*Institute for Materials Research, Tohoku University, Sendai 980-8577, Japan*

<sup>2</sup>*Institute of Scientific and Industrial Research, Osaka University, Ibaraki, Osaka 567-0047, Japan*

<sup>3</sup>*WPI Advanced Institute for Materials Research, Tohoku University, Sendai 980-8577, Japan*

<sup>4</sup>*CREST, Japan Science and Technology Agency, Tokyo 102-0076, Japan*

<sup>5</sup>*Advanced Science Research Center, Japan Atomic Energy Agency, Tokai 319-1195, Japan*

(Received 11 May 2014; published 3 November 2014)

We report successful spin injection into the surface states of topological insulators by using a spin pumping technique. By measuring the voltage that shows up across the samples as a result of spin pumping, we demonstrate that a spin-electricity conversion effect takes place in the surface states of bulk-insulating topological insulators  $\text{Bi}_{1.5}\text{Sb}_{0.5}\text{Te}_{1.7}\text{Se}_{1.3}$  and Sn-doped  $\text{Bi}_2\text{Te}_2\text{Se}$ . In this process, the injected spins are converted into a charge current along the Hall direction due to the spin-momentum locking on the surface state.

DOI: 10.1103/PhysRevLett.113.196601

PACS numbers: 72.25.Pn, 72.25.Dc, 73.20.-r, 75.76.+j

Detection and manipulation of electrons' spins are key prerequisites for spin-based electronics or spintronics [1]. The spin pumping technique has proved versatile [2–10] for injecting spins into materials as a result of magnetization  $M$  precession [11]. In a bilayer film consisting of a ferromagnet on top of a paramagnet, magnetization precession in the ferromagnet generates nonequilibrium spins whose polarization axis is parallel to the precession axis in the paramagnet near the interface upon excitations of ferromagnetic resonance (FMR) [2]. The spin pumping also exerts torque on the precessing magnetization in the ferromagnet and enhances the damping constant for magnetization precession (Gilbert damping constant) [2–10,12]. The spin polarization in the paramagnet decays due to spin relaxation, the length scale of which is characterized by the spin diffusion length  $\lambda$  [13].

Topological insulators (TIs) are a new class of quantum materials that possess topologically protected metallic surface states [14–16], while the interior is insulating [Fig. 1(a)]. Furthermore, conduction electrons on the surface states behave as Dirac fermions that bear a special characteristic called spin-momentum locking [14–16]; namely, in the surface states of TIs, the direction of the electron's motion uniquely determines its spin direction and vice versa. Examples are shown in Fig. 1(b): here, at the Fermi level, right-moving (+ $x$  direction) and left-moving (− $x$  direction) electrons have spins pointing to + $y$  and − $y$  (or − $y$  and + $y$ ) directions, respectively. Hence, if a spin imbalance is induced in the surface state by spin pumping, a charge current  $J_c$  is expected to show up along the “Hall” direction defined by

$$J_c \parallel (\mathbf{z} \times \boldsymbol{\sigma}), \quad (1)$$

where  $\boldsymbol{\sigma}$  is the direction of the spin polarization and  $\mathbf{z}$  is the unit vector perpendicular to the plane. Here, due to the strictly 2D nature, spins do not “flow” along the  $z$  direction

within the surface state and the converted charge current  $J_c$  has the 2D nature. Hence, the mechanism of this spin-electricity conversion is different from that in the inverse spin Hall effect, where a spin current flowing within a finite thickness of a sample is converted into a 3D charge current along the Hall direction.

In this Letter, we demonstrate spin-electricity conversion resulting from the spin-momentum locking for bulk-insulating topological insulators  $\text{Bi}_{1.5}\text{Sb}_{0.5}\text{Te}_{1.7}\text{Se}_{1.3}$  [17,18] and Sn-doped  $\text{Bi}_2\text{Te}_2\text{Se}$  [19] by using the spin pumping technique.  $\text{Bi}_{1.5}\text{Sb}_{0.5}\text{Te}_{1.7}\text{Se}_{1.3}$  (BSTS) is a bulk TI in which electric conduction through its surface state is dominant at low temperature, thanks to the nearly perfect

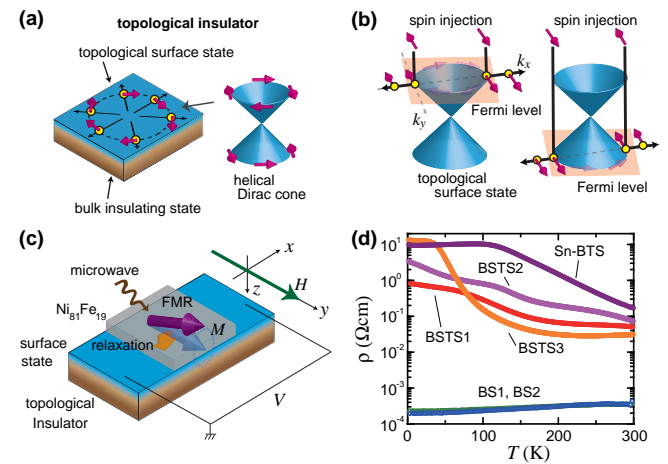


FIG. 1 (color online). (a) Schematic illustrations of a topological insulator, which has a conducting surface state consisting of helical Dirac fermions. (b) Concept of spin-electricity conversion effects on a topological surface state. (c) A schematic illustration of the experiment of the spin-electricity conversion effects. (d) Temperature ( $T$ ) dependence of the resistivity ( $\rho$ ) for  $\text{Bi}_2\text{Se}_3$  (BS),  $\text{Bi}_{1.5}\text{Sb}_{0.5}\text{Te}_{1.7}\text{Se}_{1.3}$  (BSTS), and Sn-doped  $\text{Bi}_2\text{Te}_2\text{Se}$  (Sn-BTS) samples.

carrier compensation in the bulk part [17,18,20,21]; in contrast, in stoichiometric compounds such as  $\text{Bi}_2\text{Se}_3$  and  $\text{Bi}_2\text{Te}_3$ , a sizable amount of bulk carriers due to unintentional doping from crystalline defects are inevitable [15,18,22]. The details of the topological surface states in BSTS have been elucidated by angle-resolved photoemission spectroscopy [23]. We also studied Sn-doped (0.4%)  $\text{Bi}_2\text{Te}_3\text{Se}$  (Sn-BTS), which was recently reported to be even more bulk insulating than BSTS [19]. Currently, BSTS and Sn-BTS are the best bulk TI materials for studies of the topological surface states [14].

The single crystals of BSTS,  $\text{Bi}_2\text{Se}_3$ , and Sn-BTS were grown by a Bridgman method in evacuated quartz tubes [17–19]. Figure 1(c) shows a schematic illustration of the present experiment. Immediately after TI samples are exfoliated using a blade in air, they were transferred into a vacuum chamber, and then 20-nm-thick  $\text{Ni}_{81}\text{Fe}_{19}$  thin films were deposited in a high vacuum by electron-beam evaporation on cleaved surfaces of TIs. The sizes of the BSTS and Sn-BTS samples were  $4 \times 1 \times 0.1 \text{ mm}^3$  (BSTS1),  $4 \times 3 \times 0.1 \text{ mm}^3$  (BSTS2),  $2 \times 1.5 \times 0.2 \text{ mm}^3$  (BSTS3), and  $2.5 \times 1 \times 0.3 \text{ mm}^3$  (Sn-BTS). We performed FMR and dc-voltage measurements for the  $\text{TI}|\text{Ni}_{81}\text{Fe}_{19}$  samples by using coplanar waveguides, where the width of the signal line is  $500 \mu\text{m}$  and the characteristic impedance was designed to be  $50 \Omega$  [24]. The microwave was applied through the waveguides in a static magnetic field and the frequency was kept at 5 GHz in the measurement of the spin-electricity conversion effect. Two electrodes were attached to both ends of TIs and the generated electromotive force was measured with a nanovoltmeter. The in-plane resistivity and Hall resistivity were measured down to 2 K by the conventional four-probe method in a superconducting magnet.

Figure 1(d) shows the temperature ( $T$ ) dependence of the resistivity ( $\rho$ ) for the samples used in the present study. We measured three BSTS samples (BSTS1, BSTS2, and BSTS3) and one Sn-BTS sample, as well as two  $\text{Bi}_2\text{Se}_3$  (BS) samples (BS1 and BS2) for comparison. The resistivity of all the BSTS and Sn-BTS samples monotonically increases with decreasing  $T$  below 200 K, which indicates that the bulk conduction is well suppressed at low temperature [17–21]. In contrast, the resistivity of the BS samples shows a metallic  $T$  dependence with a small magnitude of  $\sim 10^{-4} \Omega\text{cm}$ ; the bulk conduction is dominant in the BS samples [18].

Figure 2(a) shows the magnetic field ( $H$ ) dependence of the amplitude of the microwave transmittance through the sample,  $|S_{21}|$ , which presents negative peaks around  $\mu_0 H = \pm 30 \text{ mT}$  corresponding to the FMR of  $\text{Ni}_{81}\text{Fe}_{19}$ . At the FMR condition of the  $\text{Ni}_{81}\text{Fe}_{19}$  layer ( $H \equiv H_r$ ), the absorption of microwave in  $\text{Ni}_{81}\text{Fe}_{19}$  causes a decrease in  $|S_{21}|$ . The linewidth of the FMR spectrum carries important information on the relaxation of magnetization, or the Gilbert damping constant ( $\alpha$ ) [25]. In Fig. 2(b), we

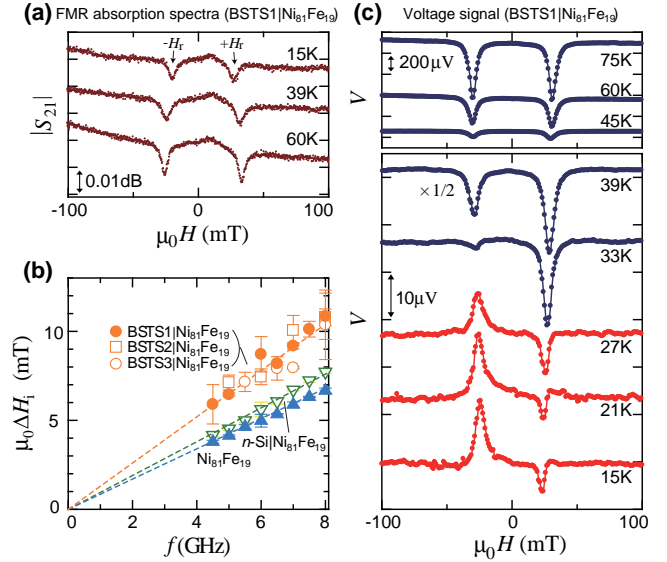


FIG. 2 (color online). (a) Magnetic-field ( $H$ ) dependence of the FMR spectrum ( $|S_{21}|$ ) at several temperatures for  $\text{BSTS1}|\text{Ni}_{81}\text{Fe}_{19}$ . (b) Frequency ( $f$ ) dependence of the half-maximum full-width (HMF,  $\Delta H$ ) of the FMR spectrum for  $\text{BSTS}|\text{Ni}_{81}\text{Fe}_{19}$  samples,  $n\text{-Si}|\text{Ni}_{81}\text{Fe}_{19}$ , and  $\text{Ni}_{81}\text{Fe}_{19}$  film alone.  $\Delta H_i (= \Delta H - \Delta H_0)$  is the intrinsic part of HMF, where  $\Delta H_0$  is the extrinsic part of HMF originating from the sample inhomogeneity [11]. The broken lines are merely guides to the eyes. (c) Magnetic-field ( $H$ ) dependence of the electromotive force ( $V$ ) at various temperatures for  $\text{BSTS1}|\text{Ni}_{81}\text{Fe}_{19}$ ; the data are shifted for clarity. The microwave power ( $P_{\text{in}}$ ) was 0.4 mW and the frequency ( $f$ ) was 5 GHz.

show the frequency ( $f$ ) dependence of the half-maximum full-width (HMF) of the FMR spectrum ( $\Delta H_i \propto f\alpha$ ) for  $\text{BSTS}|\text{Ni}_{81}\text{Fe}_{19}$  and for  $\text{Ni}_{81}\text{Fe}_{19}$  alone at 15 K [11]. As shown in Fig. 2(b), the linear  $f$  dependence of  $\Delta H_i$  is observed for our samples and the slope ( $\propto \alpha$ ) for  $\text{BSTS}|\text{Ni}_{81}\text{Fe}_{19}$  is greater than that for  $\text{Ni}_{81}\text{Fe}_{19}$  alone. The increase in  $\alpha$  in the presence of BSTS gives evidence for spin injection into the attached BSTS from  $\text{Ni}_{81}\text{Fe}_{19}$  [2–10,12]; this is the experimental realization of spin injection from a ferromagnet into a TI.

In Fig. 2(c), we show the results of the electromotive-force measurement with external magnetic field ( $H$ ) at various temperatures for  $\text{BSTS1}|\text{Ni}_{81}\text{Fe}_{19}$ . At the FMR condition ( $H = H_r$ ), a sharp peak (or dip) in the voltage ( $V$ ) arises [Fig. 2(c)]. At 75 K, the peak height  $V_0$  (measured from the background) is almost symmetric between  $-H_r$  and  $+H_r$ , and its absolute magnitude reaches  $\sim 0.5 \text{ mV}$ , while it decreases with decreasing  $T$ . Below 39 K, the voltage signal presents an asymmetric shape and  $V_0$  is different for  $-H_r$  and  $+H_r$ . This asymmetry becomes more pronounced at lower temperature, and below 27 K, even a sign reversal between  $-H_r$  and  $+H_r$  is observed. This sign reversal is what is expected from Eq. (1), since the direction of the injected spin reverses between  $-H_r$  and  $+H_r$ . In Sec. J of the Supplemental Material [11], the antisymmetric



signal is shown to be clearly correlated with the surface transport.

We note that this signal is irrelevant to the voltage generation inside the  $\text{Ni}_{81}\text{Fe}_{19}$  film, since such a Hall-type signal was not observed in control samples. In Fig. 3(a), we show a voltage signal near the FMR of  $\text{Ni}_{81}\text{Fe}_{19}$  for BSTS1, BSTS2, BS1,  $n$ -type Si, and  $n$ -type InAs of the same size. Here, as examples of conventional conductors, we used  $n$ -type Si ( $n$ -Si) and  $n$ -type InAs ( $n$ -InAs).  $\rho$  of  $n$ -Si at 295 K ( $\sim 1 \Omega\text{cm}$ ) is almost the same as that for BSTS at 15 K [Fig. 1(d)]. Though a slight increase in  $\alpha$  indicates spin injection into  $n$ -Si [Fig. 2(b)],  $V_0$  at FMR for  $n$ -Si/ $\text{Ni}_{81}\text{Fe}_{19}$  is clearly symmetric between  $-H_r$  and  $+H_r$ ; no antisymmetric signal is observed. Also for  $n$ -InAs, which is a semiconductor with low carrier concentration ( $< 3 \times 10^{16} \text{ cm}^{-3}$  at 295 K) but has a conducting electron accumulation layer on the surface [26], antisymmetric signal is not observed. Furthermore, for BS1, where its bulk conduction is much more prominent than the conduction from the topological surface state, antisymmetric signal is also absent. The symmetric signal, whose sign and magnitude seem to be random among BS,  $n$ -Si, or  $n$ -InAs samples [11], can be attributed to the Seebeck effect due to a small temperature-gradient along the sample plane that is peaked at FMR; similar symmetric signals have been reported in spin-pumping experiments for conventional semiconductor films [8]. By contrast, not only in BSTS1/ $\text{Ni}_{81}\text{Fe}_{19}$  but also in BSTS2/ $\text{Ni}_{81}\text{Fe}_{19}$ , clear antisymmetric signals with the same sign are observed. These results suggest that the antisymmetric signal observed in the BSTS samples is generated in the topological surface state of BSTS.

The microwave-power ( $P_{\text{in}}$ ) dependence of the voltage signal also confirms that the electromotive force for BSTS is associated with the surface state. Figure 3(b) shows the  $H$  dependence of  $V$  at several  $P_{\text{in}}$  values for BSTS2/ $\text{Ni}_{81}\text{Fe}_{19}$ . The sign reversal is observed at all  $P_{\text{in}}$  values and the magnitude increases with increasing microwave power ( $P_{\text{in}}$ ). The values of  $V_0$  at 15 and 39 K are shown in Fig. 3(c) as a function of microwave absorption power at FMR,  $\Delta P$  [11]. At 39 K,  $V_0$  shows a nonlinear dependence on the absorption power ( $\Delta P$ ); this is attributed to the Seebeck effect in BSTS, because the  $\Delta P$  dependence of the Seebeck voltage ( $= S\Delta T$ ) is expected to be nonlinear due to the variation of the Seebeck coefficient  $S$  by the heating effect caused by FMR and/or microwave energy loss on the waveguide. The antisymmetric (odd) signal observed at 15 K is, by contrast, proportional to  $\Delta P$  (i.e.,  $V \propto \Delta P$  [11]), which clearly indicates that the antisymmetric signal is of different origin.

The magnitude of  $V_0$  is almost the same between  $-H_r$  and  $+H_r$  for BSTS2/ $\text{Ni}_{81}\text{Fe}_{19}$ , while it is somewhat different in BSTS1/ $\text{Ni}_{81}\text{Fe}_{19}$  [Fig. 3(a)]. We separate the antisymmetric part from the symmetric part in  $\tilde{V} = V_0/\Delta P$  at 15 K by calculating  $\tilde{V}^a \equiv [\tilde{V}(H) - \tilde{V}(-H)]/2$ . Figure 4(a)

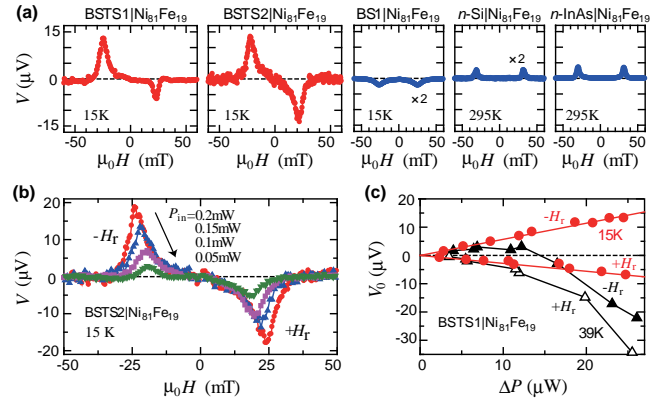


FIG. 3 (color online). (a) Electromotive force ( $V$ ) for BSTS1/ $\text{Ni}_{81}\text{Fe}_{19}$ , BSTS2/ $\text{Ni}_{81}\text{Fe}_{19}$ , and BS1/ $\text{Ni}_{81}\text{Fe}_{19}$  at 15 K, for  $n$ -Si/ $\text{Ni}_{81}\text{Fe}_{19}$  and  $n$ -InAs/ $\text{Ni}_{81}\text{Fe}_{19}$  at 295 K. The microwave power ( $P_{\text{in}}$ ) was 0.4 mW (BSTS1/ $\text{Ni}_{81}\text{Fe}_{19}$ ), 0.15 mW (BSTS2/ $\text{Ni}_{81}\text{Fe}_{19}$ ), 0.4 mW (BS1/ $\text{Ni}_{81}\text{Fe}_{19}$ ), 0.13 mW ( $n$ -Si/ $\text{Ni}_{81}\text{Fe}_{19}$ ), and 0.063 mW ( $n$ -InAs/ $\text{Ni}_{81}\text{Fe}_{19}$ ). The frequency ( $f$ ) was 5 GHz. (b) Magnetic-field ( $H$ ) dependence of electromotive force ( $V$ ) at 15 K for BSTS2/ $\text{Ni}_{81}\text{Fe}_{19}$  at several values of microwave power ( $P_{\text{in}}$ ). The frequency ( $f$ ) was 5 GHz. (c) The absorption power ( $\Delta P$ ) dependence of  $V_0$  (peak value of  $V$  measured from the background) at 15 and 39 K for BSTS1/ $\text{Ni}_{81}\text{Fe}_{19}$ .

shows resulting  $\tilde{V}^a$  for the three BSTS/ $\text{Ni}_{81}\text{Fe}_{19}$  samples, as well as for the BS/ $\text{Ni}_{81}\text{Fe}_{19}$  control samples, as functions of  $H$ . The sign of  $\tilde{V}^a$  is positive at  $-H_r$  and negative at  $+H_r$  for all the BSTS/ $\text{Ni}_{81}\text{Fe}_{19}$  samples. The magnitude of  $\tilde{V}^a$  is similar among the three BSTS/ $\text{Ni}_{81}\text{Fe}_{19}$  samples, but it tends to be larger in samples with larger  $\rho$  [see Fig. 1(d)]. In the BS samples (BS1/ $\text{Ni}_{81}\text{Fe}_{19}$  and BS2/ $\text{Ni}_{81}\text{Fe}_{19}$ ), the symmetric part is dominant as shown in Fig. 3(a), and  $\tilde{V}^a$  is negligibly small.

We have formulated a theoretical model for the spin-electricity conversion effect on the topological surface state, as illustrated in Fig. 4(b) [11]. The spin polarization on the surface state  $\langle \sigma_y \rangle$  is induced by the spin pumping driven by FMR in  $\text{Ni}_{81}\text{Fe}_{19}$  [2,10,12,27]. Owing to the spin-momentum locking in the topological surface state, the spin polarization per unit area  $\langle \sigma_y \rangle/A$  ( $A$ : area) gives rise to a shift of the Fermi circle of the helical Dirac fermions toward the  $x$  direction, which induces the electric field along the Hall direction according to  $E_x = -(4\pi\hbar/ek_F\tau)(\langle \sigma_y \rangle/A)$  [Fig. 4(b)] in the diffusive transport regime [11,28]. Here,  $k_F$  and  $\tau$  are the Fermi momentum and the scattering time of the helical Dirac fermions, respectively. The sign of the produced voltage is consistent with the experimental results [Figs. 4(a) and 4(b)]. The induced spin polarization is related to the spin pumped rate  $\Sigma$  via  $\langle \sigma_y \rangle = \eta\Sigma\tau$  [11]. Here,  $\eta$  is a phenomenological parameter quantifying the spin-injection efficiency affected by spin flip and leakage into residual bulk carriers, by reflection of spins to the ferromagnet, and also by the effective spin-exchange coupling at the interface. From the



experimental data, the value of  $\eta$  is estimated to be  $\sim 10^{-4}$  for BSTS1 and BSTS2. Here, because of imperfect insulation of bulk states, about 15% of the injected spins contribute to the spin-electricity conversion effect [11].

Note that, since the spin pumping induces spin polarization directly on the Fermi level of the surface state, the voltage generation is obviously dominated by the surface spin polarization, in contrast to experiments with circularly polarized light [29,30] where interband excitations generates electron-hole pairs and photocurrents. Also, as already noted, the spin-electricity conversion effect in the present surface-electron system is different from the inverse spin Hall effect [2–10], in which the spin current ( $J_s$ ) flowing in a paramagnet is converted into a charge current. Although the injected spins partly dissipate into the bulk state, they do not produce measurable ISHE signal in the bulk, as confirmed by control experiments for BS samples [Fig. 3(a)]. It is worth mentioning that the present spin-electricity conversion effect is rather similar to that reported in Rashba-split systems [31,32], but the efficiency is, in principle, much higher in TIs than that in the Rashba-split system [33]. The spin-momentum locking on a single Dirac cone predicts efficient spin-electricity conversion in TIs even at room temperature as long as the surface state is robust, while in the Rashba-split systems where a pair of bands exist, one of the bands counteracts the effect of the other.

Finally, to firm up our interpretation of the origin of the spin-electricity conversion effect, we show in Fig. 4(c) the data for a Sn-BTS sample possessing a large activation gap for the bulk conduction channel [Fig. 1(d)] [19]. In line with the large  $\rho$  value that extends to higher temperatures than in BSTS samples, the sign reversal in  $V_0$  between  $-H_r$  and  $+H_r$  is observed at high temperatures, even at 160 K. Figure 4(d) shows the  $T$  dependences of symmetric ( $V^s \equiv [V(H) + V(-H)]/2$ ) and antisymmetric ( $V^a \equiv [V(H) - V(-H)]/2$ ) parts of  $V$  at temperatures below 220 K, where  $V$  is well fitted using a Lorentz function. The symmetric part  $V^s$  changes sign at  $\sim 160$  K, which should be attributed to a change in the dominant carriers if  $V^s$  is due to the Seebeck effect. Indeed, the Hall coefficient ( $R_H$ ) changes sign around this temperature [Fig. 4(e)], below which the surface transport becomes dominant [19]. In contrast, the antisymmetric part  $V^a$  increases with decreasing  $T$ , which is opposite to what is expected for the possible contamination of the Nernst effect. The fact that the antisymmetric signal becomes noticeable in Sn-BTS below as high as 200 K [Fig. 4(d)], which coincides with the onset of the surface-dominated transport inferred from the  $R_H(T)$  behavior [Fig. 4(e)], gives strong support to the interpretation that  $V^a$  is a result of the spin-electricity conversion in the surface state.

In summary, we have demonstrated spin-electricity conversion induced by spin pumping for bulk-insulating millimeter-thick TIs attached with Py. This experimental

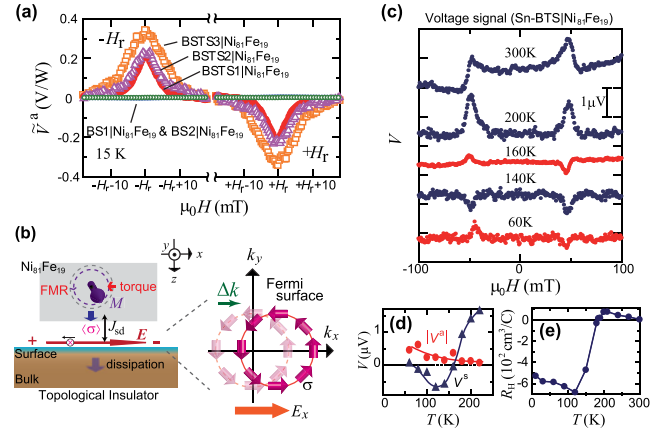


FIG. 4 (color online). (a) The antisymmetric part of  $V$  divided by the absorption power ( $\Delta P$ ), denoted  $\tilde{V}^a$ , for BS[Ni<sub>81</sub>Fe<sub>19</sub>] and BSTS[Ni<sub>81</sub>Fe<sub>19</sub>] samples at 15 K. (b) A schematic illustration of the theoretical mechanism for the observed effect. (c) Magnetic-field ( $H$ ) dependence of electromotive force ( $V$ ) at various temperatures for Sn-BTS/Ni<sub>81</sub>Fe<sub>19</sub>. The microwave power ( $P_{in}$ ) was 0.05 mW. (d) Temperature ( $T$ ) dependences of symmetric ( $V^s$ ) and antisymmetric ( $V^a$ ) parts of  $V$  for Sn-BTS/Ni<sub>81</sub>Fe<sub>19</sub> below 220 K. Solid curves are guides to the eyes. (e)  $T$  dependence of the Hall coefficient ( $R_H$ ) in Sn-BTS.  $R_H$  is defined by the slope of the Hall resistivity at 5 T.

condition is totally different from other related works [34–36], where bulk-metallic nanometer-thick Bi<sub>2</sub>Se<sub>3</sub> films were used and thus the (inverse) spin Hall effect by bulk-state carriers cannot be neglected. The spin-electricity conversion signal was not observed in bulk-metallic TIs or conventional semiconductors, which indicates that this phenomenon arises on the topological surface state owing to the spin-momentum locking. Though the efficiency of the spin-electricity conversion in the present work is as small as  $\eta \sim 10^{-4}$ , the spin-momentum locking on topological surface states can, in principle, lead to efficient conversion between spin and electricity.

We thank G. Tatara, Y. Fujikawa, K. Ando, and R. Iguchi for fruitful discussions and T. An and Z. Qiu for experimental help. This work was supported by CREST-JST (Creation of Nanosystems with Novel Functions through Process Integration), JSPS (NEXT Program and KAKENHI No. 24244051, No. 24740211, No. 25220708, and for JSPS Fellows), AFOSR (AOARD 124038), and MEXT [Innovative Area Topological Quantum Phenomena (No. 22103004, No. 25103702, and No. 25103703)].

- [1] S. Maekawa, S. O. Valenzuela, E. Saitoh, and T. Kimura, *Spin Current* (Oxford University Press, Oxford, 2012).
- [2] R. H. Silsbee, A. Janossy, and P. Monod, *Phys. Rev. B* **19**, 4382 (1979).
- [3] E. Saitoh, M. Ueda, H. Miyajima, and G. Tatara, *Appl. Phys. Lett.* **88**, 182509 (2006).

- [4] A. Azevedo, L. H. V. Leao, R. L. Rodriguez-Suarez, A. B. Oliveira, and S. M. Rezende, *J. Appl. Phys.* **97**, 10C715 (2005).
- [5] K. Ando *et al.*, *J. Appl. Phys.* **109**, 103913 (2011).
- [6] O. Mosendz, J. E. Pearson, F. Y. Fradin, G. E. W. Bauer, S. D. Bader, and A. Hoffmann, *Phys. Rev. Lett.* **104**, 046601 (2010).
- [7] M. V. Costache, M. Sladkov, S. M. Watts, C. H. van der Wal, and B. J. van Wees, *Phys. Rev. Lett.* **97**, 216603 (2006).
- [8] K. Ando and E. Saitoh, *Nat. Commun.* **3**, 629 (2011).
- [9] A. K. Patra, S. Singh, B. Barin, Y. Lee, J.-H. Ahn, E. del Barco, E. R. Mucciolo, and B. Özyilmaz, *Appl. Phys. Lett.* **101**, 162407 (2012).
- [10] Y. Kajiwara *et al.*, *Nature (London)* **464**, 262 (2010).
- [11] See Supplemental Material at <http://link.aps.org/supplemental/10.1103/PhysRevLett.113.196601> for details on experimental methods, theory, and additional data and analysis.
- [12] T. Yokoyama, J. Zang, and N. Nagaosa, *Phys. Rev. B* **81**, 241410(R) (2010).
- [13] J. Bass and W. P. Pratt, Jr., *J. Phys. Condens. Matter* **19**, 183201 (2007).
- [14] Y. Ando, *J. Phys. Soc. Jpn.* **82**, 102001 (2013).
- [15] M. Z. Hasan and C. L. Kane, *Rev. Mod. Phys.* **82**, 3045 (2010).
- [16] X.-L. Qi and S.-C. Zhang, *Rev. Mod. Phys.* **83**, 1057 (2011).
- [17] A. A. Taskin, Z. Ren, S. Sasaki, K. Segawa, and Y. Ando, *Phys. Rev. Lett.* **107**, 016801 (2011).
- [18] Z. Ren, A. A. Taskin, S. Sasaki, K. Segawa, and Y. Ando, *Phys. Rev. B* **84**, 165311 (2011).
- [19] Z. Ren, A. A. Taskin, S. Sasaki, K. Segawa, and Y. Ando, *Phys. Rev. B* **85**, 155301 (2012).
- [20] J. Lee, J. Park, J.-H. Lee, J. S. Kim, and H.-J. Lee, *Phys. Rev. B* **86**, 245321 (2012).
- [21] K. Segawa, Z. Ren, S. Sasaki, T. Tsuda, S. Kuwabata, and Y. Ando, *Phys. Rev. B* **86**, 075306 (2012).
- [22] D. O. Scanlon, P. D. C. King, R. P. Singh, A. de la Torre, S. McKeown Walker, G. Balakrishnan, F. Baumberger, and C. R. A. Catlow, *Adv. Mater.* **24**, 2154 (2012).
- [23] T. Arakane, T. Sato, S. Souma, K. Kosaka, K. Nakayama, M. Komatsu, T. Takahashi, Z. Ren, K. Segawa, and Y. Ando, *Nat. Commun.* **3**, 636 (2012).
- [24] Z. Qiu, T. An, K. Uchida, D. Hou, Y. Shiomi, Y. Fujikawa, and E. Saitoh, *Appl. Phys. Lett.* **103**, 182404 (2013).
- [25] S. Mizukami, Y. Ando, and T. Miyazaki, *Phys. Rev. B* **66**, 104413 (2002).
- [26] D. C. Tsui, *Phys. Rev. Lett.* **24**, 303 (1970).
- [27] K. Nomura and N. Nagaosa, *Phys. Rev. B* **82**, 161401(R) (2010).
- [28] D. Culcer, *Physica (Amsterdam)* **44E**, 860 (2012).
- [29] D. Hsieh, F. Mahmood, J. W. McIver, D. R. Gardner, Y. S. Lee, and N. Gedik, *Phys. Rev. Lett.* **107**, 077401 (2011).
- [30] J. W. McIver, D. Hsieh, H. Steinberg, P. Jarillo-Herrero, and N. Gedik, *Nat. Nanotechnol.* **7**, 96 (2012).
- [31] V. M. Edelstein, *Solid State Commun.* **73**, 233 (1990).
- [32] J. C. R. Sánchez, L. Vila, G. Desfonds, S. Gambarelli, J. P. Attané, J. M. De Teresa, C. Magén, and A. Fert, *Nat. Commun.* **4**, 2944 (2013).
- [33] D. Pesin and A. H. MacDonald, *Nat. Mater.* **11**, 409 (2012).
- [34] A. R. Mellnik *et al.*, *Nature (London)* **511**, 449 (2014).
- [35] P. Deorani, J. Son, K. Banerjee, N. Koirala, M. Brahlek, S. Oh, and H. Yang, *Phys. Rev. B* **B90**, 094403 (2014).
- [36] M. Jamali, J.-S. Lee, Y. Lv, Z. Zhao, N. Samarth, and J.-P. Wang, [arXiv:1407.7940](https://arxiv.org/abs/1407.7940).

# Electrical Detection of the Spin Polarization Due to Charge Flow in the Surface State of the Topological Insulator $\text{Bi}_{1.5}\text{Sb}_{0.5}\text{Te}_{1.7}\text{Se}_{1.3}$

Yuichiro Ando,<sup>\*,†,‡,⊥</sup> Takahiro Hamasaki,<sup>‡,⊥</sup> Takayuki Kurokawa,<sup>‡</sup> Kouki Ichiba,<sup>‡</sup> Fan Yang,<sup>§</sup> Mario Novak,<sup>§</sup> Satoshi Sasaki,<sup>§</sup> Kouji Segawa,<sup>§</sup> Yoichi Ando,<sup>\*,§</sup> and Masashi Shiraishi<sup>\*,†</sup>

<sup>†</sup>Department of Electronic Science and Engineering, Kyoto University, Kyoto 615-8531, Japan

<sup>‡</sup>Graduate School of Engineering Science, Osaka University, Toyonaka, Osaka 560-8531, Japan

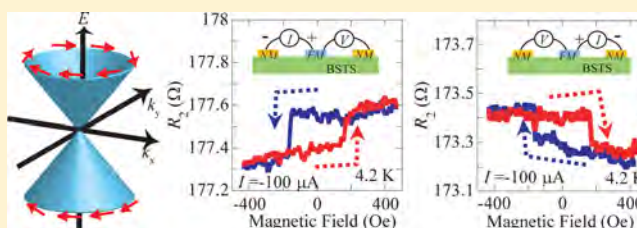
<sup>§</sup>Institute of Scientific and Industrial Research, Osaka University, Ibaraki, Osaka 567-0047, Japan

## S Supporting Information

**ABSTRACT:** We detected the spin polarization due to charge flow in the spin nondegenerate surface state of a three-dimensional topological insulator by means of an all-electrical method. The charge current in the bulk-insulating topological insulator  $\text{Bi}_{1.5}\text{Sb}_{0.5}\text{Te}_{1.7}\text{Se}_{1.3}$  (BSTS) was injected/extracted through a ferromagnetic electrode made of  $\text{Ni}_{80}\text{Fe}_{20}$ , and an unusual current-direction-dependent magnetoresistance gave evidence for the appearance of spin polarization, which leads to a spin-dependent resistance at the BSTS/ $\text{Ni}_{80}\text{Fe}_{20}$  interface.

In contrast, our control experiment on  $\text{Bi}_2\text{Se}_3$  gave null result. These observations demonstrate the importance of the Fermi-level control for the electrical detection of the spin polarization in topological insulators.

**KEYWORDS:** topological insulator, spin-momentum locking, spin current, electrical spin detection



Three-dimensional (3D) topological insulators (TIs) represent a new quantum state characterized by topologically protected gapless surface states with massless Dirac Fermions.<sup>1–4</sup> One of the most prominent properties of the TI surface state is spin-momentum locking, that is, spin quantization axis of the conduction electron in the TI surface state is perpendicularly locked to the carrier momentum as schematically shown in Figure 1a.<sup>4</sup> Due to this spin-momentum locking, dissipationless pure spin currents exist in the TI surface state in thermal equilibrium.<sup>4</sup> Furthermore, it is expected that charge current naturally induces spin polarization whose axis and the sign can be controlled by the direction of the charge flow.

The spin texture in the Dirac-cone of the TI surface state has been investigated by means of spin- and angle-resolved photoemission spectroscopy (ARPES), which confirmed the spin-momentum locking in the TI surface state.<sup>5–8</sup> In order to realize spintronic devices using 3D TIs based on their spin-momentum-locked characteristics, extractions of the spin polarized currents from the TI surface state and their detections by all-electrical methods are desirable.<sup>9–14</sup> Recently, a successful detection of the charge-current-induced spin polarization on the TI surface state based on the measurements of the conventional spin accumulation voltage has been reported by Li et al.<sup>11</sup> Intriguingly, their study was implemented by using  $\text{Bi}_2\text{Se}_3$  (BS), whose bulk state is not really insulating;<sup>11</sup> therefore, they needed to use very thin films to enhance the contribution of the surface state to the total conductance. In fact, Li et al. reported<sup>11</sup> that the spin accumulation voltage

diminishes quickly with increasing thickness in their BS devices, and the maximum thickness was 45 nm. Hence, utilization of more bulk-insulating TIs would allow more efficient spin detection. Also, it would be useful to detect the spin polarization with a method other than the spin accumulation voltage measurements.

In this Letter, we report successful detection of the spin polarization due to charge flow in a bulk-insulating TI,  $\text{Bi}_{1.5}\text{Sb}_{0.5}\text{Te}_{1.7}\text{Se}_{1.3}$  (BSTS), by using magnetoresistance measurement whose principle is different from the spin accumulation voltage measurements.<sup>11</sup> The magnetotransport studies of BSTS have been used to demonstrate the surface-dominated transport in this compound,<sup>15,16</sup> and the ARPES study has confirmed its Fermi level to be located in a bulk band gap, realizing the intrinsic insulating state.<sup>17</sup> In the present magnetoresistance measurements, we observed a rectangular hysteresis behavior which is governed by the resistance at the interface between BSTS and the ferromagnetic  $\text{Ni}_{80}\text{Fe}_{20}$  (Py) electrode used for current injection/extraction; our data indicate that at 4.2 K the interface resistance changes both with the magnetization direction of Py and with the current direction. This peculiar magnetoresistance disappears when BS is used in the devices instead of BSTS or when the BSTS device is heated to 300 K.

**Received:** July 7, 2014

**Revised:** October 3, 2014

**Published:** October 20, 2014



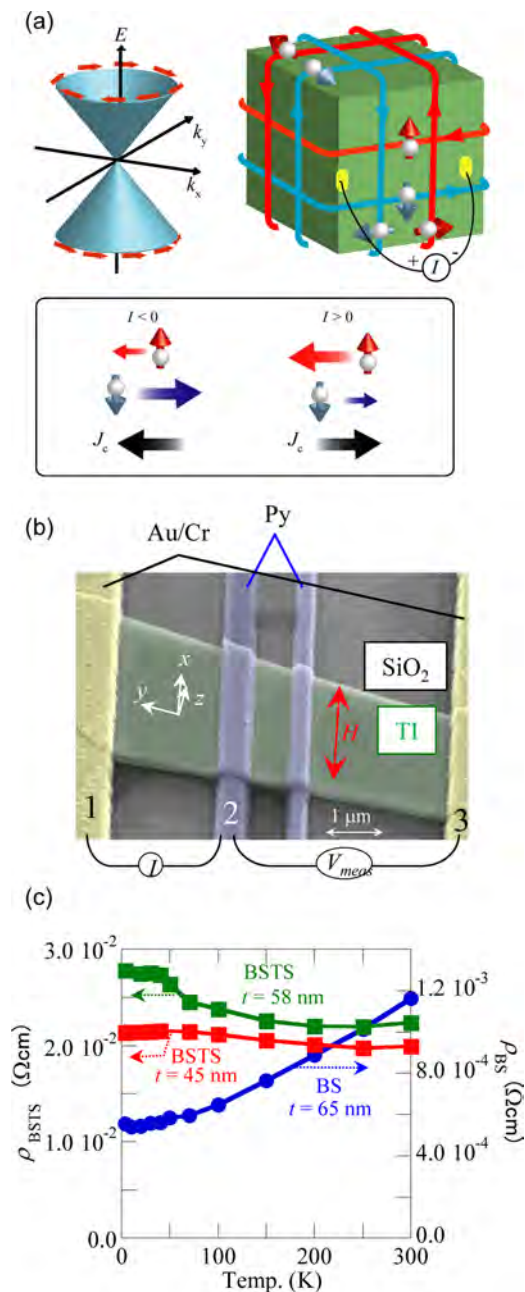


**Figure 1.** Device structure of TI-based spin devices and electrical properties of TI. (a) Schematic illustrations of the spin-momentum-locked surface state of 3D TIs: energy dispersion with the spin quantization axes shown by arrows (left); real-space image of the momentum direction and the spin quantization axes (right); relationship between charge and spin currents (bottom). (b) False-color SEM image of a typical TI device for the spin-dependent magnetoresistance measurements. (c) Temperature dependences of the resistivity of exfoliated BSTS and BS flakes.

**Fabrication of TI-Based Spin Devices.** Figure 1b shows a scanning electron microscope (SEM) image of a typical TI device. Single crystals of BSTS and BS were grown by a Bridgman method in evacuated quartz tubes.<sup>15,16</sup> Mechanically exfoliated TI flakes, with the thickness of several tens of nanometers, were put on a thermally oxidized SiO<sub>2</sub> (500 nm in thickness) layer formed on a Si substrate. The actual thickness of the TI flakes were measured by a combination of laser microscope and atomic force microscope. For magneto-

resistance measurements, two nonmagnetic Au/Cr electrodes and several Py electrodes were fabricated by using electron beam lithography and electron beam evaporation. The width of the Py electrodes was 500–800 nm. Charge currents are injected/extracted between a Au/Cr electrode and a Py electrode, which causes a spin accumulation at the TI/Py interface; it is because of the current-induced spin polarization in the TI surface due to the spin momentum locking. As a result, the interface resistance is expected to become dependent on the magnetization direction of the Py layer as well as the current direction. We also made standard Hall-bar devices with six nonmagnetic Au/Cr electrodes using the BSTS flakes on the same wafer, which were used for characterizing the resistivity of the TI channel in the magnetoresistance devices.

**Temperature Dependence of Resistivity of Exfoliated TI Channels.** The temperature dependences of the resistivity of three of our TI samples, whose cross-sectional area  $S = tw$  is given by the thickness  $t$  and the width  $w$  of the flakes, is shown in Figure 1c. The resistivity of the BSTS flakes,  $\rho_{\text{BSTS}}$ , used for this resistivity characterization are essentially reproducible and always presents weakly semiconducting behavior above  $\sim 50$  K, although the behavior at lower temperature was sample dependent, presumably due to different levels of disorder. Nevertheless, thanks to the topological protection of the surface state,<sup>18</sup> our BSTS samples always present plateau-like resistivity behavior at sufficiently low temperature [below  $\sim 75$  K (50 K) in the  $t = 45$  nm (58 nm) sample shown in Figure 1c]. The observed behavior is essentially the same as that in bulk BSTS crystals,<sup>15,16</sup> indicating that the electrical properties are maintained after exfoliation. In contrast, the resistivity of the BS flakes,  $\rho_{\text{BS}}$ , is much smaller than  $\rho_{\text{BSTS}}$  and presents metallic behavior throughout the measured temperature range, which comes from the dominance of the degenerate bulk transport channel<sup>12</sup> due to the Fermi level  $E_F$  located above the conduction band bottom.<sup>19</sup>

**Electrical Detection of the Spin Polarization in the Surface State of Bi<sub>1.5</sub>Sb<sub>0.5</sub>Te<sub>1.7</sub>Se<sub>1.3</sub>.** Magnetoresistance measurements were performed in a multiterminal scheme employing ferromagnetic contacts<sup>9,10</sup> to detect the spin polarization on the TI surface. In this scheme, a DC current  $I$  is applied between contacts 1 and 2, whereas the voltage is measured between contacts 2 and 3; because there is no current flow between contacts 2 and 3, this measurement reads only the voltage drop occurring at the contact 2,  $V_2$ , see Figure 1b.<sup>20–23</sup> When the contact 2 is made of a ferromagnet, a spin-dependent resistance can be detected through  $V_2$ , because the charge current in the TI surface state is spin polarized due to the spin-momentum locking. It is noted that magnetoresistance in this study is caused by spin polarized current injected into/extracted from TI surface state by means of an electric field, which is different from previous studies.<sup>11,12</sup> (see Supporting Information S1) The interfacial resistance  $R_2 (= V_2/I)$  as a function of the in-plane magnetic field  $H$  for a BSTS device (Device A) at  $I = 100$   $\mu\text{A}$ , measured at 4.2 K, is shown in Figure 2a. A rectangular hysteresis feature with steep resistance changes at  $\pm 150$  Oe can be recognized, as indicated by dotted arrows; here,  $R_2$  becomes higher when the magnetization of the Py electrode is aligned along the  $-x$  direction. Importantly, when the polarity of  $I$  is reversed, the pattern of the rectangular hysteresis feature reverses, as shown in Figure 2b, where  $R_2$  now becomes lower when the magnetization is aligned along the  $-x$  direction.



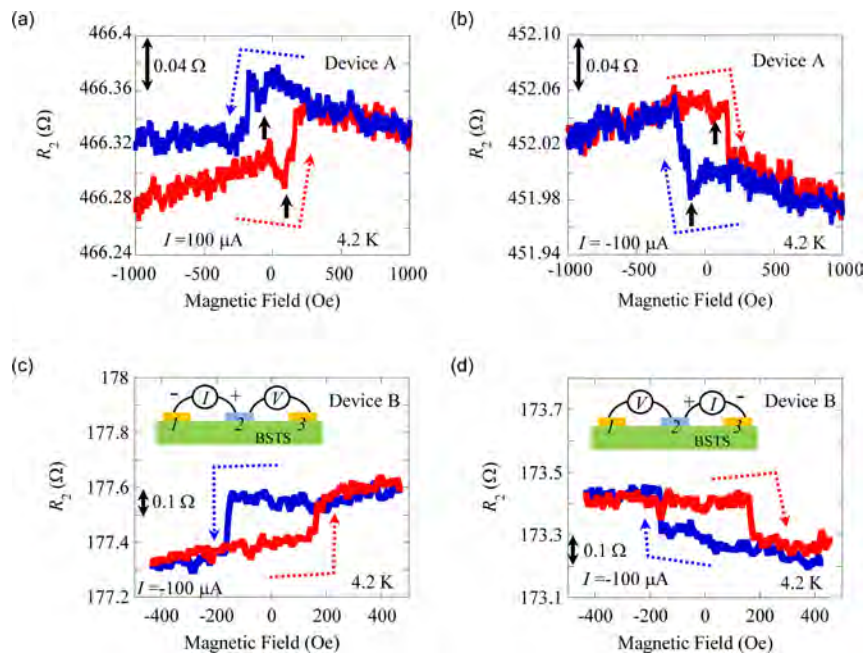


**Figure 2.** Electrical detection of the spin polarization in the surface state of  $\text{Bi}_{1.5}\text{Sb}_{0.5}\text{Te}_{1.7}\text{Se}_{1.3}$ . (a, b) Magnetic-field ( $H$ ) dependences of the interface resistance  $R_2$ , measured at 4.2 K in BSTS device A at bias currents of (a)  $+100 \mu\text{A}$  and (b)  $-100 \mu\text{A}$ ; the thickness of the BSTS flake was 34 nm. (c, d)  $R_2$  vs  $H$  curves for device B made with a 23 nm-thick BSTS flake, measured at 4.2 K for  $I = -100 \mu\text{A}$ . The charge current was applied from contact 2 to contact 1 in (c), and from contact 2 to contact 3 in (d).

Moreover, the reversal of the rectangular hysteresis feature is also observed when the current–voltage scheme is changed as shown in Figure 2c and d. Such a behavior indicates that the direction of the spin polarization reverses with the current direction, which is a natural consequence of the spin-momentum locking in the surface state. In this respect, it is important to note that the sign of the spin-dependent signal is consistent with the left-handed helicity of the topological surface state of BSTS above the Dirac point.<sup>4</sup> Furthermore, we have also measured  $R_2$  vs  $H$  for the case when  $H$  is parallel to the current. As shown in Figure S4 of the Supporting Information, the rectangular hysteresis is not observed in this geometry, which strongly supports our conclusion.

In passing, because the dip features marked by thick arrows in Figure 2a and b are attributed to the anisotropic magnetoresistance (AMR) of the Py electrode, one can be confident that the rectangular hysteresis feature is not due to the AMR effect of the Py electrode. This rectangular hysteresis behavior was reproduced in several BSTS devices. Therefore, it is reasonable to conclude that the charge-current-induced spin polarization is detected at the TI/ferromagnet interface in terms of a peculiar magnetoresistance feature.

**Temperature and Current Dependences of the Spin Signals.** The temperature dependence of the magnitude of the spin signal was also investigated in devices A and C. The  $R_2$  vs  $H$  curve measured at 300 K in device A at  $I = +100 \mu\text{A}$  is shown in Figure 3a. The rectangular hysteresis behavior has disappeared, whereas the AMR signal is kept being observed. In device C, neither the rectangular hysteresis nor the AMR signal was observed at 300 K [the inset of Figure 3b]; in fact, the temperature dependence of the magnitude of the spin signals,  $\Delta V_2$ , in device C [main panel of Figure 3b] indicates that  $\Delta V_2$  decreases monotonically with increasing temperature and vanishes at around 150 K. Although the bulk conduction usually becomes dominant at 300 K even in a bulk-insulating

TI, in our devices the fraction of the surface conductance in the total conductance is expected to be not reduced significantly because the total resistance of our BSTS flakes changes by less than a factor of 1.3 between 4.2 and 300 K. Also, it is useful to note that, whereas the entering into the surface-dominated transport regime occurs at 50–100 K in BSTS,<sup>15</sup>  $\Delta V_2$  keeps increasing with decreasing temperature even below 50 K [see Figure 3b]. Therefore, the disappearance of the spin signal in BSTS should be due to a mechanism other than the dominance of the bulk transport. In this regard, a possible origin is the reduction in the spin polarization of Py,<sup>24–26</sup> but it would be useful to test other ferromagnets or to insert a tunneling barrier for elucidating the key factor to prohibit the detection of the spin polarization at room temperature in the present devices. In passing, the difference in the observability of the AMR signal between samples A and C is most likely due to a difference in the shape of the Py electrode; remember, when a Py electrode is sharp and smooth, the shape magnetic anisotropy becomes stronger, which leads to a steep magnetization change. As a result, the AMR signal whose origin is resistance reduction when the magnetization direction is perpendicular to the charge-current direction is diminished.

The dependence of  $\Delta V_2$  on current  $I$  in the device B is shown in Figure 3c. One can see that the relationship is essentially linear. From the spin-charge coupled transport equations given by Burkov and Hawthorn,<sup>9</sup> magnetoresistance in the FM/TI surface state/NM structure is expressed as

$$\Delta V_2 = \frac{8\pi\hbar\eta I}{e^2 k_F w} \quad (1)$$

where  $\eta$  is the spin polarization of the injected/extracted current from the Py electrode,  $\hbar$  is the reduced Planck constant,  $e$  is the elementary charge,  $k_F$  is the Fermi wavenumber, and  $w$  is the width of the TI channel. Because  $\Delta V_2$  is proportional to  $I$  in eq 1, our result in Figure 3c is consistent with the theoretical

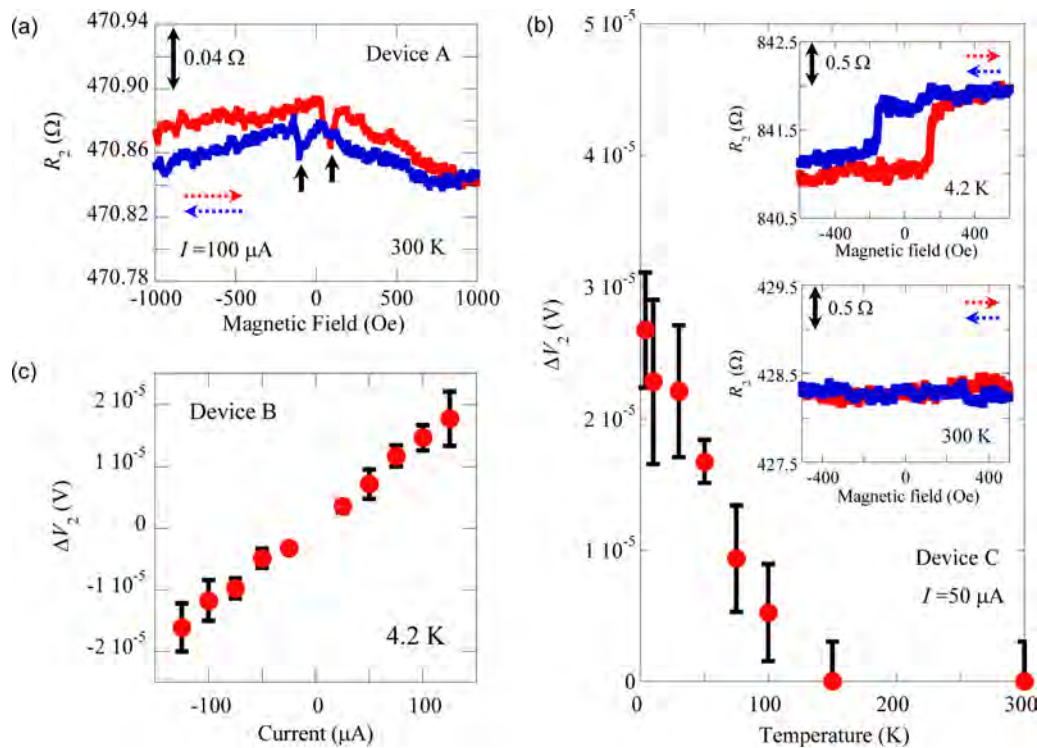


**Figure 3.** Temperature and current dependence of the spin signal. (a)  $R_2$  vs  $H$  curves of device A at  $I = +100 \mu\text{A}$  measured at 300 K. (b) Temperature dependence of  $\Delta V_2$  in device C (67 nm thick) at  $I = +50 \mu\text{A}$ . The upper and lower insets show  $R_2$  vs  $H$  curves measured at 4.2 and 300 K, respectively. (c)  $I$  dependence of the magnitude of the spin signal,  $\Delta V_2$ , of device B measured at 4.2 K.

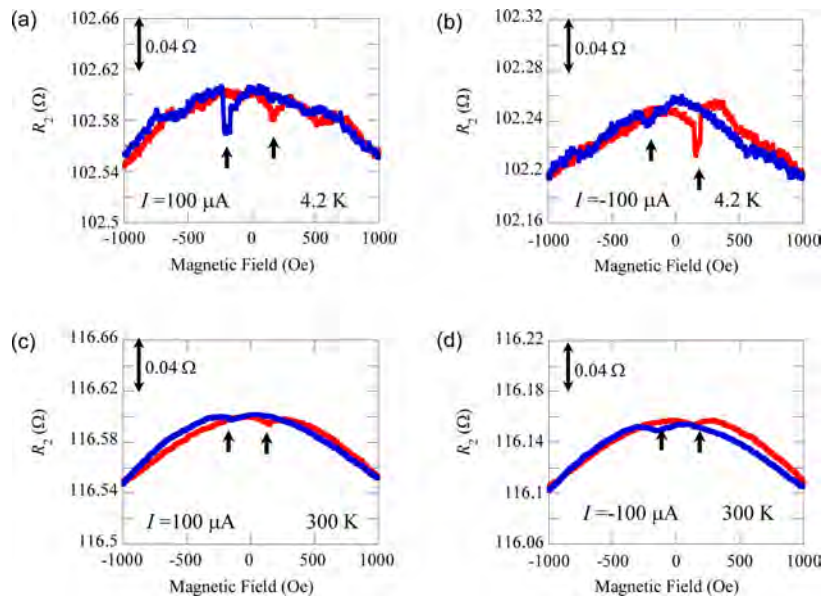


**Figure 4.** Magnetoresistance in  $\text{Bi}_2\text{Se}_3$ -based device.  $R_2$  vs  $H$  curves of a 72 nm-thick BS device measured at 4.2 K for (a)  $I = +100 \mu\text{A}$  and (b)  $I = -100 \mu\text{A}$ , and at 300 K for (c)  $I = +100 \mu\text{A}$  and (d)  $I = -100 \mu\text{A}$ , respectively.

expectation. When we use the value  $k_F \approx 0.1 \text{ \AA}^{-1}$  for BSTS,<sup>27</sup>  $\eta$  is calculated to be 0.05–0.5%. Such a small  $\eta$  is reasonably understood as a result of the conductance mismatch problem between the metallic Py electrode and the relatively high-resistance TI channel, which leads to a small magnetoresistance.<sup>28</sup> Note that a diffusive transport is assumed in the model used here, and the current-induced spin density in the TI surface state is given by  $I/(2ev_F)$ .<sup>9</sup>

As a control experiment, we also measured the magnetoresistance of many BS-based devices. The  $R_2$  vs  $H$  curves of a BS device measured at 4.2 and 300 K are shown in Figure 4a–d for both current polarities. One can see that no rectangular hysteresis feature was observed irrespective of the temperature, although AMR signals were observed at both low and high temperatures. Although the magnetoresistance measurements were performed for more than ten BS devices, no rectangular hysteresis signals were observed, which is due to the dominant

bulk conduction at all temperatures. Clearly, to observe a sizable spin-related signal in BS devices, the thickness should be less than 30 nm,<sup>11</sup> which is difficult to achieve with exfoliated flakes.

In summary, detection of the charge-current-induced spin polarization has been demonstrated by using the spin-dependent magnetoresistance at a TI/Py interface, for which the bulk-insulating TI Bi<sub>1.5</sub>Sb<sub>0.5</sub>Te<sub>1.7</sub>Se<sub>1.3</sub> was used for enhancing the fraction of the surface current. Control experiments using Bi<sub>2</sub>Se<sub>3</sub>-based devices have clarified the importance of the Fermi-level control for the electrical detection of the spin polarization in topological insulators.

## ■ ASSOCIATED CONTENT

### Supporting Information

Comparison between local and nonlocal magnetoresistance measurements. Charge current through the bottom and side surface. Magnetoresistance when the magnetic field is parallel to the current. This material is available free of charge via the Internet at <http://pubs.acs.org>.

## ■ AUTHOR INFORMATION

### Corresponding Authors

\*E-mail: ando@kuee.kyoto-u.ac.jp.

\*E-mail: y\_ando@sanken.osaka-u.ac.jp.

\*E-mail: mshiraishi@kuee.kyoto-u.ac.jp.

### Author Contributions

<sup>†</sup>These authors contributed equally

### Notes

The authors declare no competing financial interest.

## ■ ACKNOWLEDGMENTS

This work was supported by JSPS (KAKENHI No. 25220708), MEXT (Innovative Area “Topological Quantum Phenomena” KAKENHI Nos. 22103004 and 25103715 and Innovative Area “Nano Spin Conversion Science” KAKENHI No. 26103003), and AFOSR (AOARD 124038).

## ■ REFERENCES

- (1) Fu, L.; Kane, C. L.; Mele, E. J. *Phys. Rev. Lett.* **2007**, *98*, 106803.
- (2) Hsieh, D.; Qian, D.; Wray, L.; Xia, Y.; Hor, Y. S.; Cava, R. J.; Hasan, M. Z. *Nature* **2008**, *452*, 970–974.
- (3) Hasan, M. Z.; Kane, C. L. *Rev. Mod. Phys.* **2010**, *82*, 3045–3067.
- (4) Yoichi, Ando *J. Phys. Soc. Jpn.* **2013**, *82*, 102001.
- (5) Hsieh, D.; Xia, Y.; Wray, L.; Qian, D.; Pal, A.; Dil, J. H.; Osterwalder, J.; Meier, F.; Bihlmayer, G.; Kane, C. L.; Hor, Y. S.; Cava, R. J.; Hasan, M. Z. *Science* **2009**, *323*, 919–922.
- (6) Nishide, A.; Taskin, A. A.; Takeichi, Y.; Okuda, T.; Kakizaki, A.; Hirahara, T.; Nakatsuji, K.; Komori, F.; Ando, Y.; Matsuda, I. *Phys. Rev. B* **2010**, *81*, 041309.
- (7) Hsieh, D.; Xia, Y.; Qian, D.; Wray, L.; Dil, J. H.; Meier, F.; Osterwalder, J.; Patthey, L.; Checkelsky, J. G.; Ong, N. P.; Fedorov, A. V.; Lin, H.; Bansil, A.; Grauer, D.; Hor, Y. S.; Cava, R. J.; Hasan, M. Z. *Nature* **2009**, *460*, 1101–1105.
- (8) Souma, S.; Kosaka, K.; Sato, T.; Komatsu, M.; Takayama, A.; Takahashi, T.; Kriener, M.; Kouji, Segawa; Ando, Yoichi *Phys. Rev. Lett.* **2011**, *106*, 216803.
- (9) Burkov, A. A.; Hawthorn, D. G. *Phys. Rev. Lett.* **2010**, *105*, 066802.
- (10) Hong, S.; Diep, V.; Datta, S.; Chen, Y. P. *Phys. Rev. B* **2012**, *86*, 085131.
- (11) Li, C. H.; van't Erve, O. M.; Robinson, J. T.; Liu, Y.; Li, L.; Jonker, B. T. *Nat. Nanotechnol.* **2014**, *9*, 218–224.
- (12) Shiomi, Y.; Nomura, K.; Kajiura, Y.; Eto, K.; Novak, M.; Segawa, Kouji; Ando, Yoichi; Saitoh, E. *Phys. Rev. Lett.* **2013**, in press.
- (13) Mellnik, A. R.; Lee, J. S.; Richardella, A.; Grab, J. L.; Mintun, P. J.; Fischer, M. H.; Vaezi, A.; Manchon, A.; Kim, E.-A.; Samarth, N.; Ralph, D. C. *Nature* **2014**, *511*, 449–451.
- (14) Tang, J.; Chang, L.-T.; Kou, X.; Murata, K.; Choi, E. S.; Lang, M.; Fan, Y.; Jiang, Y.; Montazeri, M.; Jiang, W.; Wang, Y.; He, L.; Wang, K. L. *Nano Lett.* **2014**, *14*, 5423–5429.
- (15) Taskin, A. A.; Ren, Zhi; Sasaki, Satoshi; Segawa, Kouji; Ando, Yoichi *Phys. Rev. Lett.* **2011**, *107*, 016801.
- (16) Ren, Z.; Taskin, A. A.; Sasaki, S.; Segawa, K.; Ando, Yoichi *Phys. Rev. B* **2011**, *84*, 165311.
- (17) Arakane, T.; Sato, T.; Souma, S.; Kosaka, K.; Nakayama, K.; Komatsu, M.; Takahashi, T.; Ren, Z.; Segawa, Kouji; Ando, Yoichi *Nat. Commun.* **2012**, *3*, 636.
- (18) Taskin, A. A.; Sasaki, S.; Segawa, K.; Ando, Y. *Phys. Rev. Lett.* **2012**, *109*, 066803.
- (19) Xia, Y.; Qian, D.; Hsieh, D.; Wray, L.; Pal, A.; Lin, H.; Bansil, A.; Grauer, D.; Hor, Y. S.; Cava, R. J.; Hasan, M. Z. *Nat. Phys.* **2009**, *5*, 398–402.
- (20) Dash, S. P.; Sharma, S.; Patel, R. S.; Jong, M. P.; Jansen, R. *Nature* **2009**, *462*, 491–494.
- (21) Sasaki, T.; Oikawa, T.; Shiraishi, M.; Suzuki, Y.; Noguchi, K. *Appl. Phys. Lett.* **2011**, *98*, 012508.
- (22) Ando, Y.; Maeda, Y.; Kasahara, K.; Yamada, S.; Masaki, K.; Hoshi, Y.; Sawano, K.; Izunome, K.; Sakai, A.; Miyao, M.; Hamaya, K. *Appl. Phys. Lett.* **2011**, *99*, 012113.
- (23) Ando, Y.; Kasahara, K.; Yamada, S.; Maeda, Y.; Hoshi, Y.; Sawano, K.; Miyao, M.; Hamaya, K. *Phys. Rev. B* **2012**, *85*, 035320.
- (24) Villamor, E.; Isasa, M.; Hueso, L. E.; Casanova, F. *Phys. Rev. B* **2013**, *88*, 184411.
- (25) Huiwen, J.; Allred, J. M.; Ni, N.; Tao, J.; Neupane, M.; Wray, A.; Xu, S.; Hasan, M. Z.; Cava, R. J. *Phys. Rev. B* **2012**, *85*, 165313.
- (26) Schmalhorst, J.; Thomas, A.; Kämmerer, S.; Schebaum, O.; Ebke, D.; Sacher, M. D.; Reiss, G.; Hütten, A.; Turchanin, A.; Götzhäuser, A.; Arenholz, E. *Phys. Rev. B* **2007**, *75*, 014403.
- (27) Kim, S.; Yoshizawa, S.; Ishida, Y.; Eto, K.; Segawa, K.; Ando, Y.; Shin, S.; Komori, F. *Phys. Rev. Lett.* **2014**, *112*, 136802.
- (28) Schmidt, G.; Ferrand, D.; Molenkamp, L. W.; Filip, A. T.; van Wees, B. J. *Phys. Rev. B* **2012**, *62*, 4790(R).



# Top gating of epitaxial $(\text{Bi}_{1-x}\text{Sb}_x)_2\text{Te}_3$ topological insulator thin films

Fan Yang, A. A. Taskin, Satoshi Sasaki, Kouji Segawa, Yasuhide Ohno, Kazuhiko Matsumoto, and Yoichi Ando<sup>a)</sup>

*Institute of Scientific and Industrial Research, Osaka University, Ibaraki, Osaka 567-0047, Japan*

(Received 18 February 2014; accepted 13 April 2014; published online 25 April 2014)

The tunability of the chemical potential for a wide range encompassing the Dirac point is important for many future devices based on topological insulators. Here, we report a method to fabricate highly efficient top gates on epitaxially grown  $(\text{Bi}_{1-x}\text{Sb}_x)_2\text{Te}_3$  topological insulator thin films without degrading the film quality. By combining an *in situ* deposited  $\text{Al}_2\text{O}_3$  capping layer and a  $\text{SiN}_x$  dielectric layer deposited at low temperature, we were able to protect the films from degradation during the fabrication processes. We demonstrate that by using this top gate, the carriers in the top surface can be efficiently tuned from *n*- to *p*-type. We also show that magnetotransport properties give evidence for decoupled transport through top and bottom surfaces for the entire range of gate voltage, which is only possible in truly bulk-insulating samples. © 2014 AIP Publishing LLC. [<http://dx.doi.org/10.1063/1.4873397>]

Topological insulators (TIs) are a class of insulators possessing an energy gap in the bulk and helically spin-polarized gapless states on the surface.<sup>1–3</sup> In the last few years, great efforts and progress have been made to synthesize high-quality, bulk-insulating TI materials in various ways.<sup>4–13</sup> As the materials issues being solved, the focus and interest of experimentalists start to shift to the realization of the theoretically proposed TI devices for applications ranging from spintronics to quantum computing.<sup>1–3</sup> For such devices, an efficient gate control to tune the Fermi level in a wide range is usually essential, and already many gating experiments have been done on TI materials by using different gating techniques.<sup>12–20</sup> Among the various gating techniques, top gating has an advantage to provide local control of the chemical potential, which is favorable in many applications. However, a damage-free method to fabricate efficient top gates on TIs has not yet been fully developed.

To achieve efficient top-gate controls of TI materials, there are two main difficulties. One is to obtain bulk-insulating samples, because the unwanted bulk carriers bring the Fermi level far away from the Dirac point and screen the electric field. This difficulty is being solved by means of chemical doping, in both single crystals<sup>4–10,12,13</sup> and thin films.<sup>11</sup> The other difficulty is the degradations of the sample surface during the fabrication processes, especially during the deposition of the dielectric material. It has been shown that the usual methods to deposit dielectric materials such as atomic layer deposition (ALD) can cause heavy damage to the TI surface;<sup>15</sup> such a damage would lower the surface mobility and also introduce a large number of impurity states to pin the surface chemical potential, making its gate tuning to be difficult.<sup>15</sup> It is thus important to develop a method to fabricate top gates with minimal damage to the TI surface.

In this Letter, we report our top-gating results on  $(\text{Bi}_{1-x}\text{Sb}_x)_2\text{Te}_3$  topological-insulator thin films grown by molecular beam epitaxy (MBE). Following Ref. 11, the composition of the films was optimized for achieving the bulk-insulating state. We show that a combination of an

*in situ* deposited  $\text{Al}_2\text{O}_3$  capping layer and a 200-nm-thick  $\text{SiN}_x$  dielectric layer deposited by the hot-wire chemical vapor deposition (CVD) technique at  $<80^\circ\text{C}$  makes it possible to fabricate nearly damage-free top gate, with which an efficient ambipolar gating is possible. The mobility and carrier density of both top and bottom surfaces were estimated by fitting the magnetic-field dependences of the Hall resistivity,  $R_{yx}(B)$ , to the two-band model for a range of gate voltage  $V_g$ . The mobility of the top surface,  $700\text{--}1300\text{ cm}^2\text{ V}^{-1}\text{ s}^{-1}$  depending on  $V_g$ , is found to be always higher than that of the bottom surface. The weak antilocalization (WAL) effect was observed in the entire range of  $V_g$  and its analysis allows us to conclude that the top and bottom surfaces are always decoupled in our films irrespective of  $V_g$ . Our top gating technique is useful for realizing TI devices that require both the local control of the chemical potential encompassing the Dirac point and a high mobility of the surface state.

The  $(\text{Bi}_{1-x}\text{Sb}_x)_2\text{Te}_3$  thin films were grown on sapphire (0001) substrates. In this work, the thickness was fixed at 20 nm, for which the optimized flux ratio between Bi and Sb to obtain bulk-insulating films was 0.15. After the growth, the sample was transferred to an attached electron-beam deposition chamber to deposit 4-nm-thick  $\text{Al}_2\text{O}_3$  capping layer, during which the sample holder was cooled by running water to keep the sample temperature below  $100^\circ\text{C}$ . The inset of Fig. 1(b) is an atomic force microscope (AFM) image of a typical film used in this experiment, a 20-nm-thick  $(\text{Bi}_{1-x}\text{Sb}_x)_2\text{Te}_3$  film capped with a 4-nm-thick  $\text{Al}_2\text{O}_3$  capping layer. One can see atomically flat triangles with sharp edges, indicating that the  $\text{Al}_2\text{O}_3$  layer is uniformly deposited. The step height at the edge of each triangle is about 1 nm, corresponding to the thickness of the growth unit (quintuple layer) of  $(\text{Bi}_{1-x}\text{Sb}_x)_2\text{Te}_3$ .

The films were fabricated into top-gated Hall-bar devices by five steps described in the following. All metal electrodes of the devices were made of 50-nm-thick Pd films deposited by magnetron sputtering.

The first step was to pattern the film into a Hall-bar shape with photolithography and wet etching. Following the wet-etching recipe for  $\text{Bi}_2\text{Te}_3$  films,<sup>23</sup> we etched our

<sup>a)</sup>Electronic mail: [y\\_ando@sanken.osaka-u.ac.jp](mailto:y_ando@sanken.osaka-u.ac.jp)



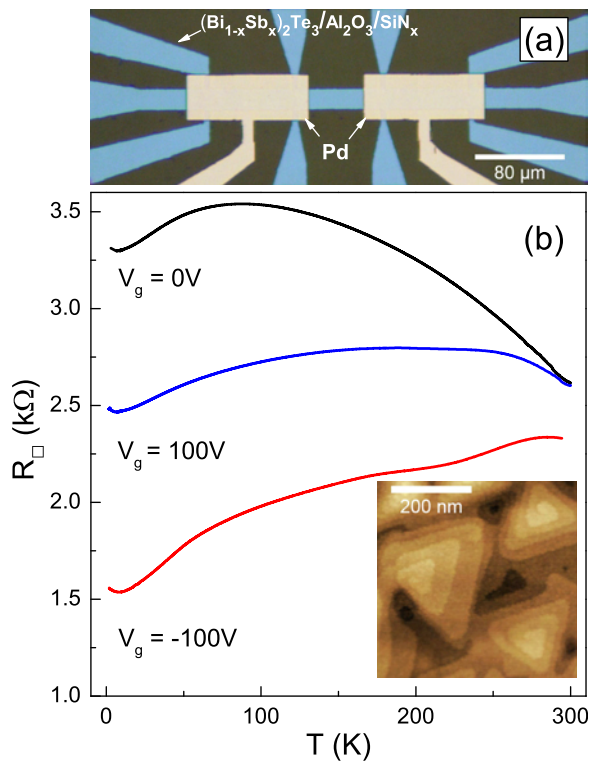


FIG. 1. (a) Optical microscope image of the device. (b) Temperature dependences of  $R_{\square}$ , taken at  $V_g = 100$  V, 0 V, and  $-100$  V. Inset: AFM image of a 20-nm-thick  $(\text{Bi}_{1-x}\text{Sb}_x)_2\text{Te}_3$  film capped with 4-nm-thick  $\text{Al}_2\text{O}_3$ .

$(\text{Bi}_{1-x}\text{Sb}_x)_2\text{Te}_3$  films by using the solution of 1 HCl: 0.8  $\text{H}_2\text{O}_2$ : 8  $\text{CH}_3\text{COOH}$ : 16  $\text{H}_2\text{O}$  (volume ratio); the mass concentrations of HCl,  $\text{H}_2\text{O}_2$ , and  $\text{CH}_3\text{COOH}$  used for making this etchant were 36%, 33%, and 99.7%, respectively. In the second step, the resist pattern for metal contacts was defined with photolithography, and the sample was dipped into 2.4% tetramethylammonium hydroxide solution for several minutes to remove the  $\text{Al}_2\text{O}_3$  capping layer in the contact area, followed by Pd deposition and lift-off. The third step was to deposit the dielectric layer for the top gates. A 200-nm-thick  $\text{SiN}_x$  layer was deposited by hot-wire CVD, during which the sample temperature was kept lower than  $80^\circ\text{C}$ ,<sup>24</sup> since there is no resist mask for this deposition, the  $\text{SiN}_x$  layer covers everywhere, including the Pd contacts on the arms of the Hall bar. The fourth step was thus to open a window in the  $\text{SiN}_x$  layer on the top of each Pd contact; this was done by photolithography and subsequent dry etching. In the final step, the top-gate electrodes were fabricated by photolithography, Pd deposition, and lift-off.

The measurements were performed in a  $^4\text{He}$  cryostat with a base temperature of 1.8 K, by using a standard lock-in technique. The excitation current was  $1\ \mu\text{A}$ . Using the Hall-bar-shaped samples as shown in Fig. 1(a), both the longitudinal sheet resistance  $R_{\square}$  and the Hall resistance  $R_{yx}$  were obtained by four terminal measurements, as a function of temperature  $T$  and magnetic field  $B$ . The gate voltage  $V_g$  was applied in the range of  $\pm 100$  V. When the gate voltage is cycled, we observed a hysteresis in both  $R_{\square}$  and  $R_{yx}$ ; this is probably due to impurity states that trap charges. Hence, to keep consistency in the data, all curves shown here were taken upon decreasing  $V_g$  from  $+100$  V to  $-100$  V.

Figure 1(b) shows the  $R_{\square}$  vs.  $T$  curves measured at three gate voltages. One can see that the effect of top gating on the  $R_{\square}(T)$  behavior is large; in particular,  $R_{\square}$  changes by more than a factor of two at low temperature. One may notice that there is a weak upturn in all three curves at the lowest temperatures; such an upturn has been reported for TI thin films in the past,<sup>25–27</sup> and is discussed to be due to electron interaction effects.<sup>28,29</sup>

The  $R_{yx}(B)$  curves showed significant and complicated changes when  $V_g$  is varied. In Fig. 2, to present its changes in an comprehensible manner, we divide the  $R_{yx}(B)$  curves measured at various  $V_g$  values into three groups [Figs. 2(a)–2(c)] and discuss them separately:

In the first group [Fig. 2(a)], the slopes of the curves are negative, corresponding to  $n$ -type carriers. The negative slope increases with decreasing  $V_g$ , becoming the steepest at  $V_g = 26$  V. Hence, in this regime the number of mobile electrons decreases as  $V_g$  is reduced. Below  $V_g = 50$  V, the  $R_{yx}(B)$  curves start to show nonlinearity.

In the second group [Fig. 2(b)], while the dominant carriers are still  $n$ -type, the slope now decreases with decreasing  $V_g$ , and the  $R_{yx}(B)$  curves become more nonlinear at lower  $V_g$ . This suggests that the chemical potential of the top surface is lowered sufficiently to cross the Dirac point and  $p$ -type carriers start to show up on the top surface; on the other hand, the bottom surface, which feels screened electric field and is less sensitive to  $V_g$ , still harbors  $n$ -type carriers.

In the third group [Fig. 2(c)], as  $V_g$  is lowered into large negative values, the slope of  $R_{yx}(B)$  changes from negative to positive, indicating a switchover in the dominant carrier type. In this regime, the density of  $p$ -type carriers in the top surface steadily increases with decreasing  $V_g$ , causing the whole  $R_{yx}(B)$  curve to show positive slope at  $V_g = -100$  V.

The  $V_g$  dependences of the Hall coefficient  $R_H$  and  $R_{\square}$  are summarized in Fig. 2(d). Since the  $R_{yx}(B)$  curves were nonlinear in the majority of the  $V_g$  range, we define the slopes of  $R_{yx}(B)$  at  $B = 0$  and  $8.9$  T as the  $R_H$  values at those fields. The insets in Fig. 2(d) depict the location of the chemical potential at the top and bottom surfaces for different  $V_g$  regimes. At high positive and negative gate voltages, the carrier type of the top surface is  $n$  and  $p$ , respectively. However, at  $V_g = 26$  V,  $|R_H|$  reaches a maximum, meaning that the number of mobile carriers becomes minimal at this  $V_g$ ; such a behavior is expected when the Fermi level of the top surface hits the Dirac point. The peak in  $R_{\square}$  is located at  $V_g = 13$  V, which is a little different from the maximum position of  $|R_H|$ . Such a behavior is frequently reported in gating results of TIs<sup>16,17,20</sup> and is likely to be due to a difference in the mobility of the carriers in the top and bottom surfaces.

The observed ambipolar gating suggests that the chemical potential in our sample is located within the bulk band gap in the majority of the  $V_g$  range, where the main contribution to the transport comes from the two surfaces channels. Therefore, one would expect that the two-band model<sup>3</sup> to consider two independent surface channels would describe the  $R_{yx}(B)$  behavior. Indeed, as we show below, for the  $V_g$  range of  $0$ – $50$  V, the fitting of the  $R_{yx}(B)$  data to the two-band model gives reasonable and consistent parameters for the two surfaces, which reconfirms that it is not necessary to consider an additional bulk channel. It should be noted,

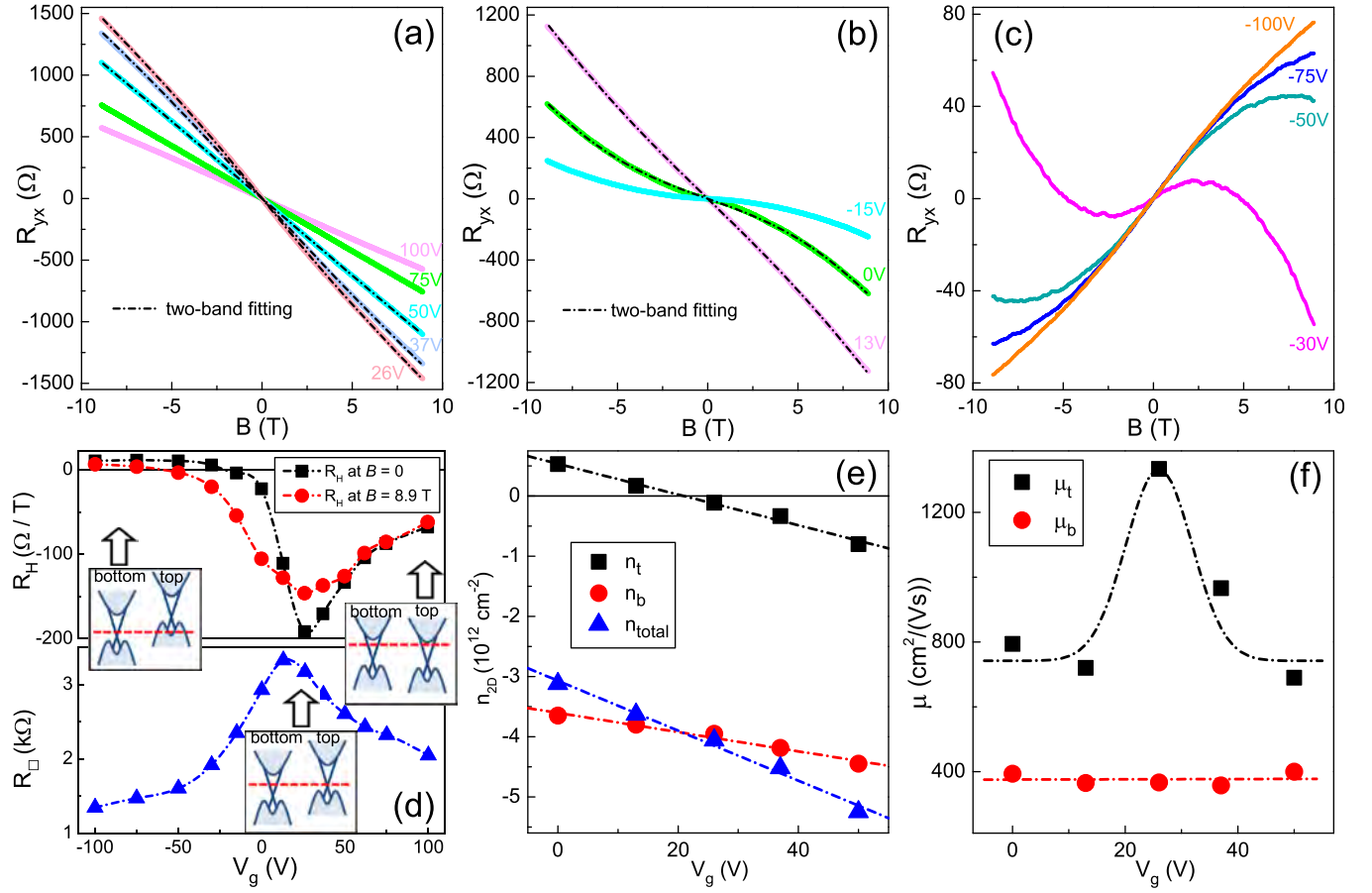


FIG. 2. (a)–(c)  $R_{yx}$  vs.  $B$  data at different  $V_g$  values. The dashed-dotted lines in (a) and (b) show fittings to the two-band model. (d)  $V_g$  dependence of  $R_H$  (upper panel) and  $R_□$  (lower panel). The insets are schematic band diagrams for three characteristic regimes. (e) Sheet carrier density vs.  $V_g$  for the top ( $n_t$ ) and bottom ( $n_b$ ) channels, as well as their sum ( $n_{total}$ ). (f) Mobility vs.  $V_g$  for top and bottom surfaces. The data in (e) and (f) are the results of the two-band analysis.

however, that at large positive  $V_g$  values, the  $R_{yx}(B)$  curves becomes essentially linear and featureless, which prohibits us from extracting reliable information from the two-band analysis. Also, since the top of the bulk valence band is located close to the Dirac point,<sup>11</sup> at negative  $V_g$  values the Fermi level at the top surface is brought into the bulk valence band, causing the top surface to harbor conventional inversion layer (topologically trivial two-dimensional states with  $p$ -type carriers) alongside the  $p$ -type Dirac fermions; this causes the transport to occur through three channels, and one should not apply the two-band analysis for  $V_g \leq 0$ .

In the two-band model,<sup>3</sup> the composite Hall resistivity is given as

$$R_{yx}(B) = \left(\frac{B}{e}\right) \frac{(n_t \mu_t^2 + n_b \mu_b^2) + B^2 \mu_t^2 \mu_b^2 (n_t + n_b)}{(n_t \mu_t + n_b \mu_b)^2 + B^2 \mu_t^2 \mu_b^2 (n_t + n_b)^2}, \quad (1)$$

where  $n_t$ ,  $n_b$ ,  $\mu_t$ ,  $\mu_b$  correspond to the sheet carrier densities and mobilities of the top and bottom surfaces. Although there are four fitting parameters, one can put a constraint that the observed zero-field sheet resistance  $R_□|_{B=0}$  must be consistent with  $1/(en_t \mu_t + en_b \mu_b)$ , which reduces the number of free parameters to three.<sup>3</sup>

The fittings of the data for  $V_g = 0$ –50 V to Eq. (1) are shown in Figs. 2(a) and 2(b), and the obtained parameters are shown in Figs. 2(e) and 2(f). One can see that both  $n_t$  and  $n_b$  present linear  $V_g$  dependences, and the slope is larger for

$n_t(V_g)$  (i.e., the top surface is more efficiently gated), which is reasonable and reassures our assumption of two transport channels. The sign change in  $n_t$  at  $V_g \approx 26$  V indicates that the Fermi level of the top surface hits the Dirac point at this  $V_g$ .

In Fig. 2(f), one can see that  $\mu_t$  presents a peak value of  $1300 \text{ cm}^2 \text{ V}^{-1} \text{ s}^{-1}$  near the Dirac point, and elsewhere  $\mu_t$  remains around  $750 \text{ cm}^2 \text{ V}^{-1} \text{ s}^{-1}$ . Such an enhancement of the mobility near the Dirac point is often observed in graphene and is due to the vanishing of the phase space available for scattering.<sup>30,31</sup> One may also notice that the bottom-surface mobility  $\mu_b \approx 375 \text{ cm}^2 \text{ V}^{-1} \text{ s}^{-1}$  is much lower than  $\mu_t$ , meaning that the electron scattering is stronger at the interface with sapphire substrate than at the interface with  $\text{Al}_2\text{O}_3$  capping layer. We have also measured the  $R_{yx}(B)$  curves in capping-layer free  $(\text{Bi}_{1-x}\text{Sb}_x)_2\text{Te}_3$  films without any patterning nor gate fabrication, and in such pristine films,  $\mu_t$  was found to be typically  $\sim 800 \text{ cm}^2 \text{ V}^{-1} \text{ s}^{-1}$ . This indicates that the  $\text{Al}_2\text{O}_3$  capping layer is indeed effective in keeping the top-surface mobility from degradation. In passing, we observed that the capping layer tends to dope  $p$ -type carriers to the surface, causing the top surface band to be slightly bent up.

Now, we discuss the WAL effect in our films to see if the top and bottom surfaces are decoupled. In Figs. 3(a) and 3(b), we plot the magnetoresistance  $\Delta R_□(B) [\equiv R_□(B) - R_□|_{B=0}]$  for various  $V_g$  values, and the curves are divided into two groups. In the first group [Fig. 3(a)], the

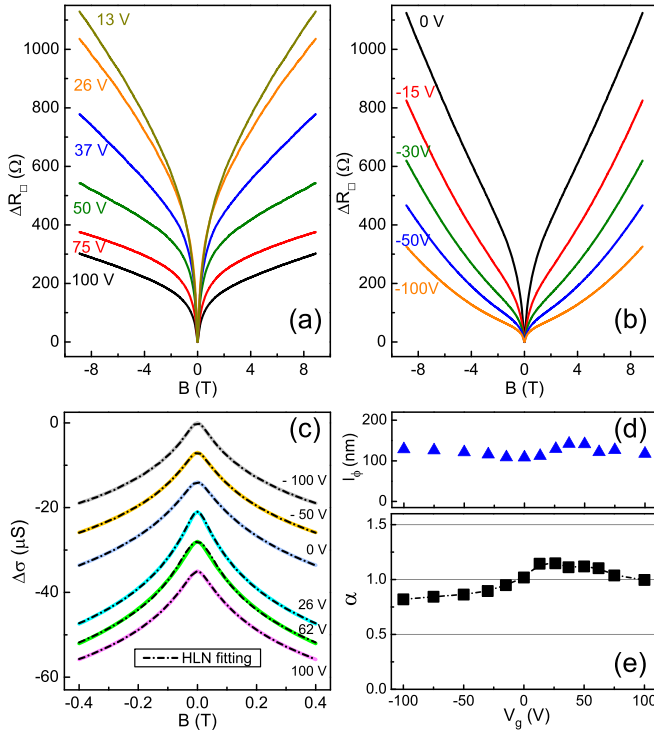


FIG. 3. (a) and (b) Magnetoresistance at different gate voltages; (a) is for  $V_g \geq 13$  V and (b) is for  $V_g \leq 0$  V. (c) Magnetoconductance at representative  $V_g$  values; the curves are shifted vertically for clarity. The dashed-dotted lines are the fittings to Eq. (2). (d) and (e)  $V_g$  dependences of (d)  $l_\phi$  and (e)  $\alpha$  obtained from the fittings.

magnetoresistance presents negative curvature throughout the magnetic-field range, while in the second group [Fig. 3(b)] the magnetoresistance seems to contain a parabolic background. Since the boundary between the two groups is  $V_g = 13$  V, where  $R_{\square}$  reaches the maximum, the change in the background in the magnetoresistance appears to be correlated with the change in the carrier type. However, the origin of this intriguing behavior is not known at the moment.

Despite the change in the high-magnetic-field background, the cusp structure in the low-magnetic-field part of  $R_{\square}(B)$  can always be reliably analyzed as the WAL behavior. The WAL in TIs has been intensively studied both theoretically<sup>32,33</sup> and experimentally.<sup>16,17,21,22,34–36</sup> The peculiar magnetic-field dependence of the electrical conductivity  $\sigma$  associated with WAL is described by the simplified Hikami-Larkin-Nagaoka (HLN) formula

$$\Delta\sigma(B) = -\alpha \frac{e^2}{\pi h} \left[ \Psi\left(\frac{1}{2} + \frac{\hbar}{4e l_\phi^2 B}\right) - \ln\left(\frac{\hbar}{4e l_\phi^2 B}\right) \right], \quad (2)$$

where  $\Psi(x)$  is the digamma function and  $l_\phi$  is the phase coherence length. The parameter  $\alpha$  is presumably 0.5 when there is only one transport channel, and it is doubled when there are two channels. We have calculated  $\sigma(B)$  from the data of  $R_{\square}(B)$  and  $R_{xx}(B)$  to do the proper matrix inversion.

As shown in Fig. 3(c) for representative  $V_g$  values, all the  $\Delta\sigma(B)$  curves are well fitted with the HLN formula. The parameters extracted from the fittings are plotted in Figs. 3(d) and 3(e). The  $l_\phi$  value [Fig. 3(d)] is essentially independent of  $V_g$ , and its average value of  $\sim 120$  nm is much

larger than the film thickness. More importantly, the  $\alpha$  value [Fig. 3(e)] is found to be close to 1 throughout our  $V_g$  range,<sup>37</sup> pointing to the existence of two independent channels that are presumably the top and bottom surfaces. It has been elucidated that in TI thin films, residual bulk carriers couple the top and bottom surfaces through the bulk to produce a single diffusive transport channel for the WAL effect, which results in the  $\alpha$  value of 0.5.<sup>14,16,17,35</sup> The  $\alpha$  value close to 1 has been observed only in two situations: (i) a depletion layer is formed in the film due to a strong band bending at high gate voltages to electrically isolate the gated surface,<sup>16,17</sup> or (ii) films are relatively thick (which avoids the hybridization of the top and bottom surface states) and bulk carriers are negligible.<sup>35</sup> In this regard, the  $\alpha$  value in our film is nearly independent of  $V_g$ , which rules out the former possibility and points to the latter. Thus, the analysis of the WAL behavior corroborates the conclusion that our films are truly bulk-insulating.

In summary, we developed a damage-free method to fabricate efficient top gates on  $(\text{Bi}_{1-x}\text{Sb}_x)_2\text{Te}_3$  topological-insulator thin films. The carrier type in the top surface can be tuned from  $n$  to  $p$ , and their mobility reaches  $1300 \text{ cm}^2 \text{ V}^{-1} \text{ s}^{-1}$  near the Dirac point. The magnetotransport properties give evidence that our films are bulk insulating with decoupled top and bottom surfaces. The top gating method developed here would be useful for the realization of future devices based on TIs.

We acknowledge M. Kishi for technical assistance and Nanotechnology Open Facilities in Osaka University for nano-fabrication facilities. This work was supported by JSPS (KAKENHI Nos. 24740237, 24540320, 25400328, and 25220708), MEXT (Innovative Area “Topological Quantum Phenomena” KAKENHI), and AFOSR (AOARD 124038).

<sup>1</sup>M. Z. Hasan and C. L. Kane, *Rev. Mod. Phys.* **82**, 3045 (2010).

<sup>2</sup>X. L. Qi and S. C. Zhang, *Rev. Mod. Phys.* **83**, 1057 (2011).

<sup>3</sup>Y. Ando, *J. Phys. Soc. Jpn.* **82**, 102001 (2013).

<sup>4</sup>Y. L. Chen, J. G. Analytis, J. H. Chu, Z. K. Liu, S. K. Mo, X. L. Qi, H. J. Zhang, D. H. Lu, X. Dai, Z. Fang, S. C. Zhang, I. R. Fisher, Z. Hussain, and Z. X. Shen, *Science* **325**, 178 (2009).

<sup>5</sup>D. Hsieh, Y. Xia, D. Qian, L. Wray, J. H. Dil, F. Meier, J. Osterwalder, L. Patthey, J. G. Checkelsky, N. P. Ong, A. V. Fedorov, H. Lin, A. Bansil, D. Grauer, Y. S. Hor, R. J. Cava, and M. Z. Hasan, *Nature (London)* **460**, 1101 (2009).

<sup>6</sup>Z. Ren, A. A. Taskin, S. Sasaki, K. Segawa, and Y. Ando, *Phys. Rev. B* **82**, 241306 (2010).

<sup>7</sup>Z. Ren, A. A. Taskin, S. Sasaki, K. Segawa, and Y. Ando, *Phys. Rev. B* **84**, 165311 (2011).

<sup>8</sup>A. A. Taskin, Z. Ren, S. Sasaki, K. Segawa, and Y. Ando, *Phys. Rev. Lett.* **107**, 016801 (2011).

<sup>9</sup>Z. Ren, A. A. Taskin, S. Sasaki, K. Segawa, and Y. Ando, *Phys. Rev. B* **85**, 155301 (2012).

<sup>10</sup>S. S. Hong, J. J. Cha, D. Kong, and Y. Cui, *Nat. Commun.* **3**, 757 (2012).

<sup>11</sup>J. S. Zhang, C. Z. Chang, Z. C. Zhang, J. Wen, X. Feng, K. Li, M. H. Liu, K. He, L. L. Wang, X. Chen, Q. K. Xue, X. C. Ma, and Y. Y. Wang, *Nat. Commun.* **2**, 574 (2011).

<sup>12</sup>J. G. Checkelsky, Y. S. Hor, R. J. Cava, and N. P. Ong, *Phys. Rev. Lett.* **106**, 196801 (2011).

<sup>13</sup>D. Kong, Y. Chen, J. J. Cha, Q. Zhang, J. G. Analytis, K. Lai, Z. Liu, S. S. Hong, K. J. Koski, S.-K. Mo, Z. Hussain, I. R. Fisher, Z. X. Shen, and Y. Cui, *Nat. Nanotechnol.* **6**, 705 (2011).

<sup>14</sup>J. Chen, H. J. Qin, F. Yang, J. Liu, T. Guan, F. M. Qu, G. H. Zhang, J. R. Shi, X. C. Xie, C. L. Yang, K. H. Wu, Y. Q. Li, and L. Lu, *Phys. Rev. Lett.* **105**, 176602 (2010).

<sup>15</sup>H. Liu and P. D. Ye, *Appl. Phys. Lett.* **99**, 052108 (2011).

- <sup>16</sup>J. Chen, X. Y. He, K. H. Wu, Z. Q. Ji, L. Lu, J. R. Shi, J. H. Smet, and Y. Q. Li, *Phys. Rev. B* **83**, 241304 (2011).
- <sup>17</sup>H. Steinberg, J. B. Laloč, V. Fatemi, J. S. Moodera, and P. Jarillo-Herrero, *Phys. Rev. B* **84**, 233101 (2011).
- <sup>18</sup>M. R. Lang, L. He, F. X. Xiu, X. X. Yu, J. S. Tang, Y. Wang, X. F. Kou, W. J. Jiang, A. V. Fedorov, and K. L. Wang, *ACS Nano* **6**, 295 (2012).
- <sup>19</sup>D. Kim, S. Cho, N. P. Butch, P. Syers, K. Kirshenbaum, S. Adam, J. Paglione, and M. S. Fuhrer, *Nat. Phys.* **8**, 460 (2012).
- <sup>20</sup>X. Y. He, T. Guan, X. X. Wang, B. J. Feng, P. Cheng, L. Chen, Y. Q. Li, and K. H. Wu, *Appl. Phys. Lett.* **101**, 123111 (2012).
- <sup>21</sup>J. Lee, J. Park, J. H. Lee, J. S. Kim, and H. J. Lee, *Phys. Rev. B* **86**, 245321 (2012).
- <sup>22</sup>B. Xia, P. Ren, A. Sulaev, P. Liu, S. Q. Shen, and L. Wang, *Phys. Rev. B* **87**, 085442 (2013).
- <sup>23</sup>T. Ngai and U. Ghoshal, paper presented at the 26th International Conference on Thermoelectrics, Jeju, Korea, 2007.
- <sup>24</sup>K. Maehashi, Y. Ohno, K. Inoue, K. Matsumoto, T. Niki, and H. Matsumura, *Appl. Phys. Lett.* **92**, 183111 (2008).
- <sup>25</sup>M. H. Liu, C. Z. Chang, Z. C. Zhang, Y. Zhang, W. Ruan, K. He, L. L. Wang, X. Chen, J. F. Jia, S. C. Zhang, Q. K. Xue, X. C. Ma, and Y. Y. Wang, *Phys. Rev. B* **83**, 165440 (2011).
- <sup>26</sup>J. Wang, A. M. DaSilva, C. Z. Chang, K. He, J. K. Jain, N. Samarth, X. C. Ma, Q. K. Xue, and M. H. W. Chan, *Phys. Rev. B* **83**, 245438 (2011).
- <sup>27</sup>Y. Takagaki, B. Jenichen, U. Jahn, M. Ramsteiner, and K. J. Friedland, *Phys. Rev. B* **85**, 115314 (2012).
- <sup>28</sup>H. K. Pal, V. I. Yudson, and D. L. Maslov, *Phys. Rev. B* **85**, 085439 (2012).
- <sup>29</sup>E. J. König, P. M. Ostrovsky, I. V. Protopopov, I. V. Gornyi, I. S. Burmistrov, and A. D. Mirlin, *Phys. Rev. B* **88**, 035106 (2013).
- <sup>30</sup>Y. B. Zhang, Y. W. Tan, H. L. Stormer, and P. Kim, *Nature* **438**, 201 (2005).
- <sup>31</sup>K. I. Bolotin, K. J. Sikes, Z. Jiang, M. Klima, G. Fudenberg, J. Hone, P. Kim, and H. L. Stormer, *Solid State Commun.* **146**, 351 (2008).
- <sup>32</sup>H. Z. Lu and S. Q. Shen, *Phys. Rev. B* **84**, 125138 (2011).
- <sup>33</sup>I. Garate and L. Glazman, *Phys. Rev. B* **86**, 035422 (2012).
- <sup>34</sup>H. T. He, G. Wang, T. Zhang, I. K. Sou, G. K. L. Wong, J. N. Wang, H. Z. Lu, S. Q. Shen, and F. C. Zhang, *Phys. Rev. Lett.* **106**, 166805 (2011).
- <sup>35</sup>D. Kim, P. Syers, N. P. Butch, J. Paglione, and M. S. Fuhrer, *Nat. Commun.* **4**, 2040 (2013).
- <sup>36</sup>L. Zhang, M. Dolev, Q. I. Yang, R. H. Hammond, B. Zhou, A. Palevski, Y. L. Chen, and A. Kapitulnik, *Phys. Rev. B* **88**, 121103 (2013).
- <sup>37</sup>Following Ref. 26, one can estimate the possible impact of the electron interaction effects on the WAL analysis; in our case, the screening parameter  $\tilde{F}_\sigma$  estimated from the  $\sigma(T)$  behavior is only  $\sim 0.1$ , introducing an error in  $\alpha$  of only up to 10%.



# Superconductor derived from a topological insulator heterostructure

Satoshi Sasaki, Kouji Segawa, and Yoichi Ando\*

*Institute of Scientific and Industrial Research, Osaka University, Ibaraki, Osaka 567-0047, Japan*

(Received 7 April 2014; revised manuscript received 19 November 2014; published 1 December 2014)

Topological superconductors (TSCs) are of significant current interest because they offer promising platforms for finding Majorana fermions. Here we report on a superconductor synthesized by intercalating Cu into a naturally formed topological insulator (TI) heterostructure consisting of  $\text{Bi}_2\text{Se}_3$  TI units separated by nontopological  $\text{PbSe}$  units. Interestingly, in this TI-based superconductor, the specific-heat behavior suggests the occurrence of unconventional superconductivity with gap nodes. The existence of gap nodes in a strongly spin-orbit coupled superconductor would give rise to spin-split Andreev bound states that are the hallmark of topological superconductivity. Hence, this superconductor emerges as an intriguing candidate TSC.

DOI: [10.1103/PhysRevB.90.220504](https://doi.org/10.1103/PhysRevB.90.220504)

PACS number(s): 74.10.+v, 74.25.Bt, 74.70.Dd, 74.78.Fk

A major theme in current condensed matter physics is to understand and explore the roles of topology in quantum mechanics. In topological insulators (TIs), a nontrivial topology of the quantum-mechanical wave functions leads to the appearance of gapless conducting states at the boundary (i.e., edge or surface) [1–3]. Topological superconductors (TSCs) are conceptually similar to TIs and are characterized by gapless quasiparticle states at the boundary [1,4–6], but an important distinction from TIs is that the boundary state of a TSC is a good place to look for Majorana fermions [7–9], which possess a distinct property that particles are their own antiparticles and would be useful for fault-tolerant topological quantum computing. In this context, superconductors derived from TIs are of particular interest, because the strong spin-orbit coupling inherent to TIs may lead to unconventional pairing that is a prerequisite to TSCs [9]. However, there have been only a few cases in which superconductivity is found in doped TIs [10–16], and it is strongly desired that a superconductor with promising indications of unconventional superconductivity be discovered in a doped TI.

Recently, two of the authors have contributed to the discovery of an interesting topological insulator [17],  $(\text{PbSe})_5(\text{Bi}_2\text{Se}_3)_6$ . This is a member of the Pb-based homologous series of compounds [18],  $(\text{PbSe})_5(\text{Bi}_2\text{Se}_3)_{3m}$  ( $m = 1, 2, \dots$ ), which form natural multilayer heterostructures of a topological insulator ( $\text{Bi}_2\text{Se}_3$ ) and an ordinary insulator ( $\text{PbSe}$ ). It was found that at  $m = 2$ , the  $\text{PbSe}$  unit works as a block layer and the topological boundary states are encapsulated in each  $\text{Bi}_2\text{Se}_3$  unit, making the system to possess quasi-two-dimensional (quasi-2D) states of topological origin throughout the bulk [17]. Hence, the  $m = 2$  material is a peculiar type of TI filled with quasi-2D topological bands that originate due to the nontrivial  $Z_2$  topology of the  $\text{Bi}_2\text{Se}_3$  unit.  $\text{Bi}_2\text{Se}_3$  consists of a stack of Se-Bi-Se-Bi-Se quintuple layers (QLs), and the  $m = 2$  member of  $(\text{PbSe})_5(\text{Bi}_2\text{Se}_3)_{3m}$  has 2 QLs in its  $\text{Bi}_2\text{Se}_3$  unit [see Fig. 1(a)]. In the middle of this 2-QL unit is a van der Waals gap, into which intercalations of atoms or molecules are possible.

Motivated by the occurrence of superconductivity in  $\text{Bi}_2\text{Se}_3$  upon Cu intercalation [10,19], we tried to make  $(\text{PbSe})_5(\text{Bi}_2\text{Se}_3)_6$  (hereafter called PSBS) superconducting via Cu intercalation. We first grew high-quality, single-phase crystals of PSBS ( $m = 2$ ) with an improved method [20], and adopted the electrochemical technique which we developed for making high-quality  $\text{Cu}_x\text{Bi}_2\text{Se}_3$  superconductors [19]; as a result, we have succeeded in synthesizing a superconductor [20]. Intriguingly, this material,  $\text{Cu}_x(\text{PbSe})_5(\text{Bi}_2\text{Se}_3)_6$  (called CPSBS), turned out to be quite different from its cousin,  $\text{Cu}_x\text{Bi}_2\text{Se}_3$ : First, this superconductor presents an unusual specific-heat behavior which suggests unconventional superconductivity. Second, nearly 100% superconducting samples can sometimes be synthesized, which makes it easier to elucidate its intrinsic nature.

Figure 1(b) shows the resistivity data for PSBS and CPSBS ( $x = 1.36$ ). The Cu intercalation causes a sharp superconducting transition at 2.85 K, and at the same time, it introduces moderate electron scattering to enhance the residual resistivity. The carrier density increases from  $n_e \simeq 4 \times 10^{20}$  in PSBS to  $1.2 \times 10^{21} \text{ cm}^{-3}$  in CPSBS ( $x = 1.36$ ), which suggests that each intercalated Cu introduces about 0.7 electrons on average [20]. The Hall resistivity data indicate that the transport is governed by only one band (see Fig. S1(b) of the Supplemental Material [20]), suggesting that the topological and nontopological bands of the  $\text{Bi}_2\text{Se}_3$  unit [17] may well have merged at the chemical potential of CPSBS. Such a merger does not preclude the occurrence of bulk topological superconductivity [21].

As shown in Figs. 1(c) and 1(d), in the present set of samples the onset of superconductivity was essentially independent of  $x$  and was always around 2.9 K for  $x = 0.3$ –2.3, whereas the shielding fraction (the fraction of the sample volume from which the magnetic field is kept out due to superconductivity after zero-field cooling) was very much sample dependent; note that, in the case of type-II superconductors, the shielding fraction is a better measure of the superconducting volume fraction than the Meissner fraction measured upon field cooling, because the latter is significantly affected by flux trapping. The random nature of the obtained shielding fraction vs  $x$  signifies the difficulty in synthesizing a homogeneous superconductor with intercalation, and apparently the Cu atoms in the majority of our samples are inhomogeneously

\*y\_ando@sanken.osaka-u.ac.jp

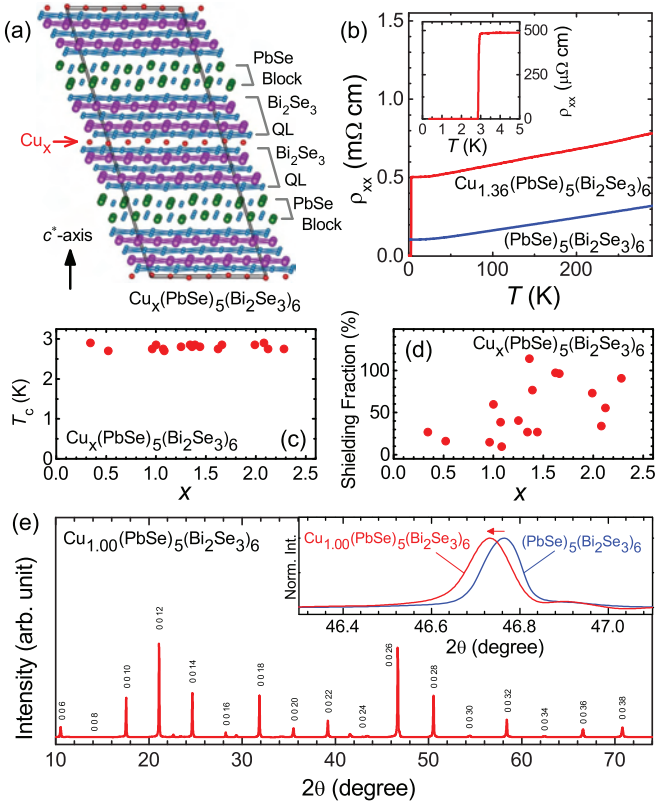


FIG. 1. (Color online)  $\text{Cu}_x(\text{PbSe})_5(\text{Bi}_2\text{Se}_3)_6$  superconductor. (a) Crystal structure [32] based on the data for PSBS [18]. Cu atoms are intercalated into the van der Waals gaps marked by red arrow. (b) Temperature dependencies of the resistivity  $\rho_{xx}$  for PSBS and CPSBS ( $x = 1.36$ ). Inset shows the sharp superconducting transition at 2.85 K. (c) Onset  $T_c$  measured by dc magnetic susceptibility for samples with various  $x$  values. (d) Shielding fractions of the samples presented in (c) at 1.8 K. (e) XRD pattern measured on a cleaved surface ( $ab$  plane) of a superconducting CPSBS sample with  $x = 1.00$  (shielding fraction  $\sim 60\%$ ), where the peak pattern is essentially the same as that of pristine PSBS. Inset compares the positions of the prominent (0 0 26) peak for PSBS and CPSBS, which demonstrates that the periodicity perpendicular to the layers is slightly enlarged from 50.460(1) Å to 50.508(1) Å after the Cu intercalation.

intercalated; nevertheless, we have confirmed that the superconducting portion is not forming a “shell” in our samples [20]. Furthermore, we have been able to achieve essentially 100% shielding fraction in a few samples with  $x = 1.3$ –1.7, and in those special samples the roles of the nonsuperconducting phase can be largely neglected. The x-ray diffraction (XRD) data from cleaved surfaces of single-crystalline CPSBS indicate that the system essentially preserves the same crystal structure of PSBS with a slightly elongated  $c^*$  axis, as is expected for an intercalated material [Fig. 1(e)]; however, it is beyond the scope of this Rapid Communication to precisely determine the crystallographic structure, including the exact position of Cu, of this complicated material with a large unit cell.

In the following, we focus on two samples with  $x = 1.36$  and 1.66, which presented essentially 100% shielding fractions as shown in Figs. 2(a) and 2(c). Figures 2(b) and 2(d) show

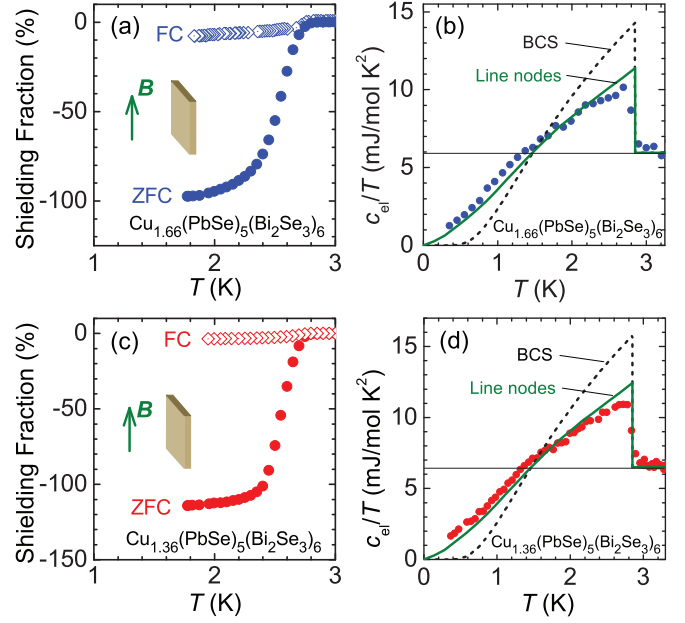


FIG. 2. (Color online) Shielding fraction and specific heat. (a) and (c) Temperature dependencies of the dc magnetic susceptibility measured in 0.2 mT applied parallel to the  $ab$  plane with the field-cooling (FC) and zero-field-cooling (ZFC) procedures for (a)  $x = 1.66$  and (c)  $x = 1.36$ , presented in terms of the shielding fraction. Since the demagnetization effect is minimal for this geometry and the sample shape was irregular, we did not make any correction for it [the  $x = 1.66$  (1.36) sample was 0.23 (0.16) mm thick and  $1.6 \pm 0.3$  ( $1.7 \pm 0.35$ ) mm long along the  $B$  field]. (b) and (d) Superconducting transition in  $c_{el}/T$  in 0 T obtained after subtracting the phonon contribution determined in 2 T (see Fig. S2 [20]). The dashed line is the weak-coupling BCS behavior (coupling constant  $\alpha = 1.76$ ) for  $T_c$  of 2.85 K. The green solid line is the theoretical curve for  $d$ -wave pairing on a simple cylindrical Fermi surface with line nodes along the axial direction [23]. Horizontal solid line corresponds to  $\gamma_N$ .

the behavior of the electronic specific heat  $c_{el}$  in terms of  $c_{el}/T$  vs  $T$  for the two samples; those data were obtained after subtracting the phonon contribution determined in 2 T described in Fig. S2 of the Supplemental Material [20]. The two samples consistently present two unconventional features that become apparent when compared with the conventional weak-coupling BCS behavior [22] shown with dashed lines: First, the jump height at  $T_c$  is much smaller than the prediction of the BCS theory,  $1.43\gamma_N$ , where  $\gamma_N$  is the normal-state electronic specific-heat coefficient corresponding to the horizontal solid lines. Second,  $c_{el}/T$  decreases much more slowly than the BCS behavior; in particular,  $c_{el}/T$  keeps showing a sizable temperature dependence even at our lowest temperature of 0.35 K ( $T/T_c = 0.12$ ), whereas  $c_{el}/T$  should already become negligible at such a low temperature in the BCS case. (Strong-coupling BCS theory makes these discrepancies worse.) It is reassuring that those unconventional features are exactly reproduced in two different samples.

Such a peculiar behavior in  $c_{el}/T$  suggests the existence of nodes in the superconducting gap for the following reasons: First, when the gap has nodes, the averaged gap magnitude becomes smaller than the fully gapped case,

and the specific-heat jump is naturally reduced [6,22]; the green solid line in Figs. 2(b) and 2(d) gives an example for the  $d$ -wave superconductivity with line nodes [23]. Second, in contrast to the conventional BCS case in which  $c_{el}/T$  decreases exponentially at low  $T$  because of a finite activation energy, the existence of nodes allows thermal excitations of quasiparticles down to very low temperatures, changing the  $T$  dependence of  $c_{el}/T$  from exponential to a power law [6].

As one can see in Figs. 2(b) and 2(d), our data, particularly the strong  $T$  dependence near 0 K, bear striking similarity to the theoretical  $c_{el}/T$  behavior expected for a superconductor with line nodes [23], which points to the realization of unconventional superconductivity in CPSBS. Of course, specific-heat measurements alone are not sufficient for unambiguously nailing down the existence of nodes, because a multiband superconductor with a very small gap in one of the bands or an anisotropic  $s$ -wave superconductor with very small gap minima would give rise to a  $c_{el}/T$  behavior similar to what we found in CPSBS. Hence, phase-sensitive measurements are crucially important in the future research of this material. Also, STM and NMR experiments would be very useful for elucidating the unconventional superconductivity.

Note that in the case of nodal superconductors, impurity scattering causes a finite density of quasiparticle states at 0 K, causing  $(c_{el}/T)_{T \rightarrow 0}$  to be finite even in a 100% superconducting sample; this may also be the case in the present system, given the relatively large residual resistivity. Also, it is prudent to mention that the spin-orbit scattering [24] is pair breaking and may mimic the  $c_{el}/T$  behavior observed here, so its role should be elucidated in future. Nevertheless, it is fair to note that in  $\text{Cu}_x\text{Bi}_2\text{Se}_3$ , where the spin-orbit scattering should be of similar strength, the  $c_{el}/T$  behavior was found to obey the BCS theory [19].

Due to the quasi-2D nature of the parent material PSBS [17], the superconductivity in CPSBS is likely to be realized on a quasi-2D Fermi surface, which is distinct from the three-dimensional (3D) bulk Fermi surface of  $\text{Bi}_2\text{Se}_3$ . This implies that the theory of 3D topological superconductivity proposed for  $\text{Cu}_x\text{Bi}_2\text{Se}_3$  [9] is not directly applicable. Nevertheless, it is still expected that strong spin-orbit coupling responsible for the topological nature of the parent material causes the effective pairing interaction to become spin dependent, which would lead to unconventional superconductivity [9]. When the Fermi surface is quasi-2D, a node in the unconventional superconducting gap is naturally extended along the  $c^*$  axis, forming a line node in the 3D Brillouin zone. It is thus expected that, if gap nodes were to be present in CPSBS, the  $c_{el}/T$  behavior should be close to that of a superconductor with line nodes.

The possible existence of line nodes in CPSBS is further supported by the magnetic-field dependence of the specific heat. Figure 3(a) shows the  $c_{el}/T$  vs  $T$  plots for various magnetic fields applied perpendicular to the  $ab$  plane described in Fig. S2 of the Supplemental Material [20], from which we extract the magnetic-field dependence of  $c_{el}$  at the lowest temperature, 0.35 K; here, to make our best effort to quantify its behavior, the data are corrected for a small Schottky anomaly [20], which is only  $\lesssim 20\%$  even at the upper critical

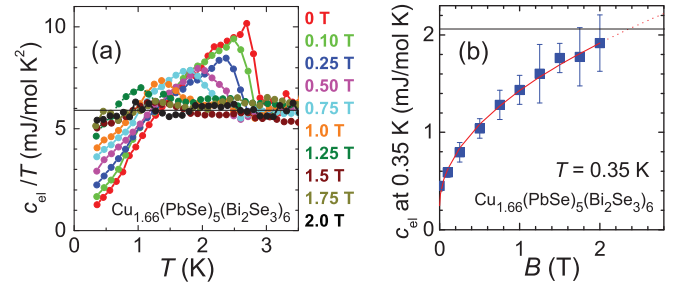


FIG. 3. (Color online) Specific heat in magnetic fields. (a) Temperature dependencies of  $c_{el}/T$  in various magnetic fields ( $B \perp ab$ ) for  $x = 1.66$ . Small Schottky anomaly that becomes nonnegligible above  $\sim 1.5$  T has been subtracted (see [20]). Horizontal solid line corresponds to  $\gamma_N$ . (b) Magnetic-field dependence of  $c_{el}$  at 0.35 K taken from the data in (a). The red solid line is the best fit of the function  $aB^n + c_0$  to the data, yielding  $n = 0.50 \pm 0.06$ ,  $a = 1.2 \pm 0.1$  ( $\text{mJ mol}^{-1} \text{K}^{-1} \text{T}^{-n}$ ), and  $c_0 = 0.25 \pm 0.09$  ( $\text{mJ mol}^{-1} \text{K}^{-1}$ ). Horizontal solid line corresponds to  $\gamma_N T$  at  $T = 0.35$  K.

field and is comparable to the error bar. The obtained  $c_{el}(B)$  behavior at 0.35 K [Fig. 3(b)] is clearly nonlinear in  $B$ . Note that in conventional BCS superconductors  $c_{el}$  increases essentially linearly with  $B$ , because the number of induced quasiparticles is proportional to the number of vortices. On the other hand, in nodal superconductors, the Doppler shift of the quasiparticle excitations (so-called Volovik effect) causes more quasiparticles to be created per vortex than in the BCS case [25]; for line nodes, Volovik showed [25] that  $c_{el}$  increases as  $\sim \sqrt{B}$ . Indeed, our data are best described with  $c_{el} \sim B^{0.5}$ , supporting the existence of line nodes.

Figures 4(a) and 4(c) show the magnetic-field-induced resistive transitions at various temperatures in  $B \perp ab$  and in  $B \parallel ab$ , respectively, from which the resistive upper critical fields  $B_{c2\perp}(T)$  and  $B_{c2\parallel}(T)$  are extracted. We plot in Figs. 4(b) and 4(d) the magnetic field values at which 2%, 50%, and 98% of the normal-state resistivity  $\rho_N$  is recovered at a given temperature. It is customary to use 50%  $\rho_N$  for defining  $B_{c2}$  [13,14,26]. In Fig. 4(b), the onset temperatures of the specific-heat transitions in  $B \perp ab$  determined for the same sample (see Fig. S5(a) of the Supplemental Material [20]) are also shown. Extrapolations of the 50%  $\rho_N$  data in Figs. 4(b) and 4(d) give  $B_{c2\perp} = 2.6$  T and  $B_{c2\parallel} = 4.3$  T at 0 K, yielding the coherence lengths  $\xi_{ab} = 11.3$  nm and  $\xi_{c^*} = 6.8$  nm. The relatively small anisotropy in  $B_{c2}$  may seem strange for a superconductor with a quasi-2D Fermi surface, but a similar situation has been found in  $\text{BaFe}_2\text{As}_2$ -based superconductors [27,28] and is believed to be due to a finite  $k_z$  dispersion of the cylindrical Fermi surface.

The  $B_{c2}(T)$  behavior expected for a conventional superconductor from the Werthamer-Helfand-Hohenberg (WHH) theory [29] tends to saturate for  $T \rightarrow 0$ , as shown with solid lines in Figs. 4(b) and 4(d). On the other hand, our experimental data present much weaker tendency toward saturation. We note that the Pauli paramagnetic limit [29],  $B_{\text{Pauli}} = 1.84T_c = 5.3$  T, is larger than our  $B_{c2}$ , so the violation of the conventional behavior is not as strong as in the case of exotic superconductors such as  $\text{UBe}_{13}$  [26]. Nevertheless, similar violations of the WHH theory to those found here



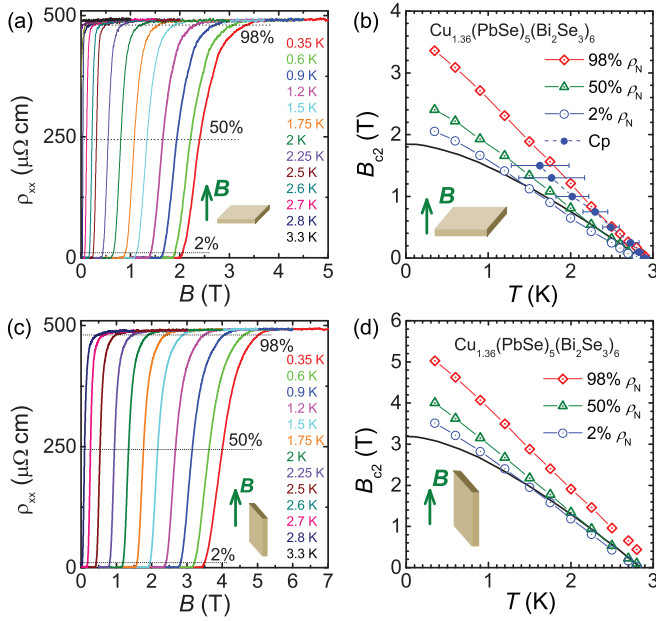


FIG. 4. (Color online) Upper critical field  $B_{c2}$ . (a) and (c) Magnetic-field-induced resistive transitions measured at various temperatures in the  $x = 1.36$  sample for (a)  $B \perp ab$  and (c)  $B \parallel ab$ . Three levels of the resistivity  $\rho_{xx}$  in those transitions, corresponding to 2%, 50%, and 98% of  $\rho_N$  (shown by dotted lines), are used for determining the depinning, mid-point, and onset fields, respectively; 50%  $\rho_N$  is the definition of  $B_{c2}$ . (b) and (d)  $B$  vs  $T$  phase diagrams obtained from the data in (a) and (c), respectively. The black solid lines are the conventional  $B_{c2}(T)$  behavior given by the WHH theory, which is determined by the  $(dB_{c2}/dT)_{T=T_c}$  value (0.936 T/K for  $B \perp ab$  and 1.615 T/K for  $B \parallel ab$ ). In (b), the onset temperatures of the specific-heat transitions in various magnetic fields measured in the same sample (see [20]) are also shown for comparison.

have been discussed as being indicative of unconventional superconductivity in  $\text{Cu}_x\text{Bi}_2\text{Se}_3$  [13] and in  $\text{Bi}_2\text{Se}_3$  under high pressure [14].

We have further characterized the CPSBS superconductor by measuring the lower critical field  $B_{c1}$ , which was determined to be 0.34 mT for  $B \parallel ab$  at 0 K (Fig. S6(c) of the Supplemental Material [20]). Knowing  $B_{c1\parallel}$ ,  $B_{c2\perp}$ , and  $B_{c2\parallel}$ , one can obtain the Ginzburg-Landau parameter  $\kappa_{ab} = 192$ , the penetration depths  $\lambda_{ab} = 1.3 \mu\text{m}$  and  $\lambda_{c^*} = 2.2 \mu\text{m}$ , and the thermodynamic critical field  $B_c = 16.6 \text{ mT}$  [20]. The long penetration depths are consistent with the low carrier density and moderate disorder in CPSBS.

It is striking that all the bulk properties of the superconductor CPSBS shown here point to possible occurrence of unconventional superconductivity accompanied with line nodes. The existence of line nodes implies a sign-changing gap function, which generically gives rise to surface Andreev bound states [30]. Strong spin-orbit coupling causes such surface Andreev states to be spin-split and form spin-non-degenerate Kramers pairs, which means that they become helical Majorana fermions [9]. Indeed, nodal superconductors with strong spin-orbit coupling have been discussed as being topological [11,31]. Therefore, the superconductivity in CPSBS has a good chance to be topological and harbor Majorana fermions. We should note, however, that the present data do not fully guarantee that CPSBS realizes a topological superconductivity, because a nodal gap can also be found in anisotropic  $s$ -wave superconductivity. To nail down the topological nature, making a Josephson junction with a conventional superconductor to measure a nontrivial current-phase relationship coming from boundary Majorana fermions [7,8] would be a smoking-gun experiment.

We thank T. Toba for his help in synthesizing the samples, K. Eto and M. Kriener for technical assistance, and L. Fu, Y. Tanaka, A. Taskin, and A. Yamakage for helpful discussions. This work was supported by Japan Society for the Promotion of Science (KAKENHI 24740237, 24540320, and 25220708), MEXT (Innovative Area “Topological Quantum Phenomena” KAKENHI), Air Force Office of Scientific Research (AOARD 124038), and the Inamori Foundation.

- [1] X.-L. Qi and S.-C. Zhang, *Rev. Mod. Phys.* **83**, 1057 (2011).
- [2] M. Z. Hasan and C. L. Kane, *Rev. Mod. Phys.* **82**, 3045 (2010).
- [3] Y. Ando, *J. Phys. Soc. Jpn.* **82**, 102001 (2013).
- [4] A. P. Schnyder, S. Ryu, A. Furusaki, and A. W. W. Ludwig, *Phys. Rev. B* **78**, 195125 (2008).
- [5] Y. Tanaka, M. Sato, and N. Nagaosa, *J. Phys. Soc. Jpn.* **81**, 011013 (2012).
- [6] Y. Maeno, S. Kittaka, T. Nomura, S. Yonezawa, and K. Ishida, *J. Phys. Soc. Jpn.* **81**, 011009 (2012).
- [7] J. Alicea, *Rep. Prog. Phys.* **75**, 076501 (2012).
- [8] C. W. J. Beenakker, *Annu. Rev. Condens. Matter Phys.* **4**, 113 (2013).
- [9] L. Fu and E. Berg, *Phys. Rev. Lett.* **105**, 097001 (2010).
- [10] Y. S. Hor, A. J. Williams, J. G. Checkelsky, P. Roushan, J. Seo, Q. Xu, H. W. Zandbergen, A. Yazdani, N. P. Ong, and R. J. Cava, *Phys. Rev. Lett.* **104**, 057001 (2010).
- [11] S. Sasaki, M. Kriener, K. Segawa, K. Yada, Y. Tanaka, M. Sato, and Y. Ando, *Phys. Rev. Lett.* **107**, 217001 (2011).
- [12] S. Sasaki, Z. Ren, A. A. Taskin, K. Segawa, L. Fu, and Y. Ando, *Phys. Rev. Lett.* **109**, 217004 (2012).
- [13] T. V. Bay, T. Naka, Y. K. Huang, H. Luigjes, M. S. Golden, and A. de Visser, *Phys. Rev. Lett.* **108**, 057001 (2012).
- [14] K. Kirshenbaum, P. S. Syers, A. P. Hope, N. P. Butch, J. R. Jeffries, S. T. Weir, J. J. Hamlin, M. B. Maple, Y. K. Vohra, and J. Paglione, *Phys. Rev. Lett.* **111**, 087001 (2013).
- [15] G. Goll, M. Marz, A. Hamann, T. Tomanic, K. Grube, T. Yoshino, and T. Takabatake, *Physica B* **403**, 1065 (2008).
- [16] N. P. Butch, P. Syers, K. Kirshenbaum, A. P. Hope, and J. Paglione, *Phys. Rev. B* **84**, 220504(R) (2011).
- [17] K. Nakayama, K. Eto, Y. Tanaka, T. Sato, S. Souma, T. Takahashi, K. Segawa, and Y. Ando, *Phys. Rev. Lett.* **109**, 236804 (2012).
- [18] L. Fang, C. C. Stoumpos, Y. Jia, A. Glatz, D. Y. Chung, H. Claus, U. Welp, W. K. Kwok, and M. G. Kanatzidis, *Phys. Rev. B* **90**, 020504(R) (2014).



- [19] M. Kriener, K. Segawa, Z. Ren, S. Sasaki, and Y. Ando, *Phys. Rev. Lett.* **106**, 127004 (2011).
- [20] See Supplemental Material at <http://link.aps.org/supplemental/10.1103/PhysRevB.90.220504> for materials and methods, supplemental data, and additional discussions.
- [21] T. H. Hsieh and L. Fu, *Phys. Rev. Lett.* **108**, 107005 (2012).
- [22] M. Tinkham, *Introduction to Superconductivity* (McGraw-Hill, New York, 1975).
- [23] H. Won and K. Maki, *Phys. Rev. B* **49**, 1397 (1994).
- [24] K. Maki, in *Superconductivity*, edited by R. D. Parks (Marcel Dekker, New York, 1969).
- [25] G. E. Volovik, Pis'ma v ZhETF **58**, 457 (1993) [*JETP Lett.* **58**, 469 (1993)].
- [26] M. B. Maple, J. W. Chen, S. E. Lambert, Z. Fisk, J. L. Smith, H. R. Ott, J. S. Brooks, and M. J. Naughton, *Phys. Rev. Lett.* **54**, 477 (1985).
- [27] H. Q. Yuan, J. Singleton, F. F. Balakirev, S. A. Baily, G. F. Chen, J. L. Luo, and N. L. Wang, *Nature (London)* **457**, 565 (2009).
- [28] M. A. Tanatar, N. Ni, C. Martin, R. T. Gordon, H. Kim, V. G. Kogan, G. D. Samolyuk, S. L. Bud'ko, P. C. Canfield, and R. Prozorov, *Phys. Rev. B* **79**, 094507 (2009).
- [29] N. R. Werthamer, E. Helfand, and P. C. Hohenberg, *Phys. Rev.* **147**, 295 (1966).
- [30] S. Kashiwaya and Y. Tanaka, *Rep. Prog. Phys.* **63**, 1641 (2000).
- [31] M. Sato and S. Fujimoto, *Phys. Rev. Lett.* **105**, 217001 (2010).
- [32] K. Momma and F. Izumi, *J. Appl. Crystallogr.* **44**, 1272 (2011).

## ARTICLE

Received 2 Apr 2014 | Accepted 6 Feb 2015 | Published 12 Mar 2015

DOI: 10.1038/ncomms7547

# Topological proximity effect in a topological insulator hybrid

T. Shoman<sup>1</sup>, A. Takayama<sup>2</sup>, T. Sato<sup>1</sup>, S. Souma<sup>2</sup>, T. Takahashi<sup>1,2</sup>, T. Oguchi<sup>3</sup>, Kouji Segawa<sup>3</sup> & Yoichi Ando<sup>3</sup>

It is well known that a topologically protected gapless state appears at an interface between a topological insulator and an ordinary insulator; however, the physics of the interface between a topological insulator and a metal has largely been left unexplored. Here we report a novel phenomenon termed topological proximity effect, which occurs between a metallic ultrathin film and a three-dimensional topological insulator. We study one bilayer of bismuth metal grown on the three-dimensional topological insulator material TlBiSe<sub>2</sub>, and by using spin- and angle-resolved photoemission spectroscopy, we found evidence that the topological Dirac-cone state migrates from the surface of TlBiSe<sub>2</sub> to the attached one-bilayer Bi. We show that such a migration of the topological state occurs as a result of strong spin-dependent hybridization of the wave functions at the interface, which is also supported by our first-principles calculations. This discovery points to a new route to manipulating the topological properties of materials.

<sup>1</sup>Department of Physics, Tohoku University, Sendai 980-8578, Japan. <sup>2</sup>WPI Research Center, Advanced Institute for Materials Research, Tohoku University, Sendai 980-8577, Japan. <sup>3</sup>Institute of Scientific and Industrial Research, Osaka University, Ibaraki, Osaka 567-0047, Japan. Correspondence and requests for materials should be addressed to T.S. (email: t-sato@arpes.phys.tohoku.ac.jp) or to Y.A. (email: y\_ando@sanken.osaka-u.ac.jp).

The topological surface state of three-dimensional topological insulators (3D TIs) is protected by time-reversal symmetry and characterized by a linearly dispersing Dirac-cone energy band with helical spin texture<sup>1–5</sup>. This peculiar surface state is a consequence of interfacing TIs with an ordinary insulator, including vacuum. When a hybrid structure of a 3D TI and a superconductor is fabricated, it has been predicted that superconducting proximity effect occurring at the interface would lead to the appearance of two-dimensional (2D) topological superconductivity hosting Majorana fermions<sup>6</sup>. Also, when a 3D TI is in contact with a ferromagnetic insulator, the resulting magnetic proximity effect at the interface leads to the opening of a gap at the Dirac point<sup>7,8</sup>, which is prerequisite to realizing topological magnetoelectric effects<sup>9,10</sup>. On the other hand, no such exotic phenomena have been discovered for the interface between a TI and a metal; in fact, despite the obvious importance of understanding the TI/metal interface for device applications, there have been only a limited number of experimental studies of such an interface<sup>11–13</sup>, while several theoretical predictions have been made on possible proximity effects occurring in TI heterostructures involving semiconductor, graphene, metal and

normal-insulator interfaces<sup>14–18</sup>. To search for nontrivial effects at the TI/metal interface, it would be better if the energy bands in the metal are spin split, because spin-dependent phenomena can be more easily studied in such a metal.

In the following, we present spin- and angle-resolved photoemission spectroscopy (ARPES) measurements of the TI/metal interface, and show a novel phenomenon termed topological proximity effect, in which the topological Dirac-cone state migrates from the TI surface to an attached metal film. We have chosen ultrathin (only one-bilayer (1BL) thick) 2D films of Bi metal where the Rashba splitting of the energy bands is strong. Also, one would expect the interface effect to become stronger if the energy states of a TI hybridize more strongly with those in a metal. This consideration led us to choose the ternary chalcogenide TI material TlBiSe<sub>2</sub> (ref. 19), in which layers of Tl, Se and Bi are covalently bonded and stacked in the sequence of -Tl-Se-Bi-Se- along the [111] direction (Fig. 1a). This material has a nontopological cousin, TlBiS<sub>2</sub> (refs 20,21), which is useful for making a control experiment. The covalent nature of the interlayer bonding in TlBiX<sub>2</sub> (X = S, Se) would leave dangling bonds on the cleaved surface and cause strong hybridization with

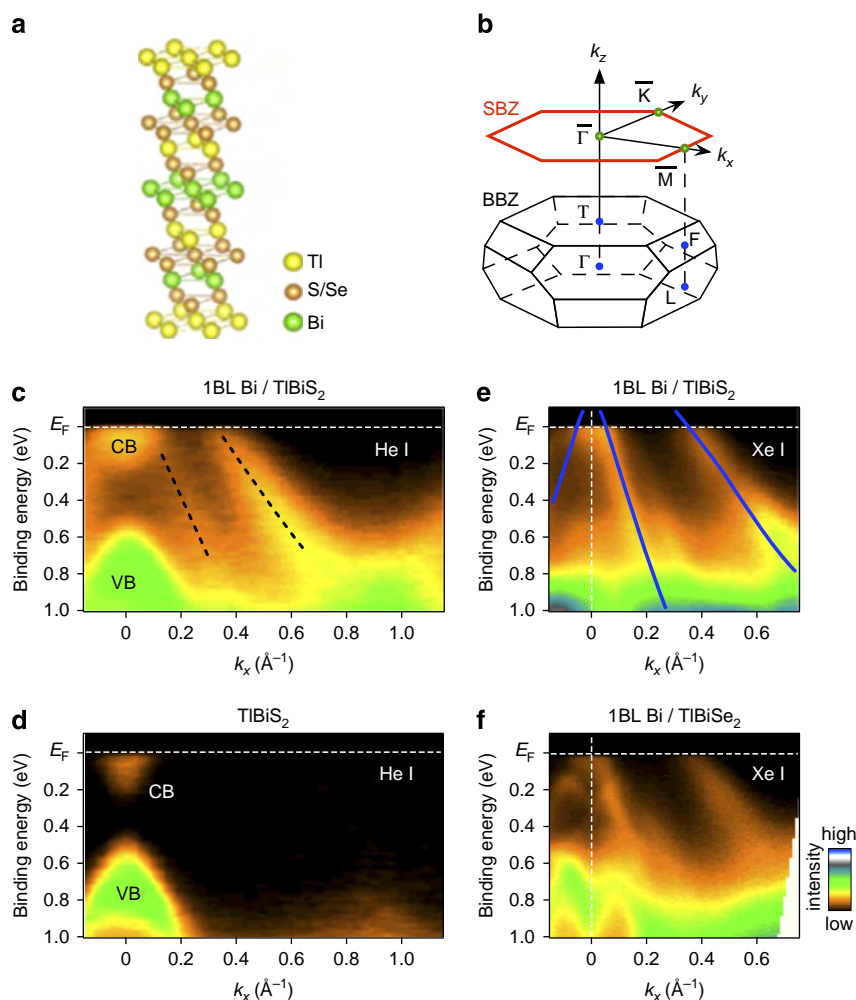


**Figure 1 | Electronic structure of one-bilayer Bi on TlBiS<sub>2</sub>.** (a) Crystal structure of TlBi(S,Se)<sub>2</sub>. (b) Surface and bulk Brillouin zone (SBZ and BBZ respectively) of TlBiX<sub>2</sub> (X = S, Se). (c,d) Comparison of the near- $E_F$  ARPES intensity between 1BL Bi/TlBiS<sub>2</sub> and pristine TlBiS<sub>2</sub> measured along the  $\bar{\Gamma}$ - $\bar{M}$  ( $k_x$ ) cut with the He-I photons ( $h\nu = 21.218$  eV) at  $T = 30$  K. CB and VB denote the bulk conduction and valence bands of TlBiS<sub>2</sub>, respectively. (e,f) ARPES intensity around the  $\bar{\Gamma}$  point measured with the Xe-I photons ( $h\nu = 8.437$  eV) for 1BL Bi on nontopological TlBiS<sub>2</sub> and on topological TlBiSe<sub>2</sub>, respectively. Calculated band structure for free-standing 1BL Bi is overlaid in e with an upward energy shift of  $\sim 0.4$  eV, which takes into account the heavily hole-doped nature of the Bi film due to charge transfer to the TlBiX<sub>2</sub> substrate.

deposited metals; this is in contrast to  $\text{Bi}_2\text{Se}_3$  or  $\text{Bi}_2\text{Te}_3$ , whose surfaces have no dangling bonds and consequently the surface states present just a weak hybridization<sup>11</sup> and no change in the topology<sup>12</sup> when interfaced with Bi. It should be noted that 1BL Bi is structurally unstable in a free-standing form and it can only exist on some substrate; it turned out that  $\text{TlBiS}_2$  is a useful non-invasive substrate for 1BL Bi to identify the pristine Bi-derived bands, because of its nontopological nature and the resulting absence of any surface state<sup>20,21</sup>. We have traced the variation of the electronic states upon depositing Bi on  $\text{TlBiS}_2$ , and our core-level analysis suggests that the Bi atoms first passivate the dangling bonds on the cleaved surface and then start to grow layer by layer (Supplementary Figs 1 and 2; Supplementary Notes 1 and 2).

## Results

**Rashba spin-splitting of 1BL Bi/ $\text{TlBiS}_2$ .** Let us start by presenting our control experiment on Bi/ $\text{TlBiS}_2$  hybrid. As one can see in the ARPES data along the  $\bar{\Gamma}$ – $\bar{M}$  cut (the bulk and surface Brillouin zones and their high-symmetry points are depicted in Fig. 1b), the Bi deposition creates a couple of hole-like bands centred at the  $\bar{\Gamma}$  point (dashed curves in Fig. 1c) superimposed on the bulk bands of the pristine  $\text{TlBiS}_2$  (Fig. 1d). These bands are attributed to the quantum-well states (quantized bulk bands) of Bi because of their 2D nature, which can be inferred from the photon-energy invariance of the band location for the He-I ( $h\nu = 21.218$  eV) and Xe-I

( $h\nu = 8.437$  eV) photons (Fig. 1c,e). Successful fabrication of 1BL Bi films can be judged from the agreement between the observed quantum-well states (called Bi bands hereafter) and the calculated band structure for free-standing 1BL Bi (blue line in Fig. 1e).

When closely examined, the Bi bands present evidence for Rashba spin-splitting. As visualized in the second-derivative ARPES intensity plot of the energy distribution curves (EDCs) along the  $\bar{\Gamma}$ – $\bar{K}$  cut for the 1BL Bi/ $\text{TlBiS}_2$  hybrid in Fig. 2a, a pair of dispersions can be found for each of the large and small hole-like bands; we emphasize that the band dispersions determined from the peak positions in the momentum distribution curves (MDCs) by numerical fittings (Supplementary Fig. 3 and Supplementary Note 3), shown with white dots in Fig. 2a, agree with the second-derivative peaks in the EDCs, so the splitting of the bands is a robust observation. Those four bands each form a Fermi surface (labelled LO, LI, SO and SI, standing for ‘large outer’ etc.) as shown in Fig. 2b, in which the two large pockets (LI and LO) exhibit a sizable warping.

We have investigated the in-plane spin polarization by performing spin-resolved ARPES measurements at three representative  $\mathbf{k}$  points, A, B and C, shown in Fig. 2a. As one can see in the top part of Fig. 2c, the spin-resolved EDCs at point A (where the SO branch is located near  $E_F$ ; see Fig. 2a) demonstrate that the up-spin component is dominant, and consequently the spin polarization is positive. Similarly, the up-spin component is more prominent at point B (where the SI branch is located at  $\sim 0.4$  eV). At point C, on the other hand, a sign reversal in the spin

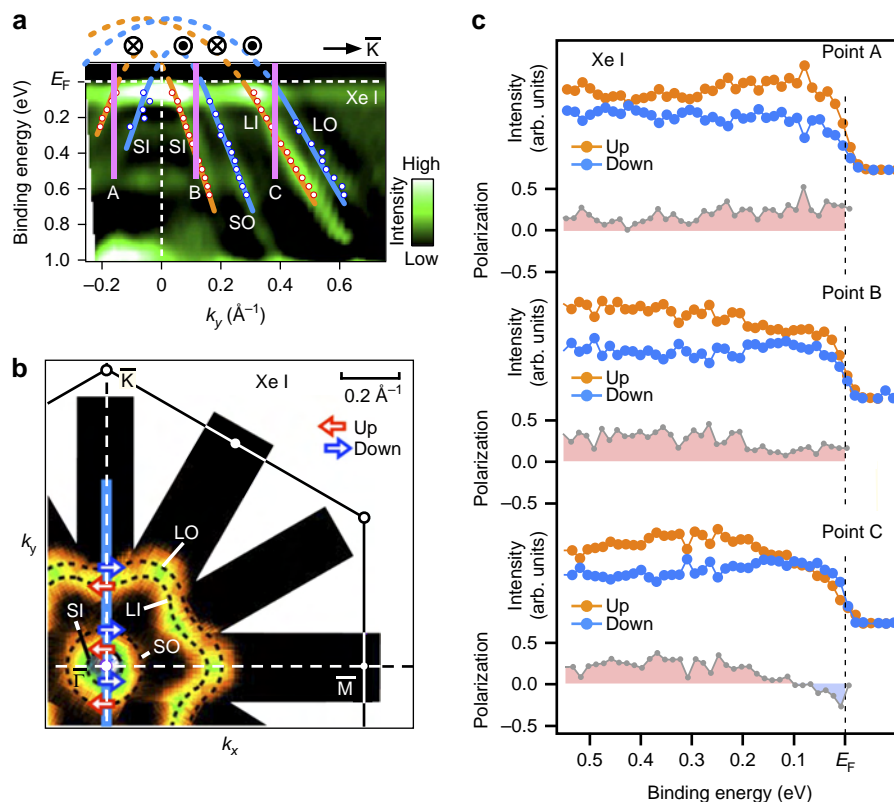


**Figure 2 | Rashba spin-splitting of one-bilayer Bi on  $\text{TlBiS}_2$ .** (a) Second-derivative intensity plot of the EDCs for 1BL Bi/ $\text{TlBiS}_2$  hybrid measured along the  $\bar{\Gamma}$ – $\bar{K}$  ( $k_y$ ) cut, together with the location of the  $\mathbf{k}$  points (solid lines) where the spin-resolved ARPES measurements were performed (points A–C). White dots are the peak position of the MDCs estimated by numerical fittings, and dashed orange and blue curves are guides to the eyes to trace the band dispersion. LO, LI, SO and SI represent the large outer, large inner, small outer and small inner hole-like bands, respectively. The direction of the spin-polarization vector for each band is also indicated. (b) ARPES intensity mapping at  $E_F$  in a 2D wave-vector plane obtained with the Xe-I photons for 1BL Bi/ $\text{TlBiS}_2$  hybrid; this intensity is obtained by integrating the spectra within  $\pm 10$  meV of  $E_F$ . Definitions of the up/down-spin vectors and the experimentally determined spin direction for each Fermi surface are also indicated. (c) Spin-resolved EDCs and corresponding energy dependence of the spin polarization at representative  $\mathbf{k}$  points (A–C) shown in a.



polarization is observed near  $E_F$ , and this is due to the contribution from the near- $E_F$  LO band, while the contribution of the LI band (located at  $\sim 0.4$  eV) causes a positive spin polarization at higher binding energy; the smallness of the spin polarization for the LO band is probably related to the suppression of photoelectron intensity due to the matrix-element effect (although we have performed measurements at other  $\mathbf{k}$  points around point C, it was difficult to observe the negative spin polarization at energies away from  $E_F$ , probably because of the strong intensity smearing of the LO and SO bands). These results establish that the four Bi bands are spin nondegenerate, and therefore they are most likely forming Rashba-split Kramers pairs (the Rashba splitting is also reproduced by first-principles calculations, as detailed later); the spin texture inferred from our spin-resolved ARPES is shown in Fig. 2a,b. The Rashba splitting is likely triggered by an electrostatic potential normal to the surface plane for vacuum/1BL Bi/TlBiSe<sub>2</sub>, which breaks space-inversion symmetry.

**Topological proximity effect in 1BL Bi/TlBiSe<sub>2</sub>.** Having understood the Bi bands from our control experiment, we now discuss the topological insulator hybrid, 1BL Bi/TlBiSe<sub>2</sub>. One may expect a simple superposition of the Bi bands and the topological Dirac-cone states of TlBiSe<sub>2</sub>, like in 1BL Bi on Bi<sub>2</sub>Te<sub>3</sub> (ref. 11). However, stronger hybridization due to the dangling bonds on TlBiX<sub>2</sub> leads to a highly nontrivial band structure. Figure 3a displays the near- $E_F$  ARPES intensity around the  $\bar{\Gamma}$  point measured with the He-I photons, which basically signifies an X-shaped Dirac-cone-like state inside the two Bi bands, SI and SO (the data for a wider energy and momentum range are shown in Fig. 1f). Obviously, the upper branch of the X-shaped band does not reach  $E_F$  but exhibits an unusual dispersing-back behaviour with the top of the dispersion at around the intersection with the SO band (white arrow); this situation is better visualized in the second-derivative image of the MDCs in Fig. 3b and the extracted

band dispersion in Fig. 3f. One can see that the X-shaped band originates from the topological Dirac-cone state in TlBiSe<sub>2</sub> because (i) it has a 2D nature as confirmed by the  $h\nu$ -invariance (Fig. 3c), (ii) its dispersion around the  $\bar{\Gamma}$  point is similar to that observed in pristine TlBiSe<sub>2</sub> (Fig. 3d) and (iii) the X-shaped band is absent in the 1BL Bi/TlBiSe<sub>2</sub> hybrid (Fig. 3e).

We speculate that the observed modulation of the X-shaped band is caused by the strong hybridization through the interface between the upper branch of the Dirac-cone surface state of TlBiSe<sub>2</sub> and the SO band of Bi, as schematically illustrated in Fig. 4a. It is important to recognize that, for such a hybridization to take place, the spin eigenvalue of the two states must agree with each other. In this respect, the upper Dirac cone and the SO band have the same clockwise-rotating spin texture, and hence they can hybridize. This causes the resulting X-shaped band to display a dispersing-back behaviour and, simultaneously, the portion of the SO band near the  $\bar{\Gamma}$  point is pushed up into the unoccupied region (see right panel of Fig. 4a). Also, this spin matching argument naturally explains the absence of hybridization between the upper Dirac cone and the SI band seen in Fig. 3b,c. As a result of this spin-dictated hybridization, two new types of bands emerge as shown in the right panel of Fig. 4a: (i) Rashba-split bands of hole character, whose Kramers point was the original Dirac point of TlBiSe<sub>2</sub> and (ii) topological Dirac-cone band (thick curves) whose Dirac point was the original Kramers point of the Rashba-split Bi bands (SO and SI) located above  $E_F$ .

**Band calculations of 1BL Bi on TlBiSe<sub>2</sub> and TlBiSe<sub>2</sub>.** Our first-principles band structure calculations for model crystals of 1BL Bi on TlBiSe<sub>2</sub> and TlBiSe<sub>2</sub> (Fig. 4b,c; see Supplementary Fig. 4 and Supplementary Note 4 for details) strongly supports the existence of Rashba-split Bi bands as well as the band diagram speculated above. As shown in Fig. 4b, the calculated band structure for 1BL Bi/TlBiSe<sub>2</sub> reproduces many important aspects of the experimental data in Fig. 2. First, we identify spin-split Bi-derived hole-like

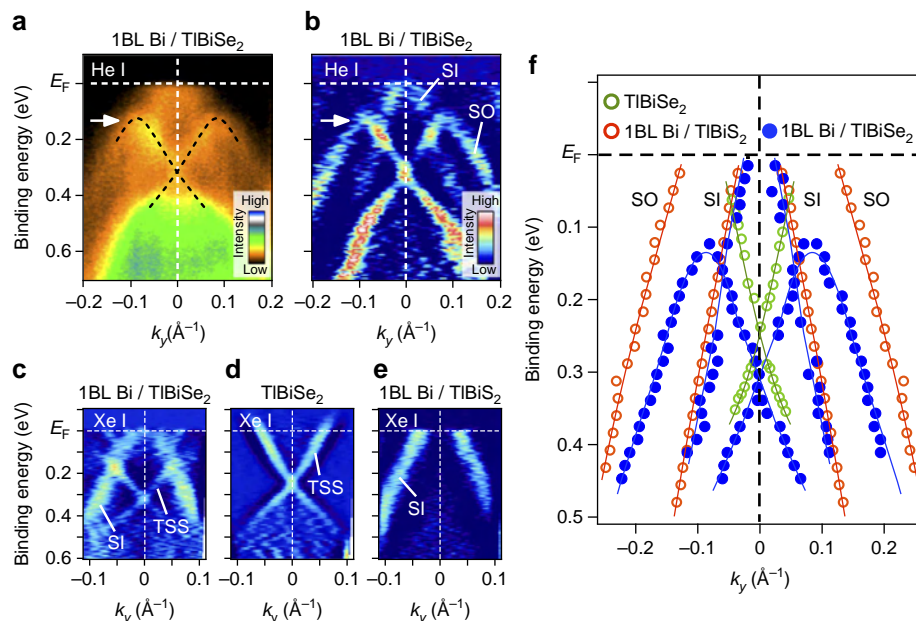


**Figure 3 | Hybridization of topological Dirac-cone and Rashba states.** (a,b) ARPES intensity and second-derivative intensity plots of the MDCs, respectively, for 1BL Bi/TlBiSe<sub>2</sub> hybrid around the  $\bar{\Gamma}$  point obtained with the He-I photons. Black dashed curves in **a** are guides to the eyes to trace the X-shaped band. White arrow indicates the top of the dispersion for this band. The Bi bands in **b** are more clearly resolved than those in Fig. 2a due to the difference in the derivative variables (that is,  $d^2A/dk^2$  versus  $d^2A/dE^2$ ), and not due to the difference in the substrates (TlBiSe<sub>2</sub> versus TlBiSe<sub>2</sub>). (c-e) Second-derivative intensity plots obtained with the Xe-I photons for 1BL Bi/TlBiSe<sub>2</sub> hybrid, pristine TlBiSe<sub>2</sub> and 1BL Bi/TlBiSe<sub>2</sub> hybrid, respectively. (f) Experimental band dispersions extracted from the peak positions of the MDCs for **b-e**.

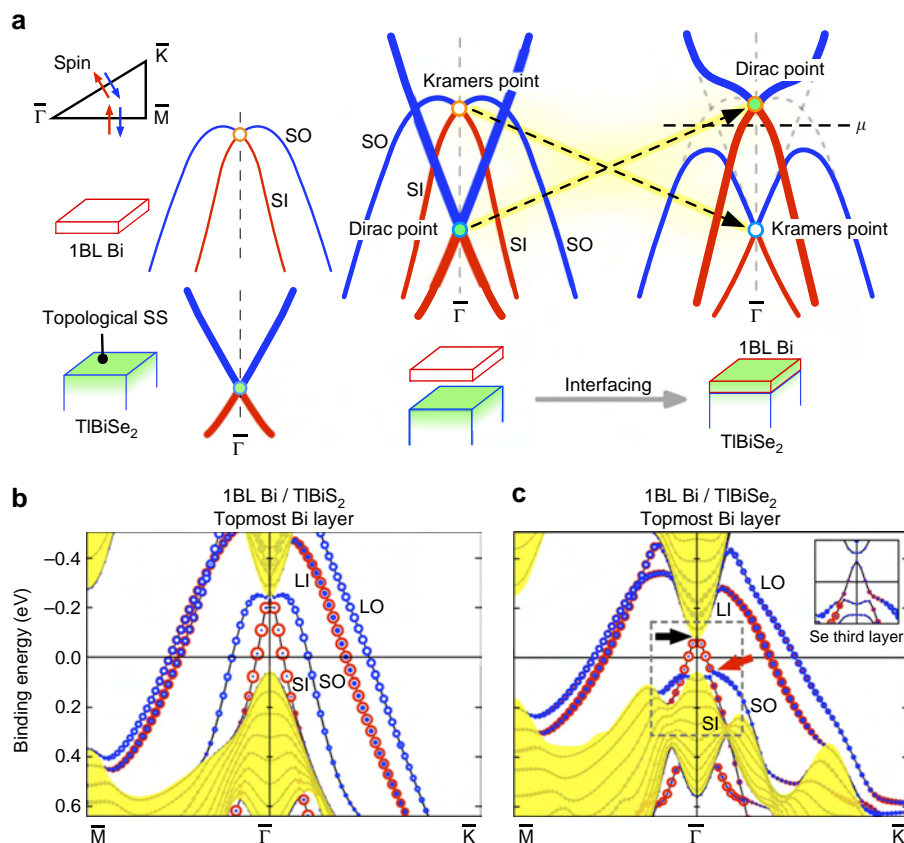


**Figure 4 | Switching between topological Dirac-cone and Rashba states.** (a) Schematic illustration of the hybridization between the Rashba-split Bi bands and the topological surface state (SS) of TlBiSe<sub>2</sub>. Horizontal dashed line in the right panel indicates the location of the chemical potential ( $\mu$ ) in our sample. Blue (red) curves indicate the clockwise- (anticlockwise-) rotating spin texture. (b,c) Calculated band structure for the slab of 1BL Bi on TlBiSe<sub>2</sub> and TlBiSe<sub>2</sub>, respectively. Spin texture is indicated by circles overlaid on the band dispersion whose colour (blue/red) and radius represent the spin component (clockwise/anticlockwise rotation) and the spin-dependent  $p$ -orbital weight at the topmost Bi layer, respectively. Projection of the bulk bands of TlBi(S/Se)<sub>2</sub> is shown by yellow shade. Black and red arrows in **c** indicate the positions of the Dirac point and the crossing between the Dirac cone and the SO band, respectively. The area enclosed by a rectangle around the  $\bar{\Gamma}$  point in **c** roughly corresponds to the energy region of the schematic band diagram in **a**. Inset to **c** shows the calculated band structure for the Se third layer around the Dirac cone, highlighting its small orbital weight in the surface state (circles are negligibly small in this scale).

bands corresponding to the LO, LI, SO and SI bands in the experiment. Remarkably, the spin texture (clockwise or anticlockwise rotation) for all of these bands is identical to the ARPES data on 1BL Bi/TlBiSe<sub>2</sub> (thanks to a small overlap of the Bi bands with the bulk-band projection of TlBiSe<sub>2</sub>, the Bi band largely keeps the free-standing-like dispersion in a wide range of the  $k$  space). Similar Rashba-split bands are also recognized in the calculated band structure of 1BL Bi/TlBiSe<sub>2</sub> (Fig. 4c), although the band structure around the  $\bar{\Gamma}$  point shows some characteristic differences from the TlBiSe<sub>2</sub> hybrid, owing to the hybridization between the Bi bands and the topological Dirac-cone states of TlBiSe<sub>2</sub>. Second, an extremely hole-doped nature of the Bi bands (chemical potential shift of  $\sim 0.4$  eV) is also reproduced by the calculation in both 1BL Bi/TlBiSe<sub>2</sub> and 1BL Bi/TlBiSe<sub>2</sub>, as a consequence of strong hybridization and resulting band repulsion between the S/Se and Bi states due to covalent bonding (note that the predicted 2D TI nature of 1BL Bi and its semiconducting property<sup>22</sup> would not have a role in the electronic states near  $E_F$  owing to a complete mismatch of the band gaps between 1BL Bi and TlBi(S/Se)<sub>2</sub>, and the physics is essentially that of a metal/insulator heterostructure). Third, in 1BL Bi/TlBiSe<sub>2</sub> (Fig. 4c), we recognize a new lower Dirac cone whose Dirac point (black arrow) is located at slightly above  $E_F$  in the calculation, in agreement with the location of the new Dirac cone expected from

ARPES; note that this lower Dirac cone and the SO band intersects without strong hybridization (red arrow), confirming the spin-dictated hybridization. It is noted that while the upper Dirac cone is not visible in this calculation because it is buried in the bulk-band projection (the calculation underestimates the bulk-band gap ( $\sim 0.1$  eV as opposed to  $\sim 0.35$  eV in the experiment<sup>19</sup>) due to the well-known limitation of the density functional theory), the lower Dirac cone must connect to an upper branch exactly at the  $\bar{\Gamma}$  point to produce a full Dirac-cone dispersion, due to its spin nondegenerate nature and the requirement of Kramers degeneracy; in other words, the spin-nondegenerate nature of the SI band and the time-reversal symmetry guarantees the existence of the upper Dirac cone. The SO band which forms the Kramers pair with the SI band in 1BL Bi/TlBiSe<sub>2</sub> (Fig. 4b) is not responsible for this band connection, since it sinks below  $E_F$  in 1BL Bi/TlBiSe<sub>2</sub> (Fig. 4c). For dispersions below  $E_F$ , by taking into account the calculated spin helical texture of the SO band and the former lower Dirac cone of the TlBiSe<sub>2</sub> surface state, the existence of the new Kramers point is also assured in 1BL Bi/TlBiSe<sub>2</sub>, even though it is buried in the bulk-band projection in the calculation.

It should be noted that the calculated Dirac cone above  $E_F$  in 1BL Bi/TlBiSe<sub>2</sub> has a dominant contribution from the  $p$  orbital of topmost and second Bi layers (85% of total weight; nearly equal

contribution from these two layers), suggesting that it is of 1BL-Bi origin and is migrated from the surface of TlBiSe<sub>2</sub> as a result of strong hybridization; this phenomenon may be called a topological proximity effect. Intriguingly, the calculated surface/interface states have an odd number of band crossings in the bulk-band-gap region between two time-reversal-invariant momenta  $\Gamma$  and  $M$  irrespective of the position of the chemical potential, as opposed to an even number of crossings in 1BL Bi/TlBiSe<sub>2</sub>, indicating that the 1BL Bi/TlBiSe<sub>2</sub> hybrid system maintains the topologically nontrivial nature unlike the TlBiSe<sub>2</sub> hybrid. This can also be confirmed by counting of experimental band crossings in Figs 2a and 4a.

## Discussion

We emphasize that a key ingredient for realizing the present topological proximity effect is to contact a TI with a quasi-2D metal thin film, rather than a 3D bulk metal; in this respect, it may be conceived as a manipulation of the boundary condition for the TI. Besides, the topological proximity effect would not be peculiar to a strongly spin-orbit-coupled metal like Bi, but it would occur for a wider range of metals as suggested in a pioneering theoretical study of proximity effects in semiconductor/TI heterostructures<sup>15</sup>. Fabrications of metal thin films on TIs with various film thickness and their characterizations via spin-resolved ARPES would be particularly useful for studying the topological proximity effect.

Topological proximity effect may also have some relevance to applications. For example, it may be possible to enhance the performance of a metallic spintronic material (for example, to generate highly-conducting channel<sup>18</sup>) by giving it the blessed property of topological protection. Also, fabrication of topologically protected spin-plasmon devices<sup>23</sup> by patterning Rashba metals on the surface of TIs may be conceivable. On the fundamental side, the topological proximity effect is the first step towards understanding the peculiarities of the metal-film/TI interface. Extending the spin-resolved ARPES technique to other TI heterostructures would prove useful for testing theoretical proposals of interesting proximity effects in a variety of TI heterostructures<sup>14–18</sup>.

## Methods

**Sample preparation.** High-quality single crystals of TlBiSe<sub>2</sub> and TlBiS<sub>2</sub> were grown by a modified Bridgman method<sup>20</sup>. To prepare the Bi film, we first cleaved the TlBiSe<sub>2</sub> or TlBiS<sub>2</sub> crystals to obtain a shiny mirror-like surface, and then deposited Bi atoms at room temperature in ultrahigh vacuum of  $1 \times 10^{-10}$  Torr. The  $1 \times 1$  surface structure originating from Bi was confirmed by the low-energy electron diffraction measurement. The film thickness was controlled by the deposition time at a constant deposition rate. The actual thickness was estimated by a quartz-oscillator thickness monitor and also from a comparison of the ARPES-derived band dispersion with the band-structure calculations for free-standing multi-layer Bi<sup>24–26</sup>.

**ARPES experiments.** ARPES measurements were performed with the MBS-A1 electron analyser equipped with high-intensity He and Xe plasma discharge lamps<sup>27</sup> without breaking the vacuum after the Bi film was grown. We used the He- $\alpha$  resonance line ( $h\nu = 21.218$  eV) and one of the Xe-I lines ( $h\nu = 8.437$  eV) to excite photoelectrons. The energy resolution for the regular and spin-resolved ARPES measurements was set at 6–20 and 40 meV, respectively. The sample temperature was kept at 30 K during the measurements. We used the Sherman function value of 0.07 to obtain spin-resolved ARPES data.

## References

- Hasan, M. Z. & Kane, C. L. Colloquium: Topological insulators. *Rev. Mod. Phys.* **82**, 3045–3067 (2010).
- Qi, X.-L. & Zhang, S.-C. Topological insulators and superconductors. *Rev. Mod. Phys.* **83**, 1057–1110 (2011).
- Ando, Y. Topological insulator materials. *J. Phys. Soc. Jpn* **82**, 102001 (2013).
- Xia, Y. *et al.* Observation of a large-gap topological-insulator class with a single Dirac cone on the surface. *Nat. Phys.* **5**, 398–402 (2009).
- Souma, S. *et al.* Direct measurement of the out-of-plane spin texture in the Dirac-cone surface state of a topological insulator. *Phys. Rev. Lett.* **106**, 216803 (2011).
- Fu, L. & Kane, C. L. Superconducting proximity effect and Majorana fermions at the surface of a topological insulator. *Phys. Rev. Lett.* **100**, 096407 (2008).
- Chen, Y. L. *et al.* Massive Dirac fermion on the surface of a magnetically doped topological insulator. *Science* **329**, 659–662 (2010).
- Xu, S.-Y. *et al.* Hedgehog spin texture and Berry's phase tuning in a magnetic topological insulator. *Nat. Phys.* **8**, 616–622 (2012).
- Qi, X.-L., Li, R., Zang, J.-D. & Zhang, S.-C. Inducing a magnetic monopole with topological surface states. *Science* **323**, 1184–1187 (2009).
- Qi, X.-L., Hughes, T. L. & Zhang, S.-C. Topological field theory of time-reversal invariant insulators. *Phys. Rev. B* **78**, 195424 (2008).
- Hirahara, T. *et al.* Interfacing 2D and 3D topological insulators: Bi(111) bilayer on Bi<sub>2</sub>Te<sub>3</sub>. *Phys. Rev. Lett.* **107**, 166801 (2011).
- Wang, Z. F. *et al.* Creation of helical Dirac fermions by interfacing two gapped systems of ordinary fermions. *Nat. Commun.* **4**, 1384 (2013).
- Miao, L. *et al.* Quasiparticle dynamics in reshaped helical Dirac cone of topological insulators. *Proc. Natl Acad. Sci. USA* **110**, 2758–2762 (2013).
- Wang, X., Bian, G., Miller, T. & Chiang, T.-C. Topological spin-polarized electron layer above the surface of Ca-terminated Bi<sub>2</sub>Se<sub>3</sub>. *Phys. Rev. B* **87**, 035109 (2013).
- Hutasoit, J. A. & Stanescu, T. D. Induced spin texture in semiconductor/topological insulator heterostructures. *Phys. Rev. B* **84**, 085103 (2011).
- Guang, L. X. *et al.* Proximity effects in topological insulator heterostructures. *Chin. Phys. B* **22**, 097306 (2013).
- Zhang, J., Triola, C. & Rossi, E. Proximity effect in graphene-topological-insulator heterostructures. *Phys. Rev. Lett.* **112**, 096802 (2014).
- Essert, S., Krueckl, V. & Richter, K. Using topological insulator proximity to generate perfectly conducting channels in materials without topological protection. *New J. Phys.* **16**, 113058 (2014).
- Sato, T. *et al.* Direct evidence for the Dirac-cone topological surface states in the ternary chalcogenide TlBiSe<sub>2</sub>. *Phys. Rev. Lett.* **105**, 136802 (2010).
- Sato, T. *et al.* Unexpected mass acquisition of Dirac fermions at the quantum phase transition of a topological insulator. *Nat. Phys.* **7**, 840–844 (2011).
- Xu, S.-Y. *et al.* Topological phase transition and texture inversion in a tunable topological insulator. *Science* **332**, 560–564 (2011).
- Murakami, S. Quantum spin Hall effect and enhanced magnetic response by spin-orbit coupling. *Phys. Rev. Lett.* **97**, 236805 (2006).
- Raghu, S., Chung, S. B., Qi, X.-L. & Zhang, S.-C. Collective modes of a helical liquid. *Phys. Rev. Lett.* **104**, 116401 (2010).
- Koroteev, Y. M., Bihlmayer, G., Chulkov, E. V. & Blügel, S. First-principles investigation of structural and electronic properties of ultrathin Bi films. *Phys. Rev. B* **77**, 045428 (2008).
- Hirahara, T. *et al.* Direct observation of spin splitting in bismuth surface states. *Phys. Rev. B* **76**, 153305 (2007).
- Takayama, A. *et al.* Tunable spin polarization in bismuth ultrathin film on Si(111). *Nano Lett.* **12**, 1776–1779 (2012).
- Souma, S., Sato, T., Takahashi, T. & Baltzer, P. High-intensity xenon plasma discharge lamp for bulk-sensitive photoemission spectroscopy. *Rev. Sci. Instrum.* **78**, 123104 (2007).

## Acknowledgements

We thank Y. Tanaka, M. Nomura, K. Nakayama, H. Kumigashira, K. Ono and S. Kimura for their assistance in ARPES measurements and K. Eto for his assistance in crystal growth. This work was supported by JSPS (KAKENHI 23224010, 24654096, 25287079 and 25220708), MEXT of Japan (Innovative Area 'Topological Quantum Phenomena'), AFOSR (AOARD 124038), the Mitsubishi Foundation, UVSOR (Proposal No. 24-536) and KEK-PF (Proposal No. 2012S2-001).

## Author contributions

T.Sh., A.T., T.Sa., S.S. and T.T. performed ARPES measurements. T.O. carried out the band-structure calculations. K.S. and Y.A. carried out the growth of the single crystals and their characterizations. T.Sh., T.Sa., and Y.A. conceived the experiments and wrote the manuscript.

## Additional information

**Supplementary Information** accompanies this paper at <http://www.nature.com/naturecommunications>

**Competing financial interests:** The authors declare no competing financial interests.

**Reprints and permission** information is available online at <http://npg.nature.com/reprintsandpermissions/>

**How to cite this article:** Shoman, T. *et al.* Topological proximity effect in a topological insulator hybrid. *Nat. Commun.* 6:6547 doi: 10.1038/ncomms7547 (2015).